Suppressing Dendrites Growth of Zinc Metal Anodes by Modulating Electrode-Electrolyte Interfaces for the Development of High-Performance Zinc-ion Batteries

高性能亜鉛イオン電池開発のための電極-電解質界面制御による亜鉛金属負極のデンドライト成長の抑制

Ruijie Zhu

Graduate School of Chemical Sciences and Engineering

Hokkaido University

September 2023

Table of Contents

Chapter 1 General Introduction

1.1 Battery energy storage systems: a bridge from fossil energy to renewable energy

Fossil fuels is a significant source of energy for modern societies; the advantages of abundance, high reliability, affordability, and high energy density make them play an important role in lighting up human civilization for a long time.[1] However, subject to drawbacks from pollution, geopolitical risks, non-renewable resources and so on, in recent decades, there have been many attempts to replace fossil fuels through the use of other renewable energy sources.[2-4] Renewable energy sources, such as solar, wind, hydropower, geothermal, and biomass, are sources of energy that are replenished naturally and continuously. They are considered more sustainable and environmentally friendly than fossil fuels because they do not emit greenhouse gases or other pollutants. Renewable energy sources are also becoming increasingly cost-

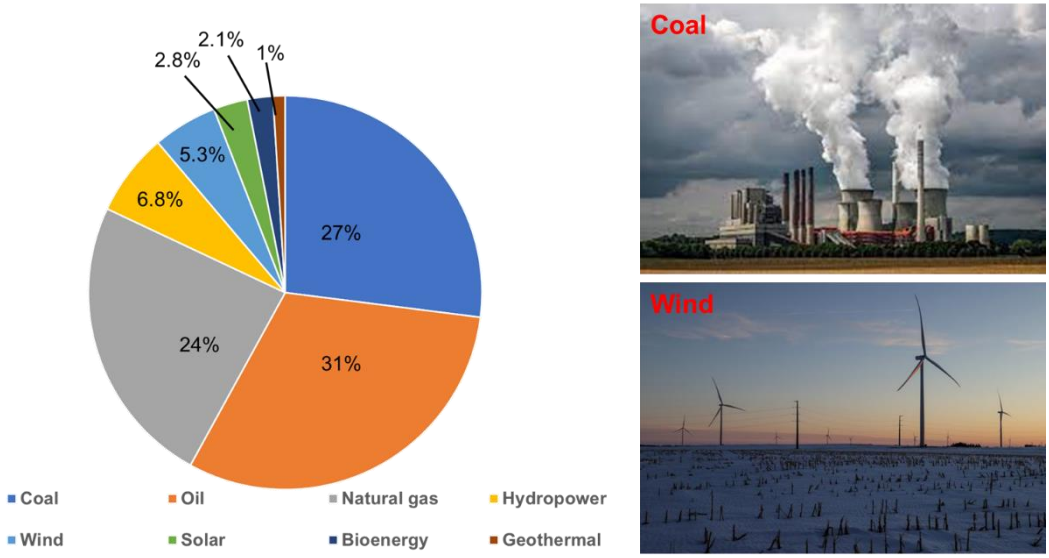

Figure 1.1 The contribution of different power generation methods to the global electricity generation share in 2021, and the use of renewable energy to replace traditional fossil energy is imminent. (The data and photos are from the website of U.S. Energy Information Administration (EIA): https://www.eia.gov/international/ and The Wall Street Journal)

competitive with fossil fuels, making them an attractive option for many consumers and businesses **(Figure 1.1)**. Taking Japan as an example, renewable energy will account for about 18% of the country's total power generation by 2019 (including about 6.7% solar, 7.7% hydroelectric and 0.7% wind).[5] However, for the intermittency of most renewable power, such a large amount of renewable energy actually struggles to provide enough power during peak electricity consumption. Even today, Japan often faces power shortages during peak electricity consumption in summer months. One of the key issues in the current utilization of renewable energy is how to store the "intermittent" renewable energy and supply it precisely to the needed area.[6] Energy storage systems can help integrate renewable energy sources like solar and wind power into the grid by storing excess energy during peak generation periods and releasing it during periods of high demand. [7] This can help reduce the reliance on traditional fossil-fuel-based power plants, leading to a more sustainable and environmentally friendly energy system. In order to achieve the effective management and application of renewable energy, it is important to establish a stable and reliable electrical energy storage system, and the energy storage system that uses batteries is considered promising **(Figure 1.2)**.

Compared with other energy storage systems, batteries are the most direct way to store electricity and can stably work for a long time with high energy density per unit volume.[8-10] The batteries can be widely used in common vehicles, including cars, ships, and even planes, to replace fossil energy with renewable energy. In all, the development of battery energy storage systems has an important relationship with the use of renewable energy, the development of new energy markets, economic growth, and the construction of a sustainable society, which makes battery research important in all aspects.[11-13]

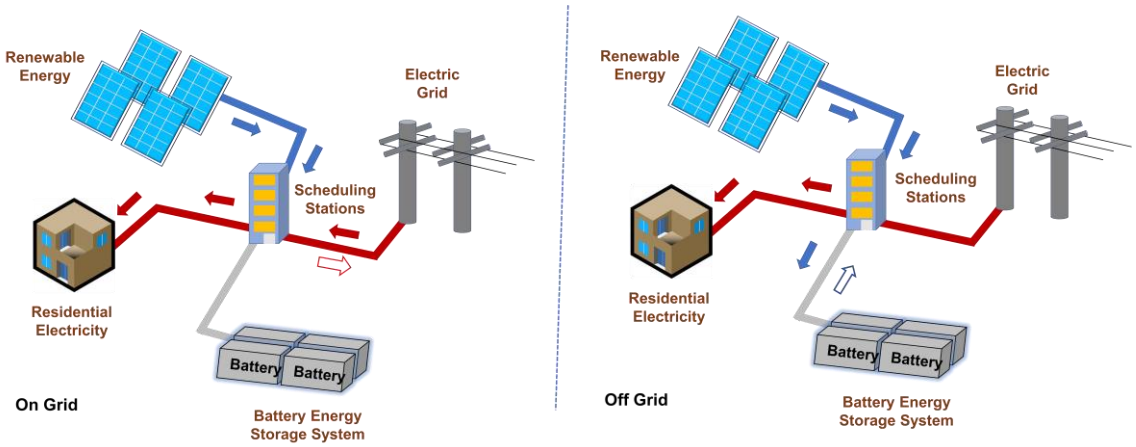

Figure 1.2 How battery energy storage systems can turn renewable energy from intermittency into continuous and reliable energy. The left and right pictures depict the situation when the system is connected to the electric grid or is not connected to the grid, respectively.

1.2 Promising batteries and their applications

Currently, many kinds of rechargeable batteries are being studied, and several types are available on the market. Here, I will briefly introduce the advantages and disadvantages of several secondary batteries, their current state of research, and their possible application scenarios.

First, lithium-ion batteries (LIBs) are rechargeable batteries that have become popular in a wide range of applications, from consumer electronics to electric vehicles. It is also considered the most promising battery that can be applied to large-scale grid energy storage at present. LIBs are famous for their high energy density, low self-discharge rate, no memory effect, and long lifespan.[14-15] However, the drawbacks of LIBs are also obvious, LIBs are expensive and are sensitive to harsh environments, e.g., high temperature, low temperature, humidity, etc., at the same time, LIBs use flammable organic electrolytes, there can be a great safety hazard when LIBs are accidentally damaged.[16-17] Cost and safety issues have greatly hindered the use of LIBs for large grid energy storage, although they are still the most reliable choice for portable electronics.[18-20]

Second, sodium-ion batteries (SIBs) are a type of rechargeable battery that use sodium ions as the charge carrier. They are a promising alternative to LIBs due to the abundance and low cost of

sodium compared to lithium. SIBs have the potential to be made into batteries with high energy density and have the advantages of low self-discharge rate and long cycle life.[21-23] However, the power density of SIBs is much lower than that of LIBs, which makes them difficult to be applied to portable electronics. In addition, research on SIBs is still at a very preliminary stage, and many problems remain to be solved, including the search for stable and reliable electrode materials.[23-25]

Third, nickel-cadmium (Ni-Cd) batteries and nickel-metal hydride (Ni-MH) batteries. These metal-based secondary batteries have been successfully commercialized for decades, but emerging battery products are squeezing their status due to unsatisfactory energy density, annoying memory effect (reduces capacity if not fully discharged before recharging), and short service life.[26-27] In fact, nowadays, the only car manufacturer that still uses Ni-MH batteries as a power battery is Toyota, and the application of NiMH batteries for grid storage is not favored.[28-30]

Fourth, redox flow batteries (RFBs) are unique rechargeable batteries that use two liquid electrolytes stored in external tanks and flow through a central stack of electrochemical cells during charge and discharge cycles. During operation, the two electrolyte solutions are pumped through a central reaction chamber, exchanging ions and creating an electrical current.[31] The key advantage of RFBs is that they can be recharged by simply replacing the spent electrolyte solutions with fresh ones, enabling them to have a potentially infinite cycle life.[32-33] Additionally, the use of external electrolyte tanks allows RFBs to be easily scaled up or down to meet specific power and energy requirements. RFBs are being considered for large-scale energy storage applications, such as grid-level renewable energy storage, due to their potential for high capacity and long cycle life[34-35]. However, challenges remain in improving their overall efficiency, reducing costs, and finding suitable electrode materials that can withstand corrosive electrolyte solutions[36].

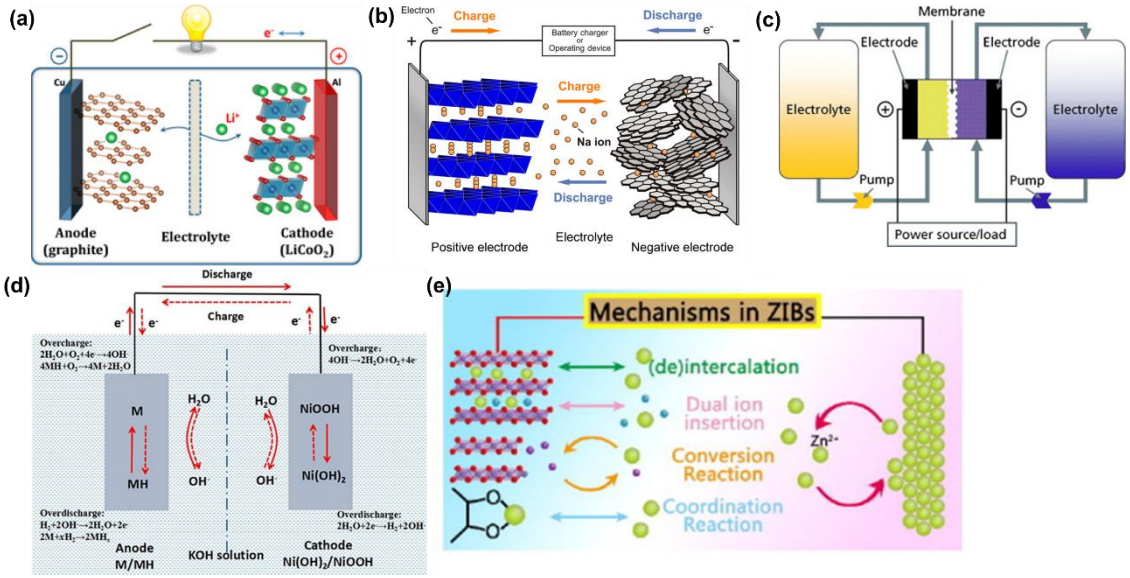

Figure 1.3 The schematic illustration of (a) LIBs, [37] (b) SIBs, [21] (c) RFBs, [32] (d) Ni-MH battery, [38] and (e) zinc ion batteries. [39]

Finally, aqueous zinc batteries (AZBs) is an old battery system, although the earliest Zn batteries did not rely on zinc-ions as carriers, but used acidic or alkaline electrolytes, until the 1990s, zinc-manganese secondary batteries using neutral electrolytes began to appear in the limelight.[40-42] Currently, AZBs using Zn metal as anode material are mainly primary batteries, but the high safety, excellent power density, and low cost of AZBs are attracting more and more attention for the development of rechargeable AZBs.[43] The configurations of the various batteries are simply listed in **Figure 1.3.**

1.3 Strengths and bottlenecks of rechargeable aqueous zinc-ion batteries

Rechargeable aqueous zinc-ion batteries (RAZIBs) are a type of energy storage device that is gaining more and more attention due to their high energy density, low cost, and environmentally friendly nature. [44-46] Generally, RAZIBs consist of an anode capable of providing zinc-ions (Zn-ions), an electrolyte with Zn-ions (or Zn-ions of the complex) as carriers, and a cathode capable of storing Zn-ions **(Figure 1.3(e))**. Due to the relatively low negative potential of Zn (-0.76V vs. standard hydrogen electrode, SHE), RAZIBs have high energy density compared to other aqueous

batteries, making them suitable for use in various applications, including portable electronics and grid energy storage. At the same time, Zn is abundant and inexpensive, making it a cost-effective material for battery production.[47-49] A simple comparison of various batteries in terms of cost and energy density is shown in **Figure 1.4**. Additionally, the use of water-based electrolytes reduces the cost of manufacturing and enhances safety; most of the manufacturing steps can be processed in the air. Finally, RAZIBs are non-flammable, and their aqueous electrolyte minimizes the risk of fire or explosion, making RAZIBs can be as regarded absolute safe.

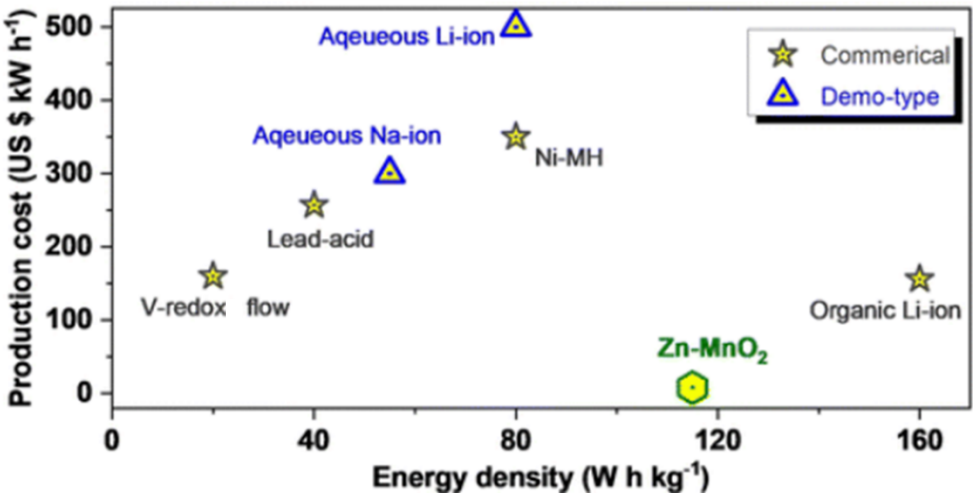

Figure 1.4 Comparing the price and energy density of the current common battery systems, RAZIBs (in the case of Zn-MnO_2 cells) have a significant price advantage and an energy density advantage to replace other battery systems than LIBs. [50]

However, RAZIBs also face some bottlenecks. As for the anode, RAZIBs suffer from a limited cycle life due to the formation of Zn dendrites during charging and discharging cycles, which can cause short circuits and reduce the battery's overall performance.[51-52] Meanwhile, although Zn metal reacts slowly with water, Zn metal is thermodynamically unstable in an aqueous solution, and corrosion is more pronounced in electrolytes with alkaline or acidic environment. Parasitic reactions on the anode side (e.g. hydrogen evolution reaction, HER) can produce a large amount of gas while generating electrochemically inactive by-products (e.g. ZnO), the consumption of

the electrolyte and the anode material results in a simultaneous decrease in the Coulombic efficiency and cyclic life of the cell **(Figure 1.5).**[53-55]

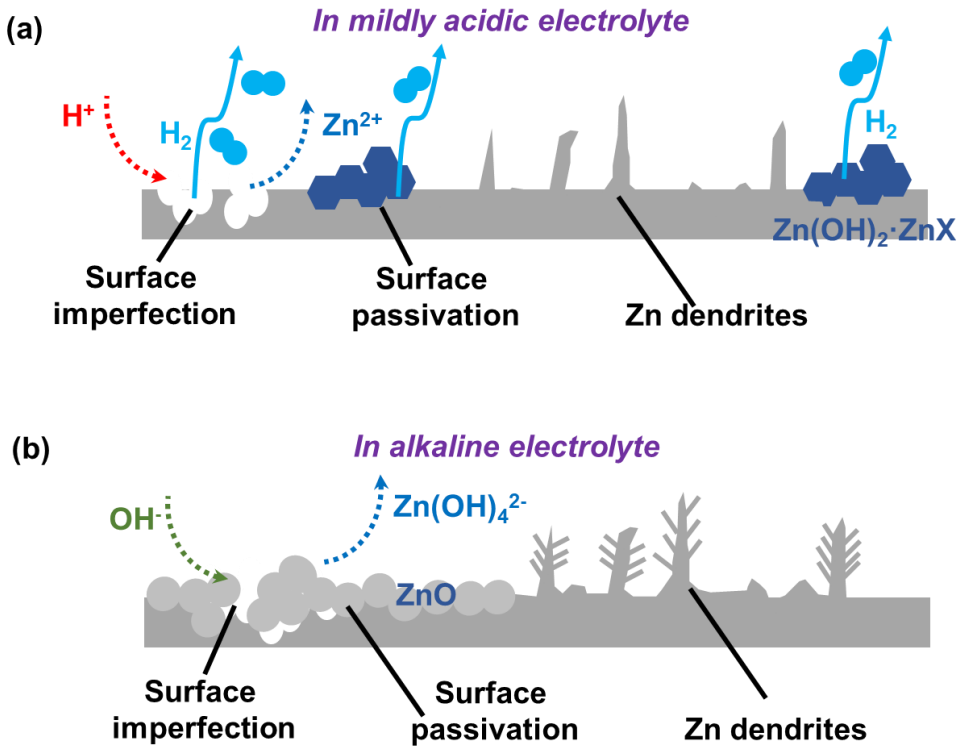

Figure 1.5 Problems faced by Zn anode in RAZIBs. (a) The situation of Zn metal anode in weakly acidic electrolytes, and (b) the problem of Zn metal anode in alkaline electrolytes.

As for the cathode in RAZIBs, the problem mainly focuse on material lifespan, energy density, and cost. The commonly used transition metal oxides, e.g., manganese dioxide (MnO_2) [56-58] and vanadium oxide (V_2O_5, VO_2) [59-61] suffer from severe capacity fading during cycling because the structure of these oxides greatly changed during charging/discharging.[62-63] In addition, these oxide materials can interact with the electrolyte including Zn-ions, H_2O molecules, and many other species in the electrolyte, resulting in a consistently inadequate understanding of these materials.[64-67] While organic cathodes, such as polyaniline, have excellent cycling stability and capacity, their production cost and discharge potential make them a difficult preference for RAZIBs cathodes.[68-69] Other materials, such as Prussian blue analog and iron hexacyanoferrate,

also have problems with easy structural damage during cycling and low discharge voltage. [70-73]Overall, the choice of cathode material in RAZIBs depends on several factors, including cost, energy density, and stability. Researchers are trying to improve the performance of these cathode materials and develop new materials that can address the limitations of existing ones.[47]

Finally, the electrolyte of RAZIBs can be classified as mildly acidic electrolytes, neutral electrolytes, and alkaline electrolytes. The basic electrolytes such as potassium hydroxide (KOH) and sodium hydroxide (NaOH) aqueous solutions show an ability to increase the discharge capacity of oxide cathode materials while providing excellent ionic conductivity, which has led to the widespread use of alkaline electrolytes in primary batteries.[74-75] Zn-ions are present in this type of electrolyte in the form of $Zn(OH)_4^{2-}$ generally. However, the cyclic lifespan of RAZIBs using alkaline electrolytes is often very limited due to the extreme instability of the Zn metal in such electrolytes. In addition, Zn generates huge Zn dendrites when plating/stripping in alkaline electrolytes, which makes the realization of reliable alkaline RAZIBs very difficult.[76-77] Neutral electrolytes, such as zinc acetate ($Zn(CH_3COO)_2$) aqueous solution can provide a relatively mild pH environment, which can slow down the corrosion of Zn to some extent, but the solubility of such salts is often not ideal, which certainly limits the use of neutral electrolytes.[78-79] Mildly acidic electrolytes, such as zinc sulfate ($ZnSO_4$) and zinc chloride ($ZnCl_2$) aqueous solutions, have high ionic conductivity and can guarantee a highly reversible Zn deposition due to the conversion between Zn metal and Zn-ion can be done directly. [80-82]However, in this type of electrolyte, Zn will spontaneously dissolve into the electrolyte, leading to instability at the anode/electrolyte interface, due to severe HER reactions. Nevertheless, these electrolytes are still most frequently used in the study of RAZIBs because of their great advantages in terms of cost, ionic conductivity, battery performance, and practical applying potential.[83]

Overall, the choice of the electrolyte in RAZIBs will depend on the specific performance requirements of the battery and the desired tradeoff between capacity and stability. Researchers are continuing to explore new electrolyte formulations and additives that can improve the performance and stability of RAZIBs across a range of pH values.

1.4 Zn dendrites formation in mildly acidic electrolyte

RAZIBs using mildly acidic electrolytes have received increasing attention in the last decade because of their excellent cyclic performance supported by such electrolytes and their potential to be used in various energy storage scenarios.[84-86] Although in the early stage, many studies believe that Zn dendrites will not generate in mildly acidic electrolyte, frustratingly, short-circuits are still commonly observed in cells using such electrolytes during cycling: Zn dendrites are still generated in mildly acidic electrolytes.[87]

Unlike the Zn dendrites formed in KOH electrolytes, which have defined tree-like morphology, the Zn dendrites formed in mildly acidic electrolytes are typically more branched and irregular in shape than those formed in KOH electrolytes.[88-92] Hence, the commonly accepted formation mechanism of Zn dendrites in mildly acidic electrolytes includes mainly 3 points (**Figure 1.6**):

1. Uneven distribution of electric field: the electric field within the battery can be uneven, leading to local high current density and the formation of Zn dendrites.[93-96]

2. The concentration gradient of an electrolyte near the electrode surface: as Zn-ions are consumed/formed during electrochemical cycling, the local concentration of Zn ions near the electrode surface can decrease/increase, leading to the formation of Zn dendrites.[93, 97-98]

3. Poor surface conditions: the poor adhesion between the separator and electrode or the uneven surface condition of the current collector can create cracks or tips where Zn dendrites can form. [99-101]

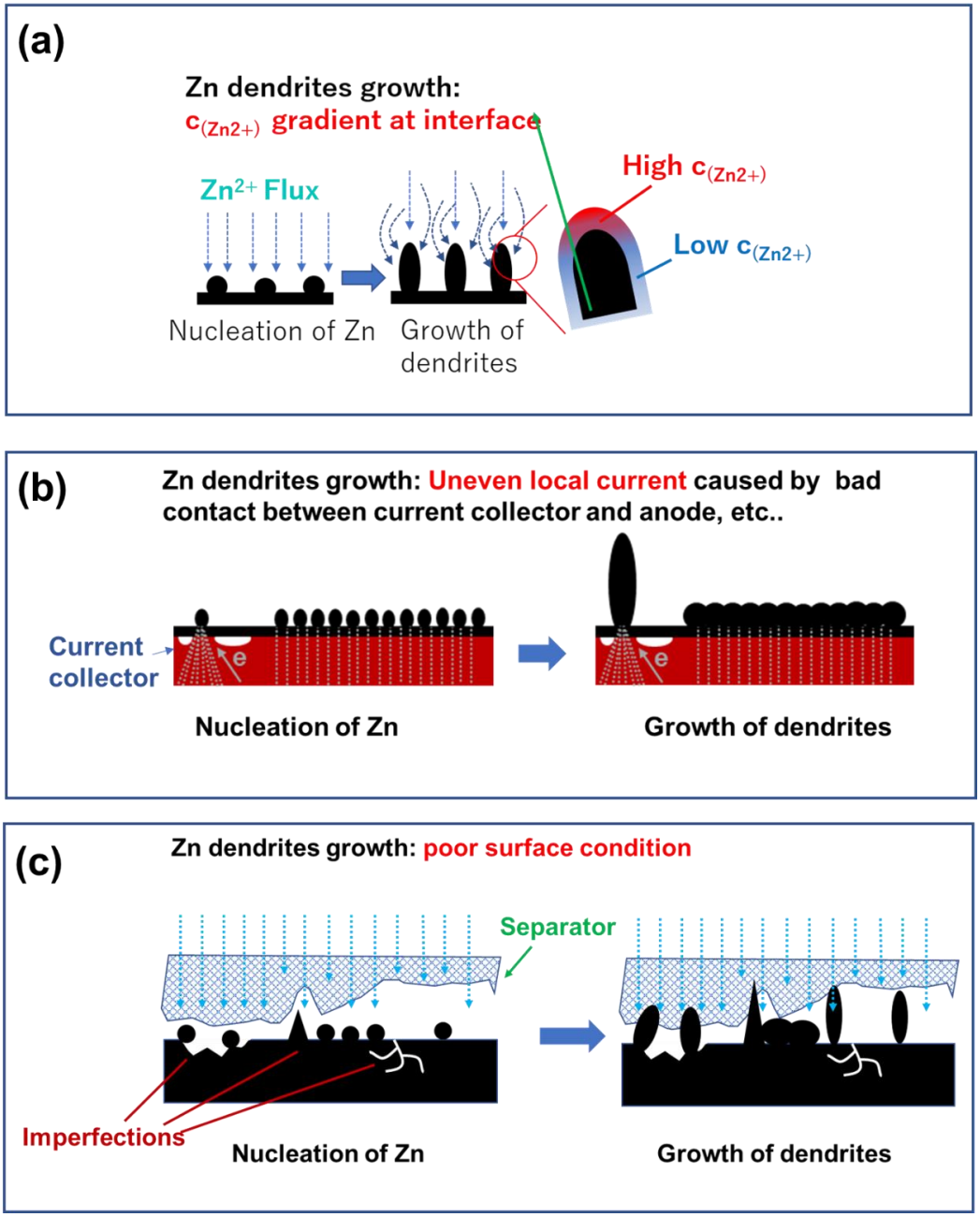

Figure 1.6 The commonly accepted mechanism of Zn dendrites formation in mildly acidic aqueous electrolyte. Schematic illustration of (a) ions concentration gradient and tip effect induce Zn dendrites growth; (b) uneven current distribution leads to high local currents that promote Zn dendrites growth; and (c) the poor surface condition induces the growth of Zn dendrites.

Considering that the dendrite morphologies of both Zn and Li have some similarities, these ideas coincide with the lithium dendrites growth has received great attention, and these ideas

about the growth mechanism of Zn dendrites have been widely accepted.[102-103] In 2019, building on these ideas, Zheng et al. proposed that lattice mismatch is the initial cause of induced Zn dendrite growth, for example, materials with similar lattice constant to the (002) crystal plane of Zn induce Zn deposition in an epitaxial manner on the (002) plane, while inconsistent materials induce Zn deposition in a haphazard manner, which aggravates the irregular distribution of current density and ion concentration on the electrode surface and thus leads to dendrite growth. [104]

However, there are some other voices around the causes of Zn dendrites generation. Some believe that the type of electrolyte will determine the generation of Zn dendrites or not, and some believe that the generation of hydroxyl zinc salts (e.g., $Zn(OH)_x \cdot ZnSO_4$) will promote the generation of Zn dendrites. In addition, some believe that the hydroxyl zinc salts can be a protective layer for the anode. The current research always lacks decisive evidence on the mechanism of Zn dendrites generation in mildly acidic electrolytes, which makes various strategies to suppress dendrite growth also encounter some difficulties in explaining their effectiveness **(Figure 1.7)**.[95, 105-107] Despite these controversies, there is a general consensus that the formation of Zn dendrites in RAZIBs is a significant challenge that must be overcome to realize these batteries for energy storage applications.

1.5 Protection strategies for Zn metal anode

In order to improve the overall performance of RAZIBs, many protection strategies for Zn anodes have been proposed. Here, some commonly employed strategies in the mildly acidic electrolytes will be introduced to demonstrate the current status of research on the anode of RAZIBs:

Modifying the electrolyte from the aspects of composition, pH, and concentration can influence the nucleation and growth of Zn crystals.[108-110] The use of highly concentrated electrolytes (HCEs) reduces the corrosion on the anode surface and reduces the effect of ion concentration gradients, thus improving the cycle life of the Zn anode.[111-112] The zinc deposition behavior can also be optimized by adding small organic molecules to form different solvated structures of Zn-ions. [113-114]

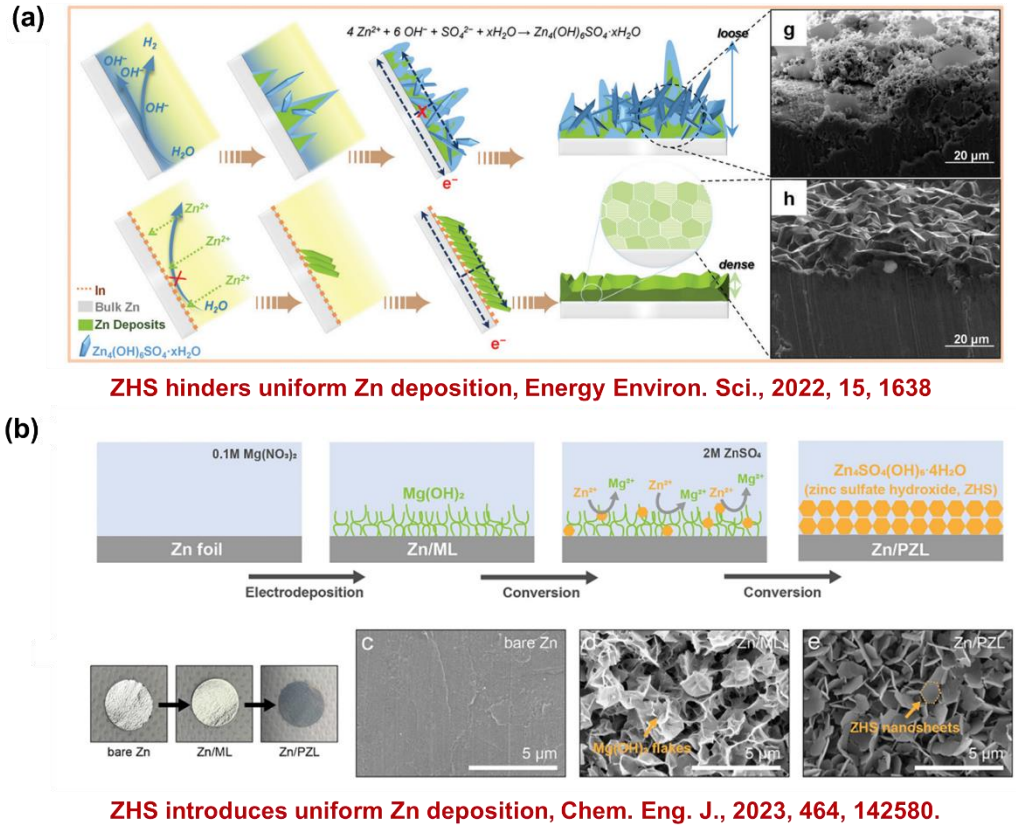

Figure 1.7 Some arguments on the cause of Zn dendrites formation. (a) Suggesting that the production of zinc hydroxy sulfate (ZHS) promotes Zn dendrites growth.[115] (b) Suggesting that ZHS itself is an excellent protective layer for Zn anode.[106]

Coating the surface of the Zn anode with a protective layer can prevent direct contact between the electrolyte and the Zn metal, reducing the likelihood of dendrite formation.[116-117] Examples of coatings include zeolite, carbonate or phosphate nanoparticles, polymers, and carbon-based materials.[118-119]

Modifying the design of the electrode can also reduce the formation of dendrites. For example, using three-dimensional electrode structures can disperse local current density and ion flux, thus regulating the deposition of Zn metal.[120-122]

Controlling external conditions of the cell, e.g., applying an external current or voltage to the electrode during charging and discharging, can also help prevent dendrite formation. The

exampled technique, known as "pulsed charging/discharging," involves applying short bursts of current or voltage to the electrode to encourage uniform deposition and dissolution of Zn metal.[123]

Among these strategies, it is obvious that interface engineering (e.g., anode surface coating, functional separators, and electrode surface optimization) plays a significant role in improving the performance and stability of the Zn metal anode. Since the interface engineering works directly at the electrolyte/electrode interface, it has a good performance for suppressing the dendrite growth and reducing the corrosion suffered by the Zn metal, improving the Zn utilization and reversibility of deposition (**Figure 1.8**). At the same time, anode interface engineering generally does not affect the performance of the cathode (and vice versa) compared to direct adjustment of the electrolyte or the application of external influences, making the search for solutions to the problems of the Zn anode at the electrolyte/electrode interface a study with both practical potential and scientific significance.

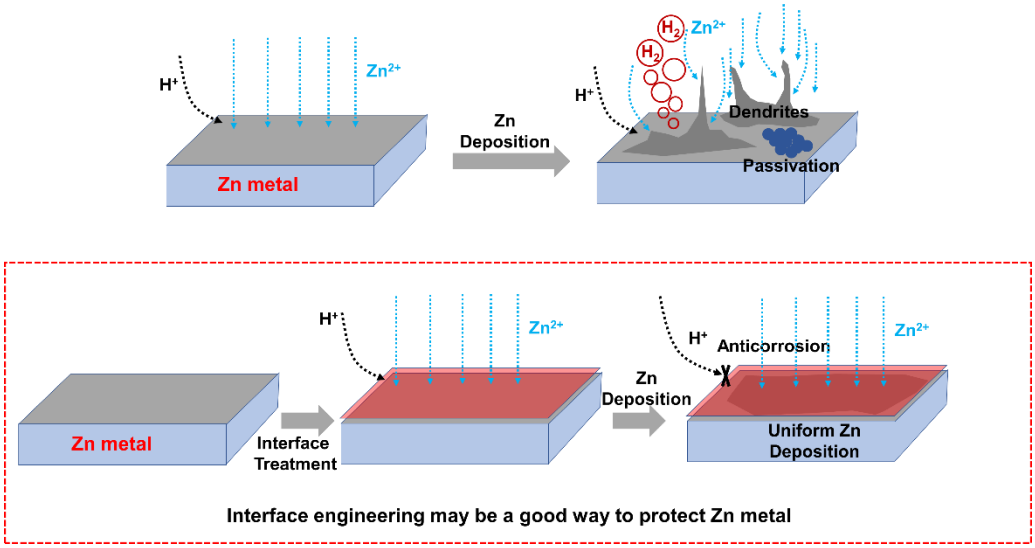

Figure 1.8 The problems that may arise when using a Zn metal anode directly in a weakly acidic electrolyte (top), and the optimization of the interface between the electrode surface and the electrolyte may be able to eliminate dendrite growth while reducing the corrosion of Zn metal by the electrolyte (bottom).

Also, these protection strategies can be used alone or in combination to improve the performance of Zn anodes in RAZIBs. It should be noted, however, that these optimization strategies reported so far are often controversial in explaining their effectiveness because studies on the causes of failure of the Zn anode are still imperfect. There are still many efforts that can be made in the practicalization of RAZIBs.

1.6 Objectives of this dissertation

1.6.1 Motivation for this study

RAZIBs have emerged as a promising alternative to many conventional batteries due to their unique advantages, including low cost, abundant, and non-flammable. On many occasions, RAZIBs are a more sustainable and environmentally friendly choice than other battery systems. Moreover, RAZIBs have shown great potential for large-scale energy storage applications, such as grid-level storage systems. The low cost and safety of RAZIBs make them an attractive option for renewable energy storage, which is essential for transitioning to a cleaner and more sustainable energy system. Furthermore, RAZIBs could also significantly impact the development of electric vehicle batteries, providing a more cost-effective and sustainable solution to the current reliance on lithium-ion batteries.

However, the current RAZIBs still face many problems, and one of the major ones is the reversibility of the Zn anode during charging/discharging and the dendrites problems. The reversibility problems are mainly caused by the corrosion of Zn by aggressive species in water, which may be accelerated in the presence of an applied current. The generation of dendrites may lead to direct damage to the cell. There is still much debate about the causes of dendrites in RAZIBs, and this has led to slow progress in developing Zn anodes that can meet the demands of real-world applications.

In order to provide a systematic approach to the protection of Zn anodes and promote the real-world application of RAZIBs, this dissertation aims to explore the causes of Zn dendrites generation in mildly acidic electrolytes, starting from the relationship between hydroxy zinc salts and parasitic reactions and Zn dendrites generation. Moreover, based on the causes of Zn dendrites

generation, several options for Zn anode protection by adjusting the electrolyte/current collector interface or the electrolyte/Zn metal interface will be proposed to provide more options for improving the performance of Zn metal anodes while validating the theory of dendrites generation. Further study in this field could lead to significant advancements in energy storage technology, which will play a crucial role in transitioning to a more sustainable energy system.

1.6.2 Outline of this dissertation

This dissertation composes of six chapters as follows:

Chapter 1 The first chapter is a general introduction, where the unique advantages of RAZIBs over other batteries and their broad application prospects are first introduced. It also introduces the current challenges in the development of RAZIBs and provides an overview of current research on Zn metal anode while pointing out the current debate on the key issue of Zn dendrites growth. Finally, the author proposes a rational mechanism for Zn dendrites growth in mildly acidic electrolytes and present a series of schemes to limit Zn dendrites growth based on optimization of the electrode-electrolyte interface.

Chapter 2 systematically analyzes the causes of Zn dendrites in mildly acidic electrolytes. The relationship between HER, zinc hydroxy sulfate (ZHS), electrodeposition current, and Zn deposition morphology is explained. Furthermore, the effect of substrate on the deposition behavior of Zn metal is explained using different metal substrates as examples. In the $ZnSO_4$ electrolyte, the HER will occur earlier than the Zn electrodeposition reaction, and the HER promotes the production and accumulation of ZHS on the anode surface. When the deposition potential of Zn is reached, Zn metal will grow together with ZHS, which will grow along the concentration gradient of Zn-ion, leading to the growth of Zn metal into dendrites together with ZHS. The electrodeposition current will largely affect the deposited morphology of Zn metal because the electrodeposition current will change both the overpotential and the ion concentration at the interface. The deposited Zn metal at high current densities (>10 mA cm^{-2}) will have a very flat morphology due to the suppression of ZHS production at high currents. Different deposition substrates, on the other hand, have different reversibility of Zn deposition because of their

different catalytic activity for HER reaction and different affinity with Zn. Here, titanium (Ti) and copper (Cu) are considered as better deposition substrates, while stainless steel (SS) and aluminum (Al) are the least suitable choices as Zn deposition substrates.

Chapter 3 builds on the conclusions of Chapter 2 and devises a strategy to optimize Zn deposition by directly changing the surface properties of the substrate. In this chapter, magnetron sputtering was used to deposit niobium (Nb) onto the surface of the Al foil, resulting in a dense Nb coating with a thickness of about several hundred nanometers on the surface of the Al foil. The Nb coating optimizes the corrosion resistance of the current collector and the performance of Zn deposition while maintaining its low-weight properties of the Al current collector. It was found that the surface of Nb has a dense passivation layer, and its composition is mainly Nb_2O_5. Since the point of zero charge (PZC) of Nb_2O_5 is almost the same as the pH of $ZnSO_4$ electrolyte, which makes ZHS cannot easily generate on its surface, the presence of Nb_2O_5 can also induce the regular deposition of Zn, which makes good Zn plating/stripping reversibility can be observed on the Nb coating surface, the Coulombic efficiency of Zn plating/stripping is higher than 99% when a high deposition capacity of 6.25 mAh cm^{-2} was applied. Meanwhile, the Al foil with Nb coating can also be directly used as a current collector for the MnO_2 cathode. RAZIBs using the resultant material as the anode/cathode current collector can be stably cycled for 120 cycles with 90% capacity retention in a harsh environment (the negative to positive ratio, N:P ratio = 3:1). Considering that the modification of the current collector mainly changes the contacted region between Zn metal and substrate, i.e., the Zn deposition behavior in the nucleation stage. The optimization of the Zn metal part is also necessary to achieve a stable Zn metal anode.

In Chapter 4, for Zn metal itself, I designed a solution for electropolishing Zn metal using a non-toxic and non-corrosive diethylene glycol (DEG) solution of sodium chloride (NaCl) as an electrolyte to optimize the performance of the Zn metal anode. By removing the excessively thick passivation layer and homogenizing the surface properties of the Zn metal, the subsequent deposition of Zn can become more uniform. At the same time, the author found that Zn is prone to deposit on the polished region. Since the mildly acidic electrolyte maintains the surface properties of the electropolished Zn metal well, Zn can be plated/stripped more than 6000 times

stably at a current density of 40 mA cm^{-2} and an areal capacity of 2 mAh cm^{-2} on the electropolished Zn foil. The polished Zn metal also exhibits better cyclic performance when charging/discharging Zn-MnO_2 cells with an areal capacity of more than 20 mAh cm^{-2}. Moreover, electropolishing of Zn metal is a treatment that can be combined with the most currently reported anode protection strategies to form a composite strategy. However, I also found that the deposition state of Zn gradually changes during the long charging/discharging cycle because the ZHS and bubbles brought by HER will accumulate on the electrode surface during the electrochemical process, making the effect of the protection strategy on the Zn anode continuously weakened.

Therefore, in Chapter 5, I used double network hydrogels with high mechanical strength as separators. The semi-solid electrolyte based on poly(2-acrylamide-2-metyl-propane sulfonic acid)-polyacrylamide (PAMPS-PAM) hydrogel can reduce the tendency of Zn metal to grow upward by a modified mechanical suppression effect, and thus forcing the Zn deposition to become uniform and flat. In this way, even if the surface properties of Zn metal change during cycling, Zn deposition will always be influenced by the separator from above. Zn deposition under hydrogel electrolyte protection exhibits a slight increase in overpotential and can be stably plated/stripped over 1000 times at 5 mA cm^{-2}, 2.5 mAh cm^{-2}. The Zn-MnO_2 cell with hydrogel electrolyte can be stably charged/discharged more than 500 times at a surface capacity of 4.5 mAh cm^{-2} with a capacity retention rate close to 50%. The success of this strategy also provides a new idea for the screening of diaphragms for RAZIBs.

In all in this dissertation, a comprehensive discussion of the mechanism of Zn dendrite growth in mildly acidic electrolytes is presented. Furthermore, based on this growth mechanism, I propose three different strategies for protecting the Zn metal anode from the perspective of adjusting the current collector-electrolyte interface and adjusting the Zn metal-electrolyte interface, respectively. I believe these works will provide new insights into the protection of Zn anode in RAZIBs and promote the development of related cell research and materials research.

Chapter 6 provides a general conclusion and perspective for effectively developing reliable Zn metal anodes, thus boosting the real-world applicable RAZIBs.

Chapter 2 Revealing the causes and factors influencing the growth of Zn dendrites in mildly acidic electrolytes.

2.1 Objective of this Chapter

The essential element of the zinc electrode faces suboptimal rechargeability (less than 1000 times) primarily due to irregular zinc morphology changes associated with high electrode porosity. This, in turn, leads to early short-circuiting in zinc-based electrochemical systems.[124-125] The uneven microstructures resulting from Zn electrodeposition, which develop into various dendritic formations, can lead to significant loss of mass and charge. This is closely related to the deterioration of interface and interfacial properties.

In the majority of instances, Zn electrodeposition must overcome a substantial overpotential barrier during nucleation before entering the growth phase. A higher crystallization overpotential promotes the formation of additional nuclei, resulting in a denser three-dimensional morphology that is perpendicular to the base plane of the substrates.[126] In some instances, Zn electrodeposition does not display a noticeable nucleation overpotential due to the underpotential deposition (UPD), which creates a well-adhered monolayer, or because it is part of an alloying process that results in the formation of a new alloy phase, [127-128] which also reduces the overpotential of subsequent Zn growth process. It generally happens to the substrates with higher work function than Zn, such as silver (Ag), copper (Cu), and gold (Au), with the deposition habit of forming a layered-like hexagonal pattern.[129] The deposition behavior was suggested to be related to the differences in atomic radii between substrates and zinc, with substrates having atomic radii more similar to zinc assumed to follow a layer-like zinc deposition pattern. Based on this idea, a graphene protective layer with minimal lattice mismatch with Zn encouraged an epitaxial zinc deposition mechanism and enhanced zinc reversibility to 99.7% at a high current density of 40.0 mA cm^{-2}.[104, 126] Nonetheless, in addition to Zn reduction, there is an inevitable, significant, and undesired hydrogen (H_2) evolution and its associated side-reactions in aqueous electrolytes. Numerous studies have been conducted on the hydrogen evolution reaction (HER) in catalysis, where H_2

evolution typically does not commence at the equilibrium potential but demands a starting overpotential. The crucial step in H_2 evolution is the chemisorption of H atom on substrates, where metals with partially occupied orbitals, such as platinum (Pt) and palladium (Pd), can lower the overpotential and facilitate H_2 formation.[130] Conversely, by increasing the polarization overpotential of H_2 evolution through using less noble foreign substrates or a complete plating/stripping process, the significantly reduced kinetics of HER would concurrently diminish the galvanic Zn corrosion, thereby collectively enhancing the Faraday efficiency of the entire electrolytic system. On the contrary, enlarging the polarization overpotential of the H_2 evolution by adopting a less noble foreign substrate or fully obstructing the active sites for H_2 adsorption will slow down the gassing kinetics. In the Zn plating/stripping process, the much-reduced kinetics of HER would simultaneously weaken the galvanic Zn corrosion, thus synergistically promoting the Faraday efficiency of the whole electrolytic system.[131] In addition, many debates exist around the causes of Zn dendrite growth in mildly acidic electrolytes. The common views include uneven distribution of interfacial ion concentration inducing dendrite generation and high local current density leading to dendrite generation. [102-103] Whether ZHS hinders the diffusion of Zn-ions on the electrode surface is also one of the main points of controversy. However, there is still no result that can well explain the cause of zinc dendrites generation. [95, 105-107] This has made it difficult for many studies to explain their effectiveness in optimizing Zn metal anodes and has left the current studies without a reliable guide to design optimization schemes for Zn anodes. [104]

In this Chapter, a universal guideline is proposed to promote Zn reversibility by making the electrochemical reaction favor Zn deposition over HER. In addition, the co-growth of insulated by-products originating from the HER process was revealed to be a detrimental factor for Zn dendrite formation. These insights helped us to determine that modulating the HER or Zn deposition activity at the Zn deposition interface would dramatically change the reliability of the Zn anode in RAZIBs.

2.2 Experimental Section

2.2.1 Preparation of the electrolytes and the electrodes

All the materials were stored in the ambient environment without special attention. The $ZnSO_4.7H_2O$ (Tokyo Chemical Industry) was dissolved into deionized water to prepare electrolyte (2 mol L^{-1} $ZnSO_4$ water solution) for all test cells except special description. The pH value of 2 mol L^{-1} $ZnSO_4$ electrolyte measured by the Meter-Lutron pH-208 was 4.05. Then, the K_2SO_4-H_2SO_4 electrolyte with a similar pH value with 2 mol L^{-1} $ZnSO_4$ electrolyte was formulated by firstly diluting 1M H_2SO_4 into deionized water with similar pH and then dissolving the calculated amount of K_2SO_4. The pH of K_2SO_4-H_2SO_4 electrolyte was measured as 4.13 in this work to calibrate the onset potential of the hydrogen evolution reaction. The glass fiber (GF/A, Whatman-100) filters were cut-off into plates with a diameter of 16 mm as separators without further treatment. The Zn foil (Nilaco company, 100 μm, purity>99.99%) was polished to remove contaminants and oxide coating in ethanol solutions and was cut into plates with a diameter of 10 mm prior to electrochemical characterizations. The graphite electrode was prepared by mixing 90 wt% graphite powder (Li-ion Chemical Industry Co., Ltd.), and 10 wt% polyvinylidene fluoride (PVDF, Du Pont-Mitsui Fluorochemicals Co. Ltd.) in N-methyl pyrrolidine (NMP, Sigma Aldrich, 99%) solvent. Then the obtained slurry was homogeneously coated on a glass pane by a blade-cast method and then transferred to a vacuum oven (80℃) to fully eliminate the NMP solvent. Then, the graphite electrode on the glass pane was soaked in methanol solvent to obtain a free-standing graphite electrode, which was finally transferred to a vacuum oven (80℃) for drying.

2.2.2 Cell assembly and electrochemical characterization

The potentials used in this study were referenced to Ag/AgCl with a saturated KCl solution in the three-electrode system and Zn/Zn^{2+} in the two-electrode system without further illustration. All testing CR-2032 coin-type cells (Hohsen Corp) used in this work were assembled in an ambient environment without special attention. All the cells remained on an open circuit potential for 4 hours before electrochemical characterizations. The galvanostatic charge-discharge tests were carried out in a battery tester system (Neware Technology Co.) at 25℃. The asymmetric

Zn||Cu cells were assembled by a stack of Zn plate, GF separator, and Cu plate with 40 μL 2 mol L^{-1} $ZnSO_4$ aqueous electrolyte. The Zn reversibility in the Zn||Cu cells was obtained from the capacity ratio of Zn stripping (controlled by the cutoff potential of 0.5 V *vs.* Zn/Zn^{2+}) to the Zn plating process (controlled by time). The configuration of the half cell is shown in **Figure 2.1.** In the second protocol, the average efficiency was calculated by the cycle number, where pre-deposited Zn was finally consumed during repeated cycling, according to Doron Aurbach's method. Linear sweep voltammetry was measured on an electrochemical workstation (Princeton VersaSTAT3). The three-electrode system is composed of Zn foil (counter electrode, CE), Ag/AgCl electrode (reference electrode, RE), and metal substrate plate (working electrode, WE), respectively. Different metal substrates were cut into rectangles into the 2 mol L^{-1} $ZnSO_4$ electrolyte with an immersion area of about 1.5 cm^2. The area of CE is controlled as 4*3 cm^2, which is directly facing the WE. All the backsides of WE and CE were covered by adhesive tape to avoid the enlargement of the contact area and undesirable side reactions. The sweep rate was 5 mV s^{-1} for Zn electrodeposition. For the HER test, the electrolyte was changed to K_2SO_4-H_2SO_4 electrolyte with a similar pH value with 2 mol L^{-1} $ZnSO_4$ electrolyte. The CE was replaced into Pt foil with an area of 2*2 cm^2 without changing the RE and WE. The sweep rate was 5 mV s^{-1} for detecting the formation of hydrogen.[132] The Electrochemical impedance spectra (EIS) of symmetric Zn cells were measured in Potentiostat/Galvanostat PGSTAT30, Autolab Co. Ltd., Netherlands, with the frequency ranging from 100 kHz to 0.1 Hz.

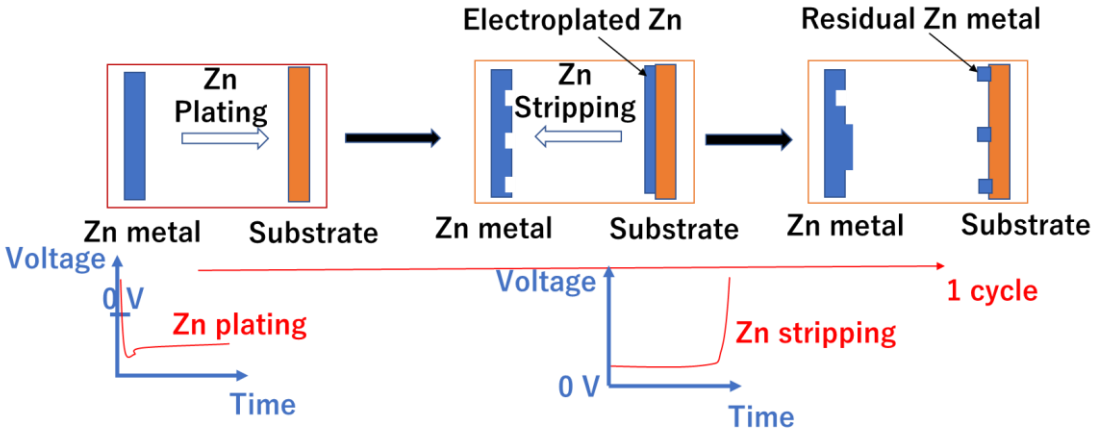

Figure 2.1 Schematic illustration for explaining the half-cell test.

2.2.3 Characterization of materials

After electrochemical tests from cells, all the electrode samples were rinsed several times in dimethoxyethane (DME) to remove the precipitated salt residues on the surface. In this chapter, a focused ion beam (FIB) technique (HITACHI FB-2100) was adopted to prepare a thin sample for high-resolution transmission electron microscopy (HRTEM) observation and the corresponding elemental mapping (**Figure 2.2**). For the Zn electrodeposition sample on Cu substrate (0.3 mA cm^{-2}, 3.0 mAh cm^{-2}), the FIB selected a flake-like structure for further scanning transmission electron microscopy (STEM) and HRTEM.

X-ray diffraction (XRD) patterns were obtained using an X-ray diffractometer (Rigaku MiniFlex600) using Cu Kα radiation. The in-plane X-ray diffraction (XRD) patterns were obtained by an X-ray diffractometer (Rigaku RINT2000 Ultima) using Cu Kα radiation. Scanning electron microscope (SEM) observations and energy dispersive spectroscopy (EDS) measurements were conducted on an SEM (ZEISS Sigma 500). High-resolution transmission electron microscopy (HRTEM) observation and elemental analysis were conducted on a Cs-corrected scanning transmission electron microscope (STEM, Titan3 G2 60-300, FEI Company). X-ray photoelectron spectroscopy depth profiles were obtained by X-ray photoelectron spectroscopy (XPS, JEOL, JPS-9200) system, and the Mg-Kα X-ray source (hν = 1253.6 eV) was chosen. Electron backscatter diffraction (EBSD) mapping was obtained from an EBSD component attached to an Auger electron spectroscopy system (JAMP-9500F), while Auger electron spectra were also obtained by the JAMP-9500F Auger electron spectroscopy system.

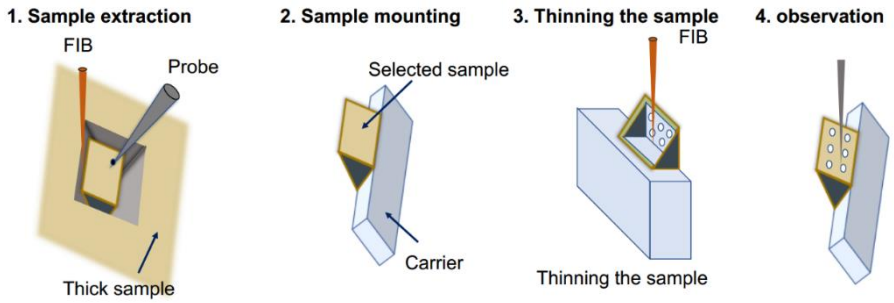

Figure 2.2 Schematic illustration for the preparation of FIB treated samples.

2.3 Results and Discussion

2.3.1 H_2 evolution prior to Zn reduction

HER is a universal and valuable cathodic reaction in electrochemical water splitting, but its gassing imposes an extra burden on aqueous energy storage systems. To figure out its role during Zn reduction, the polarization curves were measured by linear sweep voltammetry (LSV) with graphite (Gr) substrate working electrode. The adoption of Gr electrode avoids the complex interfacial interaction of other metal substrates, especially under low potentials, for example, the possible alloying processes and the UPD phenomena. In a 2 mol L^{-1} $ZnSO_4$ aqueous solution (pH 4.05), the cathodic current is typically ascribed to the sum of HER and Zn reduction **(Figure 2.3(a))**.[133] In the LSV profile, the prompt and clear response commencing at -1.03 V can be confirmed as the Zn reduction onset potential (E_R) in 2 mol L^{-1} $ZnSO_4$ electrolyte. Considering the high dependence of H_2 evolution kinetics on the activity of H^+ in electrolytes,[132] a pH-equivalent K_2SO_4-H_2SO_4 electrolyte (pH: 4.13) was formulated to exclusively investigate the HER behavior without the interference of Zn reduction (**Figure 2.3(d, e)**). In such cases, any cathodic current signal can be ascribed to H_2 formation.

The progressively increasing cathodic current demonstrated the persisting HER even at noble potential (**Figure 2.3(b)**). By comparison, the cathodic current originating from HER seems too minute to be noticeable with the adoption of Gr working electrode and may be neglected in most reports. To qualitatively measure the accumulative impact of HER, the potential of the three-electrode system was then maintained at -0.99 V (vs. Ag/AgCl electrode), where Zn reduction is not yet happened. The float-test leakage current (**Figure 2.3(c)**) and the visible bubble sites indicate the ongoing H_2 formation (**Figure 2.3(f)**). After potentiostatic measurement over 20 h, the Gr electrode surface was almost completely covered by a typical hexagonal flake-like component within the scope of millimeters in scanning electron microscope (SEM) observation (**Figure 2.4**). [134-135] The precipitated layer is composed of Zn, S and O species, which implies the concomitant passivation reaction in addition to H_2 evolution. The component was approved as zinc hydroxide sulfate hydrate (ZHS, $Zn_4(OH)_6SO_4 \cdot xH_2O$) by the strong diffraction peaks in X-ray powder diffraction (XRD) and elemental distribution in X-ray photoelectron spectroscopy

(XPS) (**Figure 2.5(a-d)**).[136-137]

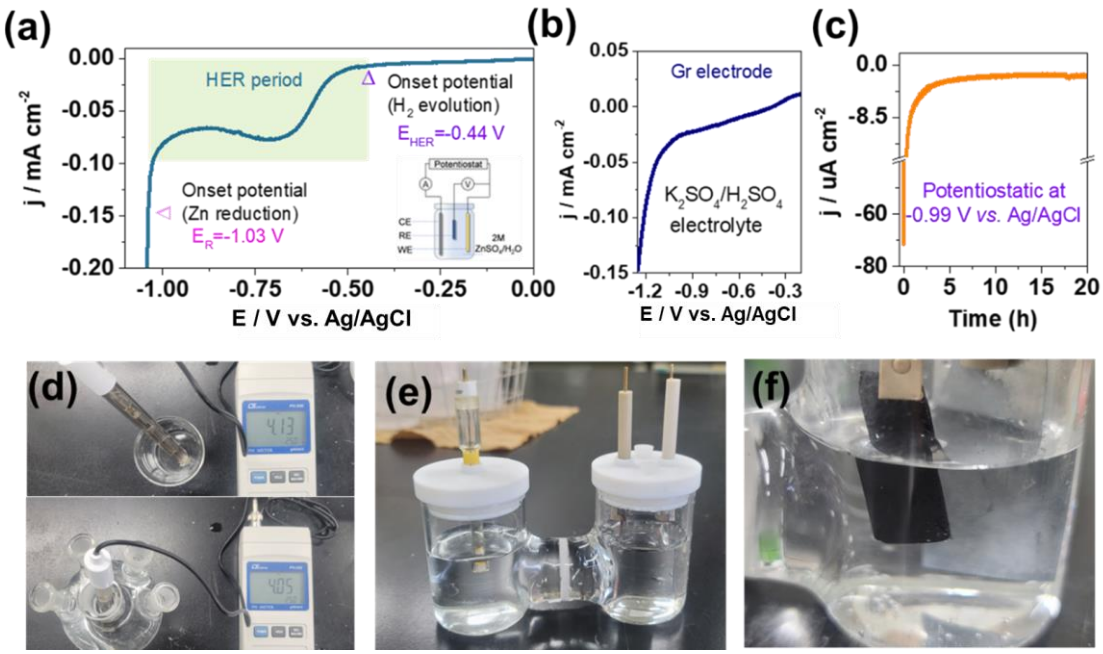

Figure 2.3 Linear sweep voltammetry (LSV) polarization curves of Gr working electrode in the (a) 2 mol L^{-1} $ZnSO_4$ electrolyte with Zn as counter electrode and (b) K_2SO_4-H_2SO_4 electrolyte with Pt as counter electrode. Potential sweep rate: 5 mV s^{-1}. (c) The current density versus time curves in the potentiostatic tests under -0.99 V *vs.* Ag/AgCl reference electrode in the 2 mol L^{-1} $ZnSO_4$ electrolyte. (d) pH values of two types of electrolytes used to calibrate the onset potentials of hydrogen evolution (upper) and Zn reduction (lower), respectively. (e) Optical picture of the three-electrode system used in this work. (f) A small amount of hydrogen absorbed on the graphite electrode surface after potentiostatic measurement over 20 h.

Moreover, the elemental distributions of XPS spectra did not reveal significant change within dozens of surface etching (whole thickness: 300 nm), which suggested the wide-ranging accumulation of the ZHS layer (**Figure 2.5(e)**). The slight shift of atomic percentage (ratio of O to Zn element) represented the distinction of hydrate water molecules from surface to inner component (**Figure 2.5(f)**). The differences may originate from the complex environment during the decomposition period or the inevitable dehydration in the vacuum atmosphere during XPS measurement. Additionally, other common substrates such as Cu, nickel (Ni), stainless steel (SUS

316), and carbon paper were also examined by potentiostatic electrodeposition at -0.99 V (vs. Ag/AgCl reference electrode). The large leakage current in the float-test can be ascribed to the sum of H_2 formation, metal oxide/metal redox reactions, or alloying process because of their complex surface reactions.[138] Moreover, all the tested substrates after the potentiostatic measurement were identically covered by the typical flake-like corrosion-product layer (**Figure 2.6 and Figure 2.7**). Taking the representative Cu substrate as an example, the XRD pattern, as well as the SEM, elemental mapping images verified the large existence of the ZHS layer (**Figure 2.7**). It substantiated that the accumulation was straightforwardly demonstrated by checking the reversibility of the Zn plating/stripping process. The Zn half-cell undergoing an intentional step to propagate ZHS species (potentiostatic measurement at 0 V vs. Zn/Zn^{2+} for 50 h) was proved permanently unable to work for Zn electrodeposition because of the whole occupation of insulated ZHS species on SUS 316 substrate (**Figure 2.8**). All the results demonstrate that the HER takes place prior to Zn reduction, and the concomitant formation of the side-product undermines the Zn reversibility.

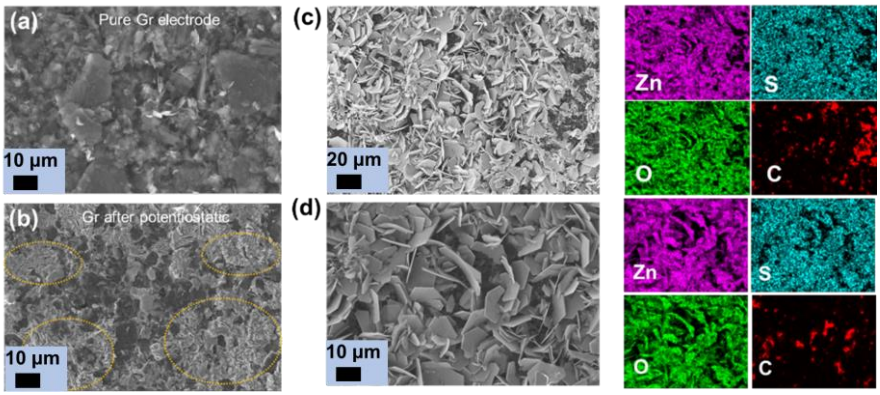

Figure 2.4 (a) The SEM image of the pristine graphite electrode (b) The SEM image of the Gr electrode surface after potentiostatic measurement over 20 h. (c, d) The SEM image of the Gr electrode surface after potentiostatic measurement and the corresponding elemental mapping. place prior to Zn reduction and the concomitant formation of side-product undermines the Zn reversibility.

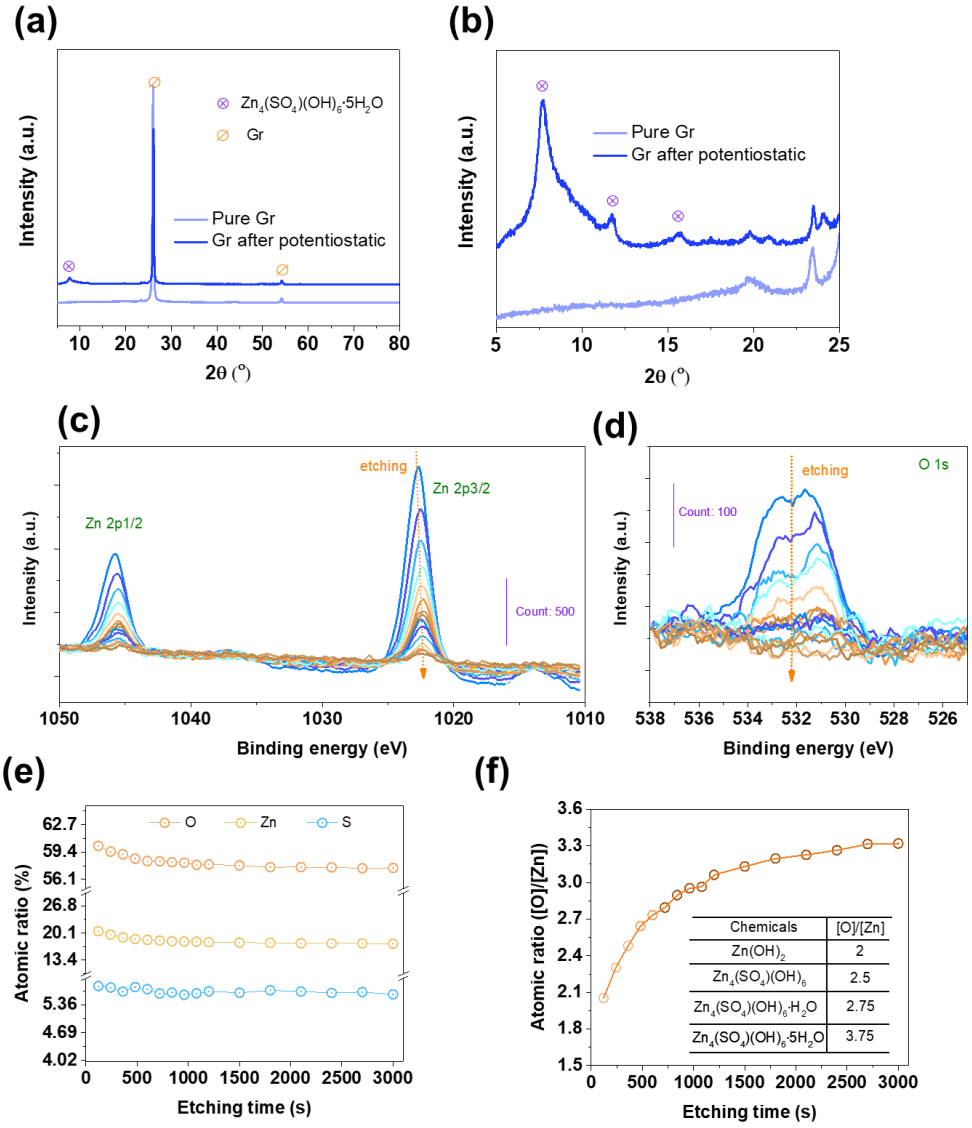

Figure 2.5 (a) The XRD patterns of the graphite electrode before and after potentiostatic measurement, (b) is the enlarged Figure (a). The XPS spectra of (c) Zn 2p and (d) O 1s that belong to the surface components on graphite electrode after potentiostatic measurement. (e) The atomic percentage (the O, Zn, S elements) of the flake-like structure from XPS spectra with the etching technique. (f) The corresponding atomic ratios of [O]/[Zn] with the etching time. The inset Table presents the atomic ratios of [O]/[Zn] of common decomposition species to compare the component distribution of the flake-like structure.

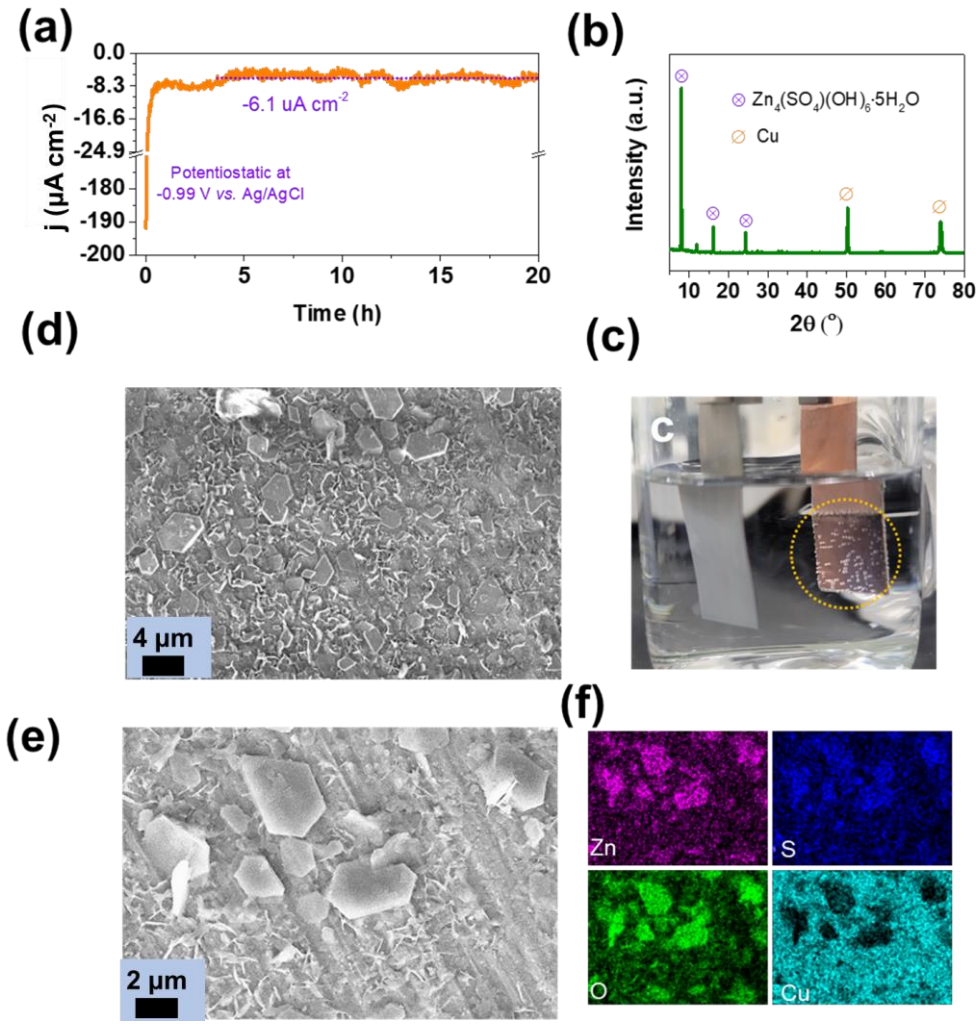

Figure 2.6 Potentiostatic measurement on Cu substrate. (a) Current profiles of the Cu substrate. (b) XRD patterns of the Cu substrates after potentiostatic measurement. (c) Optical picture of absorbed gas on Cu substrate. (d-f) SEM images and elemental mappings of the surface components.

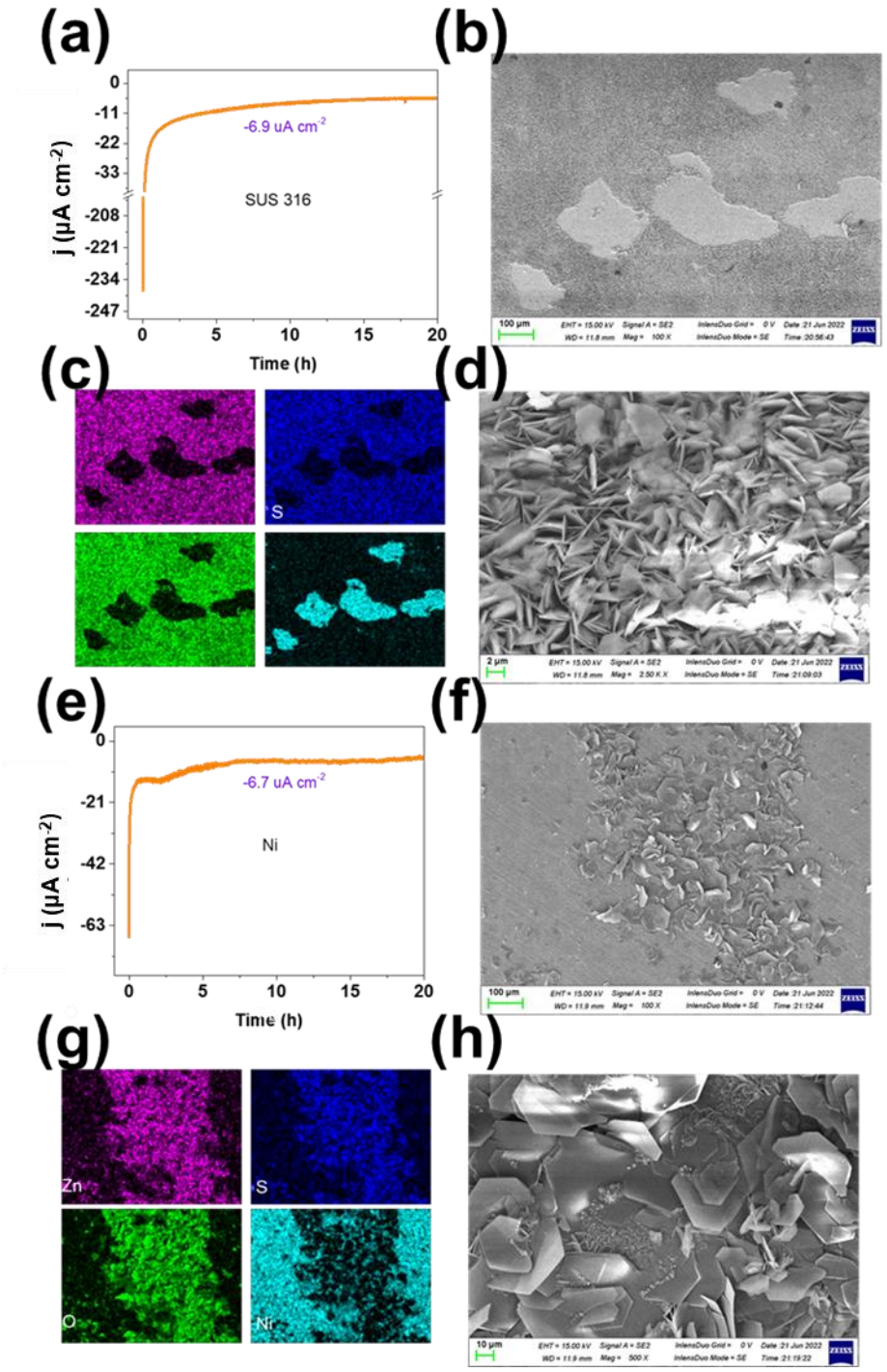

Figure 2.7 Potentiostatic curves of SUS 316 and Ni substrates and its surface component observation. Current density curves of (a) SUS 316 and (e) Ni substrate. The values inside the figures are the stabilized current after the initial period. SEM and elemental mapping of surface components after potentiostatic measurement on (b-d) SUS 316 substrate and (e-h) Ni substrate.

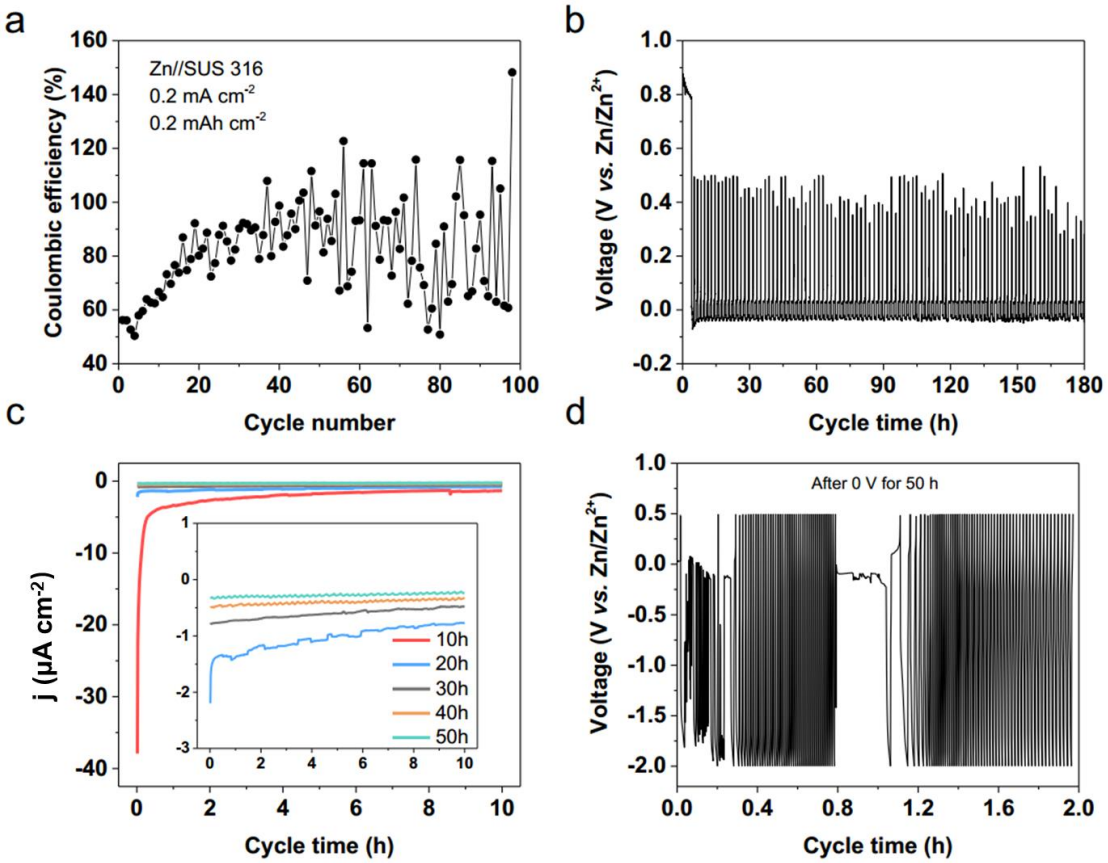

Figure 2.8 Zn electrodeposition on SUS 316 substrate. Zn reversibility on SUS 316 substrate without pretreatment (a) Zn reversibility on different cycles and (b) Voltage profiles of Zn plating/stripping process. (c) Pretreatment of potentiostatic curves of SUS 316 substrate over 50 h. (d) Voltage profiles of Zn plating/stripping process on SUS 316 substrate with pretreatment. The finding of HER prior to Zn reduction did not change despite the possible alloying reaction and the UPD phenomenon for Cu substrate.

2.3.2 Co-growth mechanism for Zn dendrites growth

Given the much-preferred kinetics for H_2 evolution, it becomes compelling to investigate the co-growth phenomenon of the Zn and ZHS during Zn plating/stripping process [139]. I firstly examined the Zn electrodeposition morphology on Cu substrate (0.3 mA cm^{-2}, 3.0 mAh cm^{-2}), which evidently displayed two types of architectures by cross-section SEM observation (**Figure 2.10(a)**) and electron backscatter diffraction (EBSD) examination (**Figure 2.9**). The flake-like structure (Region #1) may be composed of ZHS, indicated by its typical morphology and the corresponding element mapping. In contrast, the scattered structure of Region #2 has a uniform element distribution which corresponds well to pure Zn crystal. Auger electron spectroscopy (AES) was applied in an observation scope of 50×50 nm with depth profile analysis to probe the component distribution. The selected region#1 displays a distinct peak of S, belonging to the typical element of ZHS species, and maintains a strong intensity even after 5-time etching (ca. 60 nm thickness, **Figure 2.10(b)**). The depth profile suggests that the typical flake-like architecture with a high ratio of S has a uniform distribution of ZHS species (**Figure 2.10(d-f)**). Instead, region#2 has no noticeable peak assigned to the S element throughout the etching process, excluding the existence of ZHS species (**Figure 2.10(c)**).

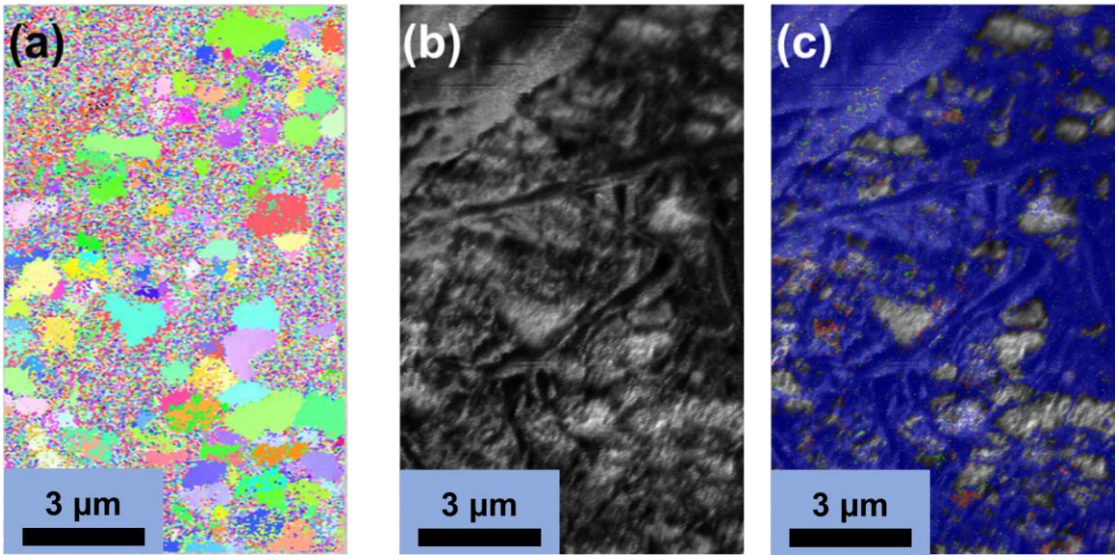

Figure 2.9 EBSD of Zn electrodeposition on Cu substrate. (a) EBSD map. (b-c) SEM images.

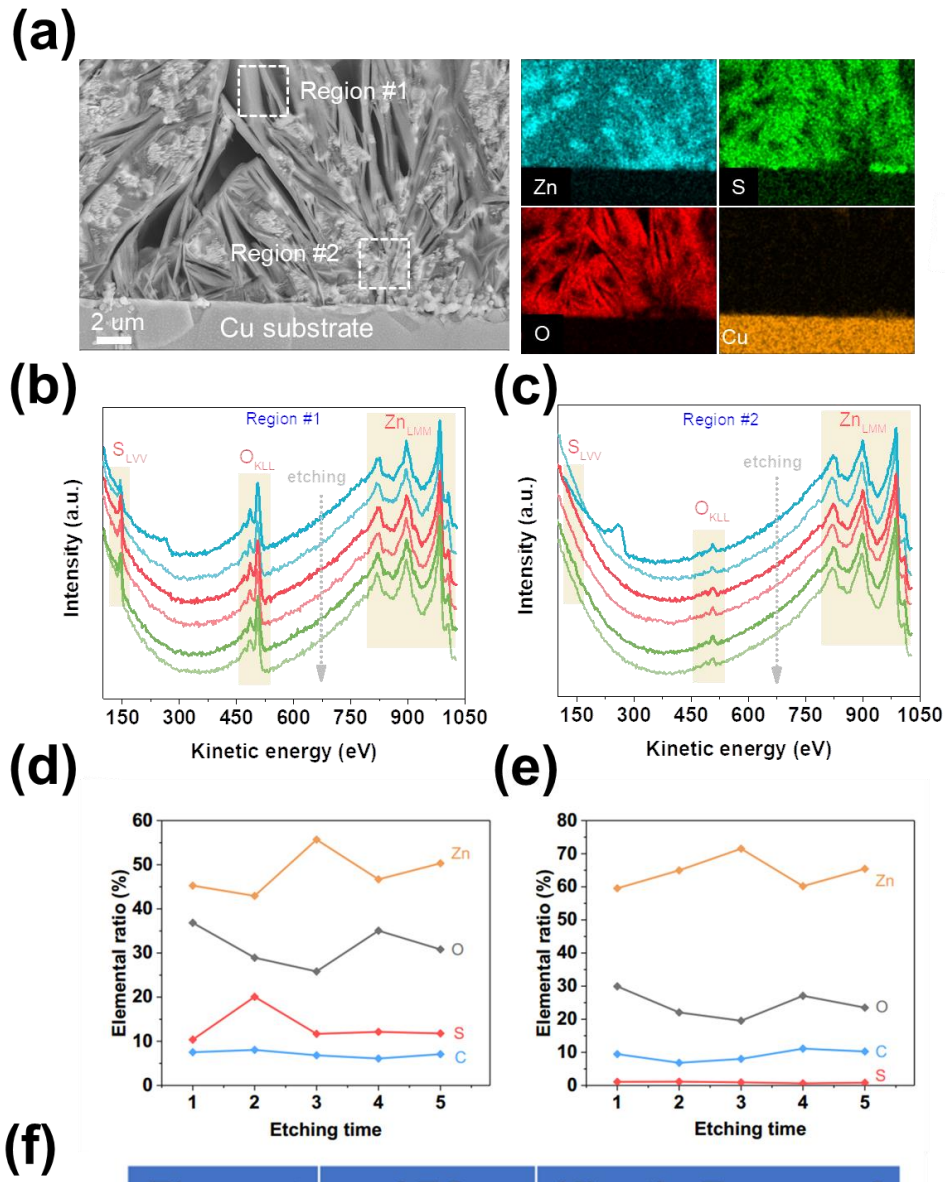

(f)

Element	AES transition	Kinetic Energy of Transition (eV)
C	KLL	272
O	KLL	508
S	KMM	152
Zn	KMM	994

Figure 2.10 Co-growth phenomenon of Zn and ZHS during Zn electrodeposition. (a) Cross-section SEM image and its corresponding elemental mapping of Zn electrodeposition on Cu

substrate. It indicates two types of representative architectures, including flake-like structure in Region#1 and scattered structure in Region#2, respectively. The AES and depth profile analysis within the scope of 50×50 nm for two representative places (b) Region#1 and (c) Region#2. AES characterizations on Region#1 and Region#2. Elemental ratio with 5-times etching for (d) Region#1 and (e) Region#2. (f) Kinetics energy of elements in this measurement.

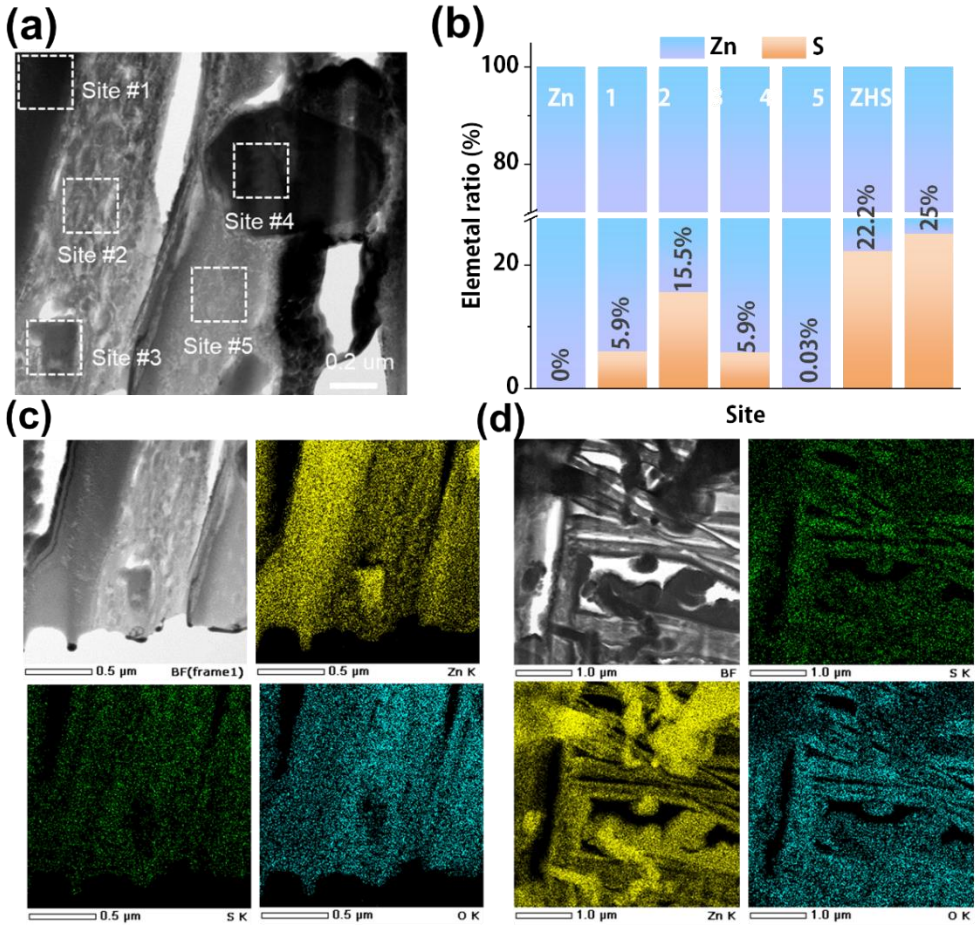

Figure 2.11 (a) The STEM observation on the flake-like structure, whose sample was obtained by FIB technique. (b) The corresponding elemental ratio (the S to Zn element) in 5 different random sites of STEM image. The elemental ratio has two limitation of pure Zn (0% S) and pure ZHS component (25% S), respectively. (c,d) STEM observation and corresponding EDS images of different regions in one FIB prepared sample.

The signal of O might be ascribed to the very thin ZnO film formed on the bulk Zn crystal once leaving the micro-environment in aqueous electrolytes.[140-141] The whole Zn electrodeposition morphology comprises pure Zn crystal and ZHS-based flake-like structures, which have never been exhaustively elaborated. It can be assumed that the interlinked co-growth of Zn crystal and ZHS species might explain the formation of bulge-like Zn dendrite and Zn loss during the plating/stripping process.[88] To intuitively identify the co-growth phenomenon, various electron microscopy characterizations were employed. First, the focused ion beam (FIB) technique was used to prepare a cross-section of the part containing abundant flake structures as a sample for observation under scanning transmission electron microscopy (STEM). As shown in **Figure 2.11(a)**, the ZHS can still be discerned in the as-prepared samples while maintaining its shape and elemental features (**Figure 2.11(c, d)**). Elemental analysis of five representative sites was carried out with limits of pure Zn and pure ZHS (**Table 2.1**). Generally, in the pure ZHS, the Zn to S atomic ratio should be close to 4:1; namely, the proportion of S atoms should be about 25% (**Figure 2.11(b)**). However, even the highest proportion of S atoms (22% in Site#5) is not consistent with the composition of ZHS, indicating that various proportions of Zn crystal mixed in the ZHS layer.

Table 2.1 Atomic ratio from TEM mapping on five different sites in one sample.

	1	**2**	**3**	**4**	**5**
O (%)	23.38	49.78	34.84	3.47	49.76
S (%)	3.68	6.7	3.5	0.28	8.99
Zn (%)	62.04	43.16	60.59	95.62	40.54
Others (%)	10.9	0.36	1.08	0.64	0.71

The high-resolution TEM (HRTEM) observation confirmed this viewpoint. As shown in **Figure 2.12**, the crystal planes that belong to the ZHS cannot be directly detected, which may be construed as the pyrolysis decomposition of ZHS during the sample preparation and pre-observation periods. However, the metallic Zn crystals can be extensively observed in many locations of the flake structures and the crystal area is mostly hundreds to thousands of square nanometers. This may suggest that during the ZHS formation, once the reduction of Zn^{2+} simultaneously occurs, a part of the newly produced Zn crystals may be wrapped into the insulated ZHS flake. The embedded Zn crystals may serve as conductive sites for subsequent nucleation of pure Zn crystal and assist the growth of complex ZHS flake with a mixed crystal structure, further inducing the Zn growth direction along the ZHS flake structure, as proved in SEM observation (**Figure 2.13**). The interwoven co-growth of Zn and ZHS incessantly enlarges the specific areas and triggers more water-related passivation, which pushes the 3D morphology of the electrode to be porous and inhomogeneous. Moreover, the growth of ZHS is a non-electrochemical process (**Eq. 2.1-2.2**),

$$2H_2O+2e^-\rightarrow H_2\uparrow+2OH^- \qquad \textbf{(Eq. 2.1)}$$

$$3Zn^{2+}+6OH^-+ZnSO_4+xH_2O\rightarrow Zn_4(OH)_6SO_4\,xH_2O \qquad \textbf{(Eq. 2.2)}$$

and its growth habit is always in the direction of the ion-concentration gradient, resulting in the deposition of Zn will inevitably become dendrite-like crystals on the substrate with a large amount of ZHS. The reaction of ZHS formation can be interpreted as an HER-promoted (electrochemically promoted) non-electrochemical reaction. So along with the HER, the generation of ZHS changes with the degree of HER proceeding. And this allows the Zn dendrites to keep growing upward: because the newly deposited solid will act as a new HER site.

In summary, the co-growth of ZHS is revealed as a root cause for Zn dendrite formation and poor Zn reversibility (**Figure 2.14**). Consequently, the key issue of developing high-performance Zn electrode lies in suppressing HER and its concomitant formation of ZHS species.

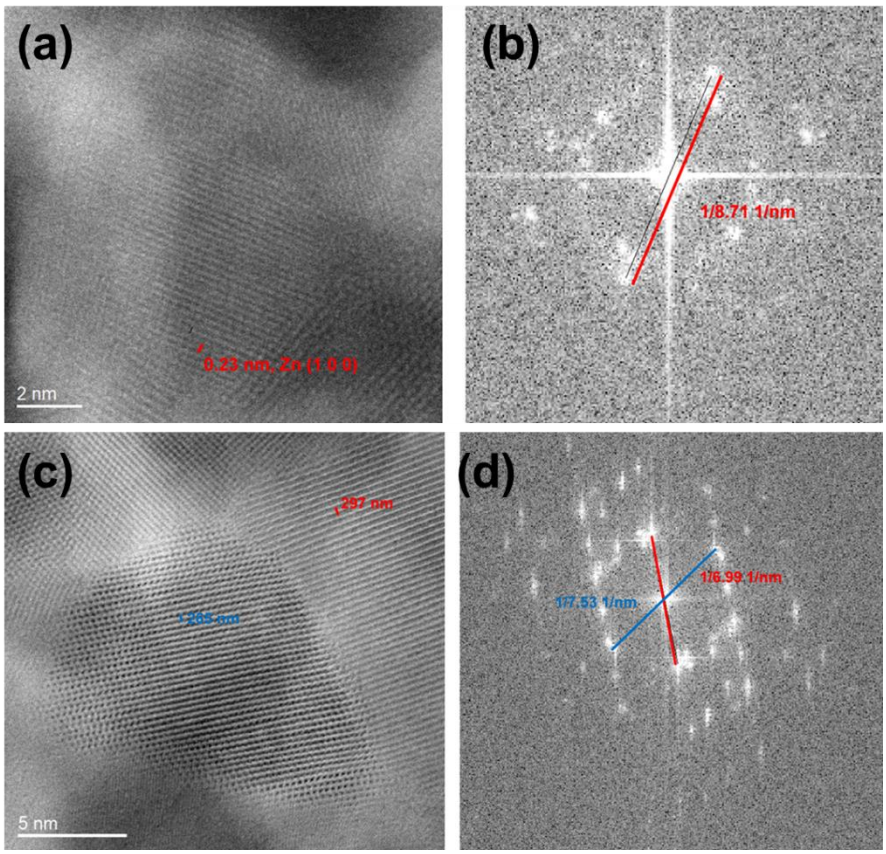

Figure 2.12 HRTEM observation of the FIB-prepared flake-like sample. (a) HRTEM image of the region where Zn <001> crystal plane is observed. (b) The treated fast Fourier transformed figure corresponding to Figure 2.12(a). (c) HRTEM images of the intersection region which indicates the co-growth of Zn and ZHS. (d) The treated fast Fourier transformed figure corresponding to Figure 2.12(c).

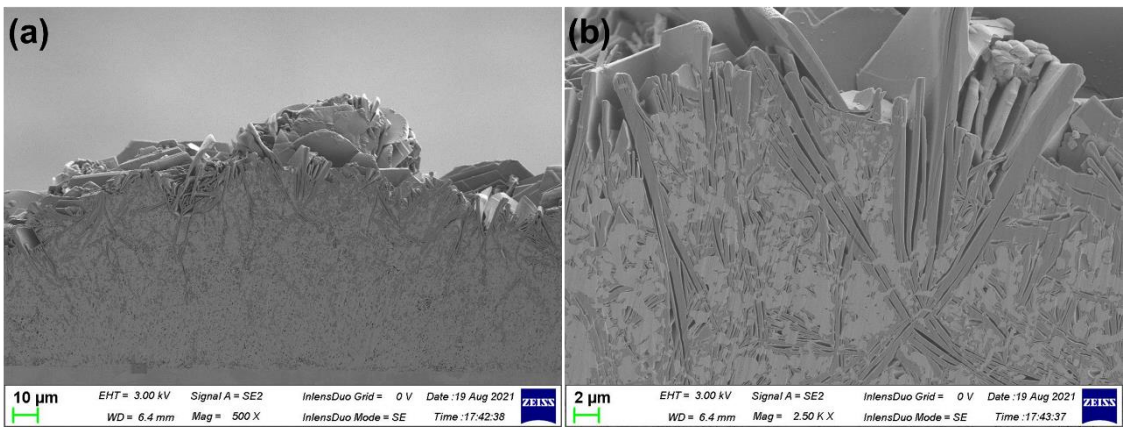

Figure 2.13 (a, b) Cross-section SEM observation of Zn electrodeposition on Cu substrate.

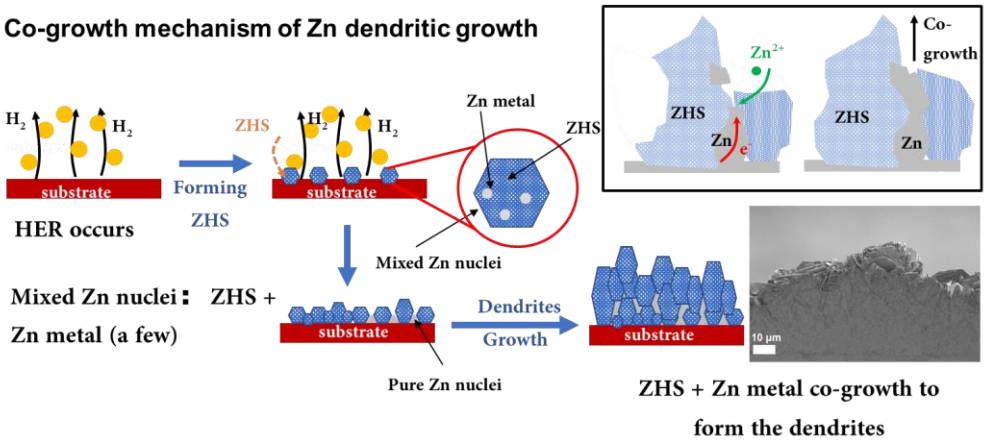

Figure 2.14 Schematic illustration for the co-growth mechanism of Zn dendrites growth.

2.3.3 Relationship between Zn reversibility and plating/stripping current density

Previous reports repeatedly corroborated the upgraded Zn reversibility under higher current density but lack a fundamental perspective.[104, 142-143] The author then tried to unravel the interwoven relationship taking into account the presence of HER and the co-growth electrodeposition phenomenon. Here, a picture of the difference between Zn plating and stripping under high and low currents is presented (**Figure 2.15**). It can be seen that the Zn plating at high currents is dense and homogeneous, while the Zn deposited at low currents shows a porous flake-like structure. Under low current density (0.3 mA cm^{-2}; 3.0 mAh cm^{-2}), the cross-section morphology of Zn plating exhibits a discernible hexagonal flake structure with high electrode porosity (**Figure 2.15(a) and Figure 2.16**). During the stripping process, the partial Zn crystal with benign ion/electron pathway began to dissolve from the root, leaving many breakages of ZHS-composed flake remnants (**Figure 2.15(c) and Figure 2.17**). The insulated residues with inhomogeneous surfaces and high porosity serve as the new substrate for subsequent Zn plating, which further severely threatens the electrodeposition morphology and Zn reversibility. By contrast, the Zn plating under high current density (30.0 mA cm^{-2}; 3.0 mAh cm^{-2}) demonstrates a closely packed architecture without the noticeable existence of flake-like ZHS species (**Figure 2.15(b) and Figure 2.18(a, b)**). Moreover, the uniform and dense electrodeposition pattern also benefits fast electron diffusion and high reversibility during the stripping process, only leaving

argon-attacked carbon during the SEM observation (**Figure 2.15(d) and Figure 2.18(a, b)**). Consequently, the neat substrate surface is well-maintained in a virtuous circle of development for Zn plating/stripping under high current density, as proved by optical observation (**Figure 2.19(a-d)**). The detailed component distributions were further investigated by Fourier transform infrared spectroscopy (FT-IR) and Raman spectroscopy (**Figure 2.19(e, f)**) on the sample after the fully stripping state. The strong peak assigned to SO_4^{2-} even after a dozen times of surface etching confirmed the high fraction of ZHS remnant produced at low-current plating/stripping, in contrast with a very thin passivation layer generated at high-current density (**Figure 2.20**). The enormous difference in morphology can be explained by the extension of the substrate effect. According to the classic volcano curve of hydrogen evolution materials, the Cu substrate is easier than Zn metal to trigger H_2 evolution.[144]

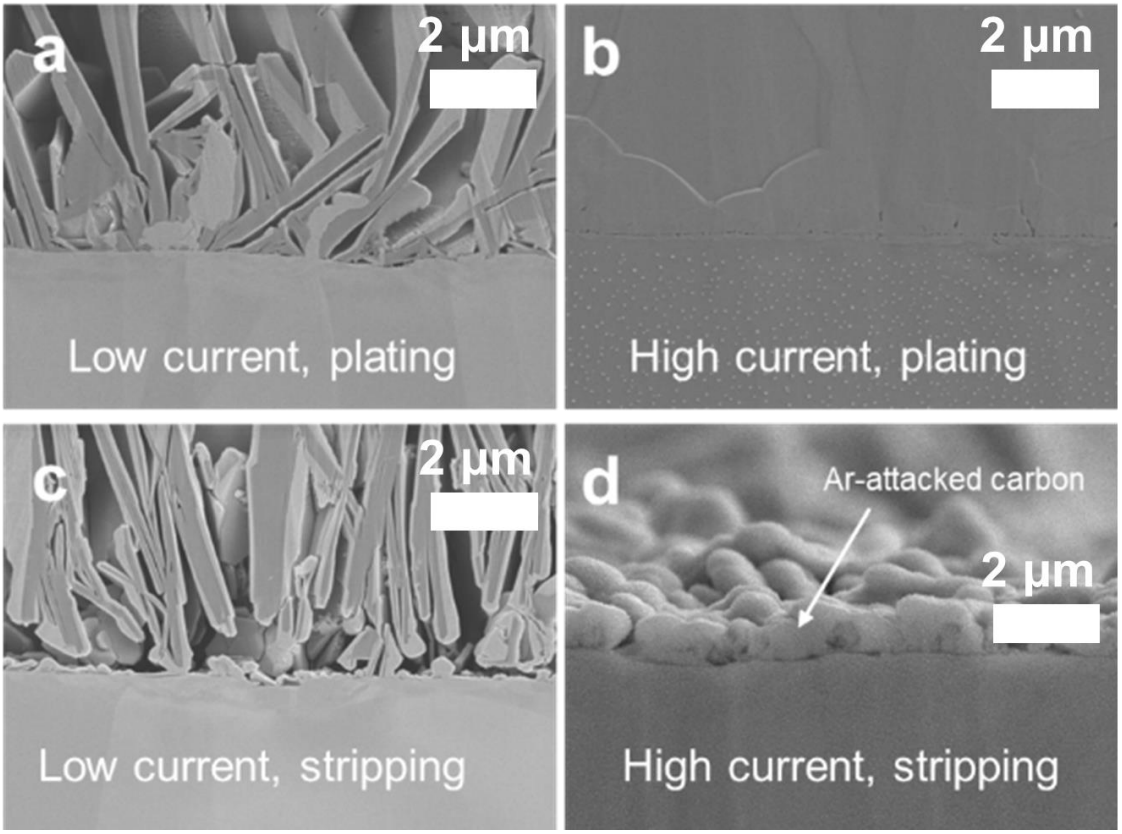

Figure 2.15 Cross-section SEM images of Zn electrodeposition on Cu substrate. Zn plating under (a) Low current density and (b) High current density. Zn stripping under (c) Low current density and (d) High current density.

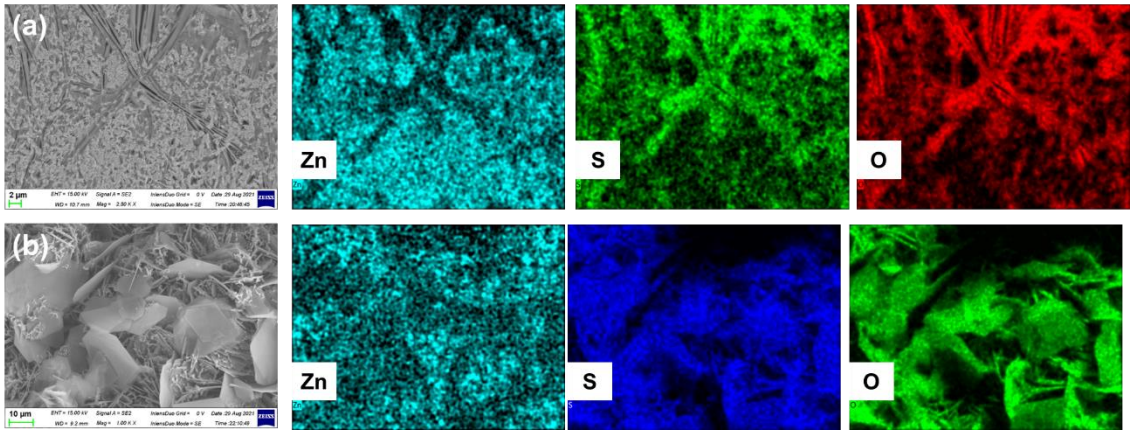

Figure 2.16 Zn electrodeposition morphology on Cu substrate at low current density. (a) Cross-section observation (b) In-plane observation.

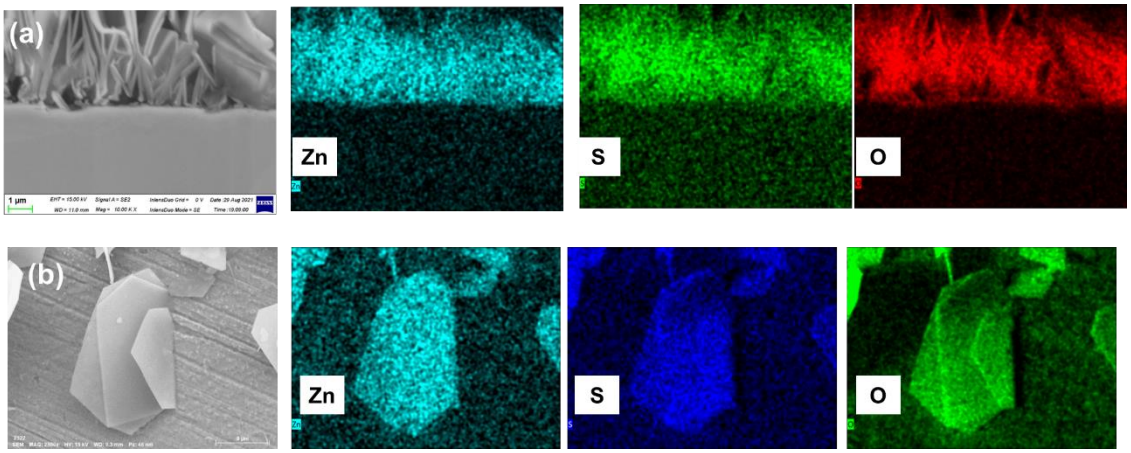

Figure 2.17 Morphology on Cu substrate after stripping state at low current density. (a) Cross-section observation**.** (b) In-plane observation.

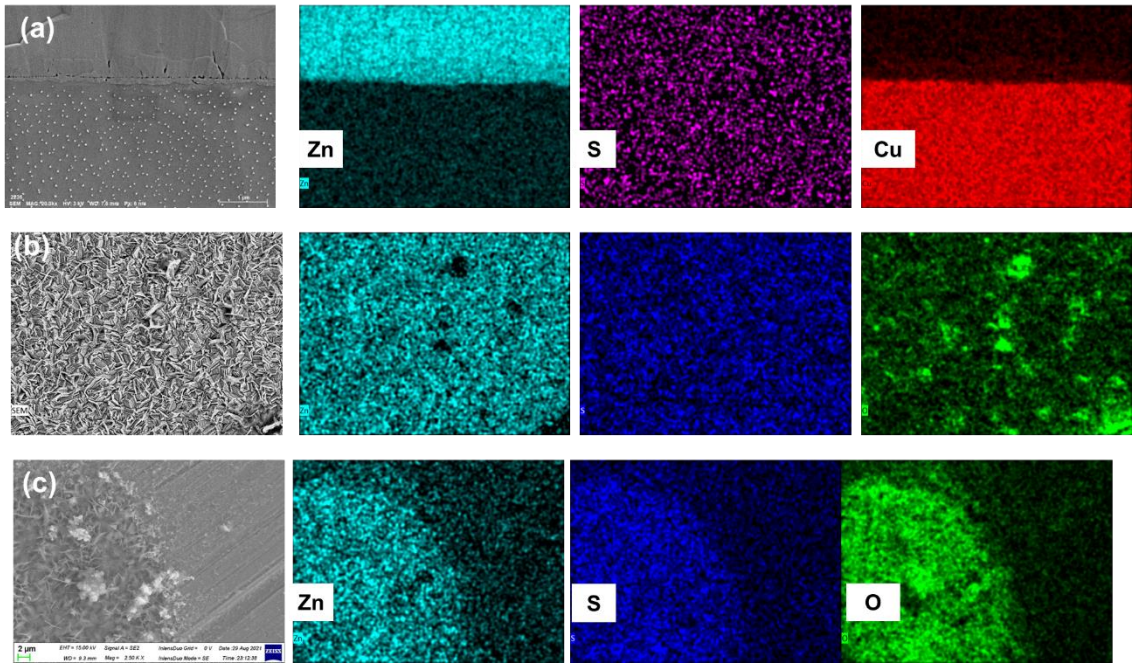

Figure 2.18 Zn electrodeposition morphology on Cu substrate at high current density. (a) Cross-section observation of Zn plating on substrate. (b) In-plane observation of Zn plating on substrate. (c) In-plane observation of Zn stripping from substrate.

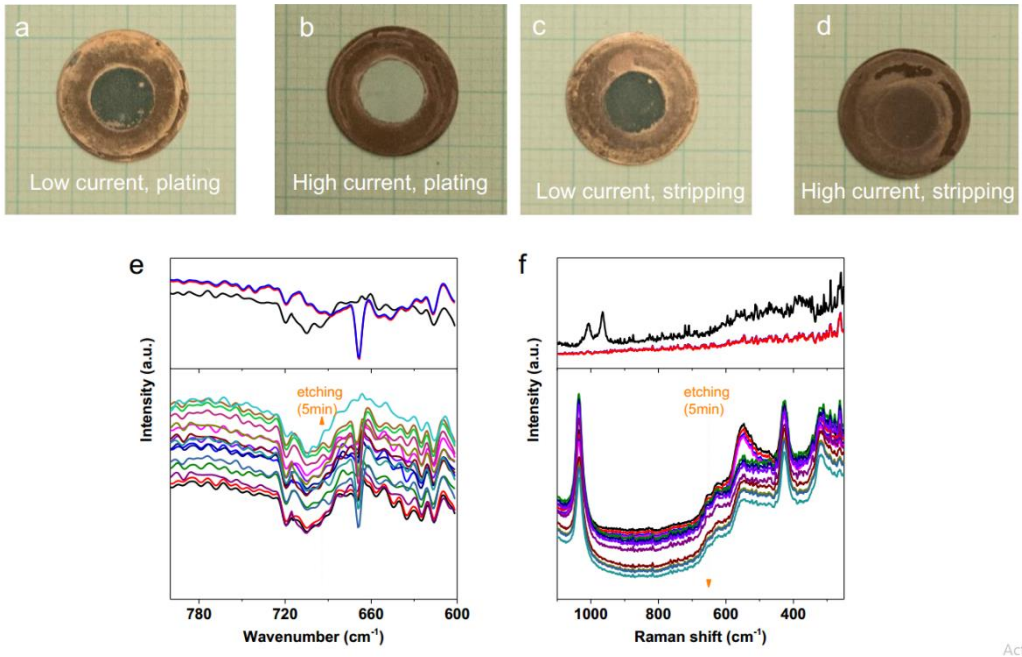

Figure 2.19 Optical picture of Cu substrate. Zn plating at (a) Low current and (b) High current. Zn plating/stripping at (c) Low current and (d) High current. Cu substrate surface component after stripping state (top: high current, bottom: low current) by (e) FT-IR spectra and (f) Raman spectra.

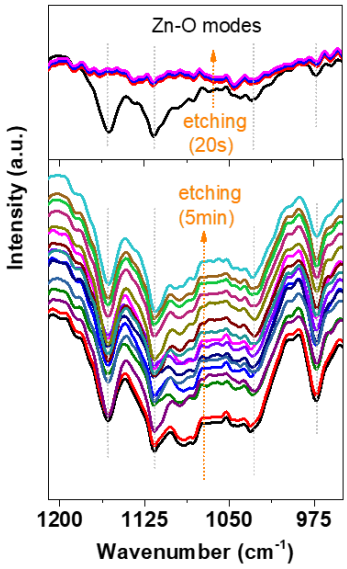

Figure 2.20 Surface component detection by FT-IR spectra for cycled Cu sample (fully Zn stripping state) at high current density (top) and low current density (bottom). The samples were prepared at the same capacity 3.0 mAh cm^{-2} under current density of low (0.3 mA cm^{-2}) and high (30.0 mA cm^{-2}), respectively.

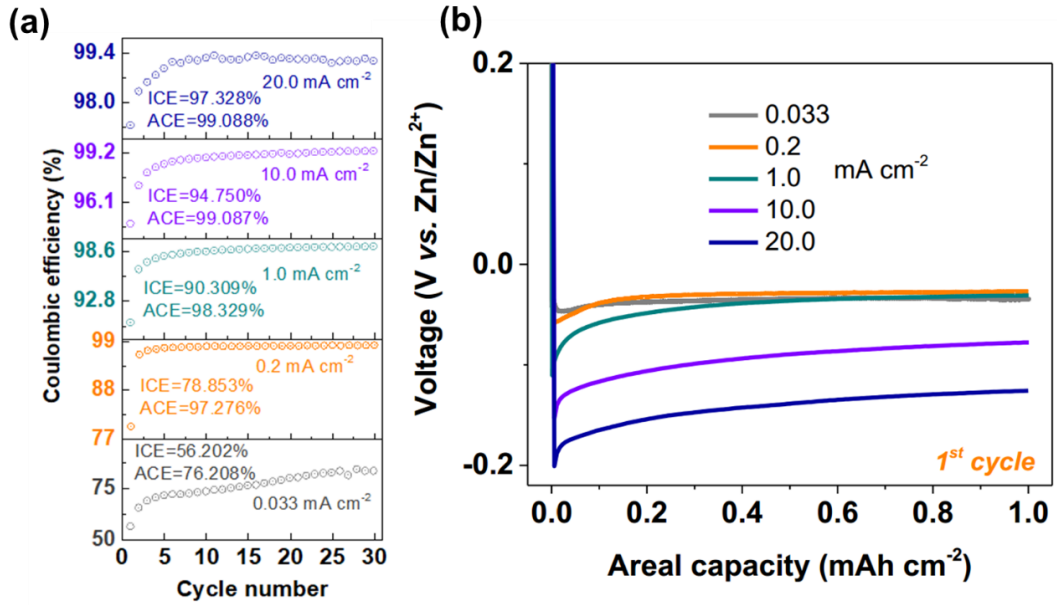

Figure 2.21 (a) Coulombic efficiency of Zn plating/stripping process at increasing current densities (from 0.033 mA cm^{-2} to 20.0 mA cm^{-2}) with the same capacity (1.0 mAh cm^{-2}). (b) Voltage profiles of Zn plating on Cu substrate under different current densities at the 1st cycle.

The concept of regulating the overpotentials of HER and Zn reduction was further demonstrated by measuring the Zn plating/stripping efficiencies at different current densities. By controlling the same areal capacity (1.0 mAh cm^{-2}) and progressively increasing the current density from 0.033 to 20.0 mA cm^{-2}, both the initial Coulombic efficiency (I.C.E.) and average Coulombic efficiency (A.C.E.) witness a tremendous increase (**Figure 2.21**). The increase of current density firstly shifts the potential of electrode to a more negative region, and thus promoting more sites of Zn nuclei for subsequent Zn growth. The critical step of forming a uniform and thin Zn layer covering the Cu substrate (or Zn alloy layer) will relatively retard the HER by contrast with the pristine Cu substrate. Instead, low current density provides a smaller driving force for spawning less Zn nuclei; therefore, Zn crystal inclines to aggregate into small hill morphology. The non-uniform Zn layer (or Zn alloy layer) cannot seamlessly cover the Cu substrate, and the exposed regions provide active sites for HER. Meanwhile, the potential quickly shifts to the Zn reduction potential at high current density and minimizes the time of staying around HER potential. Consequently, the rapid growth of a homogeneous Zn electrodeposition coating on Cu substrate under high current density would reverse the substrate effect and mitigate the HER process. Furthermore, the faster consumption of Zn^{2+} in the vicinity of the electrode and the larger concentration gradient at higher current density would scale down the reaction rate of ZHS generation (**Eq. 2.2**). This prevents the accumulation of ZHS in the plating layer during the subsequent Zn deposition process, thus ensuring high capacity, long-term and highly reversible Zn plating/stripping. The above merits obtained from high-current density working eventually eliminate the formation of ZHS and contribute to the dense and high-purity Zn metal electrodeposition (**Figure 2.22**).

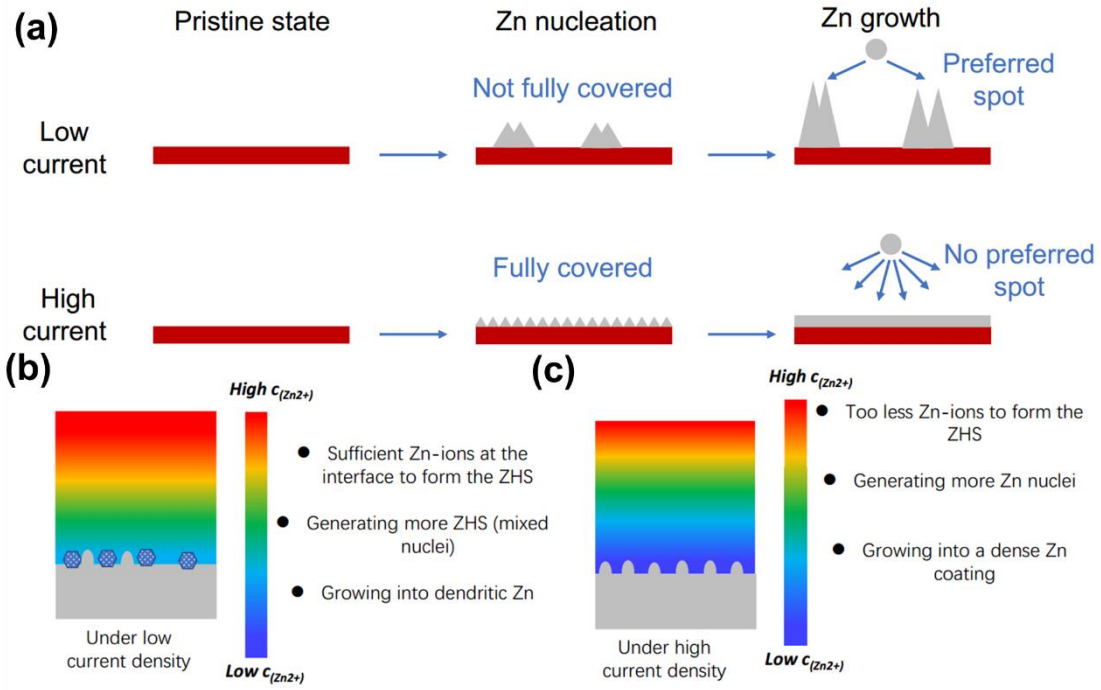

Figure 2.22 (a) Schematic illustration of (a) Zn plating at low and high current density. Schematic illustration of Zn^{2+} concentration gradient and its induced ZHS formation at (b) low current density and (c) high current density.

2.3.4 How the substrate influences the deposition behavior of Zn

Accordingly, the property of substrate effect in terms of HER and Zn reduction was further examined for the purpose of seeking a highly compatible substrate for Zn electrodeposition. The LSV test was carried out in the K_2SO_4- H_2SO_4 electrolyte (pH: 4.13). Without the interference of Zn^{2+} reduction, any commencing current signal can be attributed to HER. Of the substrate materials investigated here, Ni, Cu and SS showed higher HER activity that were indicated by larger cathodic current densities of H_2 evolution **(Figure 2.23 (a))**. The results are consistent with the conclusion of the classic volcano curve of hydrogen evolution materials except for the case of titanium (Ti). The Ti demonstrates much lower HER activities which can be explained by strong Ti-H bond and the dense and well-maintained TiO_2 coating within the potential ranges.

The very similar HER activity of Ni and SS substrates illustrates that Zn deposition and HER reaction are in most cases simultaneous, which leads to co-growth of dendrites on these substrates

before they can be covered with Zn metal. Cu, on the other hand, exhibits a lower deposition potential and has a more negative E_{HER}-E_R value (-120 mV) due to the simultaneous presence of the UPD phenomenon and the alloying process.[145-146] Ti exhibits the largest negative value (-420 mV), indicating that both Cu and Ti are better choices for anode current collectors. Enhancing the Zn affinity for Ti or enhancing the HER resistance of Cu could make these metals excellent substrates for Zn deposition. The extension of the substrate effect was further demonstrated by Zn plating/stripping efficiency (**Figure 2.25(a)**, **Figure 2.26**) and Zn electrodeposition morphology (**Figure 2.25(b)**, **Figure 2.27, Figure 2.28, Figure 2.29**). Among them, SUS 316 substrate presents the highest Zn nucleation overpotential and very short cycle life (8 cycles). After cell failure, the harvested SUS 316 surface was wholly covered by flake-like structures, which indicated the extensive accumulation of insulated ZHS species (**Figure 2.28(b) Figure 2.29(a)**). The electrochemical behavior well corresponds to the strong HER activity of SS substrate and more critically, its slight alloying process to retard Zn reduction. From this perspective, the Ni and Cu substrates significantly prolongs the cycle life to 140 and 180 cycles, respectively, with lower nucleation overpotentials. The inherent cause lies in their much more positive potentials of metal oxides converting into pure metal (e.g. $Cu^{2+}+2e^- \rightarrow Cu(s)$, + 0.34 V vs. SHE), which provides the precondition for alloying process with Zn metal (**Figure 2.24(a)**). The merits of reducing the overpotential of Zn reduction effectively compensate for the shortcoming in triggering high activity of HER, rather than promoting a comparatively compact Zn electrodeposition morphology. The exception case of Ti substrate (more precisely the TiO_2 substrate) exhibited poor Zn affinity, where most of the electrodeposited Zn was adhered onto the glass fiber separator, after cell failure over 61 cycles (**Figure 2.28(c), Figure 2.29(b)**). However, the modification studies on Ti substrate would be a competitive alternative because of its much reduced HER activity. The interfacial impedance of the Zn half-cell with different substrates was also disclosed the Zn affinity, fully consistent with the Zn electrodeposition habit (**Figure 2.30, Figure 2.31**).

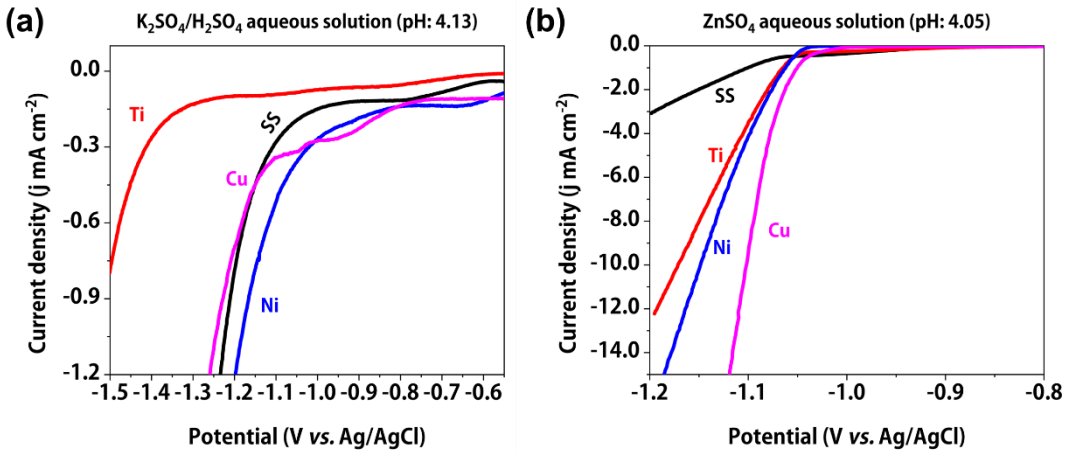

Figure 2.23 (a) LSV polarization curves with different substrate as working electrode in the (a) K_2SO_4-H_2SO_4 electrolyte with Pt as counter electrode and (b) 2 mol L^{-1} $ZnSO_4$ electrolyte with Zn as a counter electrode.

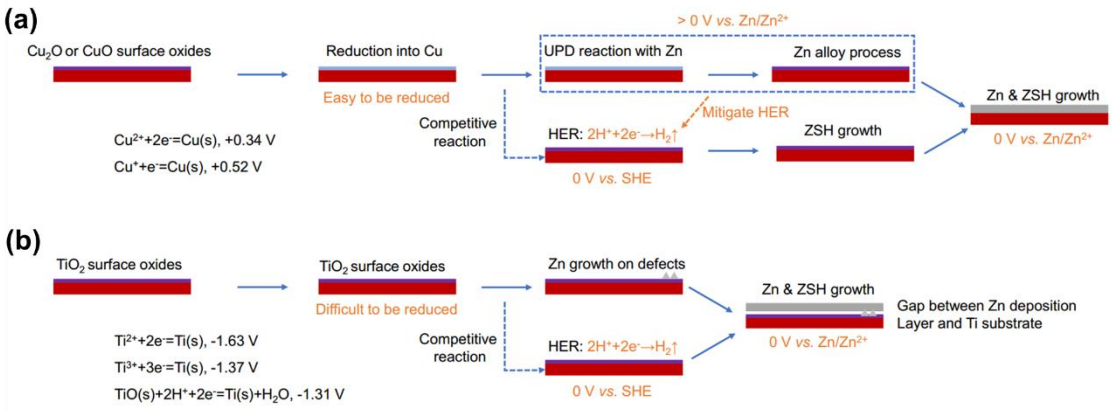

Figure 2.24 The schematical illustration of Zn plating on (a) Cu or (b) Ti substrates.

Table 2.2 Potential at 0.5 mA cm^{-2} of HER and Zn reduction on different substrate.

	HER at 0.5 mA cm^{-2} E_{HER} (V vs. Ag/AgCl)	**Zn reduction at 0.5 mA cm^{-2} E_R (V vs. Ag/AgCl)**	**E_{HER}-E_R (mV)**
SUS316	**-1.11**	**-1.07**	**-40**
Ti	**-1.46**	**-1.05**	**-410**
Ni	**-1.09**	**-1.05**	**-40**
Cu	**-1.16**	**-1.04**	**-120**

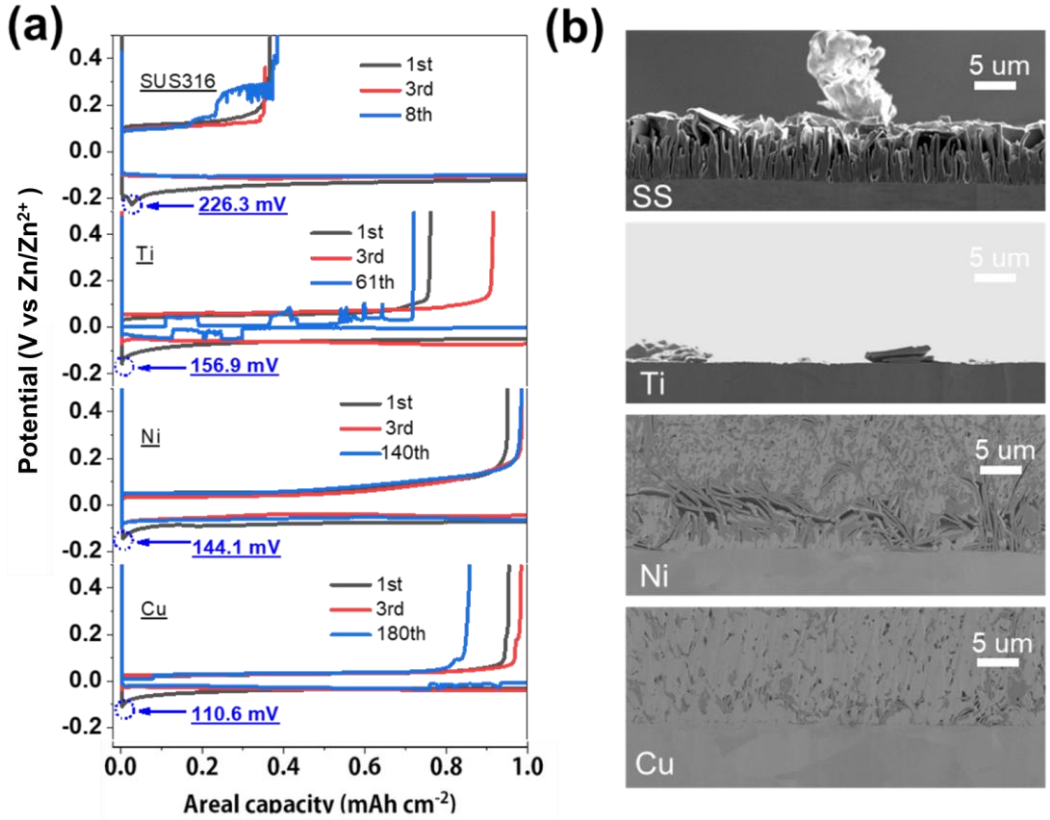

Figure 2.25 (a) The potential profiles of Zn plating/stripping and its Zn nucleation overpotential on different substrates. (b) The corresponding cross-section SEM images of Zn plating on different substrates.

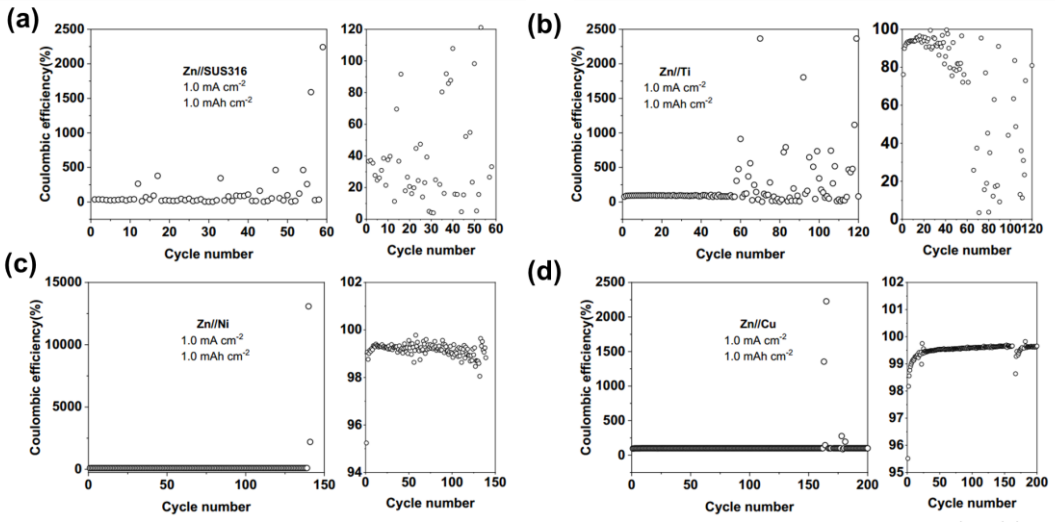

Figure 2.26 Zn plating/stripping reversibility on different substrates at 1.0 mA cm^{-2}, 1.0 mAh cm^{-2}. (a) SUS 316, (b) Ti, (c) Ni, (d) Cu.

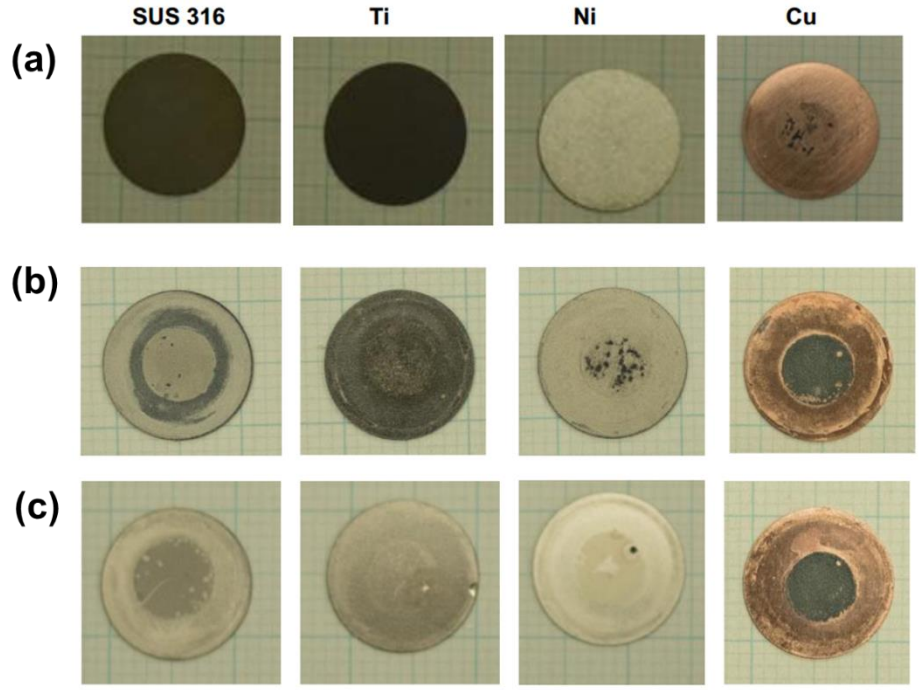

Figure 2.27 Optical picture of substrates from left to right: SUS 316, Ti, Ni, and Cu. (a) pristine state, (b) Zn plating at low current, (c) Zn plating/stripping at low current.

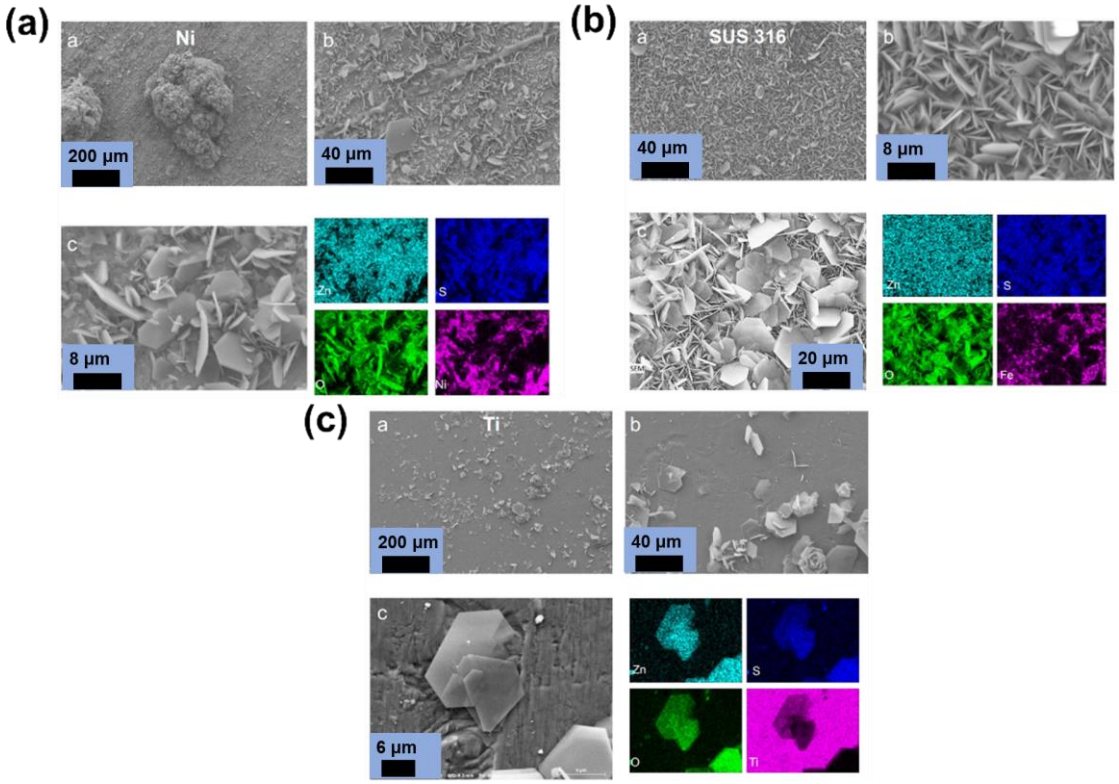

Figure 2.28 SEM observation and elemental mapping for Zn plating/stripping at low current density on (a)Ni substrate, (b) SUS 316 substrate, and (c) Ti substrate.

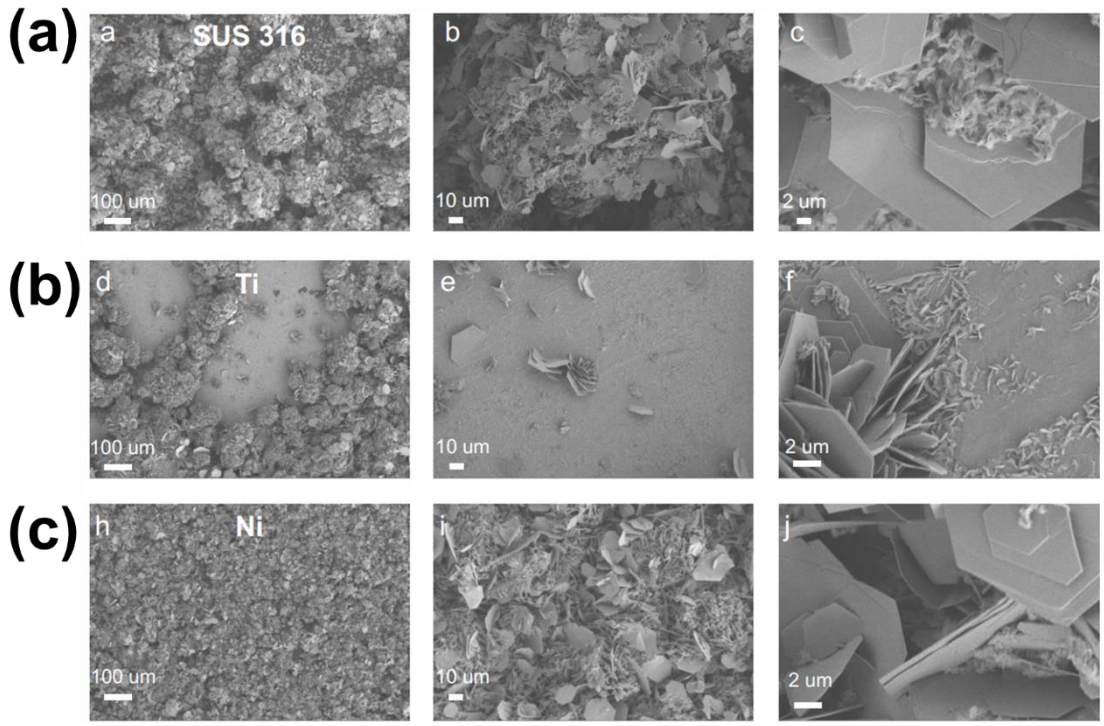

Figure 2.29 SEM observation for Zn plating at low current density on (a) SUS 316 substrate, (b) Ti substrate, and (c) Ni substrate.

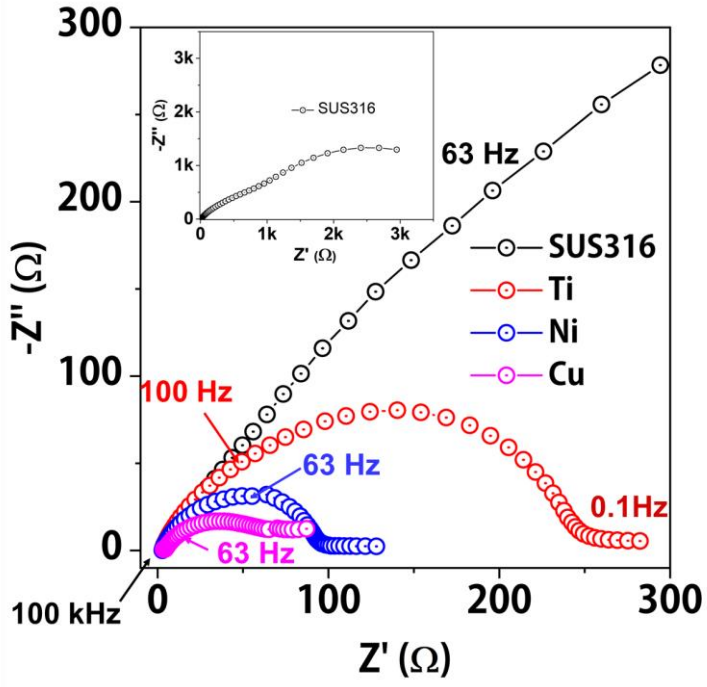

Figure 2.30 The electrochemical impedance spectroscopy of Zn plating on different substrates.

Based on the above results, the electrodeposition behaviors are correlated with the overpotential-governed reactions before Zn reduction (**Figure 2.25 (b)**). Firstly, the substrate (or electrolyte additives) might involve electrochemical self-reduction and alloying with Zn, which might favor Zn electrodeposition and mitigate the activity of HER. Otherwise, the substrate materials may provoke the HER, leaving unwanted gassing and insulated side-products, where the former factor weakens the Faraday efficiency and the latter factor accounts for the Zn dendrite formation and poor Zn utilization. The issue of Coulombic efficiency (sum of Faraday efficiency and Zn utilization) was then highly dependent on the activity of HER, more specifically, the overpotentials of HER and Zn reduction (**Figure 2.32(a)**). Then, the conceptual methodology of promoting the Coulombic efficiency of the Zn electrode by governing their overpotentials is proposed (**Figure 2.32(b)**). The universal principle lies in eliminating the formation of ZHS, via raising the overpotential of HER and simultaneously reducing the overpotential of Zn reduction. The most accessible approach to suppressing the formation of HER and ZHS species is increasing the electrodeposition current density, which proved to be a universal strategy to promote Zn reversibility and benign morphology in the various substrates (**Figure 2.33**). It can be seen that all three remaining substrates, except SUS316, have uniform Zn plating when Zn plating/stripping is performed at high current densities, and the plating can be stripped relatively thoroughly. Moreover, as an example, Ni substrates, which have excellent Zn affinity but also tend to catalyze HER reactions, have 99.58% Coulombic efficiency at a relatively high current density (10 mA cm^{-2}). In contrast, Ti substrates, which have moderate Zn affinity but also do not tend to catalyze HER reactions, can also maintain 99.57% Coulombic efficiency at 10 mA cm^{-2} **(Figure 2.34(c, d) and Figure 2.34(e, f))**. The SUS316 substrates, which have average Zn affinity and are highly susceptible to catalyzing the HER reaction to proceed, exhibit poor cycling performance (**Figure 2.34(a, b)**). A direct study of the deposited morphology of Zn on several substrates is consistent with the previously mapped schematic (**Figure 2.31**). A large number of ZHS nuclei were deposited on the SUS316 surface, which caused a few Zn nuclei to eventually grow into islands of Zn scattered on the substrate surface (**Figure 2.35**). The Zn coating on the Ti surface is dense and uniform, but the Zn coating is not in close contact with the substrate due to the presence of

an oxide layer on the titanium surface (**Figure 2.36**). For Ni, the Zn plating deposited at high currents on its surface is dense and tightly adhered, but traces of the presence of ZHS can still be seen (**Figure 2.37**). These results indicate that the comprehensive understanding of the deposition behavior of Zn in mildly-acidic electrolyte presented here is effective and instructive.

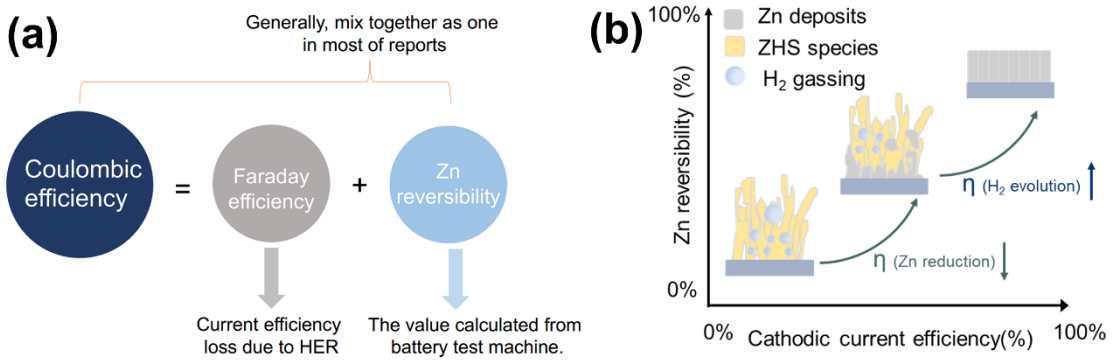

Figure 2.31 The schematical illustration of Zn plating on different types of substrates.

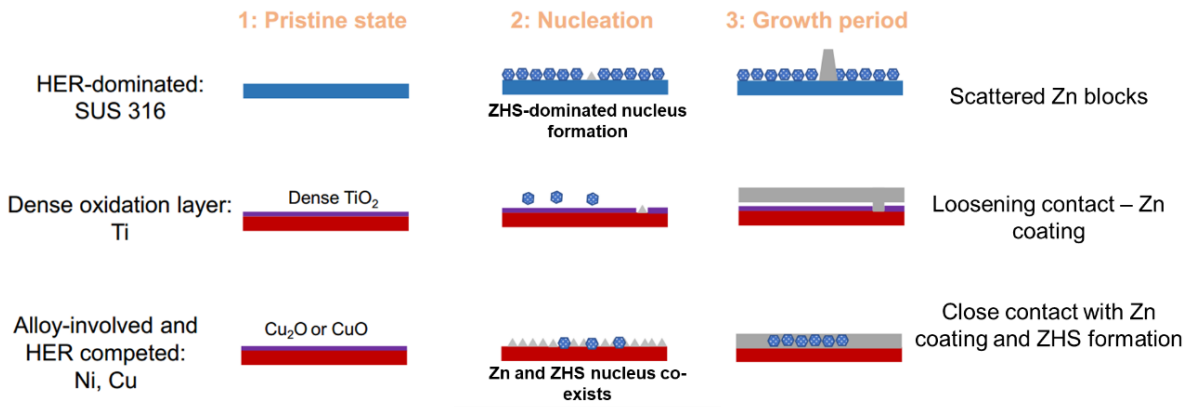

Figure 2.32 (a) Illustration of relationship between Coulombic efficiency, Faraday efficiency and Zn reversibility. (b) The correlated relationship of different Zn electrodeposition morphology (Zn reversibility) based on overpotentials of HER and Zn reduction.

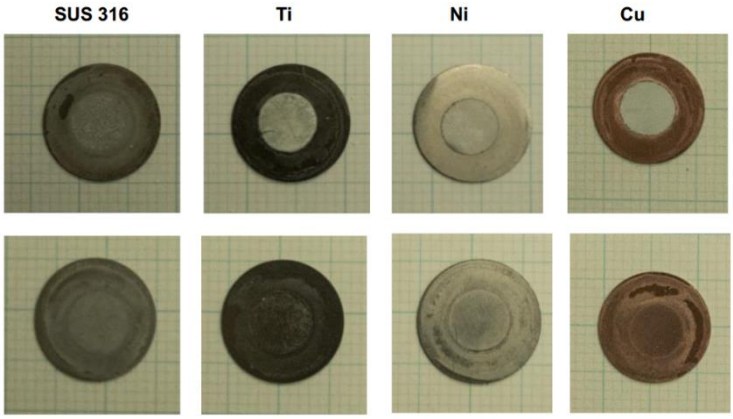

Figure 2.33 Optical picture of substrates from left to right: SUS 316, Ti, Ni, and Cu. Top: Zn plating at high current. Bottom: Zn plating/stripping at high current.

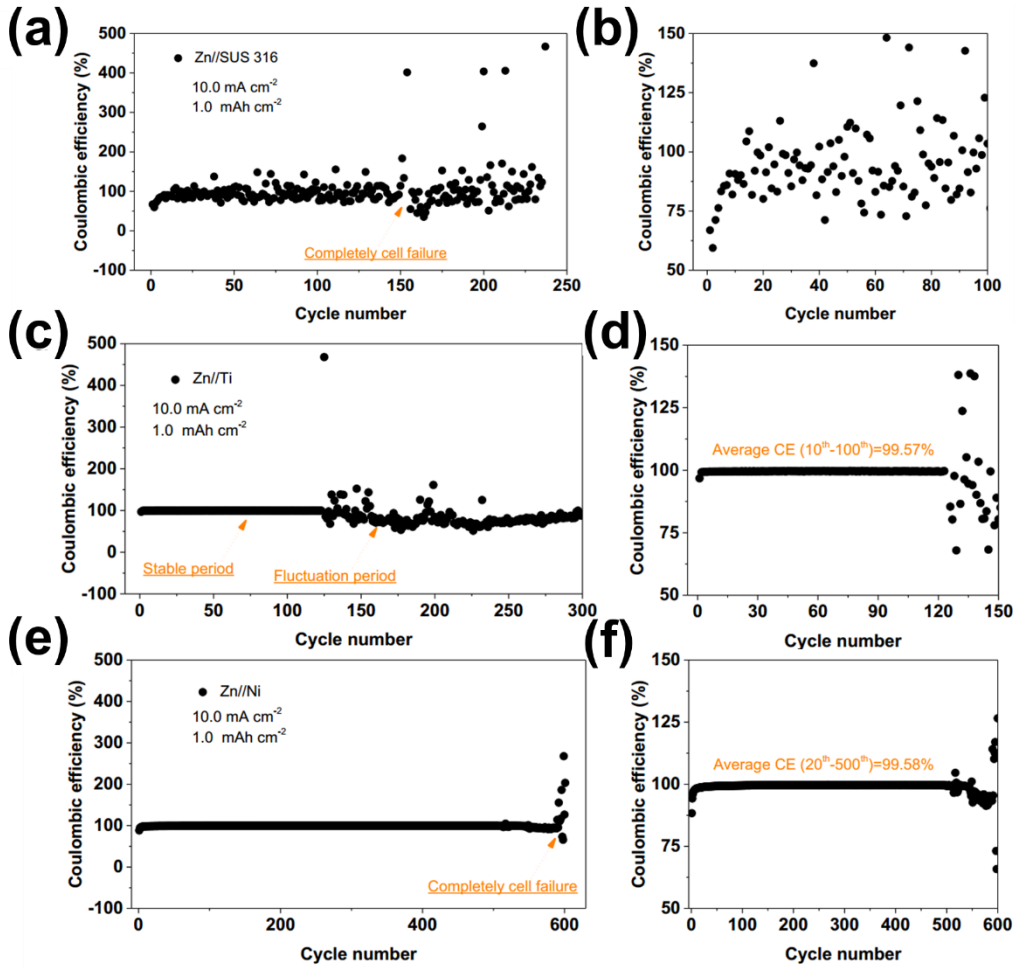

Figure 2.34 Zn plating/stripping reversibility on (a, b) SUS 316 substrate, (c, d) Ti substrate, and (e, f) Ni substrate at 10.0 mA cm^{-2}, 1.0 mAh cm^{-2}.

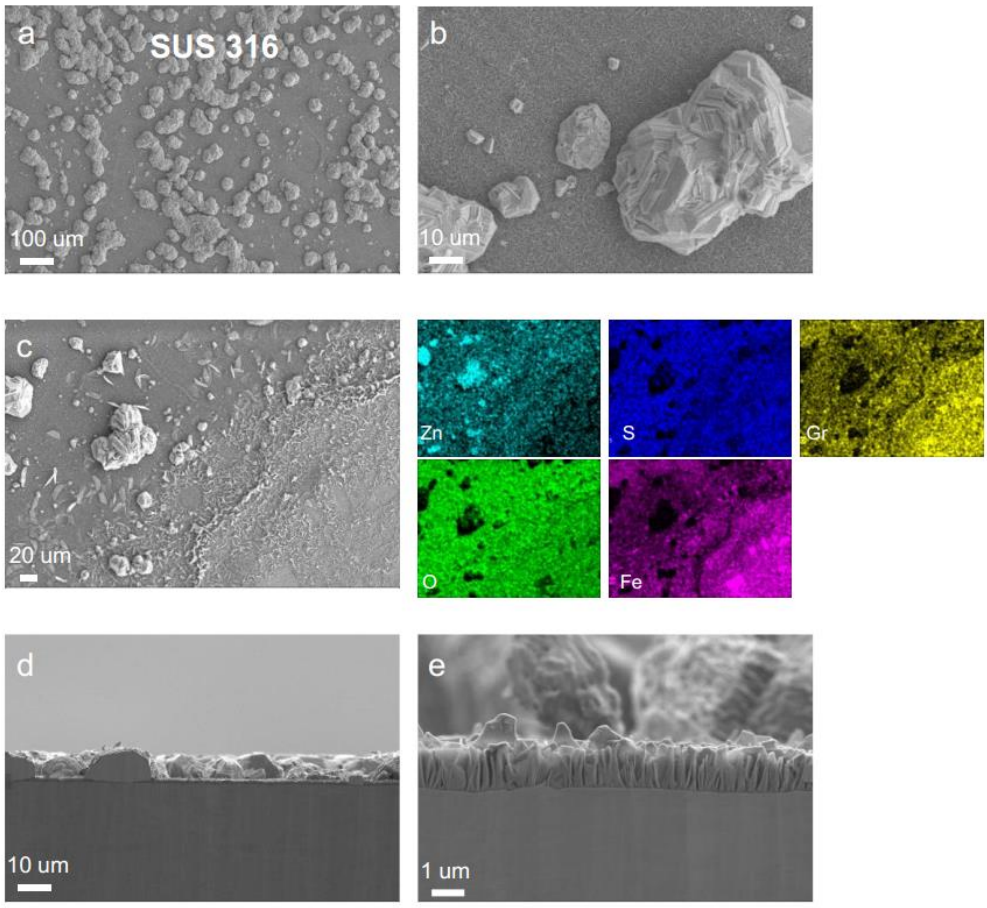

Figure 2.35 SEM observation and elemental mapping for Zn plating/stripping at high current density on SUS 316 substrate. (a-c) In-plane observation. (d-e) Cross-section observation

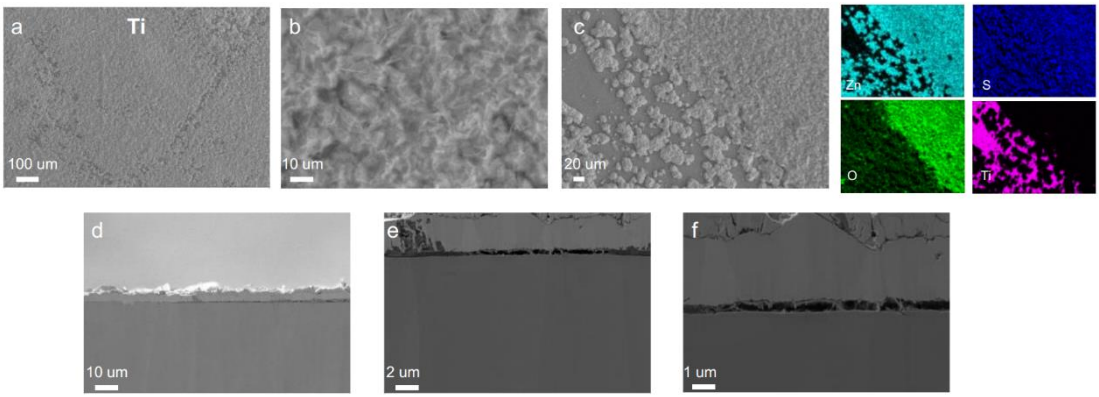

Figure 2.36 SEM observation and elemental mapping for Zn plating/stripping at high current density on Ti substrate. (a-c) In-plane observation. (d-f) Cross-section observation.

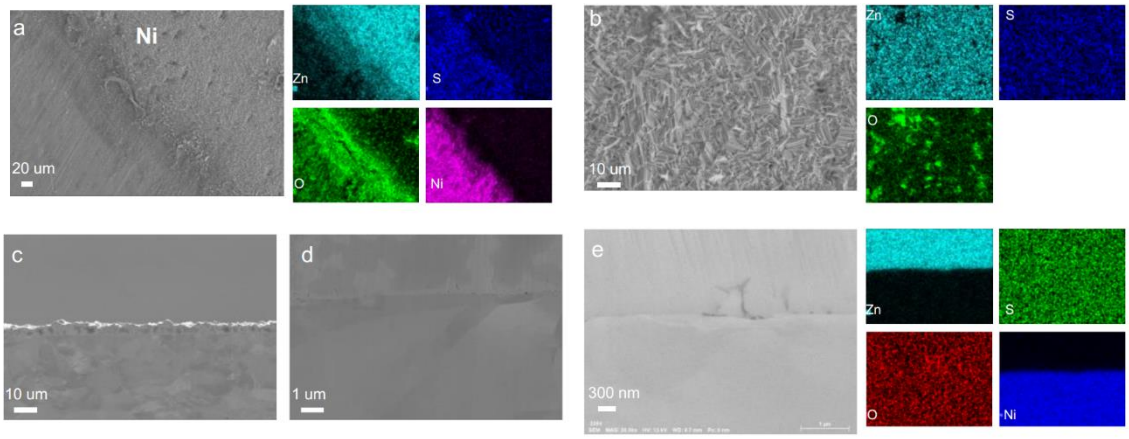

Figure 2.37 SEM observation and elemental mapping for Zn plating/stripping at high current density on Ti substrate. (a-b) In-plane observation. (c-e) Cross-section observation.

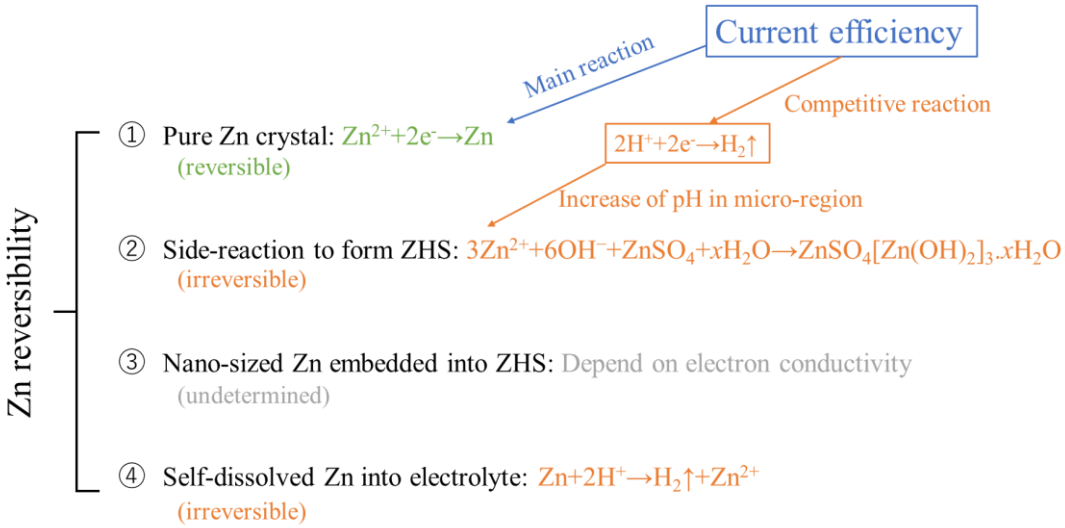

Figure 2.38 Main reactions in the $ZnSO_4$ mildly acidic aqueous electrolyte for explaining the irreversible Zn during RAZIBs working.

2.4 Conclusions

This chapter emphasizes the adverse impact of HER to Zn reversibility and provides new insight into understanding the failure mechanism of Zn electrode worked in mildly acidic aqueous electrolyte (**Figure 2.38**). First, by independently investigating the overpotential of HER and Zn reduction, the HER and its concomitant formation of insulated side-products bear the responsibility for the major Zn loss during cycling. Secondly, the by-product ZHS brought by

HER with the co-growth of Zn metal is believed to be the real reason for the growth of Zn dendrites in mildly acidic electrolytes, which is different from any previous view, but a series of subsequent validation experiments confirmed the result. To summarize, the reversibility of Zn is better when the deposition current is higher, when the HER catalytic activity of the substrate is lower, and when the affinity between the substrate and Zn is higher. Furthermore, both the HER and Zn electrodeposition are governed by overpotential were concluded, namely the factors of current density, substrate materials, electrolyte additives, and interfacial/surface modification strategies (**Figure 2.39)**. As a matter of course, the perspective of overpotential-governed HER well interpreted the commonly used "trick" of increasing current density to boost Zn reversibility. The electrochemical perspective offers a low-cost and feasible solution to mitigate parasitic side-reactions and irreversible Zn loss that plagued the rechargeability of Zn-based energy storage devices for centuries and more importantly would encourage more exploration of the Zn electrode on the right track. At the same time, it will be possible to design a more rational optimization strategy for the Zn metal anode based on this new knowledge of Zn deposition behavior.

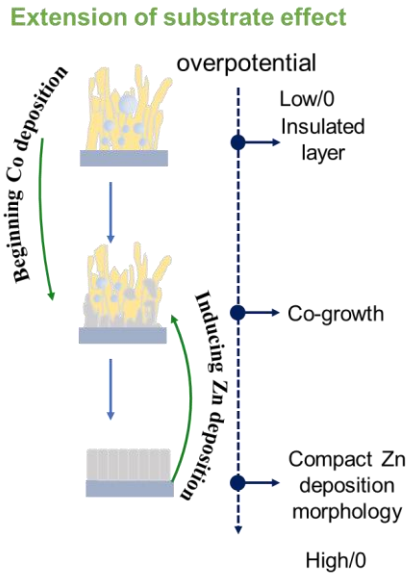

Figure 2.39 The schematic illustration of Zn electrodeposition chemistry for explaining the change in Zn morphology.

Chapter 3 Nb-coated Al foil as anode/cathode current collectors for optimized Zn deposition and high-energy-density RAZIBs.

3.1 Objective of this Chapter

As described in Chapter 2, materials with low HER catalytic activity, an excellent affinity for Zn, and high electronic conductivity are suitable as substrates, namely, the anode current collector, for Zn deposition. However, the choice of current collectors used in RAZIBs is one inconspicuous but very important issue that has not been paid much attention. Due to the corrosiveness of protic solvents to metals and the sensitivity of the water-splitting reaction, only highly conductive materials, which have excellent corrosion resistance and a lack of catalytic activity for water electrolysis, are suitable as current collectors in aqueous batteries. Therefore, only a few materials, including stainless steel,[147] copper (only for the anode),[148] nickel,[149] titanium [82], and carbon sheets[57], have been successfully employed as current collectors in AZBs so far.[150] Aluminum (Al) current collectors are widely used in LIBs, and the lightweight, low-cost, and highly conductive nature makes Al the best candidate for current collectors. Unfortunately, because Al is inevitably corroded in aqueous solutions, it is difficult to use Al as the current collector for AZBs directly. Niobium (Nb) is known for its excellent corrosion resistance because it forms a thin and stable protective passive film in aqueous solutions with a wide pH range.[151-152] Recently, some studies also pointed out that Nb_2O_5 is a good material for inducing uniform Zn deposition. [153] Moreover, Nb can form a dense and well-adhered coating on the surface of Al_2O_3 without damaging the substrate or the coating itself, even when the Al_2O_3 has a unique 3D structure, which allows Nb to form a superior anti-corrosion coating on the Al foil surface that is difficult to achieve with other coating methods.[154]

Considering these properties of Nb, in order to confirm the theory presented in Chapter 2 and to provide ideas for the design of highly reversible Zn metal anodes, in this chapter, through physical vapor deposition (PVD) method, thin Nb layers are magnetron sputtered to Al foils to make the Nb coated Al foils (Al-Nb foils), which are successfully used as the dual-purpose current collectors for both anode and cathode in RAZIBs (**Figure 3.1**). The magnetron-sputtered Nb

coating layer eliminates the influence of the insulating oxide layer on Al surface; the extremely thin oxide layer on the surface of the Nb layer can impede the corrosion of the current collector during the charging and discharging process while ensuring an excellent electronic conductivity of the current collector. PVD is a well-established technology suitable for industrial production. Since the RAZIBs supported by Al-Nb show excellent electrochemical cyclic performance and improved energy density in this study, the use of Nb coating may provide a new opportunity for realizing real-world applicable RAZIBs by providing light-weight current collectors.

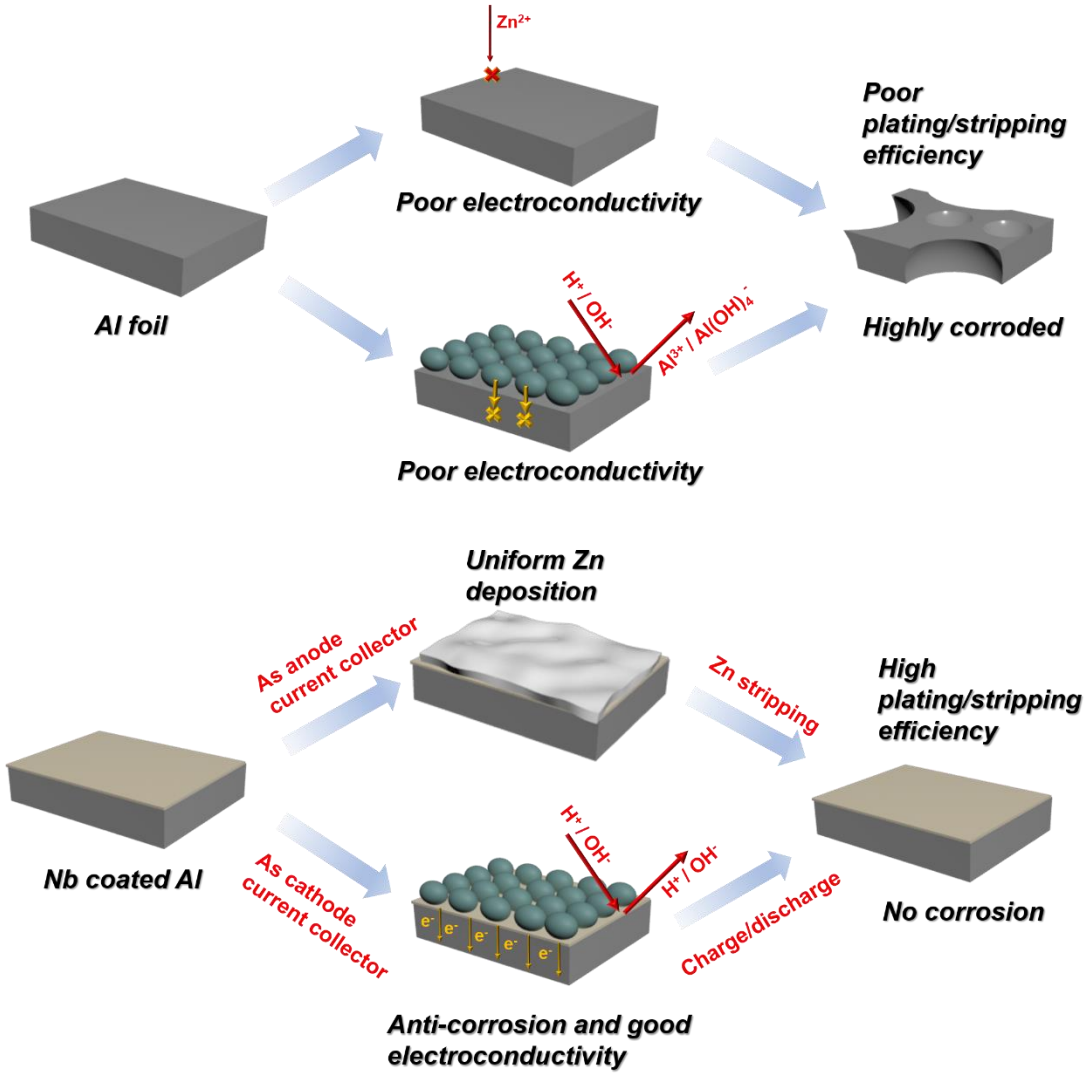

Figure 3.1 Schematic illustration of the difference between Al foil and Al-Nb when being used as anode/cathode current collectors for RAZIBs.

3.2 Experimental section

3.2.1 Preparation of the Nb-coated Al foil

First, Al foil (Hohsen, Japan) was cut to a disk whose diameter was 108 mm to fit the PVD carrier tray. The disk-shaped Al foil was then washed with surfactant and DI-water and dried in a vacuum box for 24 h. Before DC magnetron sputtering, the Al foil was sent to the chamber, which was first evacuated to less than 5×10^{-5} Pa and filled with Ar gas. During sputtering, the Ar pressure was maintained at 0.2-0.3 Pa at a constant current of 0.5 A, while the applied voltage was 250 V. The deposition times were 60 s, 300 s, 900 s, and 1500 s for preparing the Al-Nb substrates of different Nb-layer thicknesses.

3.2.2 Preparation of the cathode materials

Preparation of the α-MnO_2 nanowires: The α-MnO_2 nanowires were obtained by a one-step hydrothermal method. First, $MnSO_4$ and $KMnO_4$ were dissolved in 150 mL DI water with a molar ratio of 5:2. In this report, the amounts of $MnSO_4$ and $KMnO_4$ dissolved were 2.845g and 7.112g, respectively. The α-MnO_2 nanowires were obtained after the 12 h hydrothermal reaction that was processed at 140℃. The product was harvested after water washing and filtration.

Preparation of the VO_2: The preparation of VO_2 material was referred to the previous report.[155] First, 0.25 g commercial V_2O_5 (Tokyo Chemical Industry) was dispersed into graphene oxide (GO) suspension (2 mg mL^{-1}). After stirring, the suspension was transferred into Telfon-lined autoclave, and the reaction was processed at 180°C for 12 h. The obtained gel was then reduced by ascorbic acid (Vitamin C, VC) under 80°C in a water bath. The product can be harvested after washing and filtration.

3.2.3 Preparation of the cathodes

The vanadium dioxide (VO_2) cathode and manganese dioxide (MnO_2) cathode were prepared by pressing VO_2 (or α-MnO_2), Ketjen Black (KB,), Polytetrafluoroethylene (PTFE) mixture onto a titanium (Ti) mesh (Nilaco, Japan, 100 mesh), and the Ti mesh supported electrode was cut into disk electrodes (10 mm in diameter) for full cell test. The mixture slurry of the active materials was made by stirring the mentioned materials in 50% ethanol aqueous solution. The activated carbon (AC) electrode was prepared by pressing AC, Acetylene Black (AB) and PTFE coated

teflonized acetylene black (TAB-2®, as the binder) mixture onto a Ti mesh to make the AC disk electrode. The cathodes based on metal foils were prepared by the blade-casting method, in which, the slurry with different active materials (MnO_2, VO_2 or AC) was coated onto the Al foils or the Al-Nb foils to prepare the current collector@active material cathode.

In this chapter, the mass ratio of VO_2 (or α-MnO_2), KB and PTFE is 7:2:1. The mass ratio of AC, AB and the binder is 8:1:1. All the foils and meshes were cut into disk electrodes (10 mm in diameter) for Swagelok cells, or rectangle (5 cm × 7 cm) for pouch cells.

3.2.4 Electrochemical measurements

For the Zn||metal foil cells, the metal foils, i.e., Al foils, Al-Nb foils, Cu foils, and Zn foils, were cut into disk electrodes (diameter: 10 mm). The disk electrodes were placed in a Swagelok cell, in which Al foil (or Al-Nb foil, Cu foil) was used as the working electrode, while the Zn foil was used as the counter electrode. A piece of glass fiber filter (Advantec, GA-100) was used as a separator, and 200 μL electrolyte (2 mol L^{-1} $ZnSO_4$ aqueous solution) of pH 4.13 was added to the cell. The cells were operated under constant current, and the cut-off voltage for Zn stripping was set to 0.5 V.

For the Zn||Al-Nb@MnO_2 cells, two-electrode Swagelok cells were prepared by putting the Zn foil, Al-Nb@MnO_2 cathode, and a piece of glass fiber separator in the cell. 200 μL electrolyte, which consists of 2 mol L^{-1} $ZnSO_4$ and 0.2 mol L^{-1} $MnSO_4$ additive, was added to each cell. Constant current (CC) mode was employed for the tests, and the cut-off voltage was set at 0.8 V for discharge and 1.85 V for charge. The configuration of the full cell test is shown in **Figure 3.2.**

For the Zn||Al-Nb@AC cells, two-electrode Swagelok cells were prepared by putting the Zn foil, Al-Nb@AC cathode, and a piece of glass fiber in the cell. 200 μL electrolyte, which only contained 2 mol L^{-1} $ZnSO_4$, was added to each cell. CC mode was employed for the tests, and the cut-off voltage was set at 0.8 V for discharging and 1.8 V for charging.

For the Zn||Al-Nb@VO_2 cells, two-electrode Swagelok cells were prepared by putting the Zn foil, Al-Nb@VO_2 cathode, and a piece of glass fiber in the cell. 200 μL 2 mol L^{-1} $ZnSO_4$ electrolyte was used in each cell. CC mode was employed for the tests, and the cut-off voltage was set at 0.2 V for discharge and 1.4 V for charge.

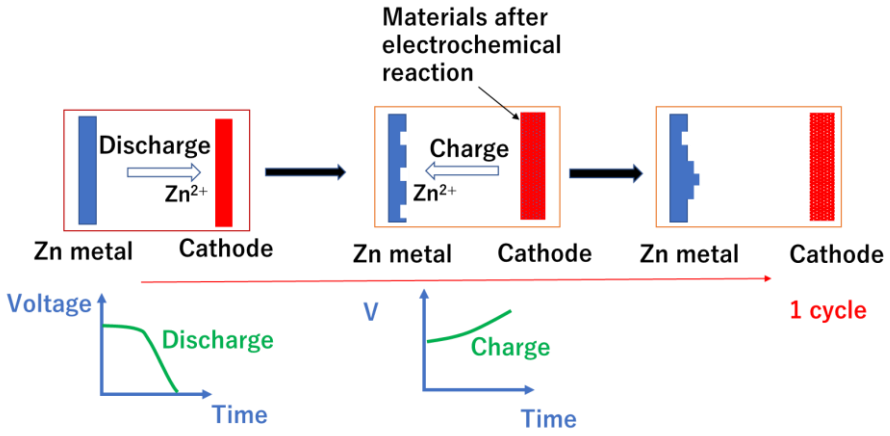

Figure 3.2 Schematic illustration for explaining the full-cell test.

For the Al-Nb@Zn||Al-Nb@MnO_2 cells, 7.5 mAh cm^{-2} Zn metal was pre-deposited onto an Al-Nb foil to prepare the Al-Nb@Zn anode. The two-electrode Swagelok cell was prepared by putting Al-Nb@Zn anode, Al-Nb@MnO_2 cathode, and a piece of glass fiber in the cell. 200 μL electrolyte, which consists of 2 mol L^{-1} $ZnSO_4$ and 0.2 mol L^{-1} $MnSO_4$ additive, was added to the cell. CC mode was employed for the tests, and the cut-off voltage was set at 0.8 V for discharge and 1.85 V for charge.

Air-assembled Zn-MnO_2 pouch cells were constructed with the same electrodes, electrolyte, and configuration. The electrode area was set at 7 cm×5 cm. The Al-Nb@Zn anode was paired with the Al-Nb@MnO_2 cathode (active MnO_2 loading: 30.0 mg cm^{-2}). Detailed parameters are presented in **Table 3.1, Table 3.2 and Table 3.3**. Constant current-constant voltage (CC-CV) mode was employed for the tests. The cut-off voltage was set at 0.8 V for discharge and 1.8 V for charge during the CC step, while the cut-off current was set at 0.1 C for the CV step.

The linear sweep voltammetry (LSV), and cyclic voltammetry (CV) measurements were all tested on an electrochemical workstation (Princeton VersaSTAT3). For the LSV tests, the sweep rate was 5 mV s^{-1}. For the CV tests, the sweep rate was 0.5 mV s^{-1}.

3.2.5 Characterization

Calculation details: The plane-wave code Vienna ab-initio simulation package (VASP) program was employed [156-157] to perform all the spin-polarized density functional theory (DFT) calculations within the generalized gradient approximation (GGA) using the Perdew-Burke-Ernzerhof (PBE)[158] formulation. The projected augmented wave (PAW) potentials[159-160] were used to describe the ionic cores and take valence electrons into account using a plane wave basis set with a kinetic energy cutoff of 500eV. The valence electron configurations applied in this work are $3s^2 3p^1$(Al), $5s^1 4d^4$(Nb), $4s^2 3d^2$(Ti), $4s^1 3d^{10}$(Cu), $2s^2 2p^4$ (O), and $1s^1$(H), respectively. Partial occupancies of the Kohn−Sham orbitals were allowed using the Gaussian smearing method and a width of 0.02 eV. The electronic energy was considered self-consistent when the energy change was smaller than 10^{-6} eV.

The G values are calculated by:

$G = H - T\Delta S = E_{DFT} + E_{ZPE} - TS$

E_{DFT} is the total energy from the DFT calculation. E_{ZPE} is the zero-point energy, S is the entropy and T is the temperature (298K).

The Cu (100) surface slab was constructed with 5 atomic layers, containing 107 Cu atoms. The Nb (100) surface slab was constructed with 5 atomic layers, containing 45 Nb atoms. The Al_2O_3 (001) surface slab was constructed with 8 atomic layers, containing 36 Al and 48 O atoms. The TiO_2 (111) surface slab was constructed with 6 atomic layers, containing 36 Ti and 56 O atoms. The Nb_2O_5 (001) surface slab was constructed with 6 atomic layers, containing 42 Nb and 93 O atoms. This slab was separated by a 15 Å vacuum layer in the z direction between the slab and its periodic images. During structural optimizations of the (110) surface models, a 3×3×1 gamma-point centered k-point grid for the Brillouin zone was used. Moreover, the atomic layers were allowed to relax fully.

Characterization: HRTEM observations, electron energy loss spectroscopy (EELS) measurements, and elemental analysis were conducted on a Cs-corrected scanning transmission electron microscope (STEM, Titan3 G2 60-300, FEI Company). Auger electron spectra were obtained by an Auger electron spectroscopy system (JAMP-9500F). X-ray photoelectron spectra depth profiles

were obtained by X-ray photoelectron spectroscopy (XPS, JEOL, JPS-9200) system, and the Mg-Kα X-ray source (hν = 1253.6 eV) was chosen. X-ray diffraction (XRD) patterns were obtained using an X-ray diffractometer (Rigaku MiniFlex600) using Cu Kα radiation. Atomic force microscopy (AFM) tests were conducted on an AFM (Hitachi, NanonaviSII). The scanning electron microscope (SEM, ZEISS Sigma 500) was used for morphology observation, combined with the energy dispersive spectroscopy (EDS) measurements. The distribution of relaxation times (DRT) simulation was conducted using the DRT tools. For the SEM observations of the cathode current collectors used in the full-cell tests were washed after being removed from the cells. After drying in a vacuum oven, the portion of the current collector was used for subsequent SEM observation. All the samples for STEM observations were prepared using an ultramicrotome (RMC Boeckeler Instruments, PowerTomeXL).

3.3 Result and discussion

3.3.1 Preparation and characterization of the Al-Nb foils.

The Al-Nb foil was prepared by depositing Nb metal onto the surface of the Al foil. Adjusting the time of magnetron sputtering resulted in different thicknesses of Nb coating. The sample with a moderate thickness to characterize the structure information of the Al-Nb foil was selected. The as-prepared Al-Nb foil has a flat and clean surface, as shown in **Figure 3.3.** The Al-Nb foil sample, obtained by sputtering Nb metal to Al foil for 15 min at the voltage of 250 V, was first treated by an ultramicrotomy to prepare an electron-transparent cross-section sample for scanning transmission electron microscopy (STEM) observation. As shown in **Figure 3.4,** a dense layer consisting of Nb and O is tightly adhered to the surface of the Al substrate. The thickness of Nb coating is around 310 nm, while the composition analysis shows that the atom ratios of Nb and O in the Nb coating layer are 86.8% and 12%, respectively **(Figure 3.4(d) and Figure 3.4(e))**. The selected area electron diffraction pattern of the Nb coating revealed a bcc pattern; thus, the coating was metallic Nb supersaturated with oxygen. The oxygen may be originated mainly from the moisture impurity in the sputtering chamber.

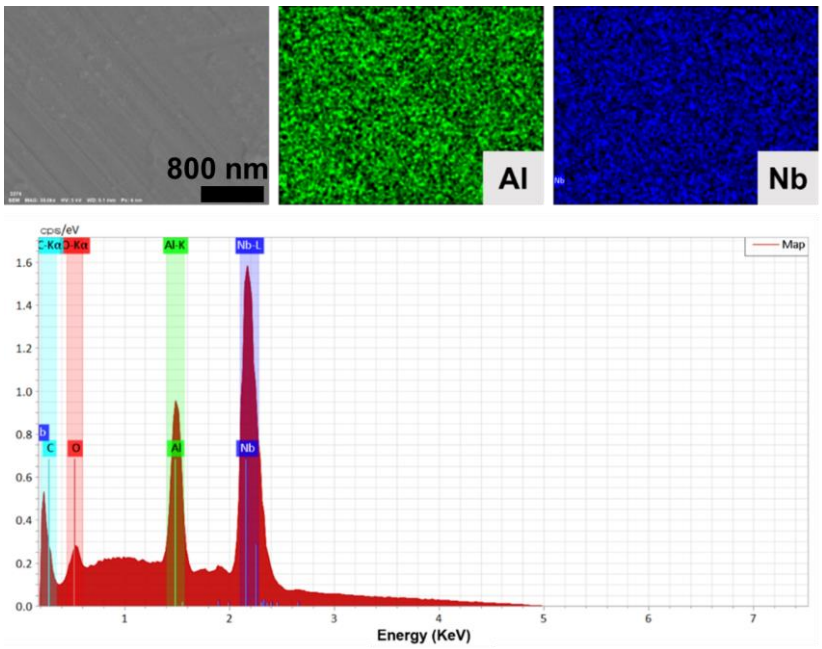

Figure 3.3 Top-view SEM image and the corresponding EDS mapping and spectra of the Al-Nb foils.

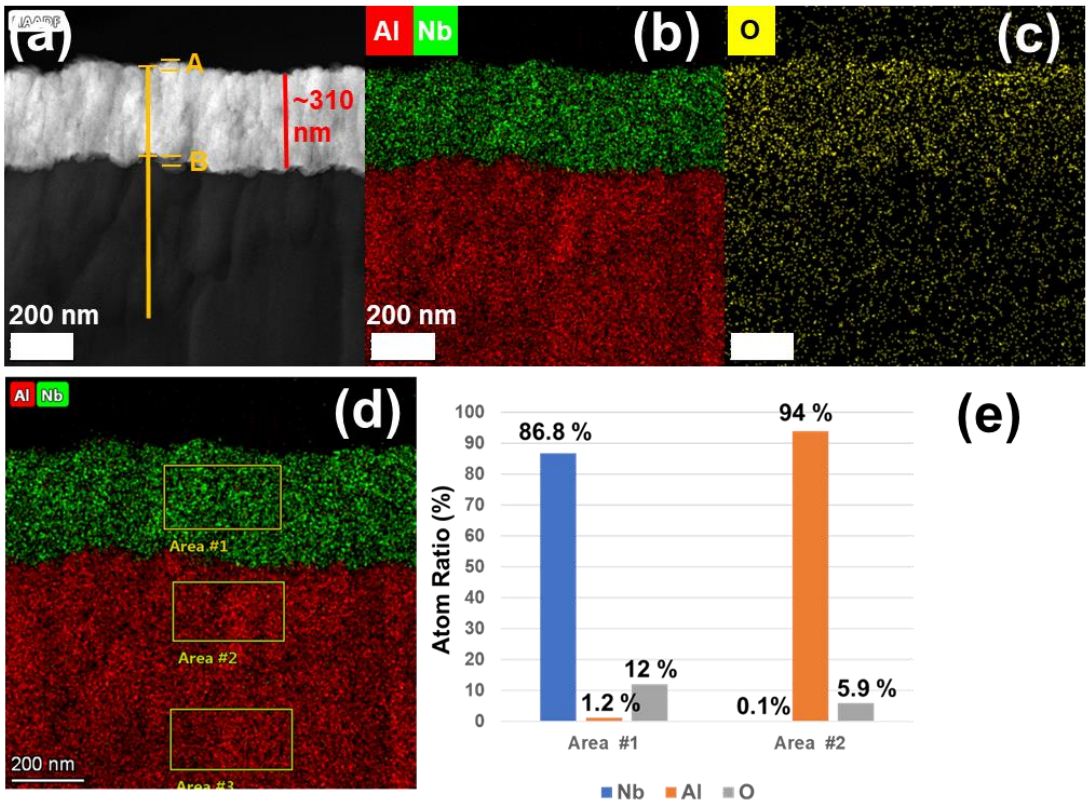

Figure 3.4 (a) Cross-sectional STEM image and (b, c) the corresponding EDS mapping of the Al-Nb foil. (d,e) Atom ratios of different regions in STEM image of the Al-Nb sample.

High-resolution transmission electron microscopy (HRTEM) observation was employed to detect the surface and interface information of the Al-Nb foil. As shown in **Figure 3.5(a)**, the top surface of the Nb coating is covered by a thin but dense oxide layer, which is naturally formed in the air with a thickness of several nanometers. Amorphous interphase with a thickness of about 5 nm was observed between the Al substrate and the Nb coating in **Figure 3.5(b)**. The amorphous interphase, possibly sourced from the naturally formed oxide layer on Al foil, tightly bonds the Al substrate and the Nb coating.[161-162] The structure model of the Al-Nb foil is depicted in **Figure 3.5(c).** Auger electron spectroscopy (AES) and electron energy loss spectroscopy (EELS) were used to understand the structure further. The AES depth profile of the Nb coating is shown in **Figure 3.5(d)**; a 30 s argon-ion (Ar^+) etching was processed before every cycle except the first one. The etching rate is 0.44 nm min^{-1} (calculated by etching SiO_2). Two peaks belonging to Nb

(MNN electronic transition,195.5 eV) and O (KLL electronic transition, 506.8 eV), respectively, are marked in the figure. The intensity of the Nb MNN peak increases with the etching, whereas the intensity of the O KLL peak shows an exact opposite trend, indicating that the passivation layer is a thin oxide film with a thickness of several nanometers. Line profile EELS spectra, recorded from the top of the orange line to the bottom of the orange line in **Figure 3.4(a)**, are presented in **Figure 3.5(e)** and **Figure 3.5(f)**. Total 100 points were recorded during the scanning. The first and the second points recorded at position A as marked in **Figure 3.4(a)** are shown in **Figure 3.5(e)**. As depicted in **Figure 3.5(e)**, the peak at roughly 245 eV is regarded as the recorded Nb-$M_{4,5}$ edge, caused by the transition of 3d electrons to the unoccupied 4f and 5p states. The peak shows a typical shape of Nb^{5+}, indicating that the main composition of the thin oxides layer is Nb_2O_5.[163] Moreover, only the first and the second points recorded a similar curve during the EELS measurement, demonstrating that the thickness of the oxide layer is about several nanometers **(Figure 3.6)**. Three points recorded at position B, as marked in **Figure 3.4(a)**, are shown in **Figure 3.5(f)**, which reveals the interphase composition. At the first point, the two peaks for the Al-$L_{2,3}$ edge can be clearly observed, indicating the simultaneous presence of Al_2O_3 and metallic Al in the interphase layer. The second and third points only show a less-obvious Al peak, demonstrating that the interphase thickness agrees with the results obtained from HRTEM observation. The composite form of both metal and oxide at the interface ensures a reliable electronic path between the Nb coating and the Al substrate. Furthermore, the extremely thin upper surface oxide layer will not unduly damage the electronic conductivity of the Al-Nb foil, which gives Al-Nb the basic possibility of being employed as a current collector.

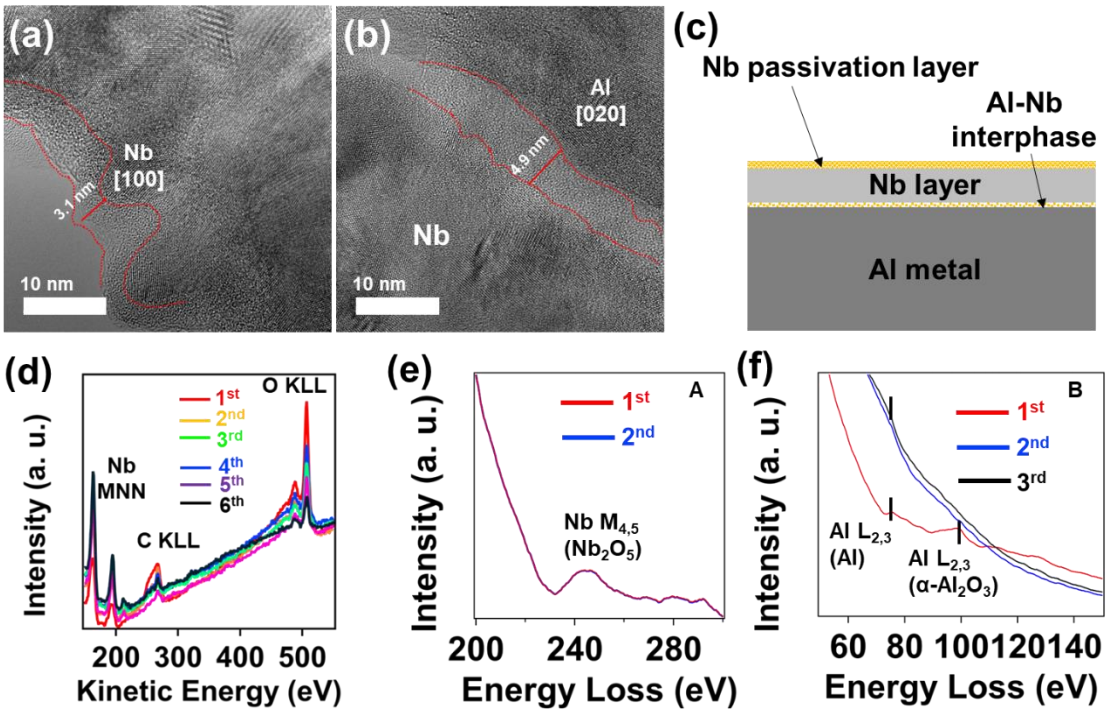

Figure 3.5 HRTEM micrograph of (a) the Nb coating at its top surface and (b) the interface between Al substrate and Nb coating. (c) Schematic illustration for the structure of Al-Nb. (d) AES depth profile of the Al-Nb. The EELS spectra of the Al-Nb taken from (e) the outer surface (position A, Figure 4.3(a)), and (f) the interface (position B, Figure 3.5(a)). The orange line shown in Figure 4.3(a) is where to capture the EELS spectra through a linear scanning method, the distance between two sampling points is about 4 nm.

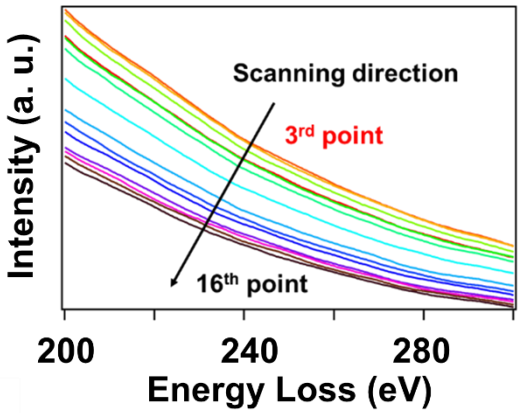

Figure 3.6 The EELS spectra of Nb taken from the outer surface (starting from the position A in Figure 3.4(a)). The peak of Nb_2O_5 no longer appears in the spectra.

3.3.2 Electrochemical properties of Al-Nb as an anode current collector

The electrochemical characteristics of Al-Nb foil were examined first as the anode current collector. Electrochemical impedance spectroscopy (EIS) was employed to understand the difference between three metallic substrates. Here, two-electrode cells were assembled using Zn foil as a counter electrode and Cu foil or Al-Nb foil or Al foil as a working electrode. 2 mol L^{-1} $ZnSO_4$ aqueous solution (aq.) was used as the electrolyte. As shown in **Figure 3.7**, the Al foil exhibits large interfacial impedance, the Al-Nb foil shows moderate value, and the Cu foil shows the lowest resistance. The highest resistance implies that the surface of Al foil is passivated by forming a thicker passive film in the aqueous solution, and this insulating passivation layer may be the culprit of the markedly reduced conductance. The conductive atomic force microscopy (c-AFM) observation also demonstrates the surface conductivity of different metal surfaces. As shown in **Figure 3.8**, the surfaces of both Al-Nb foil and Cu foil show a high number of high conductivity sites suitable for electrochemical reactions, while the conductivity on the Al surface is relatively low. The linear sweep voltammetry (LSV) tests were then conducted for Zn plating on different substrates to discuss the difficulty of Zn deposition on different metals. As shown in **Figure 3.9(a)**, in order to avoid the possible influence from the HER, the onset potential of the galvanizing is specified as the voltage at which the current density is -0.25 mA cm^{-2}. The onset potential of the growth of Zn on Cu foil, Al-Nb foil, and Al foil are -1.01 V, -1.02 V, and -1.07 V (vs. Ag/AgCl), respectively. The results indicate that the Cu foil seeds the deposition of Zn well, and the nucleation of Zn on the Al-Nb is slightly influenced due to the relatively high impedance. The significant lagging of the deposition onset potential and the low galvanizing current demonstrates that both the nucleation and the growth of Zn are greatly hindered by the passive film on the Al foil.

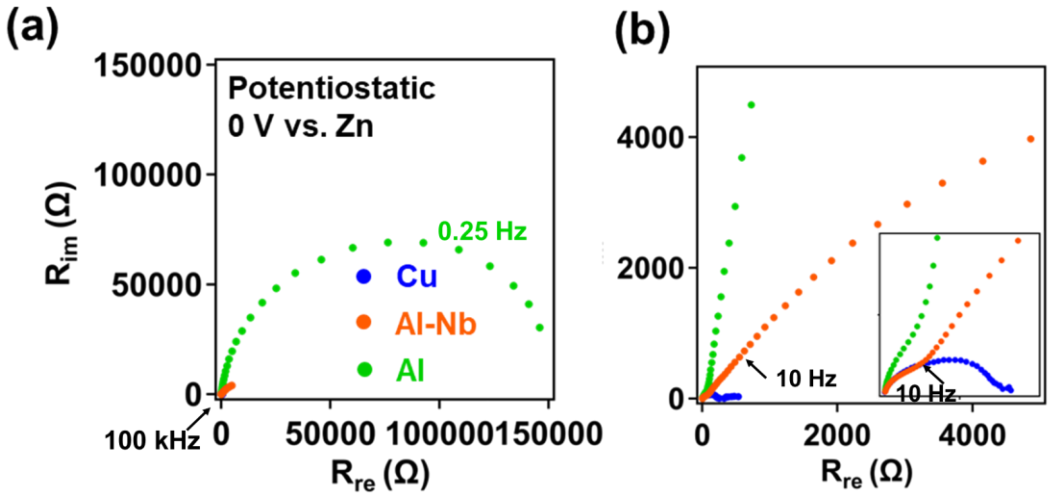

Figure 3.7 (a, b) Nyquist plots of different cells, **Figure 3.7(b)** is the enlarged **Figure 3.7(a)**.

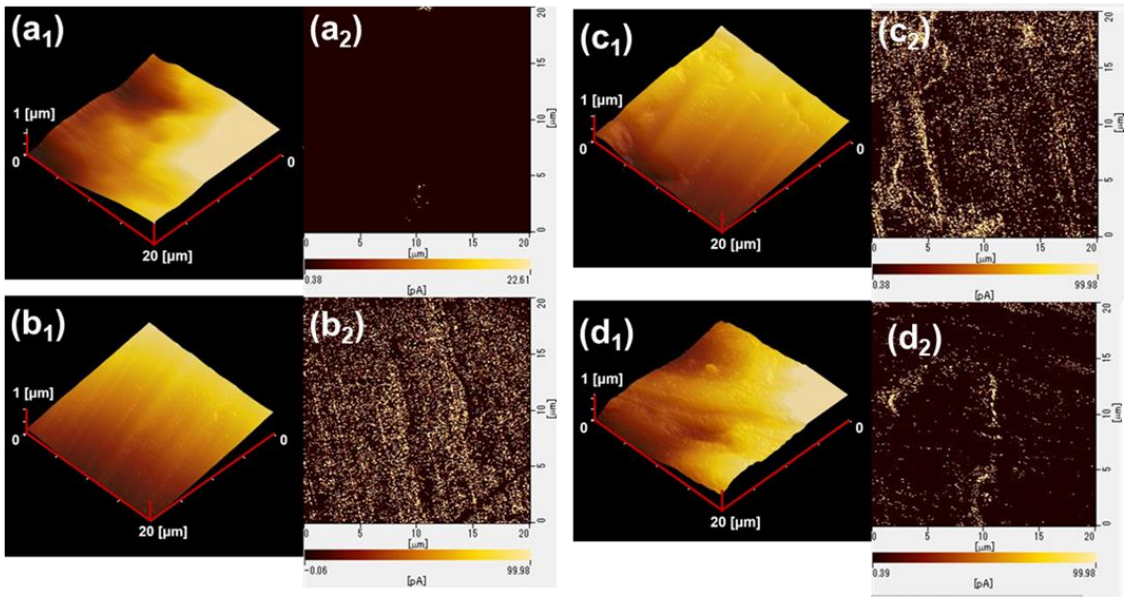

Figure 3.8 Conductive atomic force microscopy (c-AFM) observation of different metal substrates. a_1) 3D morphology and a_2) current map of the Al foil; b_1) 3D morphology and b_2) current map of the Al-Nb foil; c_1) 3D morphology and c_2) current map of the Cu foil; d_1) 3D morphology and d_2) current map of the Ti foil.

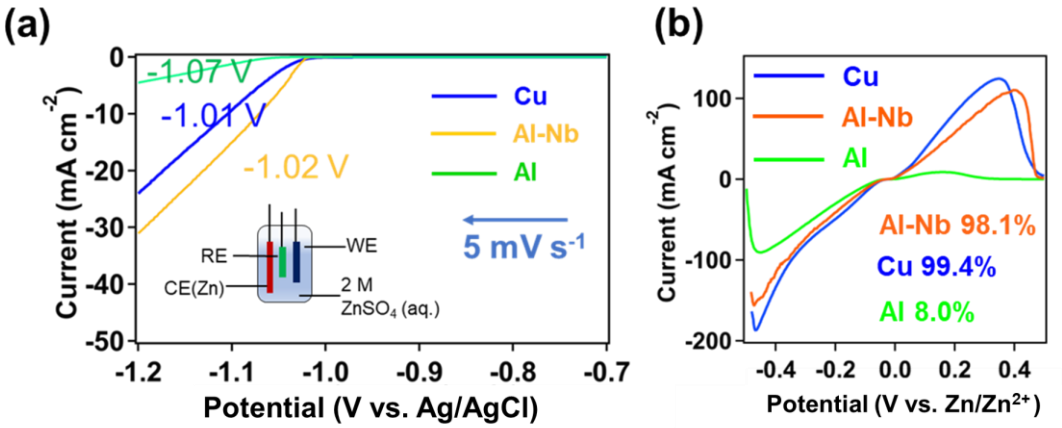

Figure 3.9 (a) LSV curves of different substrates tested in the three-electrode cell. The electrolyte is 2 mol L^{-1} $ZnSO_4$ aqueous solution. When the current density is -0.25 mA cm^{-2}, the potentials corresponding to the Cu foil, the Al-Nb foil and the Al foil are -1.01 V, -1.02 V, -1.07 V, respectively. (b) LSV curves of different Zn||Substrate cells tested in Swagelok cell.

The growing difficulty of Zn on three different substrates is as Al > Al-Nb ≈ Cu, among which the slightly higher overpotential of Al-Nb than Cu confirms the point of view that the passive film on Al-Nb will not seriously hinder the galvanizing on Al-Nb foil. The other LSV test for Zn plating/stripping procedure on different metals was also employed to discuss whether the Nb coating can optimize the galvanizing reversibility on Al foil. As shown in **Figure 3.9(b)**, the sweep started from -0.5 V (vs. Zn/Zn^{2+}) and ended at 0.5 V. The anodic peak in the positive potential region represents the stripping capability of Zn on different substrates. The ratio of the capacity generated by the negative current to the positive current reflects the reversibility of the Zn deposition. The ratio of negative/positive capacity for the Cu foil, the Al-Nb foil, and the Al foil is calculated to 99.4%, 98.1%, and 8%, respectively. An apparent conclusion is drawn after comparing the capacity ratio; that is, the Zn deposited on the Al foil is difficult to be dissolved due to the blocked electron pathway, while the stripping of Zn from Al-Nb foil shows a Zn plating/stripping reversibility that is close to Cu foil. The above discussion shows that introducing Nb coating will eliminate the conductivity degradation caused by the surface passivation of Al. Another serious problem is the formation and accumulation of zinc hydroxide sulfate

($Zn_4(OH)_6SO_4$ xH_2O, (ZHS)) in the electrolytes, which will damage the performance of the Zn anode.[164] Here, by carrying out an LSV test in a K_2SO_4 aqueous solution, the hydrogen evolution reaction (HER) activity of different substrates was examined. H_2SO_4 was added to the K_2SO_4 aqueous solution to obtain a faintly acidic solution consistent with the $ZnSO_4$ aqueous solution (pH≈4.1). As shown in **Figure 3.10**, the potentials required for the Cu foil, the Al-Nb, and the Al foil to achieve a current density of 1 mA cm^{-2} are -1.03 V, -1.54 V, and -1.59 V (vs. Ag/AgCl), respectively. In the range of Zn deposition potentials (i.e. -0.97 V to -1.1 V vs. Ag/AgCl), the HER can hardly take place on the surface of the Al-Nb foil because no significant current can be observed in this range. This indicates that the Al-Nb foil is far superior to Cu foil in inhibiting the hydrogen evolution in such an acidic condition. Then, the author employed a simple potentiostatic test to examine the formation of ZHS on different substrates in a 2 mol L^{-1} $ZnSO_4$ aqueous electrolyte when the electrodeposition of Zn is absent. Zn||substrate two-electrode cells, which employed the Zn foil as the counter electrode and the metal substrate as the working electrode, were used in the test. The potential was controlled to 0 V (vs. Zn/Zn^{2+}) during the test.

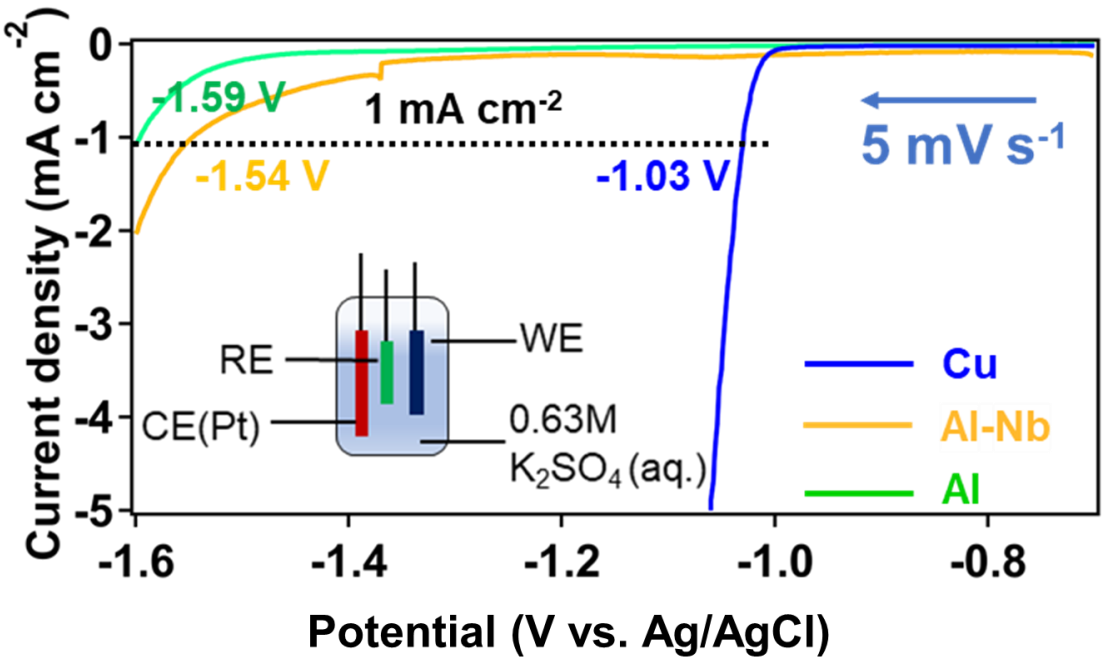

Figure 3.10 LSV curves of different substrates during HER in the three-electrode cell.

As shown in **Figure 3.11(a)**, tens of micro-ampere current were monitored on the Cu foil during the 50 hours test, whereas only 2 μA were observed on the Al-Nb foil. On the Al-Nb foil, the current recorded is mainly caused by the slight HER, but for the Cu foil, the underpotential deposition of Zn can also be regarded as a current source.[145] Hence, the HER on the Cu can also be partially influenced by the deposited Zn atom layer. The progress of the HER will increase the OH^- concentration at the electrode-electrolyte interface and promote the formation of ZHS: [115, 136]

$$2H_2O+2e^-\rightarrow H_2+2OH^- \quad \textbf{(Eq. 3.1)}$$

$$4Zn^{2+}+6OH^-+SO_4^{2-}+xH_2O\rightarrow Zn_4(OH)_6SO_4\cdot xH_2O \quad \textbf{(Eq. 3.2)}$$

The increase in OH^- concentration leads to severe corrosion to the Cu foil and causes a large amount of ZHS to accumulate on its surface, which results in a significant corrosion current. The surface condition of the metal substrates was examined by scanning electron microscopy (SEM) and energy-dispersive X-ray spectroscopy (EDS), and the results are presented in **Figure 3.11(b, c, d).** Numerous flaky ZHS covers the upper surface of the Cu foil, and the surface of Al foil is also full of ZHS residues. This shows that when used as anode current collectors, a large amount of ZHS will generate on both Al foil and Cu foil, and the accumulation of ZHS will inevitably damage the electrochemical performance of the Zn metal anode.[165] By contrast, ZHS is barely observed on the surface of Al-Nb foil, which is consistent with the extremely low current in the potentiostatic tests.

The difference between the Al foil and the Al-Nb foil can be explained by the difference in the PZC of Al_2O_3 and Nb_2O_5. In an aqueous solution, the PZC of Al_2O_3 generally appears in an alkaline environment; for example, the PZC of α-Al_2O_3 is commonly recorded when pH = 9.1.[166-167] This PZC value causes the surface of Al foil to be charged; thus, the ion in the electrolyte can be easily attracted and precipitated onto the surface to form the ZHS. In reverse, the PZC of Nb_2O_5 was considered to appear when pH = 4.1, which is quite close to the pH recorded in the $ZnSO_4$ electrolyte. [168] The surface charge density of the Al-Nb is close to 0, which makes the sedimentation of ZHS difficult, allowing Al-Nb to maintain a clean surface. These results show that when used as anode current collectors, a large amount of ZHS will generate on both Al foil

and Cu foil, and the accumulation of ZHS will damage the electrochemical performance of the Zn metal anode. By contrast, ZHS is barely observed on the surface of Al-Nb foil, which is also consistent with the extremely low current in the potentiostatic tests.

Repeated Zn plating/stripping tests on the substrates will intuitively reflect the cycling performance of the anode side when different substrates are used as anode current collectors. As shown in **Figure 3.12(a)**, Al||Zn, Al-Nb||Zn, Cu||Zn half-cells were assembled and tested under a current density of 25 mA cm^{-2}; here, the areal capacity of Zn deposition was controlled to 6.25 mA h cm^{-2} in each cycle. The Al||Zn cell only has an initial coulombic efficiency (I.C.E.) of 28.99 %, and 49.68 %, 75.41 % for the next two cycles. The badly low I.C.E. indicates that the high-resistance passivation layer on the Al metal significantly affects the electrochemical dissolution of the as-deposited Zn metal. The Cu||Zn cell and the Al-Nb||Zn cell show high I.C.E. of 96.60 % and 93.91 %, respectively. The higher I.C.E. on Cu foil is due to the unobstructed electronic pathways between Cu and Zn during the initial cycle.

Regarding the whole test, the Al-Nb||Zn cell provides a stable average coulombic efficiency (A.C.E.) of 99.17 %, while the Cu||Zn cell offers an A.C.E. of 99.34%. The high A.C.E. values show that Al-Nb owns the ability to guarantee the deposition reversibility of Zn comparable to that of Cu foil. It is also worth noting that the Al-Nb||Zn cell has a life span of 320 cycles, while the Al||Zn cell and the Cu||Zn cell survive for 49 cycles and 161 cycles before short-circuiting, respectively. Voltage profiles of the three cells are shown in **Figure 3.12(b)** and **Figure 3.12(c)**. As presented in **Figure 3.9(b),** extremely high overpotential can be observed when Zn coating is stripped from Al foil, indicating that the insulating passivation layer severely hinders the electrochemical dissolution of Zn. Comparing the performance of Al-Nb foil and Cu foil, it can be found that the overpotential of Zn deposition on Al-Nb is slightly higher than that of Cu, which can be ascribed to the relatively higher electrochemical impedance of Al-Nb. Due to a similar reason, the Zn stripping overpotential of Al-Nb is also slightly higher than that of Cu, but as being pointed out in **Figure 3.12(b)** and **Figure 3.12(b)** that the stripping overpotential (134 mV and 132 mV) at the capacity of 3.125 mAh cm^{-2} does not change during the 300 cycles, demonstrating that the Al-Nb foil can maintain a good surface condition to support the electrochemical cycling

of Zn metal anode. The optical photos and SEM images for different substrates after one cycle of Zn plating-stripping confirmed the surface condition change during the half-cell tests. As shown in **Figure 3.13(a) and 3.13(c)**, the Cu surface is covered by messy ZHS, which is the primary reason for the damaged cycling performance.

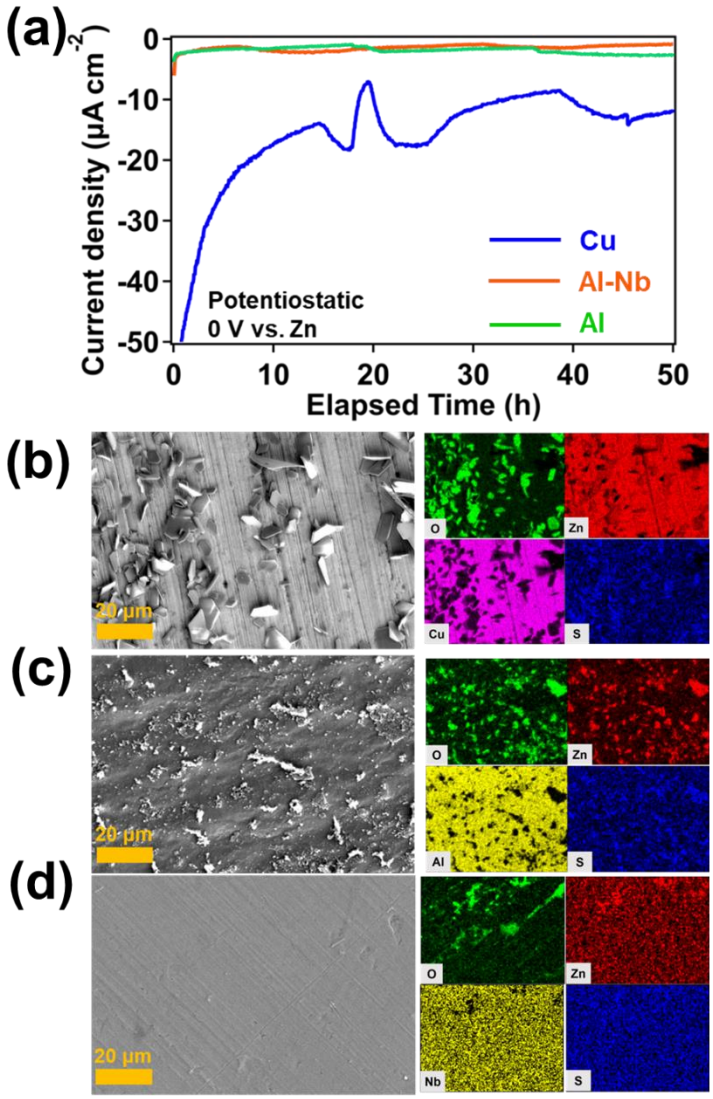

Figure 3.11 (a) Current-Time curves of the different metal substrates corroded under constant potential. SEM images and the corresponding EDS mapping of the (b) Cu foil, (c) Al foil, (d) Al-Nb foil after the potentiostatic test.

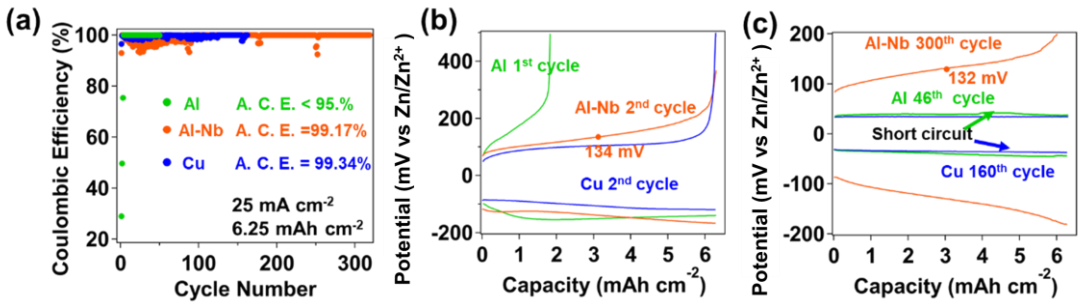

Figure 3.12 (a) Coulombic efficiency of Zn plating/stripping in Al||Zn (green), Al-Nb||Zn (orange) and Cu||Zn (blue) cells. Voltage profile of the half-cells at (b) early stage and (c) late stage.

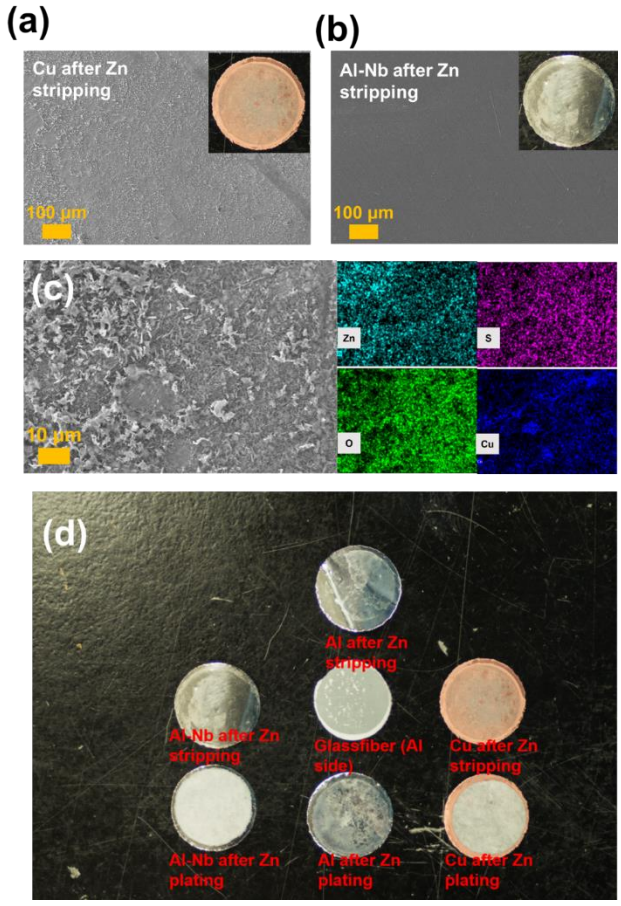

Figure 3.13 SEM images of (a) Cu foil after Zn stripping and (b) Al-Nb foil after Zn stripping, the inset optical photos are the Cu foil and the Al-Nb foil after Zn stripping. (c) SEM image and EDS mappings of the Cu foil after Zn plating/stripping for one cycle. (d) Optical photos of different metal substrates after Zn plating or Zn stripping.

As a comparison, a clean surface with a metallic luster, which belongs to the Al-Nb foil after a one-time galvanizing-stripping cycle, is shown in **Figure 3.13(b)**. In addition, optical photos of three different substrates after Zn deposition or Zn stripping are shown in **Figure 3.13(d)**. It can be seen that Al-Nb exhibits the best corrosion resistance and resistance to ZHS generation among the three substrates. It is also worth mentioning that the plating of Zn on the Al-Nb foil is also flat and smooth **(Figure 3.14)**, but the good deposition performance is not only due to its anti-corrosion properties but also due to the high current densities, by which the growth of dendritic crystals can be greatly suppressed.[101, 143]

X-ray photoelectron spectroscopy (XPS) depth profile was employed to detect the surface composition of the substrates after Zn stripping. As shown in **Figure 3.15(a)** and **3.15(b)**, the ZHS residues on Cu foil are present even at a depth of 140 nm, while the thickness of ZHS on Al foil is around 50 nm. No information from Cu 2p orbital was monitored within 80 nm depth of the Cu surface (**Figure 3.15(a)**), indicating that the ZHS layer formed on the Cu surface is very dense; thus, the current distribution and the migration of Zn atoms on the Cu surface would be undoubtedly influenced. The Al-Nb foil keeps clean after electrochemically stripping the as-deposited Zn coating, and the continuously visible peak from the Nb 2p orbital also confirms this conclusion **(Figure 3.15(c))**, by which the galvanizing and stripping can be carried out in a highly uniform way, as the author depicted in **Figure 3.16.** Reversibility tests for Zn deposition under different current densities are shown in **Figure 3.17** and **3.18**. It can be found that the coulombic efficiency of Al-Nb foil is slightly lower than that of Cu foil at low current densities, because the nucleation of Zn at low currents can be blocked by the relatively high surface impedance. The overpotential at low currents cannot reach enough to induce uniform nucleation of Zn on the Nb surface due to the existing Nb_2O_5 passivation layer, but a high CE value can still be maintained. Under the high current density and large deposition capacity, the Al-Nb can effectively reduce the proportion of side reactions presented on the collector surface, which makes Al-Nb exhibit excellent reversibility and lifetime under high current. Furthermore, electrodepositing Zn under a current density of 0.1 mA cm^{-2} will not break the Nb coating layer, indicating that the Nb coating can withstand the possible alloying reaction, thus guaranteeing the performance of Zn anode in

long-term cycling (**Figure 3.18**).

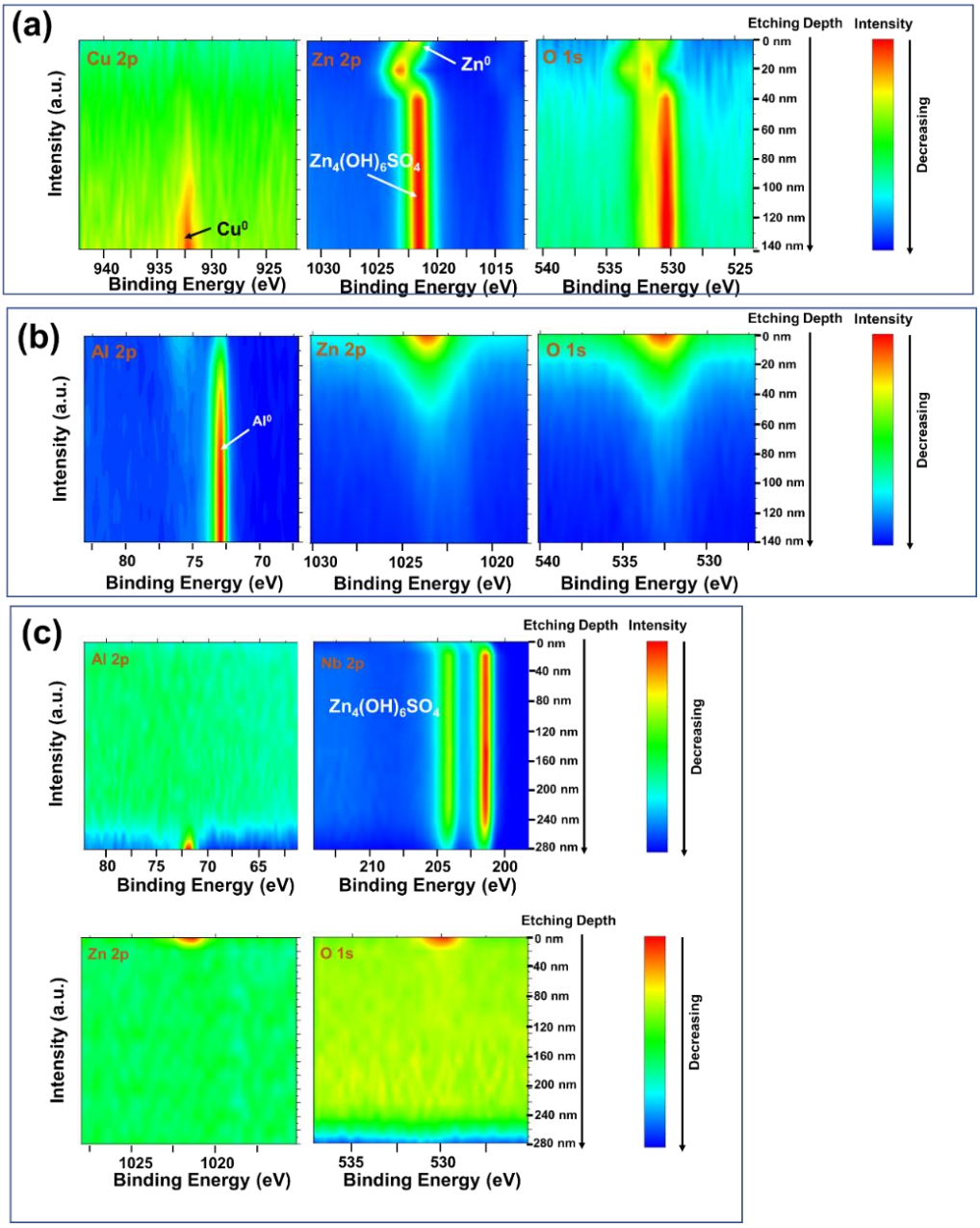

Figure 3.15 XPS depth profile of (a) the Cu foil, (b) the Al foil and (c) the Al-Nb foil after Zn stripping.

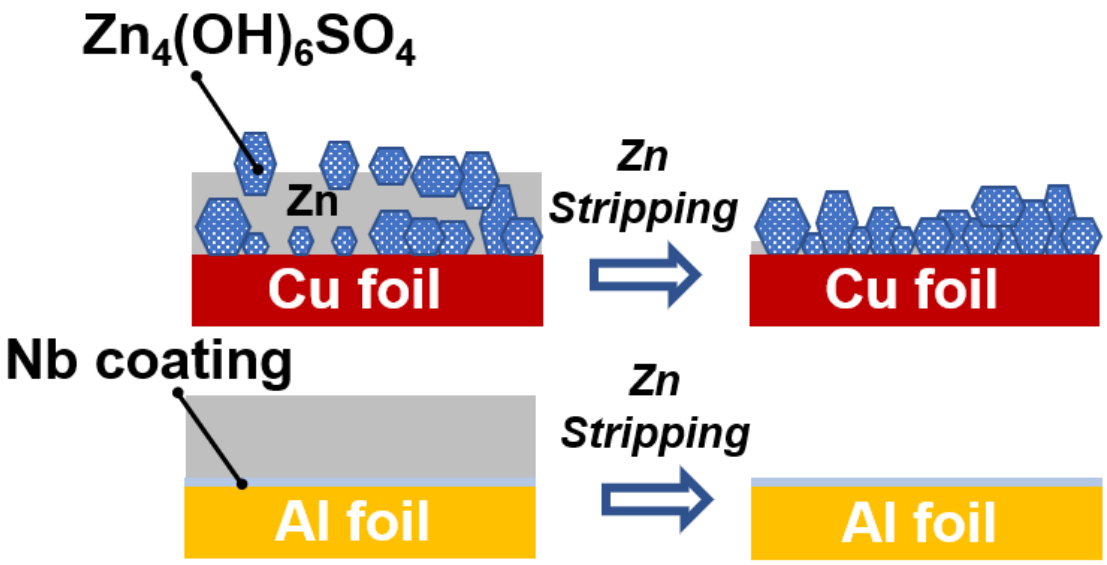

Figure 3.16 Schematic demonstration for the difference between Cu foil and Al-Nb foil.

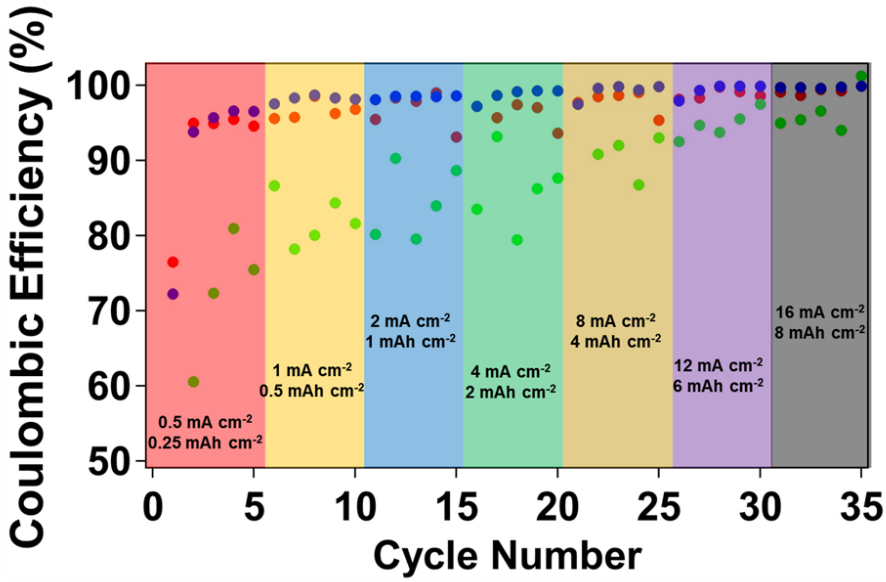

Figure 3.17 Zn plating/stripping rate performance of different substrates tested in the metal foil||Zn foil half-cells.

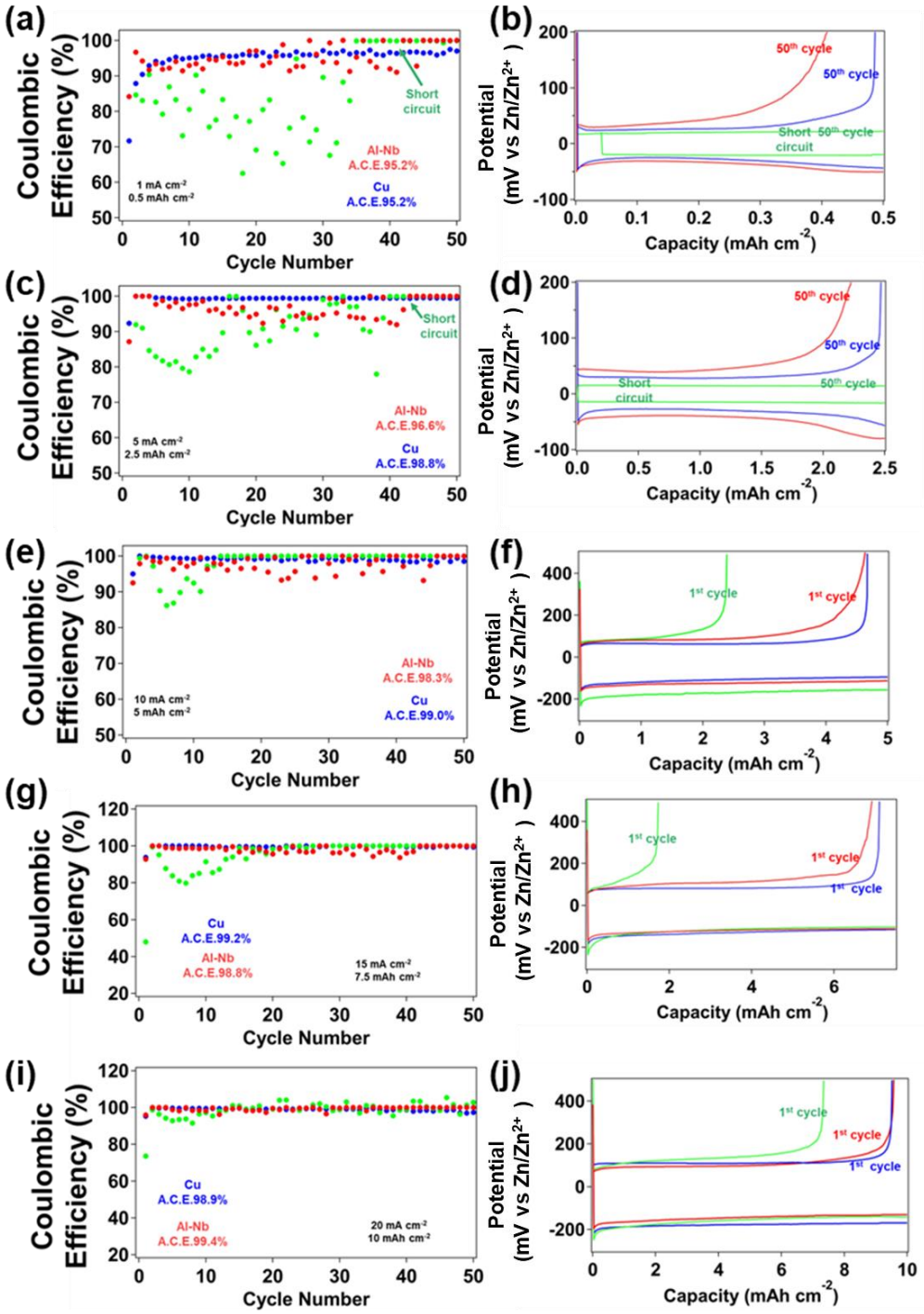

Figure 3.18 Coulombic efficiency of Zn plating/stripping when using different metal foils as the Zn deposition substrates. Coulombic efficiency of the cells tested under (a) 1 mA cm^{-2} (c) 5 mA cm^{-2} (e) 10 mA cm^{-2} (g) 15 mA cm^{-2} (i) 20 mA cm^{-2}. Corresponding potential profiles of (a) 1 mA cm^{-2} (c) 5 mA cm^{-2} (e) 10 mA cm^{-2} (g) 15 mA cm^{-2} (i) 20 mA cm^{-2}.

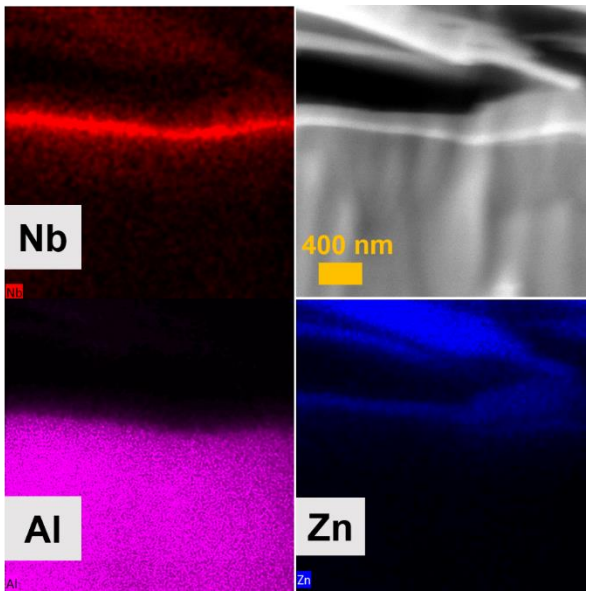

Figure 3.19 Cross-sectional SEM image and the corresponding EDS mappings of the Al-Nb foil after Zn deposition under low current density (0.1 mA cm^{-2}, 1 mAh cm^{-2}).

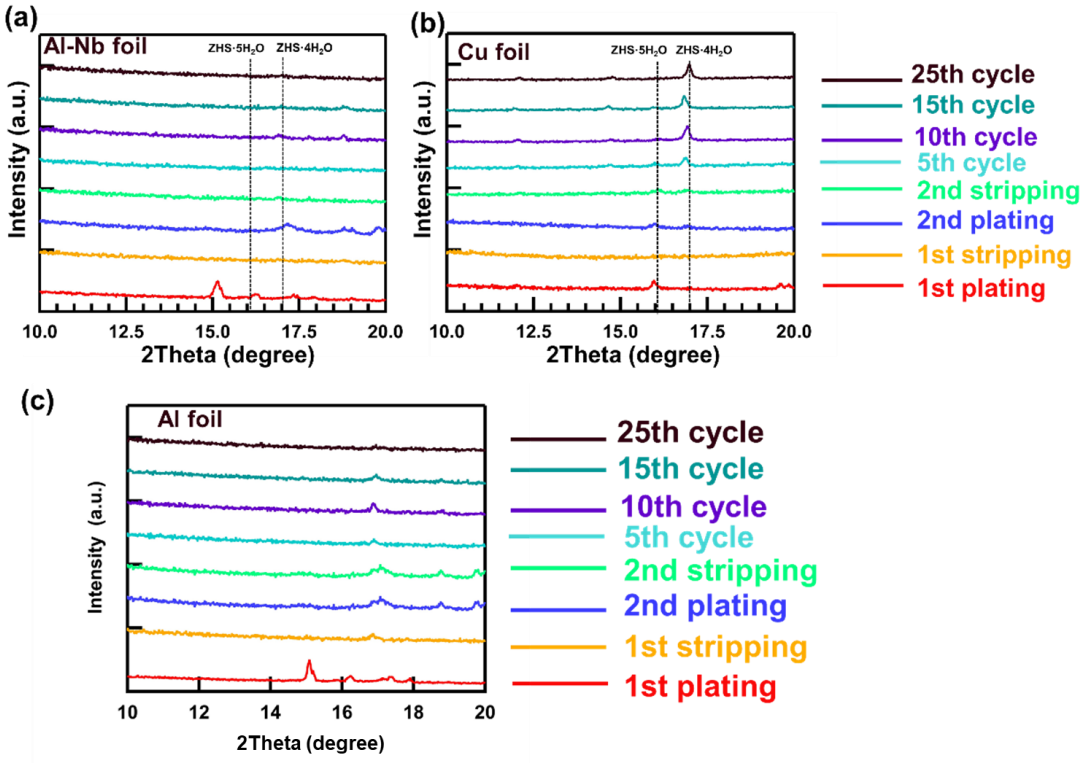

Figure 3.20 Ex-situ XRD patterns of different substrates after Zn plating/stripping. XRD patterns at different stage for (a) Al-Nb foil, (b) Cu foil, and (c) Al foil. The plating/stripping current density is 10 mA cm^{-2} and the capacity is 5 mAh cm^{-2}.

To further demonstrate the excellent performance of Nb coating in reducing ZHS formation, ex-situ XRD was applied to observe the accumulation of ZHS on different substrates during repeated Zn plating/stripping. As shown in **Figure 3.20(a),** peaks that belong to ZHS appeared on the Al-Nb after the first and the second Zn deposition, but after Zn stripping, there was almost no residual by-product on the surface of the Al-Nb foil. After a certain number of Zn plating/stripping cycles, the highly clean surface of the Al-Nb foil remained. This is attributed to the relatively low HER activity of Nb_2O_5 and the PZC close to the pH, making it difficult for ZHS to accumulate on the Al-Nb surface. In contrast, ZHS always appears on the surface of Cu (**Figure 3.20(b)**). As the cycle proceeds, ZHS will continue accumulating on the Cu surface, resulting in great risk of Zn dendrite formation on Cu, which is why Cu foil shows a much lower lifetime than Al-Nb in the half-cell test. DFT simulation was also employed to confirm the conclusion. As shown in **Figure 3.21(a)** and **Figure 3.21(b)**, for the three different substrates discussed, Cu exhibited the best catalytic performance for HER because it shows the lowest free energy barrier (0.14 eV) for the HER. The HER activity of Nb metal is also lower than Cu, while the HER activity of Nb_2O_5 and Al_2O_3 was much lower than that of the two metals. This suggests that Nb coating reduces the accumulation of ZHS in terms of reduced HER activity, thus improving the coulombic efficiency. Even though Al_2O_3 has low HER catalytic activity, the extremely high impedance of the Al_2O_3 passivation layer prevents the reversible deposition of Zn on its surface, making Al foil unsuitable as a current collector for Zn anode.

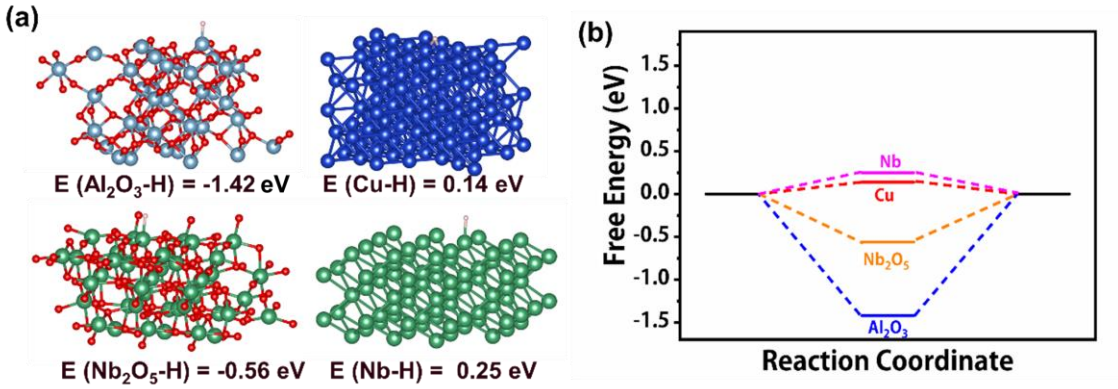

Figure 3.21 (a) The used models for DFT simulation. (b) Free-energy barriers for HER on different substrates.

3.3.3 Electrochemical properties of Al-Nb as a cathode current collector

Compared with anode current collectors, the selection of cathode current collectors in RAZIBs is more severely restricted due to more drastic pH changes and more severe corrosion at high cathode potentials. This chapter also demonstrates that Al-Nb foil is compatible when used as cathode current collectors. The Zn||MnO_2 cells were assembled by using different metal substrates as cathode current collectors. Al-Nb foil, Ti mesh, and Al foil were used to support MnO_2 cathode, denoted as Al-Nb@MnO_2, Ti@MnO_2, and Al@MnO_2, respectively. As shown in **Figure 3.22(a)**, cyclic voltammetry (CV) tests for different Zn||MnO_2 cells were conducted under a sweep rate of 0.5 mV s^{-1}. Electrochemical reactions are barely observed on the Al foil-supported MnO_2 cathode because electrons can hardly conduct through the passivated Al surface. Al-Nb foil-supported MnO_2 shows two reduction peaks at 1.20 V and 1.32 V, while Ti foil-supported MnO_2 cathode peaks at 1.23 V and 1.35 V, respectively. The difference in the peak position manifests that the electrical conductivity between the active materials and Al-Nb foil is slightly lower when compared to the Ti mesh current collector. However, the higher peak current of the Al-Nb@MnO_2 implies that the cathodes, which use Al-Nb foil as a current collector, may have a better mass-transfer performance than the conventional Ti mesh supported MnO_2 cathode. Then, the CV curves for cells with a metal foil||Zn configuration were measured, and the results are shown in **Figure 3.22(b).** The current observed in this test can represent the corrosion rate at different potentials. It is apparent that the Al foil will be strongly corroded at high potential, which can be partly ascribed to the boosted dissolution of Al metal under applied voltage and partly due to the oxygen evolution reaction (OER). The Ti mesh-related cell exhibits a rapid increase in current that starts from 1.62 V, while the current rise in the Al-Nb||Zn cell starts from 1.88 V, indicating that the Al-Nb foil has a better performance in anti-corrosion and anti-OER at high potential even when comparing it with Ti metal.

Based on this result, a constant potential test was used to evaluate the damage of the three current collectors under high voltage. As shown in **Figure 3.23(a)**, three different substrates were placed in Zn||metal foil cells. The Al showed a very high current and an increasing trend of dissolution during the 2V constant potential test, while the Al-Nb foil and Ti foil only showed a

low and stable current. The corrosion of the three substrates after the potentiostatic test is shown in **Figure 3.23(b, c, d)**, and **3.24,** it can be seen that many holes of different sizes appear on the surface of Al (**Figure 3.24(a)**), while the surfaces of Al-Nb foil and Ti foil remain almost unchanged. This indicates that the corrosion rate of Al at high voltage is much faster than the other two; only Al-Nb and Ti have the potential to be used as the current collector for RAZIBs. As shown in **Figure 3.25**, EIS results and the corresponding distribution of relaxation times (DRT) analysis also help prove the conclusion. Here, relaxation time τ_1, τ_2, and τ_3 are considered as contact resistance (including the solution resistance), film impedance, and charge transfer resistance, respectively. The film impedance of Ti foil is almost the same as the value of Al-Nb foil, while the charge transfer resistance of Al-Nb is slightly higher than that of Ti, which collaterally confirms the phenomenon observed in CV tests. Moreover, the influence of the thickness of the Nb coating is shown in **Figure 3.26**, from which the magnetron sputtering step should last for at least 5 minutes, and a longer magnetron sputtering time will bring more reliable performance. Nonetheless, the choice of the sputtering time should be adjusted according to real-world production requirements.

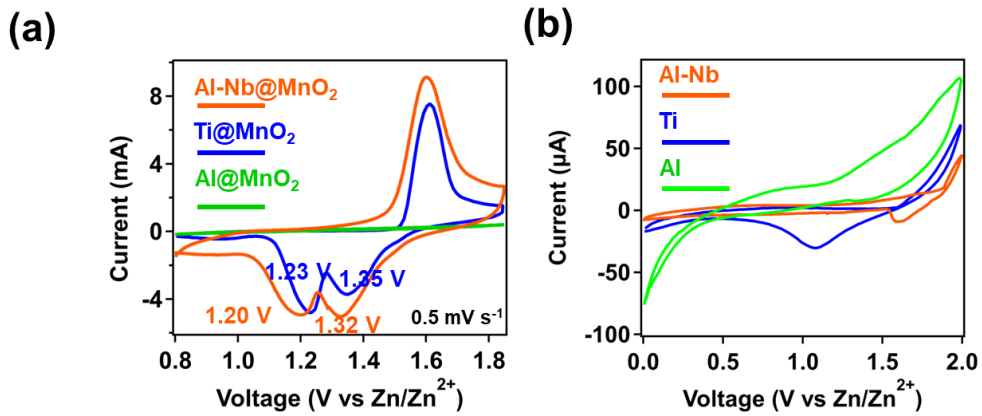

Figure 3.22 (a) CV curves of Zn||MnO_2 full cells at the scanning rate of 0.5 mV s^{-1}. (b) CV tests of Zn||metal foil half cells at the scanning rate of 0.5 mV s^{-1}.

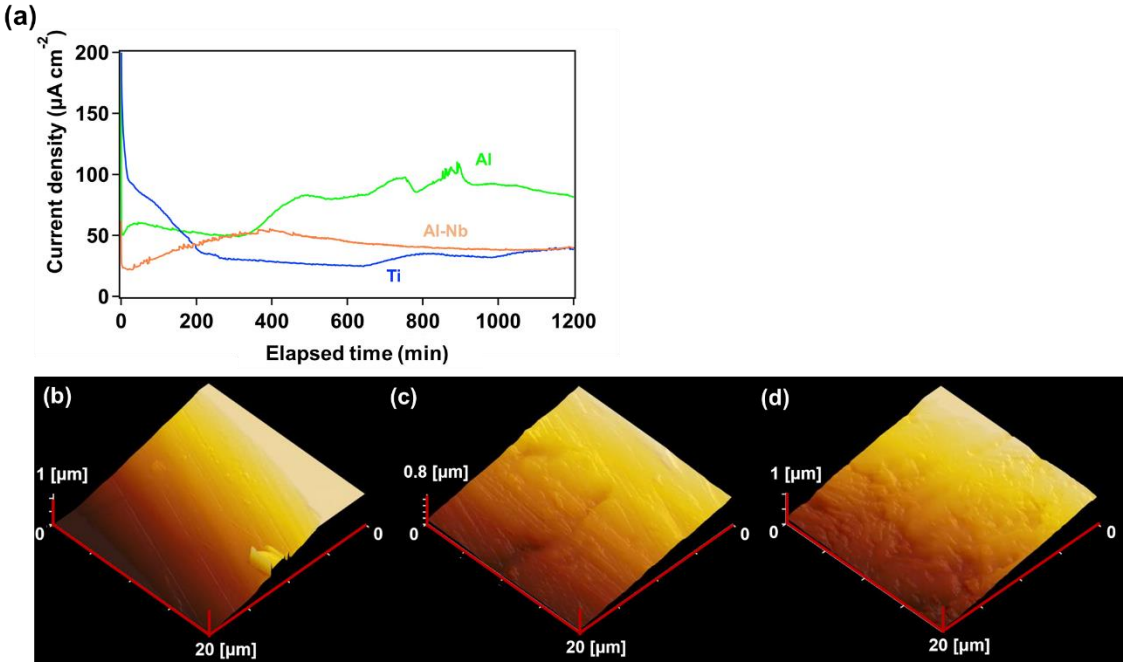

Figure 3.23 (a) Current profiles of different substrates under the 2 V (vs. Zn) potentiostatic test. AFM images of the tested (b) Al foil (c) Al-Nb foil and (d) Ti foil, respectively.

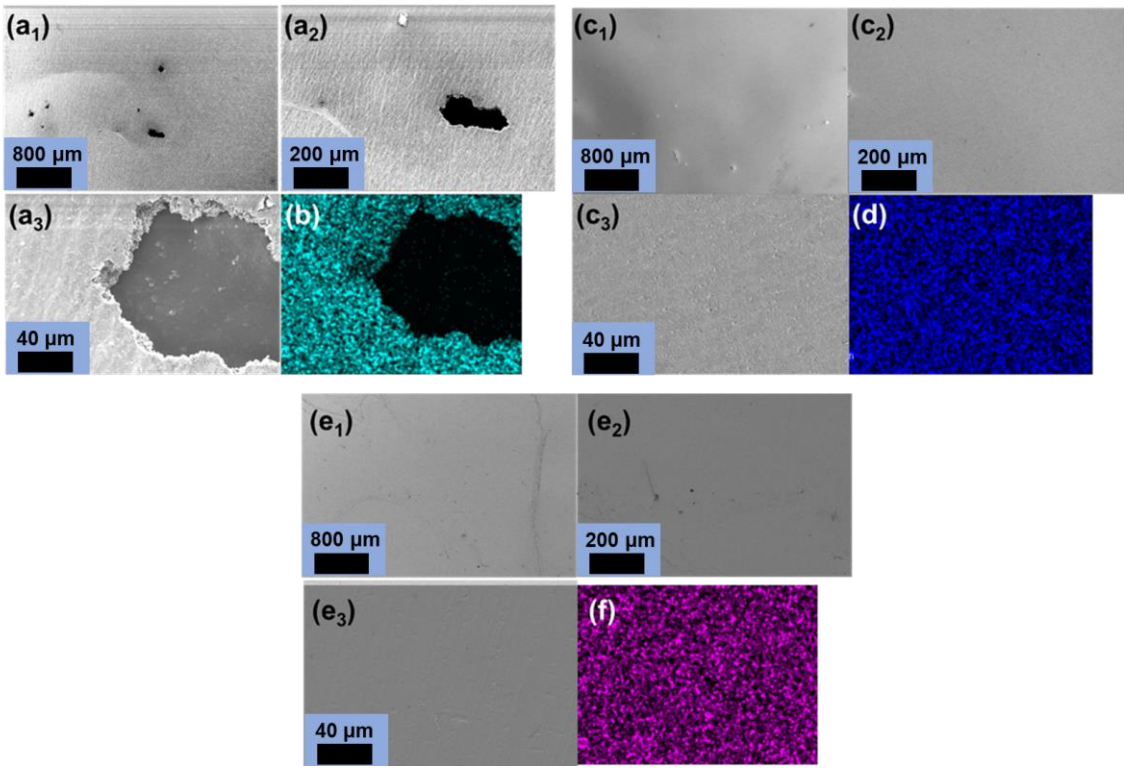

Figure 3.24 SEM images and EDS mapping of (a, b) Al foil, (c, d) Ti foil, and (e,f) Al-Nb foil after the potentiostatic test.

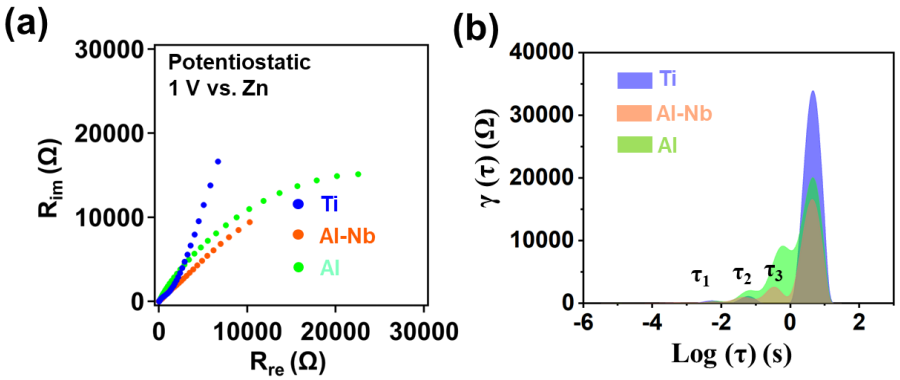

Figure 3.25 (a) Nyquist plots of different Zn||metal foil half cells. (b) DRT results corresponding to the Nyquist plots (**Figure 3.24(a)**).

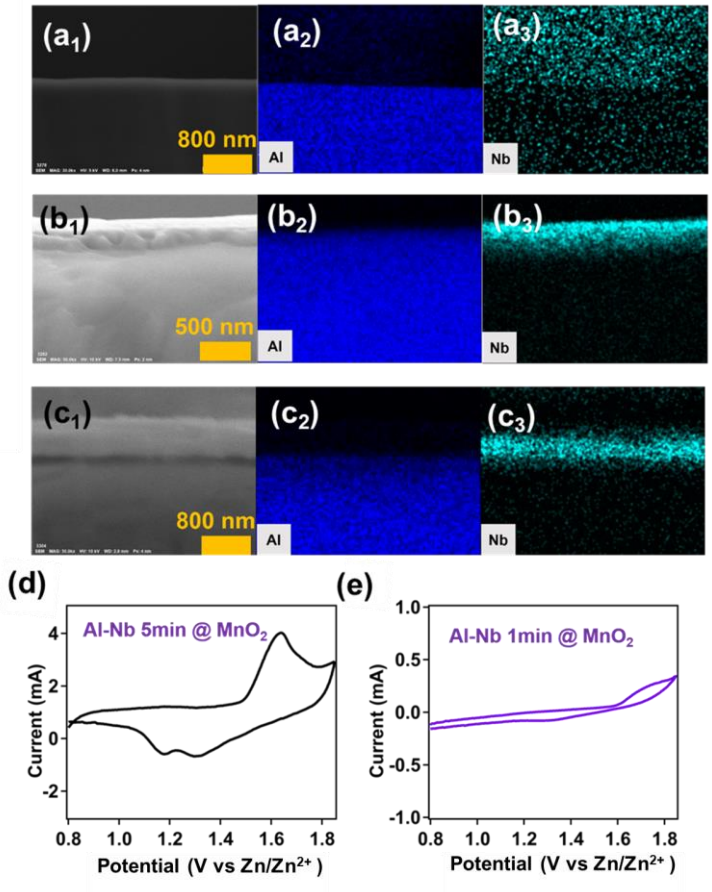

Figure 3.26 Cross sectional SEM images and the corresponding EDS mappings of the Al-Nb foils prepared by different sputtering time. (a) Sputtering for 1 min, (b) sputtering for 5 min, (c) sputtering for 25 min. CV curves obtained from (c) the Al-Nb samples prepared by sputtering for 5 min and (d) the Al-Nb samples prepared by sputtering for 1 min. The sweep rate is 0.5 mV s^{-1}.

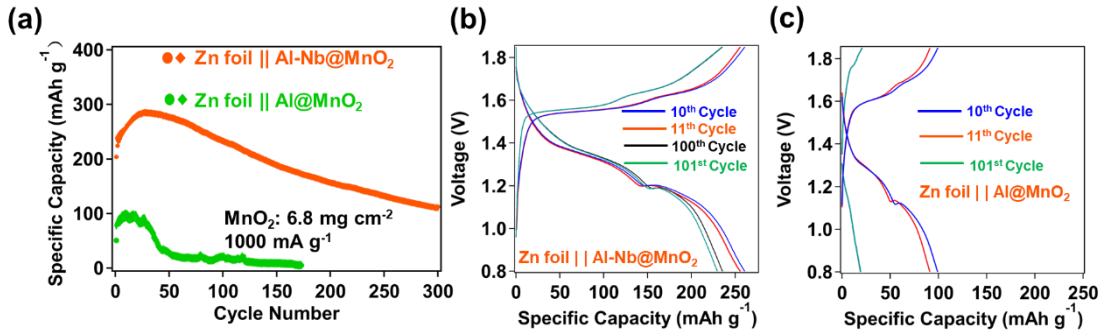

Figure 3.27 (a) Cycling performance of Zn||MnO_2 full cells with different cathode current collectors. Voltage profiles of Zn||MnO_2 cells with (b) the Al-Nb current collector and (c) the Al current collector.

In order to further investigate the possibility of using Al-Nb as cathode current collector for RAZIBs, Zn||MnO_2 cells with Al-Nb foil as cathode current collectors were tested. As shown in **Figure 3.27(a)**, the MnO_2 cathode supported by Al-Nb foil provides an initial capacity of 203.7 mAh g^{-1}, gradually increasing to 287.4 mAh g^{-1} with cycling due to the activation of electrode materials. The capacity value owned by the Al-Nb@MnO_2 cathode is close to the theoretical capacity of MnO_2, i.e., 308 mAh g^{-1} based on Mn(IV) → Mn(III), indicating that the electrochemical performance of MnO_2 cathode will not be damaged when Al-Nb is used as the current collector. As a comparison, Al@MnO_2 shows a low capacity of only 50.8 mAh g^{-1} at the first cycle. After reaching the highest capacity of around 100 mAh g^{-1}, the cathode capacity of Zn||Al@MnO_2 cell rapidly attenuates to a value lower than 10 mAh g^{-1}, indicating that not only the discharge capacity of the active material is impaired but also the cycling performance is seriously affected when Al metal is used as the cathode current collector. Voltage profiles of the Zn||Al-Nb@MnO_2 cell as shown in **Figure 3.27(b)** confirm that the overpotential shows almost no change during the 100 cycles, proving that the Al-Nb current collector does not influence the performance of the MnO_2 cathode. By comparing **Figure 3.27(b)** and **3.27(c)**, it can be found that the MnO_2 cell with Al current collector has a lower plateau voltage, which can no longer provide a normal discharge curve at the 101st cycle.

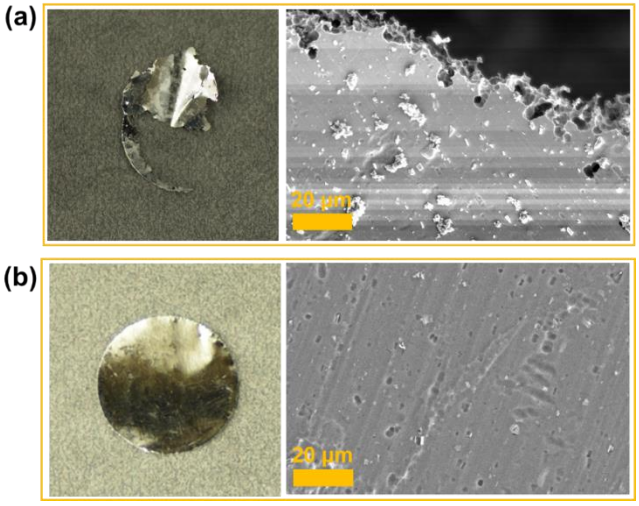

Figure 3.28 Optical photos and SEM images of (a) the Al current collector after cycling and (b) the Al-Nb current collector after cycling.

Direct observation of the as-tested current collectors can answer the problem of why the Al current collector shows a deteriorated performance after several cycles. As exhibited in **Figure 3.28(a)**, the Al current collector is severely corroded after cycling; in addition to the appearance that is no longer complete, lots of pits, which are generated by the dissolution of Al, are left on the surface. The boosted dissolution of Al may be ascribed to the dramatic changes in pH near the electrode, by which the oxide layers are repeatedly generated/dissolved due to the continuous variation between acidic and basic in interfacial pH. [136, 169] In contrast to the broken Al current collector, the Al-Nb foil can keep its intact appearance and metallic luster, and SEM observation of Al-Nb shows that it does not suffer any damage after the full-cell cycling (**Figure 3.28(b)**). The superior corrosion resistance of Al-Nb foil is attributed to the stable oxides layer on the Nb coating, which can be confirmed by the STEM observation of the tested sample (**Figure 3.29**), indicating that the oxides layer can help Al-Nb resist the attack from aggressive species in the water. Moreover, as circumstantial evidence, Al-Nb foil can be immersed in a 0.1 M KOH aqueous solution for 24 h without a noticeable change in appearance, whereas the surface of Al foil is rapidly corroded under the same conditions (**Figure 3.30**).

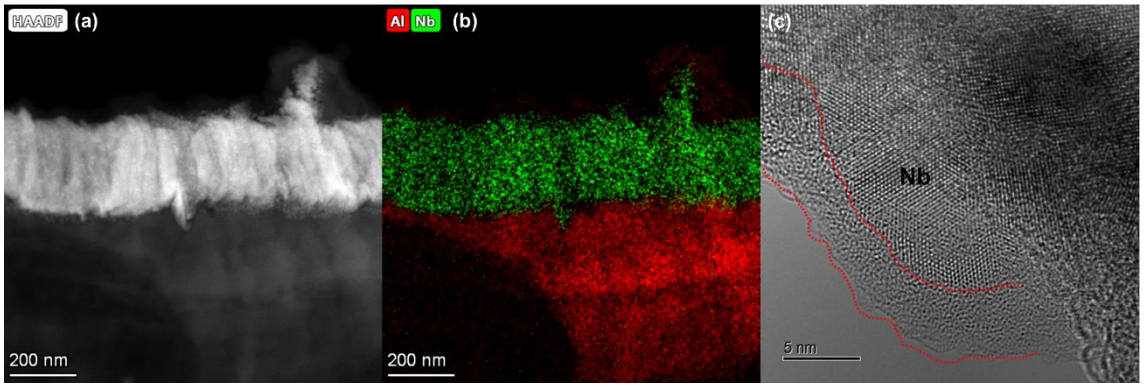

Figure 3.29 (a) STEM image and (b) the corresponding EDS mapping of the Al-Nb cathode current collector after one charge/discharge cycle. (c) HRTEM micrograph of the Nb coating after cycling.

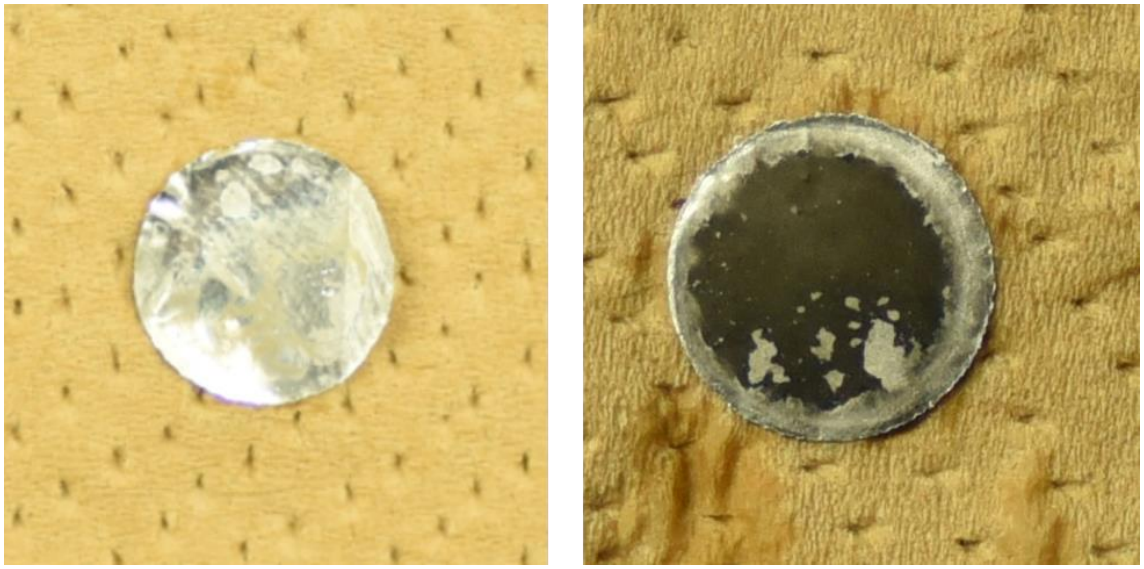

Figure 3.30 Al-Nb foil (left) and Al foil (right) after immersion in 0.1 M KOH aqueous solution for 24 h.

Different types of cells are also investigated, as shown in **Figure 3.32(a)**, in which the activated carbon (AC) based cathodes were prepared with different current collectors. The performance of the Zn||Al@AC cell is not surprisingly unstable, whereas the Zn||Al-Nb@AC cell shows a superior cyclic life span longer than 50000 cycles. In addition, the Al-Nb current collector can also successfully support vanadium dioxide (VO_2) based cathode (**Figure 3.32(b)**), demonstrating that the Al-Nb foil is compatible with various active materials and is suitable for serving as cathode current collectors in RAZIBs. Moreover, Zn||Al-Nb@MnO_2 cells with different thicknesses of Nb coating were also investigated, and the results also agree with the conclusions drawn before: the magnetron sputtering should take no less than 5 minutes. Carrying out magnetron sputtering for 1 minute is not enough to generate a complete Nb coating on the Al surface (**Figure 3.31**).

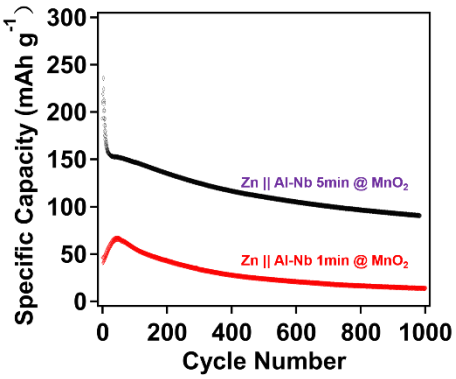

Figure 3.31 Al-Nb foil (left) and Al foil (right) after immersion in 0.1 M KOH aqueous solution for 24 h.

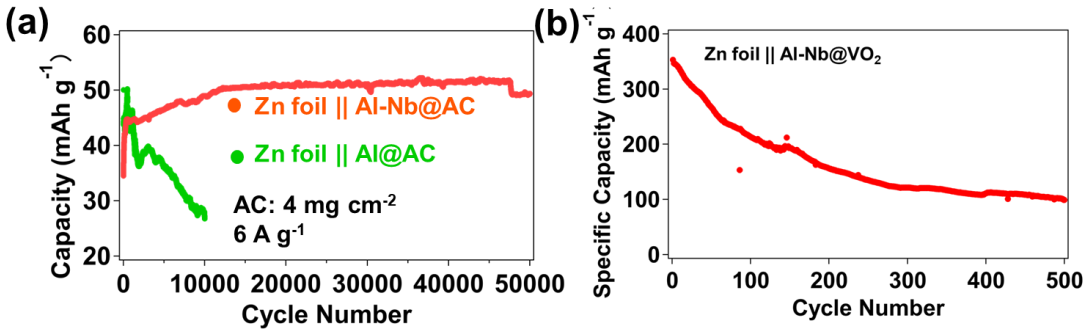

Figure 3.32 Cycling performance of Zn||MnO_2 full cells with different Al-Nb cathode current collectors.

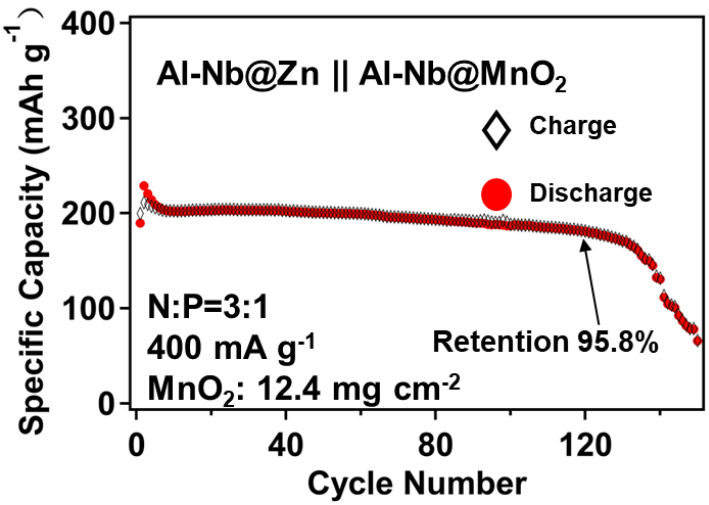

Figure 3.33 Cycling performance of the Zn||MnO_2 cell enabled by Al-Nb current collectors.

3.3.4 High performance Zn-MnO_2 batteries supported by Al-Nb current collectors

Encouraged by the impressive corrosion resistance and superior electrochemical performance of Al-Nb current collector both in anode and cathode, an attempt was made to use the Al-Nb as both anode and cathode current collectors to assemble Zn-MnO_2 full cells, intending to develop RAZIBs with good cycling stability and high energy density through using this anode/cathode dual-purpose current collector. As shown in **Figure 3.33**, a Zn-MnO_2 full cell whose cathode current collector and anode current collector are both Al-Nb foil is prepared. The load of MnO_2 on the cathode was 12.4 mg cm^{-2}, which means that the areal capacity of the cathode is approximately 2.5 mAh cm^{-2}. The optical photos and the SEM images of the prepared Al-Nb@MnO_2 electrode are shown in **Figure 3.34**. Metallic Zn is pre-plated to the Al-Nb foil to prepare the Al-Nb@Zn composite anode, and the capacity of the anode is controlled 3-times to the cathode; namely, the negative/positive ratio (NP ratio, N:P) is 3:1. The Al-Nb@Zn||Al-Nb@MnO_2 cell provides an initial capacity of 199.7 mAh g^{-1}, and the capacity retention up to 120 cycles is 95.8%, which is an excellent value under this harsh measurement condition. The uniform deposition/dissolution of Zn metal protects the cell from short circuit and guarantees a high coulombic efficiency under high capacity, while the less-blocked mass transfer and charge

transfer on the cathode current collector assure the highly stable cycling performance. Therefore, the author believe that Al-Nb foil has the potential as a current collector for RAZIBs, and it is suitable for serving as a current collector to replace the conventional Ti mesh, Cu foil or some other materials.

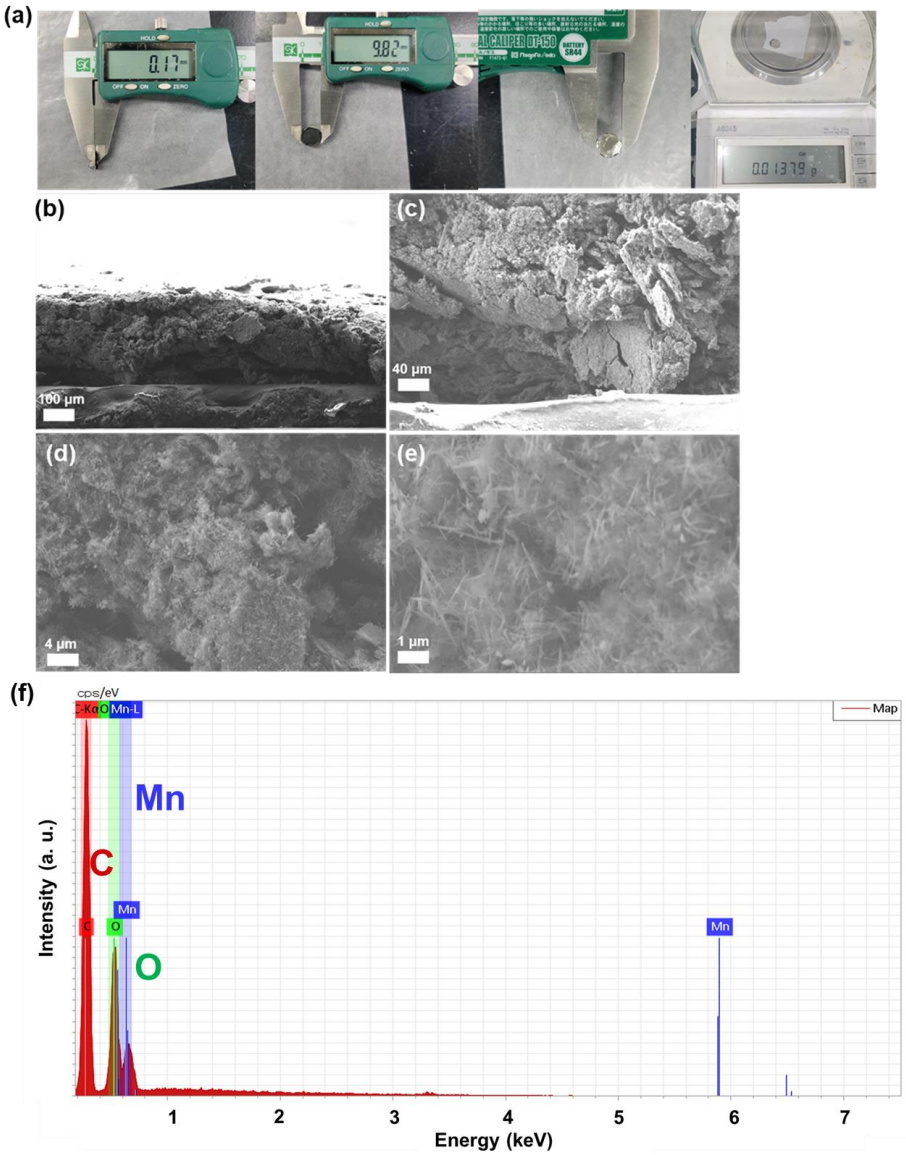

Figure 3.34 (a) Optical photos of the prepared Al-Nb@MnO_2 electrode and the physical parameters. (b, c, d, e) Cross-sectional SEM images of the Al-Nb@MnO_2 electrode. (f) The elemental mapping of Figure 3.34 (e). The observed needle-like nanowire is α-MnO_2.

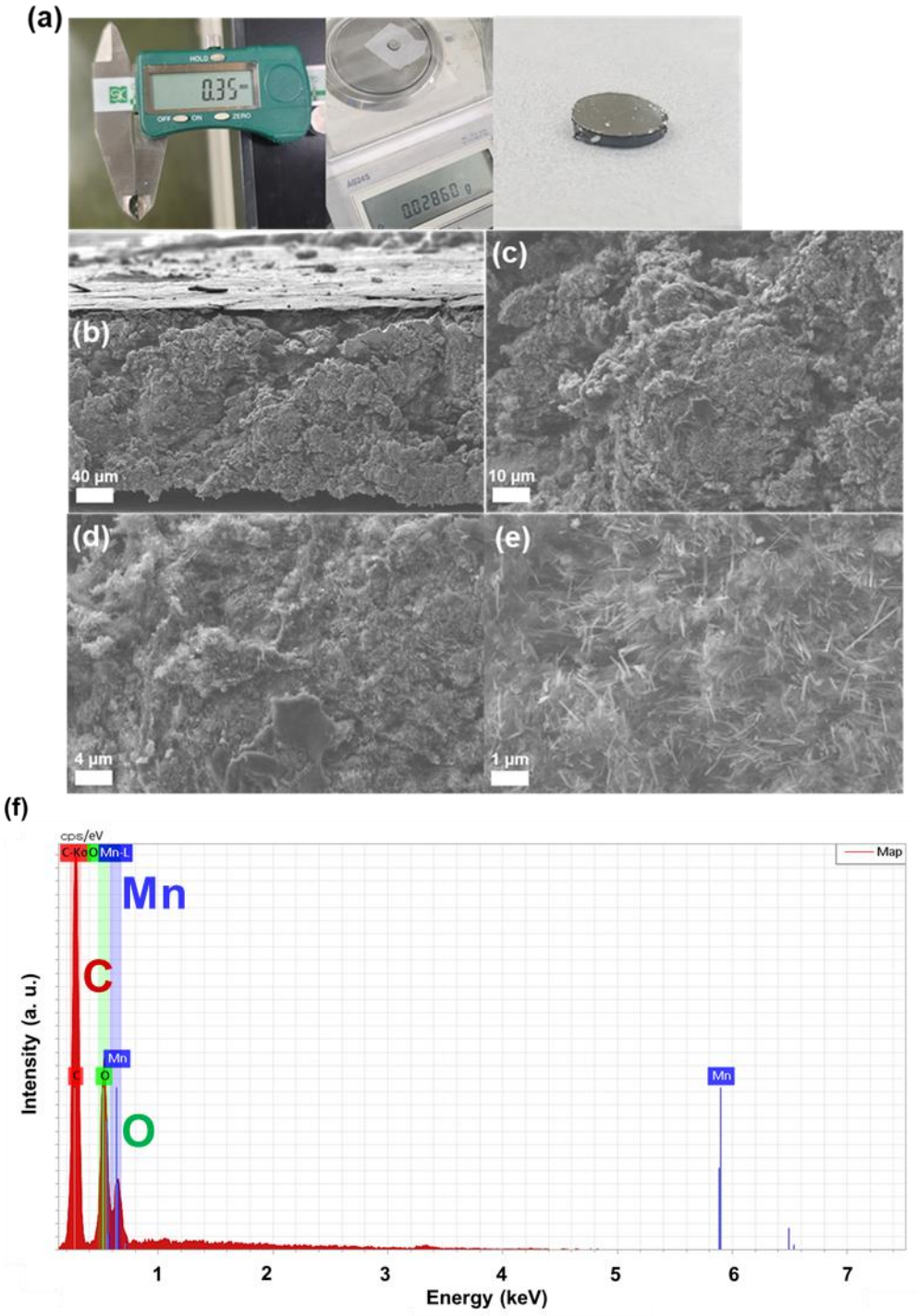

Figure 3.35 (a) Optical photos of the prepared thick Al-Nb@MnO_2 electrode and the physical parameters. (b, c, d, e) Cross-sectional SEM images of the Al-Nb@MnO_2 electrode. (f) The elemental mapping of Figure 3.35 (e).

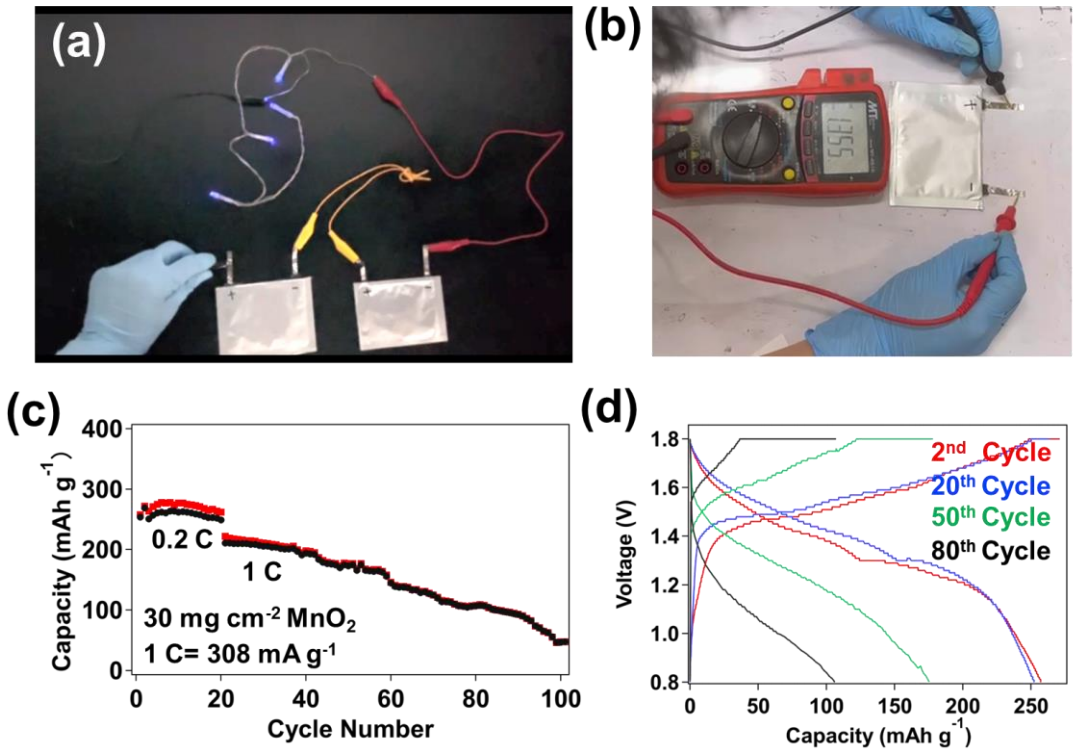

Figure 3.36 Electrochemical performance of Zn-MnO_2 pouch cell with Al-Nb current collectors. Optical photos for (a) illustrating lighting up a group of small LED lights and (b) the OCV of the pouch cell. (c) Cycling performance of the Zn-MnO_2 pouch cell. (d) Voltage profiles of the pouch cell.

Table 3.1 Electrochemical parameters of the pouch cell.

Electrochemical Parameter	Cell
MnO_2 ratio (vs. cathode)	80%
Energy density (5^{th} cycle)	339.8 Wh kg^{-1}
Active area	35 cm^2

Table 3.2 Physical parameters of the pouch cell.

Physical Parameter	Cell
Weight of composite anode (Zn+Al-Nb)	1.013 g
Weight of cathode	1.31 g
Weight of Al-Nb	0.181 g
Weight of electrolyte	3.17 g
Weight of separator	0.41 g
Weight of package + tabs	1.48 g

To further understand the advantages of using Al-Nb as current collectors for RAZIBs, Zn||MnO_2 pouch cell was assembled by using Al-Nb foils as current collectors. The area of the pouch cell was 35 cm^2, and a high-load MnO_2 cathode (30 mg cm^{-2}, 1050 mg MnO_2 in total) was used, in which the NP ratio was also controlled to 3:1, and the SEM images of the prepared thick Al-Nb@MnO_2 electrode are shown in **Figure 3.35**. The open circuit voltage (OCV) of the assembled cell is 1.355 V (**Figure 3.36(b)**), and the pouch cell can light up a string of small LED lights (**Figure 3.36(a)**). The detailed parameters of the pouch cell can be found in **Table 3.1** and **Table 3.2.** As shown in **Figure 3.36(c),** the pouch cell provides stable cyclic performance with an initial capacity of 258.0 mAh g^{-1} at 0.2 C (1 C = 308 mA g^{-1}). The cell shows a gradually decreased capacity during 1 C cycling, possibly due to the thick cathode that impedes the transport of ions in the cathode framework and the relatively high discharge rate (1 C, about 9.2 mA cm^{-2}) aggravates the problem. Voltage profiles shown in **Figure 3.36(d)** also confirm this possibility. In comparison with the healthy voltage curve of the first 20 cycles, the 80th cycle, which shows obvious pseudo-capacitor characteristics, is one of the attestations that the electrode reactions

only occur in the shallow layer of the electrode.[170] Nonetheless, the Zn||MnO_2 pouch cell could successfully work under such a harsh condition, notifying us that the Al-Nb foil is applicable in developing real-world RAZIBs. To show the advantages of using Al-Nb as current collectors in RAZIBs, the author calculates energy densities for Zn||MnO_2 pouch cells with different current collectors based on the parameters in **Table 3.1**, **Table 3.2**, and **Table 3.3**, and the results are shown in **Figure 3.37(a)**. It is apparent that the use of Al-Nb brings the highest energy density to batteries even when compared with a carbon paper current collector. Besides, with the increase in the mass of the active material (MnO_2), the simultaneous use of Al-Nb as the current collector for both anode and cathode can offer more than 12% gain in energy density in comparison with the conventional Ti mesh and Cu foil current collectors (based on one-layer pouch cell). The author lists the details of the difference in energy densities in **Figure 3.37(b)**. The red line in the figure indicates the difference in energy density between the Zn||MnO_2 pouch cells using Al-Nb foil as the anode and cathode current collectors when compared with the cells that use Ti mesh and Cu foil as the anode and cathode current collectors. Similarly, the black line represents the value when it is compared with the cell using carbon paper and Cu foil as the current collectors. It is apparent that when the cathode loading is within the real-world application range (> 52 mg cm^{-2}, corresponds to a single-layer pouch cell whose energy density is no less than 70 Wh kg^{-1}), the cell using Al-Nb foil as the current collector has a 5% advance in energy density when compared with the cell using carbon paper and Cu foil. Notably that the data is calculated based on the one-layer pouch cell, as the number of layers increases, the advantage of using Al-Nb foil will be more obvious. Considering that this technology is low-cost, easy to commercial-scale-production, and compatible with most battery optimization strategies, the use of Al-Nb is expected to facilitate the development of practical RAZIBs with high-energy-density.

Table 3.3 Physical parameters of different substrates.

	Weight (mg)	Area (cm^2)	Thickness (mm)	Areal mass-density ($mg\ cm^{-2}$)
Al foil	4.05	0.785	0.1	5.16
Al-Nb	4.06	0.785	0.1	5.17
Cu foil	13.72	0.785	0.02	17.48
Ti mesh	22.15	0.785	0.1	28.22
Carbon paper	6.07	0.785	0.04	7.73

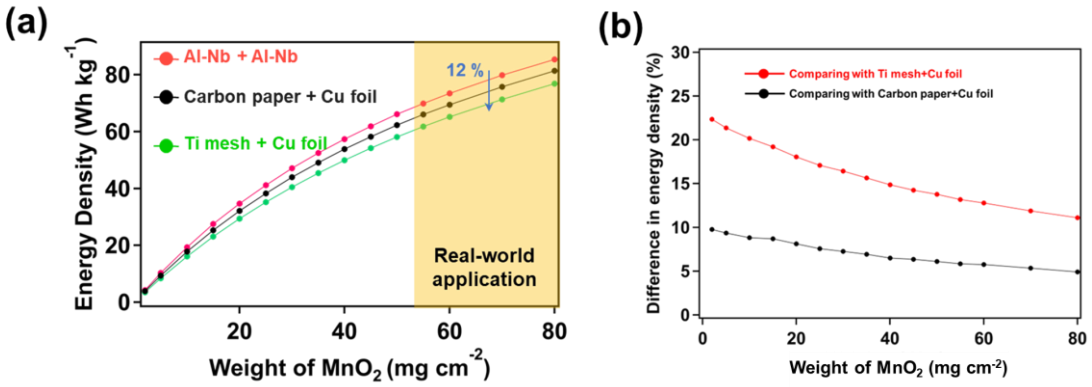

Figure 3.37 (a) The predicted energy density of the pouch cell varies with cathode loading when different current collectors are used. The orange region indicates that the cathode loading within this area meets the demands for real-world applications. (b) Differences in energy density when different current collectors are used in Zn||MnO_2 pouch cells.

3.4 Conclusions

In summary, by magnetron sputtering Nb coating onto Al foils, corrosion-resistant Al-Nb foil with superior electrochemical performance as current collectors for RAZIBs is successfully obtained. Nb coating acts as a barrier to prevent Al from being attacked by aggressive species in aqueous electrolytes, by which the Al-Nb foil can resist the formation of ZHS and regulate the deposition of Zn when used as an anode current collector. Additionally, it can also prevent corrosion at high potential when used as a cathode current collector. Furthermore, the cell that uses Al-Nb foil as both anode and cathode current collectors simultaneously shows superior cycling performance and improved energy density. It is worth mentioning that the preparation of Al-Nb foil is environmentally friendly and suitable for commercial-scale production. The author believes this technology can be extended to various aqueous batteries in the future to promote the development of high-energy density aqueous batteries.

Chapter 4 Optimizing the deposition behavior of Zn on zinc metal surfaces by electropolishing treatment.

4.1 Objective of this Chapter

The moderate electrode potential of Zn (-0.76 V vs. SHE) causes Zn metal to be corroded by water slowly. Worsely, the surface of Zn metal is always covered by a passivation layer, making a non-uniform electrode surface, thereby leading to uneven nucleation during Zn plating, which induces the severe growth of Zn dendrites.[83, 87, 171-172] Previously, He et al. confirmed that the growth of Zn dendrites was related to the detriments of the Zn metal surface, and the development of highly efficient Zn polishing technology is illustrated to have enormous significance in boosting the practical RAZIBs.[100] Considering that the experimental reproducibility of mechanical polishing is very poor, and it is costive to apply mechanical polishing for large-scale treatment of Zn metal, electropolishing is undoubtedly the best choice to obtain reliable Zn metal anodes. However, the current technology for electropolishing Zn metal is either based on concentrated orthophosphoric acid (H_3PO_4) or toxic additives (e.g. NaCN). The use of hazardous and corrosive reagents has prevented this technology from being widely used in the laboratory or in the metal industry.[173] In this chapter, the author reports a novel, low-cost and efficient electropolishing treatment for polishing Zn metal, which only uses non-corrosive and non-toxic diethylene glycol (DEG) as a solvent and a small amount of NaCl as solute. It is confirmed that metallic Zn and Al can be polished efficiently at room temperature by using this technology. Surprisingly, the used electrolyte can be recycled and reused only after a simple suction filtration, making this technology an attractive metal pretreatment strategy for applications in both laboratories and enterprises. Moreover, to further demonstrate that the polishing pretreatment of Zn metal plays a key role in the research of RAZIBs, notably stabilized electrochemical cycling performance in a mildly acidic electrolyte (2 mol L^{-1} $ZnSO_4$) is realized by using the electropolished Zn metal anode. Furthermore, the significant influence, as caused by the primitive passivation layer of Zn metal surface, on the electrochemical deposition of Zn is also revealed.

4.2 Experimental Section

4.2.1 Electropolishing method

10 g NaCl (Kanto Chemical CO., INC, 99.5%) was dissolved in 500 mL diethylene glycol (DEG, Fujifilm Wako Chemicals, 99.0+%) to form a transparent electrolyte. Zn metal foils (Nilaco company, Japan) were first carefully mechanically polished using a polishing agent (Pikal metal polish, Nihon Maryo-Kogyo Company). Subsequently, the pre-treated zinc foil (20 mm × 30 mm) was immersed in the electrolyte as the working electrode, while a piece of aluminum foil (250 cm^2) was used as the counter electrode. The constant current (50 mA cm^{-2}) was applied to the electropolishing system. When the overpotential reached around 70 V (depending on the external conditions, e.g., the volume of a beaker, surface area of the Zn foil, etc.), the increasing trend of overpotential would be gradually stopped, and the electropolish process was stopped manually to ensure that the electropolished Zn foil had a high gloss. The surrounding temperature was controlled to be 25 ℃. Moreover, the purity of the Zn foil does not affect the polishing effect, and the author has confirmed that Zn foils with a purity of 99.2%-99.9% can be electropolished successfully by this method.

Preparation of tri-ethylene glycol (TEG, Kanto Chemical CO., INC, > 93.0%), ethylene glycol (EG, Kanto Chemical CO., INC, > 99.5%) and DI-water solution of NaCl were the same as the preparation of the abovementioned DEG solution, while the electropolishing process was also conducted in the above procedures.

4.2.2 Electrochemical measurement

For the symmetric cell test: Zn||Zn symmetric cell test was conducted on an SD8 battery tester. Two-electrode Swagelok cells were assembled with electropolished Zn foils (EP Zn) or original Zn foils (Ori Zn, without electropolishing treatment). An aqueous solution of 2 mol L^{-1} $ZnSO_4$ was used as the electrolyte while a piece of glass fiber was used as the separator in each cell. During the test, Zn metal was repeatedly plated/stripped between two identical Zn electrodes at a constant current density. For the rate test of the symmetric cell, the current densities were set at 1, 2, 4, 6, 8, 10, 12, 14, 16, 18, 20, 22, 25 mA cm^{-2}. The electrolyte dosage for each cell was 200 μL. The configuration of the symmetric cell is shown in **Figure 4.1.**

For the Zn plating test: Zn plating test was performed in the Zn||Zn symmetric cell. For demonstrating the deposition selectivity of Zn on the electropolished region, a piece of Zn foil, whose lower part was electropolished while the upper part was only mechanically polished, was cut into disk electrodes along the dividing line between the upper and lower parts. The obtained "half-and-half" Zn disk electrode was used as the working electrode, and a normal Zn disk (only mechanically treated) was used as the counter electrode. Zn metal was stripped from the normal Zn disk and plated onto the "half-and-half" Zn disk.

Linear sweep voltammetry measurements were also performed using the electrochemical workstation, and the voltage range was set at -0.15 V to 0.15 V vs. Zn/Zn^{2+}.

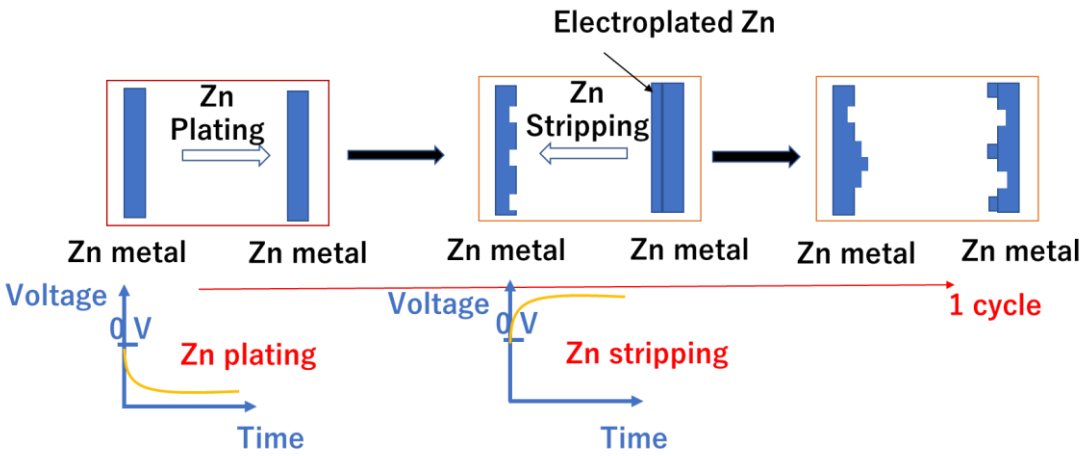

Figure 4.1 Schematic illustration for explaining the symmetric cell test.

4.2.3 Simulation details

The DRT simulation was conducted by the DRT tools, while the phase-field simulation was performed by using COMSOL Multiphysics. COMSOL Multiphysics was used to carry out the phase-field simulation of $c_{(Zn2+)}$ gradient during Zn plating. To simulate the change in $c_{(Zn2+)}$ during Zn deposition, a 2D phase-field model was employed as shown in **Figure 4.2**. The key points of the model are explained as follows.

The flux of ions in the electrolyte phase is controlled by the 1D Nernst-Planck equation:

$$\vec{J} = -D_{ion} \cdot \nabla c_{ion} - z u_{ion} F c_{ion} \nabla \phi \quad \textbf{(Eq. 4.1)}$$

$$\sum_{ion} z c_{ion} = 0 \quad \textbf{(Eq. 4.2)}$$

where J is the vector of ion transport, c_{ion} is the concentration of ion, z_{ion} is the charge of ion, u_{ion} is the mobility of the ion, and F is Faraday's constant. Φ is the potential in the electrolyte. D_{ion} is the diffusion coefficient of the charged species. For this system, only two kinds of ions are considered in the electrolyte, namely, Zn^{2+} and SO_4^{2-}.

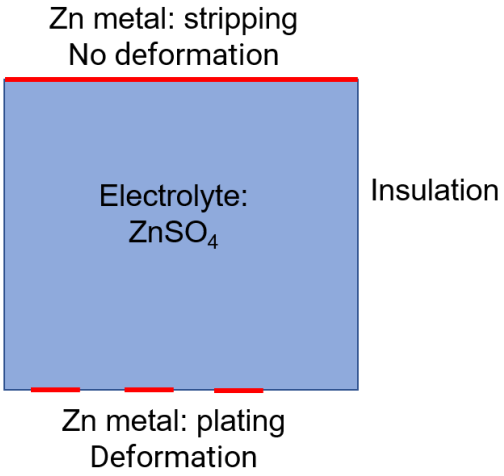

Figure 4.2 Geometric model for the simulation phase-field simulation of $c(Zn^{2+})$ gradient during Zn plating.

The Butler-Volmer equation is employed to depict the relationship between the local current density, $c_{(Zn2+)}$ and overpotential:

$$j_{loc} = j_0 (\exp(\frac{\alpha_a F \eta}{RT}) - \exp(\frac{-\alpha_c F \eta}{RT})) \quad \textbf{(Eq. 4.3)}$$

where j_{loc} is the local current density, j_0 is the exchange current density, η is the overpotential, α_a is the anodic transfer coefficient and α_c is the cathodic transfer coefficient, respectively.

The velocity field of Zn deposition is written as:

$$\vec{u} = \frac{\nabla \phi}{|\nabla \phi|} \cdot (-\frac{j_{loc}}{2F} \frac{M_{Zn}}{\rho_{Zn}}) \quad \textbf{(Eq. 4.4)}$$

where the vector u refers to the deposition of Zn metal (the fluid velocity), M_{Zn} is the molar mass

of zinc and ρ_{Zn} is the density of zinc metal.

The fluid dynamics at the phase-field interface are controlled by the Cahn-Hilliard equation:

$$\frac{\partial \xi}{\partial \tau} = \nabla \cdot \frac{\gamma \lambda}{\varepsilon_{pf}^{2}} \nabla(-\nabla \cdot \varepsilon_{pf}^{2} \nabla \xi + \xi^{3} - \xi) - \vec{u} \cdot \nabla \xi \quad \textbf{(Eq. 4.5)}$$

where ξ is the phase-field variable. γ is the mobility, λ is the mixing energy density, ε_{pf} is the interface thickness parameter. ξ was set as -1 in the electrolyte phase and 1 in the deposited Zn.

The mixing energy density and the interface thickness related to the surface tension coefficient are shown as follows:

$$\sigma^{2} = \frac{8\lambda^{2}}{9\varepsilon_{pf}^{2}} \quad \textbf{(Eq. 4.6)}$$

$$\varepsilon_{pf} = \frac{h_{max}}{16} \quad \textbf{(Eq. 4.7)}$$

where σ is the surface tension coefficient, h_{max} is the maximum mesh size.

All the boundaries except the deposition regions are insulating, and the model is based on the Tertiary-Current-Distribution, Nernst-Planck Equation interface. The used parameters are shown in **Table 4.1.**

4.2.4 Characterization

In plane X-ray diffraction (XRD) patterns were obtained by using an X-ray diffractometer (Rigaku RINT2000 Ultima) using Cu Ka radiation. The measurement conditions were as follows: angle range of the 2θ was 20º~ 80º, the sampling width was 0.02º, the scan speed was 1º min^{-1}, the divergence slit was 0.05 mm, the divergence longitudinal limit slit was 10 mm, and the angle of incidence (α) was 2°. Electron backscatter diffraction (EBSD) mapping was obtained from an EBSD component attached to an Auger electron spectroscopy system (JAMP-9500F). Surface composition of the samples were obtained by X-ray photoelectron spectroscopy (XPS, JEOL, JPS-9200) system using Mg-Kα X-ray source. Glow discharge optical emission spectroscopy (GDOES) was used to test the depth elemental distribution of the foils. Scanning electron microscopy (SEM) observation and energy dispersive spectroscopy (EDS) measurement were conducted on ZEISS Sigma 500. The surface roughness of the

foils was observed by atomic force microscope (AFM, Hitachi, NanonaviSII) by using the tapping mode. 3D morphology reconstruction of different Zn foils was conducted by using a laser scanning confocal microscope (LSCM, Lasertec Co. 1LM21D). Gloss of different samples were recorded by using a gloss checker (Horiba, IG-410).

Table 4.1. Simulation parameters.

Parameter	Value	Ref.
Φ_{anode}	0.08 V	-
j_0	2.8 mA cm^{-2}	[174]
$\alpha_a=\alpha_c$	0.5	-
$z_{Zn}=-z_{SO4}$	2	-
M_{Zn}	65 g mol^{-1}	-
ρ_{Zn}	7140 kg m^{-3}	-
D_{Zn2+}	3.68 × 10^{-10} m^2 s^{-1}	[174]
T_0	298 K	-
γ	0.5 N m^{-1}	[174]

4.3 Results and Discussion

4.3.1 Characterization of the electropolished Zn metal

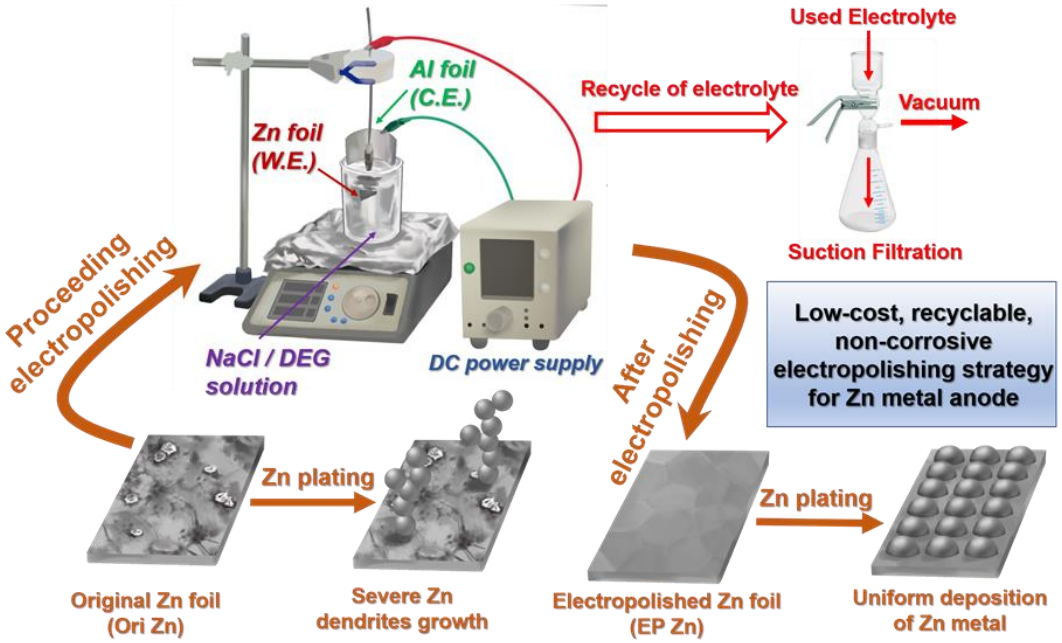

Figure 4.3 Schematic diagram for illustrating the novel electropolishing strategy, and the difference between electropolished Zn metal and non-treated Zn metal in the study of RAZIBs.

As shown in **Figure 4.3**, a Zn foil was first soaked in a DEG solution of NaCl (2 g/100 mL), which was used as the working electrode to carry out the electropolishing experiment. An Al foil with a surface area that was far larger than the Zn foil was used as the counter electrode. By electropolishing the Zn foil in the DEG solution, the contaminations and imperfections on the Zn surface could be conveniently and effectively removed in several minutes, resulting in a very clean and smooth metal surface (**Figure 4.4**). As shown in **Figure 4.4**, The electropolishing of Zn was also conducted in different solutions, including water, ethylene glycol (EG), DEG, and tri-ethylene glycol (TEG), which have different viscosities (water < EG < DEG < TEG). The results indicate that DEG with an appropriate viscosity is suitable for successfully electropolishing Zn metal. Additionally, the electrolyte becomes turbid after several times of electropolishing due to the electrolyte consumption and the dissolution of Zn metal, thus losing its effectiveness in

obtaining a cleanly polished metal surface (**Figure 4.5**).

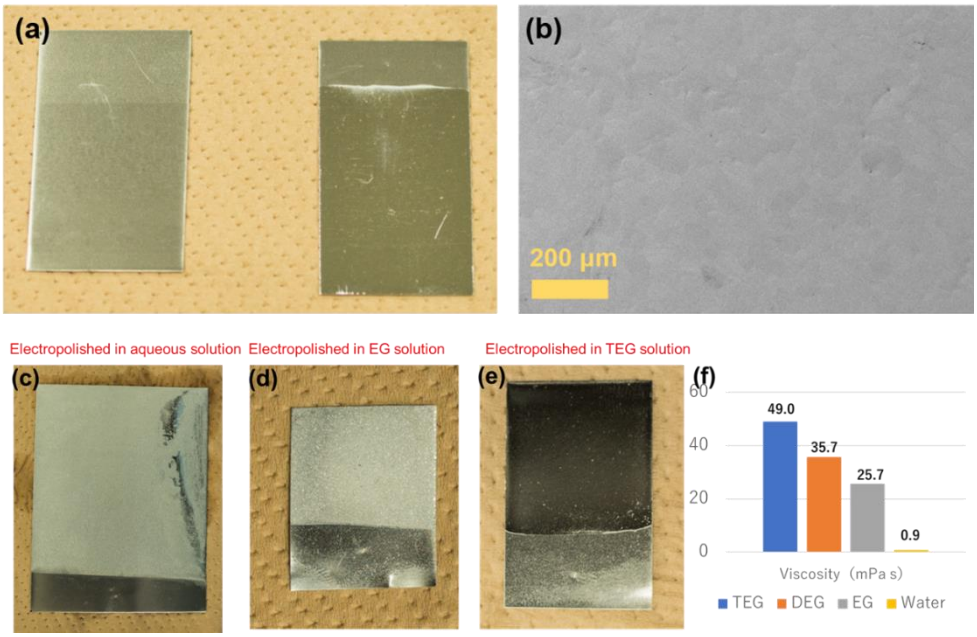

Figure 4.4 (a) Optical photos of the electropolished Zn foil (EP Zn, right) and the normal Zn foil (Ori Zn, left). (b) SEM image of the electropolished Zn. Zn foil after electropolishing process in (c) NaCl aqueous solution (2 g/100 mL), (d) NaCl/EG solution (2 g/100 mL) and (e) NaCl/TEG solution (2 g/100 mL). (f) Viscosity of different solutions. The glosses of these samples are summarized in **Table 4.2**.

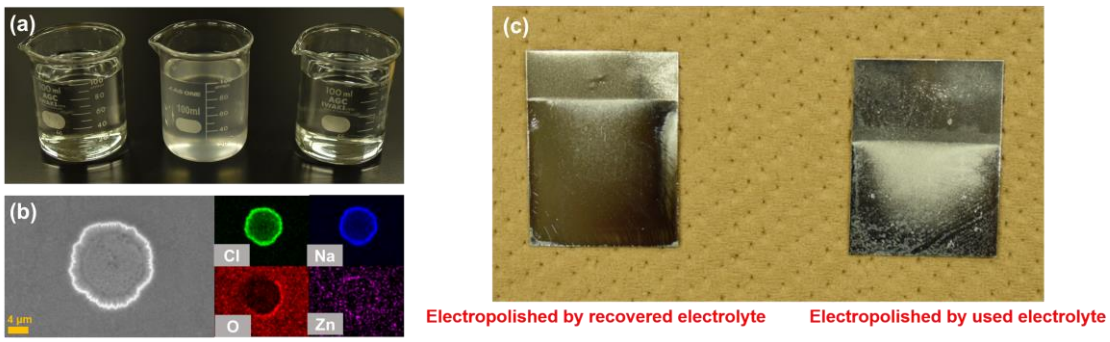

Figure 4.5 (a) Optical photos of the newly prepared electrolyte (left) and the electrolyte that was used for three times (mid) and the electrolyte after the suction filtration (right). The DEG solution became clear after suction filtration. (b) SEM image and EDS mappings of the filter residue from the DEG based electrolyte that was used. (c) The Zn foil electropolished by the recovered electrolyte (the used electrolyte after suction filtration) and the Zn foil electropolished by the used electrolyte (without suction filtration).

However, by filtrating treatment of the used electrolyte, its electropolishing capability can be fully recovered, which endows the electrolyte with superior recyclability; thereby, the cost of this technology can be further reduced. Hereafter, the electropolished Zn foil is referred to as EP Zn, while the original Zn foil was only mechanically pretreated as Ori Zn. Surprisingly, the EP Zn can seed a uniform deposition of Zn while the Ori Zn is prone to form Zn dendrites on its surface during galvanizing in a $ZnSO_4$ aqueous neutral electrolyte. The electrochemical cyclic stability of EP Zn in the $ZnSO_4$ aqueous electrolyte is also found to be far better than Ori Zn. Considering that the electrochemical cyclic stability of Zn metal plays an extremely important role in developing RAZIBs, a series of experiments were designed to explore the reasons for the difference in the electrodeposition behavior of EP Zn and Ori Zn in the $ZnSO_4$ aqueous electrolyte.

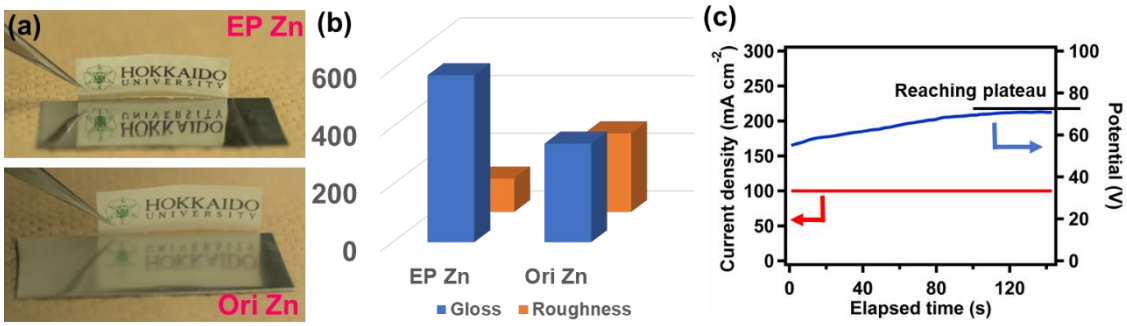

Figure 4.6 Characterization results of the Zn foils. (a) Optical photos of the mirror-like EP Zn and the conventional Ori Zn. (b) A comparison in gloss and roughness of different Zn samples to reflect their surface condition. (c) Potential-time plot of the employed galvanostatic electropolishing process.

The clean and mirror-like appearance of the EP Zn foil is shown in **Figure 4.6(a)**, in comparison to the fuzzy reflection of the Ori Zn. The gloss and roughness of EP Zn and Ori Zn were measured by using a gloss checker and a laser scanning confocal microscope (LSCM), respectively. As compared in **Figure 4.6(b)**, the glossiness of EP Zn is about 1.7-folds to that of Ori Zn, while the

surface roughness is much lower than Ori Zn. It should also be noted that the Ori Zn has undergone a preliminary polishing treatment, and it had a relatively uniform surface morphology and a higher gloss than most of the commercial Zn foils. The comparison of the gloss of metallic foils as treated by different polishing methods is shown in **Table 4.2**, in which the EP Zn foil has the highest value. The potential profile during the electropolishing of Zn foil is shown in **Figure 4.6(c)**. The potential is gradually increased from the initial value of 55.1 V to 70.6V during the first 120 seconds, indicating that the surface area of Zn foil was gradually decreased due to the dissolution of uneven Zn metal surface. Afterward, the potential is maintained constantly at around 70.7 V for 23 seconds, indicating that the surface morphology would not change anymore and the electropolishing process can be stopped. The capacity loss of Zn metal was calculated to be 3.97 mAh cm^{-2} by multiplying the applied current density (100 mA cm^{-2}) and the polishing time (143 s), which is lower than most reported electropolishing processes of Zn and is acceptable for both laboratories and enterprises. [173, 175]

Table 4.2. Gloss of different samples.

Sample	Gloss
Ori Zn (pre-treated by polishing reagent)	342
Zn foil (kept in air for 2 months)	177
EP Zn foil	579
Zn foil electropolished by water (NaCl solution)	17
Zn foil electropolished by EG (NaCl solution)	96
Zn foil electropolished TEG (NaCl solution)	395
Zn foil (polished by using #1500 sandpaper)	240
EP Zn soaked in 2mol L^{-1} $ZnSO_4$	367
Ori Zn soaked in 2mol L^{-1} $ZnSO_4$	101
EP Zn soaked in DI-water	45
Ori Zn soaked in DI-water	27

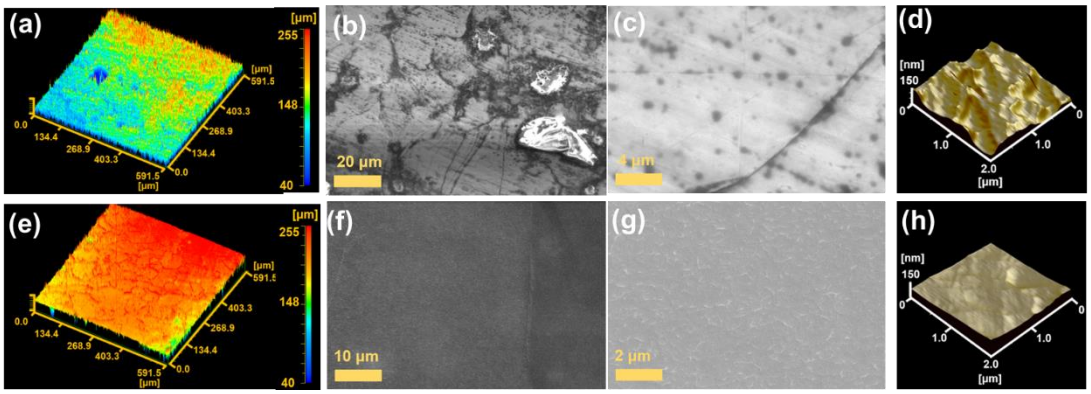

Figure 4.7 Morphology observation results of the Ori Zn by using (a) LSCM, (b,c) SEM and (d) AFM. Morphology observation of the EP Zn by using (e) LSCM, (f,g) SEM and (h) AFM.

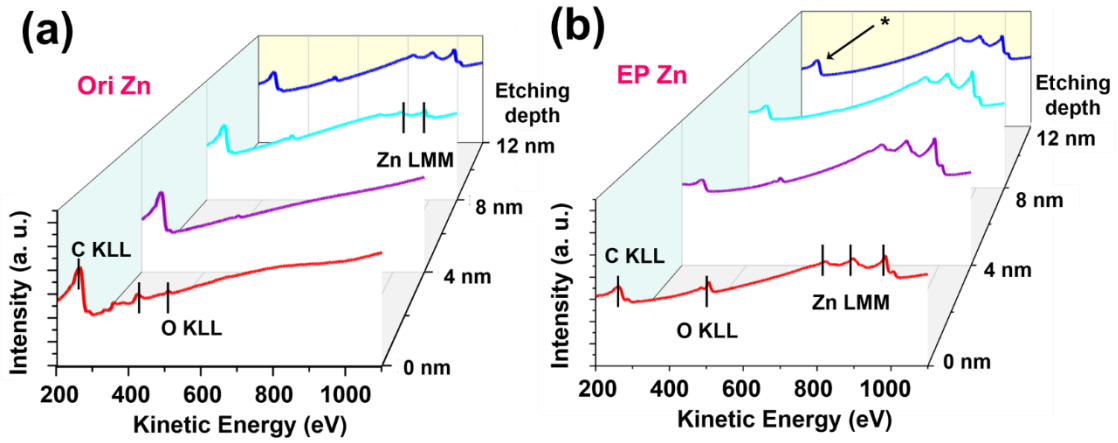

Figure 4.8 AES depth profiles of the (a) Ori Zn and (b) EP Zn. The * peak (C KLL peak reappears) is caused by the Ar^+ etching.

The morphology changes before and after electropolishing were confirmed in a series of microscopical observations. As shown in **Figure 4.7(a)**, the reconstructed 3D topography of Ori Zn contains a non-flat surface morphology, which is induced by the presence of contaminations and cracks as confirmed by the scanning electron microscopy (SEM) observation in **Figure 4.7(b, c)** The submicron morphological characterization was performed by atomic force microscope (AFM), which indicates a nonuniform surface morphology of Ori Zn in **Figure 4.7(d)**. These observations imply that by using conventional mechanical polishing pretreatment (e.g. using polishing agent), the uniformity of Zn foil surface cannot be well guaranteed. The contaminations and imperfections may cause severe Zn dendrite growth during the electrochemical Zn plating and stripping test, which was also confirmed by He et al. [100] The EP Zn exhibits a uniform and flat morphology from the millimeter to submicron scale (see **Figure 4.7(e-h)**. Using Auger electron spectra (AES), the composition differences were compared on the surface of two Zn samples. As shown in **Figure 4.8(a)** and **Figure 4.8(b)**, both the Ori Zn and EP Zn are covered by a thin passivation film that consists of carbon (C), oxygen (O), and Zn. The peak of O KLL on the Ori Zn surface is still evident even after several times etching, while the signal of Zn can hardly be seen before Ar ion etching. This indicates the presence of relatively thick contaminant carbon species on the surface of Ori Zn. In contrast, the Zn peak of EP Zn is present even before Ar etching. After removing the passivation layer of about 8 nm, Zn metal is completely exposed, indicating that electropolishing can effectively enhance the cleanliness of the Zn surface. The EDS mapping also confirmed this result (**Figure 4.9(a-f)**). Thanks to the smooth and clean surface obtained from this electropolishing method, electron backscatter diffraction (EBSD) mapping of EP Zn was clearly detected, as presented in **Figure 4.9(g-j)**, which shows a typical polycrystalline structure, indicating that the electropolishing technology can make a positive impact in assisting the careful characterization of Zn metal.

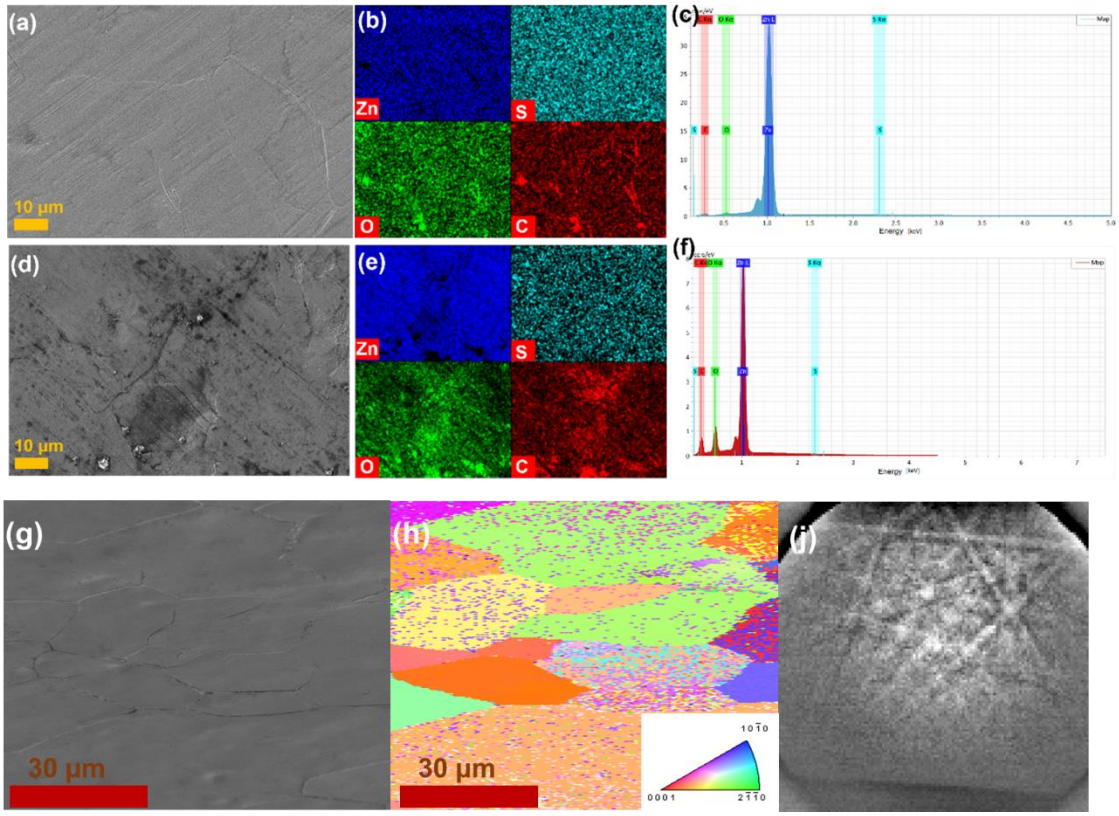

Figure 4.9 SEM images and EDS mappings of the Zn foil before and after electropolishing. (a) SEM image of the EP Zn. (b)(c) EDS mapping of the EP Zn. (d) SEM image of the untreated Zn. (e)(f) EDS mapping of the untreated Zn. The untreated Zn shows a thicker passivation layer than EP Zn (can be distinguished from the oxygen peak). (g) SEM image and (h) the corresponding EBSD map of the EP Zn, and (i) the related Kikuchi pattern (corresponding to the EBSD map).

4.3.2 Deposition selectivity of Zn on electropolished surface

An interesting and unrevealed phenomenon was observed for the first time when Zn was electroplated onto a disk electrode comprising both EP Zn and Ori Zn regions. It is found that Zn is highly preferred to deposit onto the electropolished region.

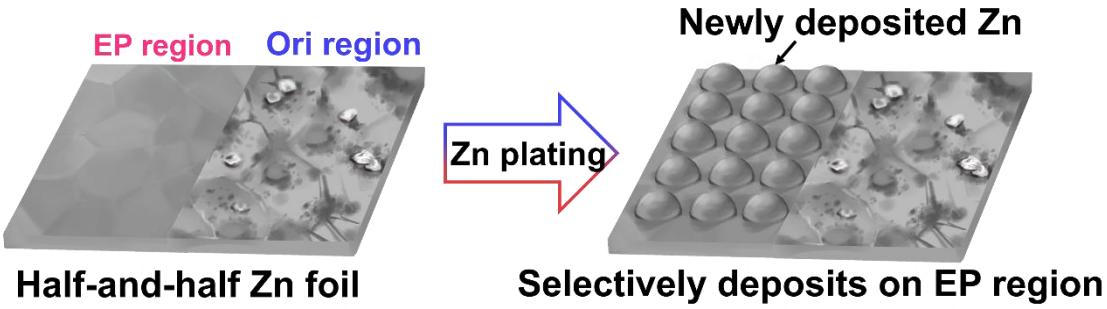

Figure 4.10 Schematic illustration for the deposition selectivity of Zn on different regions of EP Zn and Ori Zn.

As depicted in **Figure 4.10**, when Zn was electroplated onto the Zn foil electrode (named "half-and-half" Zn) whose half surface had been electropolished while the other half was the original Zn foil, almost all of the plated Zn appeared only at the electropolished region. This indicates that the deposition of Zn is highly selective on the electropolished Zn metal surface. Optical photos of the plated electrodes on the "half-and-half" Zn foil are shown in **Figure 4.11(a, b)**. When the areal capacity of Zn plating was controlled to 5 mAh cm^{-2}, nearly all of the newly deposited Zn crystals were observed only in the EP Zn region. When the areal capacity was increased to 20 mAh cm^{-2}, the newly appeared Zn crystals could fully cover the surface of EP Zn region and partially spread to the Ori Zn region, but the direct Zn deposition in the Ori Zn region was still very limited. In order to understand the above-mentioned electrodeposition selectivity, SEM observation was first employed to investigate the nucleation behavior of Zn metal in different regions. As shown in **Figure 4.11(c)**, the nucleation of Zn metal on the Ori Zn region is extremely uneven, with only a few irregular particles, while the surface of the EP Zn region is covered evenly by newly deposited hexagonal Zn flakes.

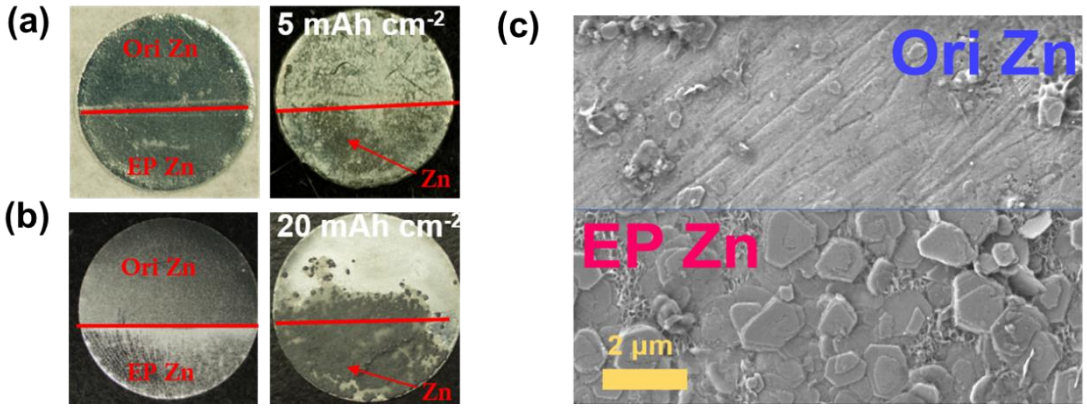

Figure 4.11 (a, b) Optical photos of the "Half-and-Half" Zn foils and after Zn plating. The controlled areal capacity of deposited Zn is 5 mAh cm^{-2} and 20 mAh cm^{-2}, respectively, and the applied current density is 1 mA cm^{-2}. (c) SEM images reflecting the Zn nucleation behavior on different substrate regions. Potential-time curves of the galvanostatic Zn plating test on EP Zn (pink) and Ori Zn (blue).

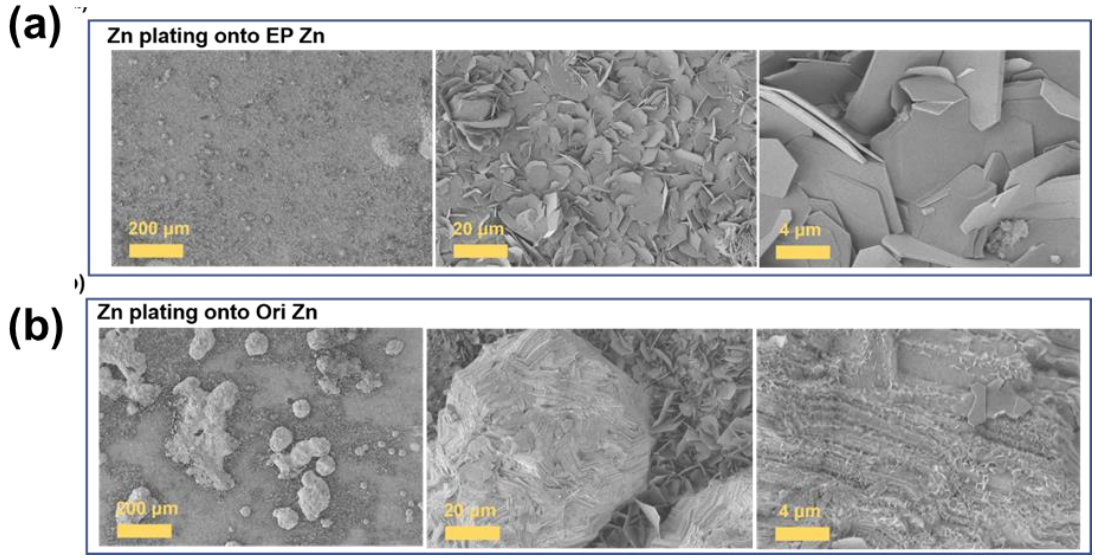

Figure 4.12 Zn deposition on different substrates. SEM images of EP Zn (a) and Ori Zn (b) after Zn plating at 1 mA cm^{-2}, with a controlled areal capacity of 2.5 mAh cm^{-2}.

The uniform nucleation behavior of Zn on EP Zn also guaranteed a relatively high uniformity of Zn crystal distribution during the subsequent Zn plating, as shown in **Figure 4.12**. The high-capacity plating to observe the short-circuit phenomena was furtherly performed, as shown in **Figure 4.13(a)**. When the areal capacity of Zn plating reached a high value of 80 mAh cm^{-2}, a short circuit was observed for the EP Zn cell, attributed to the significantly accumulated Zn crystals that penetrated the glass-fiber separator. As a comparison, a short circuit was observed for the Ori Zn cell only after that 26 mAh cm^{-2} Zn metal was deposited. From the optical images (**Figure 4.13(a)**) of different samples obtained after electroplating, it can be clearly seen that many regions of the Ori Zn foil are not covered by newly deposited Zn, while the EP Zn foil has a very uniform Zn coating on its surface. The exchange current densities of galvanizing on EP Zn (j_{EPZn}) and Ori Zn (j_{OriZn}) were compared in **Figure 4.13(c)**. The slightly higher value of j_{EPZn} than j_{OriZn} demonstrates that the deposition of Zn preferentially proceeds on EP Zn rather than Ori Zn. This might be attributed to the higher electronic conductivity of EP Zn surface than Ori Zn. Electrochemical impedance spectra (EIS) measurement was also carried out to identify the resistance characteristics of EP Zn and Ori Zn. As shown in **Figure 4.13(d)**, the semicircle from the EP Zn cell is significantly smaller than that from the Ori Zn cell, indicating that the total electrochemical impedance of the EP Zn cell is far lower than the Ori Zn cell during galvanizing. Here, distribution of relaxations times (DRT) simulation was also employed to classify the impedance in different semicircles.[176-178] As depicted in **Figure 4.13(e)**, excluding the ohmic resistance from the electrolyte, the impedance of EP Zn and Ori Zn are divided into 3 parts, i.e. contact resistance, charge transfer resistance, and ion-diffusion resistance. Among these three parts, the charge transfer resistance of EP Zn is slightly lower than that of Ori Zn, while the contact resistance is almost equal for EP Zn and Ori Zn, which is consistent with the above electronic conductivities. Compared to EP Zn, severe ion-diffusion resistance is contained on the surface of Ori Zn, implying that there should be a barrier layer that will block the diffusion of Zn^{2+} on the surface of Ori Zn. Here, the author denotes this ion-diffusion resistance as R_{film}, expressed in the equivalent circuit in **Figure 4.13(e)**. This film is believed to be from the natural passivation layer on the surface of the Zn electrode.

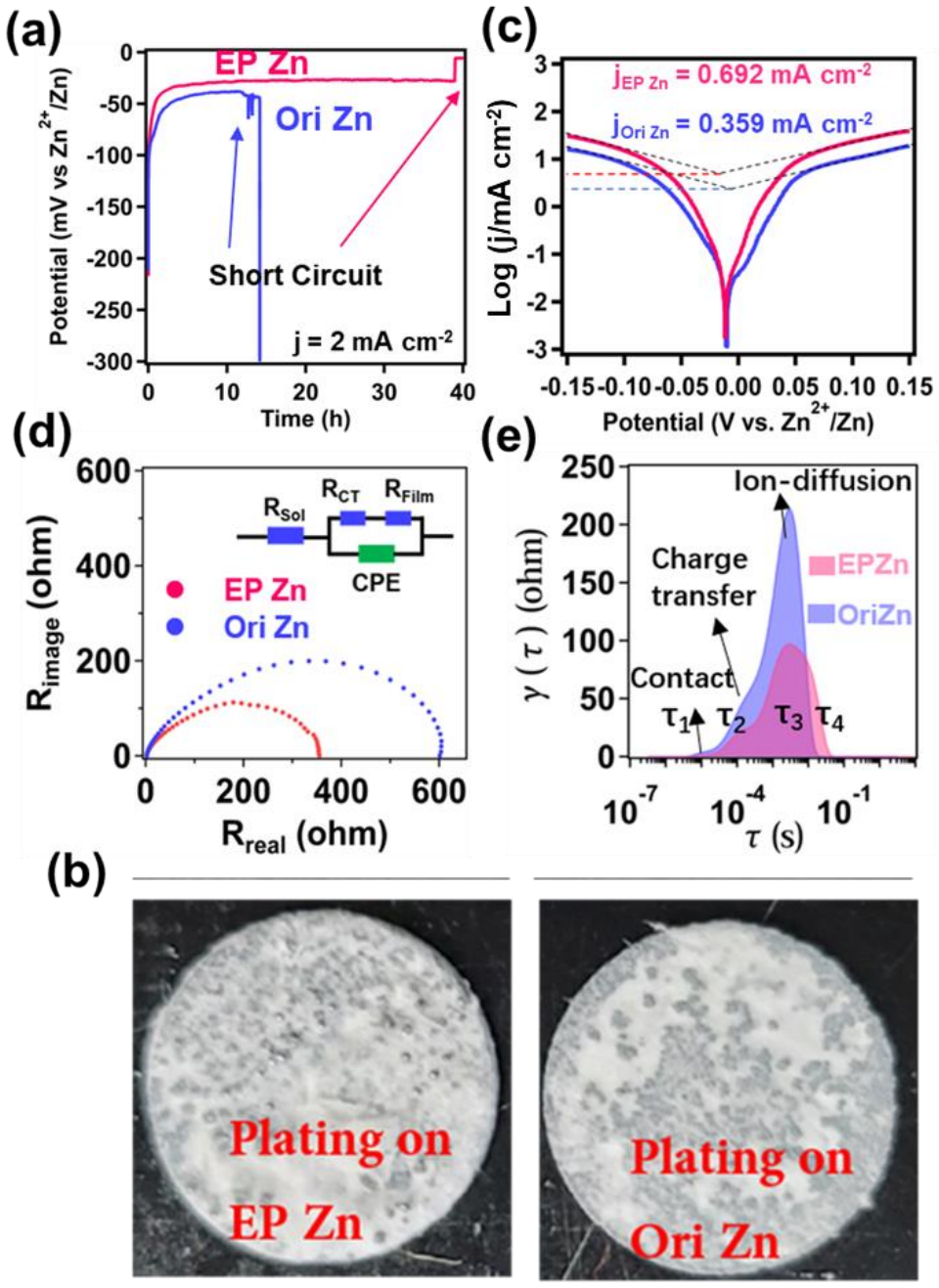

Figure 4.12 (a) Potential-time curves of the galvanostatic Zn plating test on EP Zn (pink) and Ori Zn (blue). (b) Optical photos of different Zn foils after Zn plating. (c) Polarization curves of Zn plating onto EP Zn (pink) and Ori Zn (blue). (d) Nyquist plots of EP Zn (pink) and Ori Zn (blue) obtained by a symmetric Zn||Zn cell. (e) DRT analysis of the EIS result.

4.3.3 Zn plating/stripping cycle performance of different Zn electrodes

The electrochemical cyclic performance of EP Zn and Ori Zn anodes in the neutral electrolyte was analyzed by assembling Zn||Zn symmetric cells. **Figure 4.14(a)** shows that during a rate performance test, the EP Zn cell exhibits a slightly lower overpotential than the Ori Zn cell at a low current density. Afterward, as the current density increases, the overpotential gap between the two cells gradually narrows. A "peak-plateau" typed curve can be seen from the potential profile of the first circle, indicating that the relatively high overpotential of the Ori Zn cell is mainly caused by the concentration polarization generated at the beginning of galvanizing.[179] At high current density, the potential curves of the two cells become similar, indicating that the difference between Ori Zn and EP Zn is significantly alleviated under high current density.

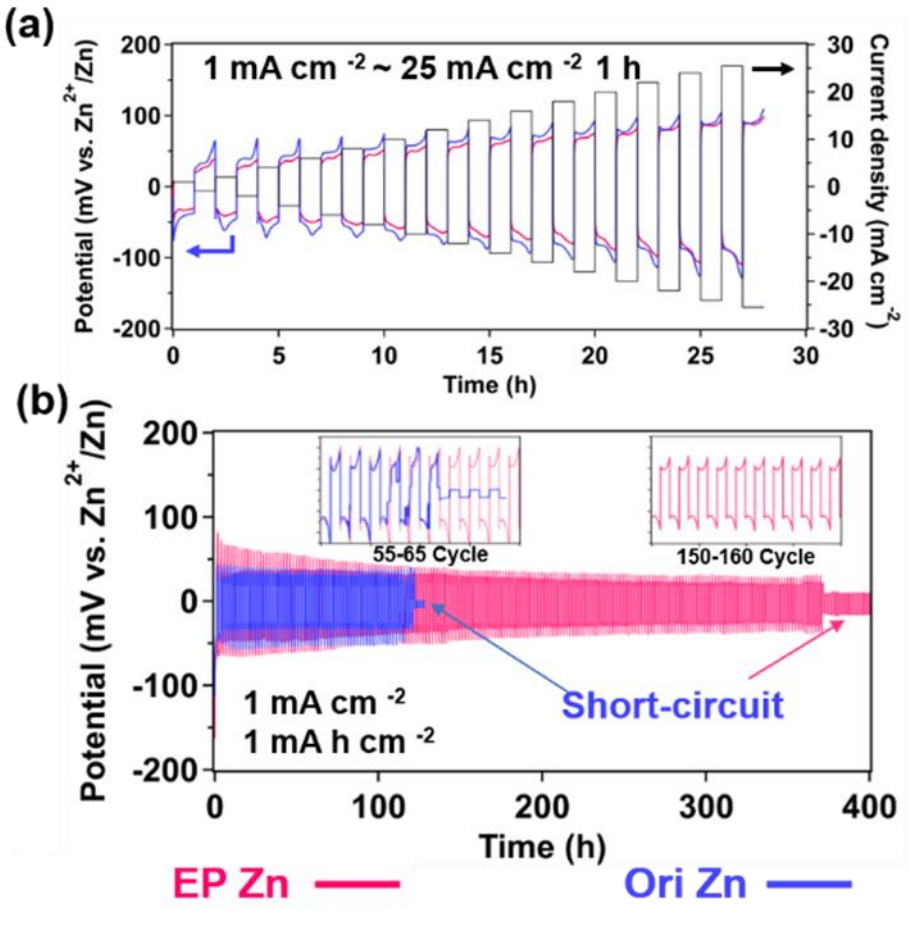

Figure 4.14 Zn||Zn symmetric cell measurement results for EP Zn and Ori Zn, including (a) rate performance and cyclic performance at (b) 1 mA cm^{-2}.

The influence of the uneven surface of Ori Zn is reflected in the symmetric cell test under low current density. As shown in **Figure 4.14(b)**, the Zn||Zn symmetric cell using two Ori Zn electrodes finally declared a short-circuit after 58 cycles due to the nonuniform deposition of Zn. In contrast, the EP Zn symmetric cell can maintain stable cyclic performance over 180 cycles, three times higher than the Ori Zn cell. This is because the electropolishing pretreatment of Zn foil can effectively avoid the uneven deposition of Zn and the formation of Zn dendrites. When the Zn||Zn symmetric cells are tested under a high current density of 40 mA cm^{-2}, the cyclic life-span of Zn metal is greatly extended, in which the EP Zn cell still exhibits a longer cyclic life than the Ori Zn (**Figure 4.15**). Previous reports have discussed the extension in the life span of Zn metal anode as-tested under high current density. [104, 143, 180-181] In my opinion, under the high current density, more regions that can be deposited with Zn are activated; at the same time the ion distribution at the interface is smoothed, benefitting the uniform Zn deposition, thereby the cyclic life-span of Zn metal anode is extended.[182] As for the EP Zn cell, it can stably work more than 6000 cycles under this high current density, which is five times longer than the Ori Zn cell. This is because the impurities and imperfections on the EP Zn surface are eliminated during the electropolishing process. Notably, the cyclic life-span of 6000 cycles has exceeded most of the currently reported Zn anodes, which have employed various performance optimization strategies, indicating that the electropolishing pretreatment of Zn can guarantee stable performance, thus enhancing the reliability of the Zn metal anode in related research.

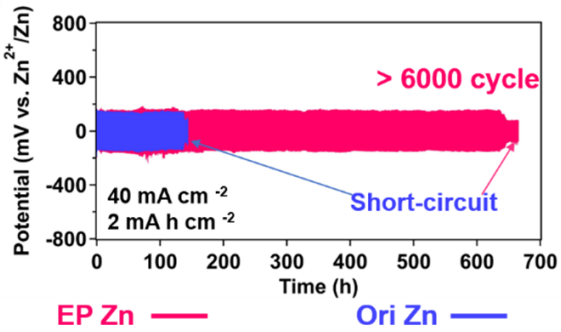

Figure 4.15 Zn||Zn symmetric cell measurement results for EP Zn and Ori Zn under a current density of 40 mA cm^{-2}.

4.3.4 Understanding the electrochemical behavior of electropolished Zn

In order to comprehensively understand the difference in the electrochemical behavior of Ori Zn and EP Zn in $ZnSO_4$ aqueous electrolyte, a simple immersion experiment was performed to analyze the surface condition of EP Zn and Ori Zn where they were kept under various environments. EP Zn foils or Ori Zn foils were soaked in deionized water (DI-water) or 2 mol L^{-1} $ZnSO_4$ solution for 3 days (**Figure 4.16(a)**)**.** The role of DI-water was to accelerate the corrosion (oxidation) of the samples since it could take a very long time to oxidize the samples naturally in the air. The use of $ZnSO_4$ solution was to reproduce the changes of Zn in the electrolyte. The appearance of different samples is compared in **Figure 4.16(b)**. The Ori Zn foil that was soaked in DI water is denoted as Sample 1, the EP Zn foil that was soaked in DI water as Sample 2, the Ori Zn foil that was soaked in 2 mol L^{-1} $ZnSO_4$ as Sample 3, and the EP Zn that was soaked in 2 mol L^{-1} $ZnSO_4$ electrolyte as Sample 4, respectively. White spots cover Sample 1 and Sample 2, and their luster was lost, while Sample 3 and Sample 4 can maintain a relatively clean appearance. SEM observation of different samples points out that the white spots are caused by the oxidation of the Zn (**Figure 4.17**), and the corrosion product layers are formed on all samples. The characteristics of the corrosion products formed in DI-water and $ZnSO_4$ solutions are obviously different. As shown in **Figure 4.18 and Figure 4.19** by the elemental dispersion spectroscopy (EDS) and X-ray diffraction (XRD) analysis, the surfaces of Sample 1 and Sample 2 are covered by small but dense bulge-like crystals, while the compounds on the surfaces of Sample 3 and Sample 4 are polygonal crystals that are comprised of Zn, O, sulfur (S) and C elements. The bulge-like crystals mainly consist of zinc hydroxide ($Zn(OH)_2$), while the polygonal crystals are considered to be zinc hydroxycarbonate ($Zn_4(OH)_6CO_3 \cdot yH_2O$) and zinc hydroxysulfate ($Zn_4(OH)_6SO_4 \cdot xH_2O$) because they can exist in the weak acidic environment.[171, 183-185] Due to the weak acidic environment in the $ZnSO_4$ aqueous solution, the nuclei of $Zn(OH)_2$ could be barely seen on the samples that were soaked in $ZnSO_4$ aqueous solution since that $Zn(OH)_2$ can be dissolved when pH < 6.[83, 186] It is hypothesized that the formation of different corrosion product layers leads to different deposition behavior of Zn, namely, the difference in electrochemical behavior of EP Zn and Ori Zn.

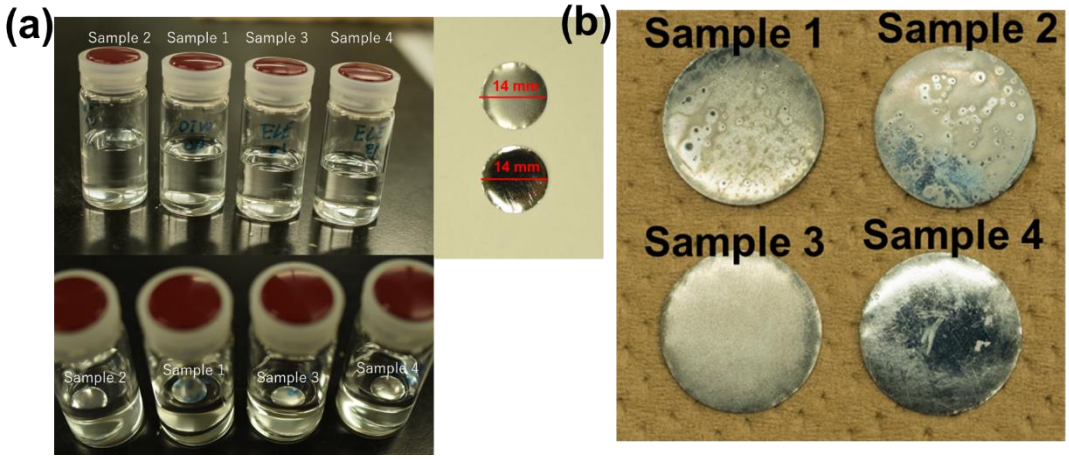

Figure 4.16 Optical photos of (a) the initial appearance of different samples in the immersion test. (b) Ori Zn after dipping in DI-water for 3 days (Sample 1), EP Zn after dipping in DI-water for 3 days (Sample 2), Ori Zn after dipping in 2 mol L^{-1} $ZnSO_4$ for 3 days (Sample 3), EP Zn after dipping in 2 mol L^{-1} $ZnSO_4$ for 3 days (Sample 4).

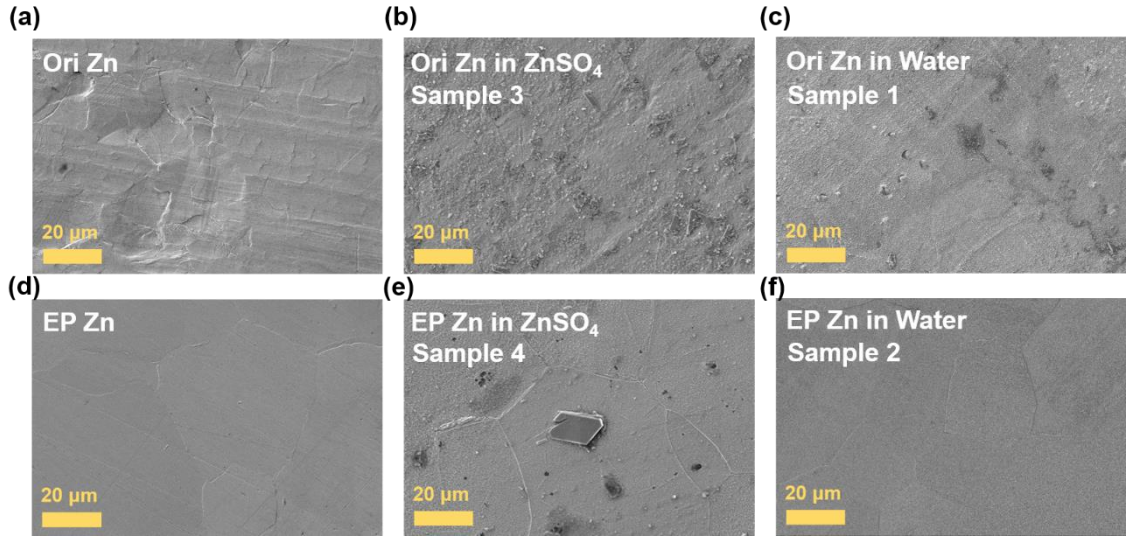

Figure 4.17 SEM images of (a) Ori Zn, (b) Ori Zn after soaking in $ZnSO_4$ solution (Sample 3), (c) Ori Zn after soaking in DI-water (Sample 1), (d) EP Zn, (e) EP Zn after soaking in $ZnSO_4$ solution (Sample 4) and (f) EP Zn after soaking in DI-water (Sample 2).

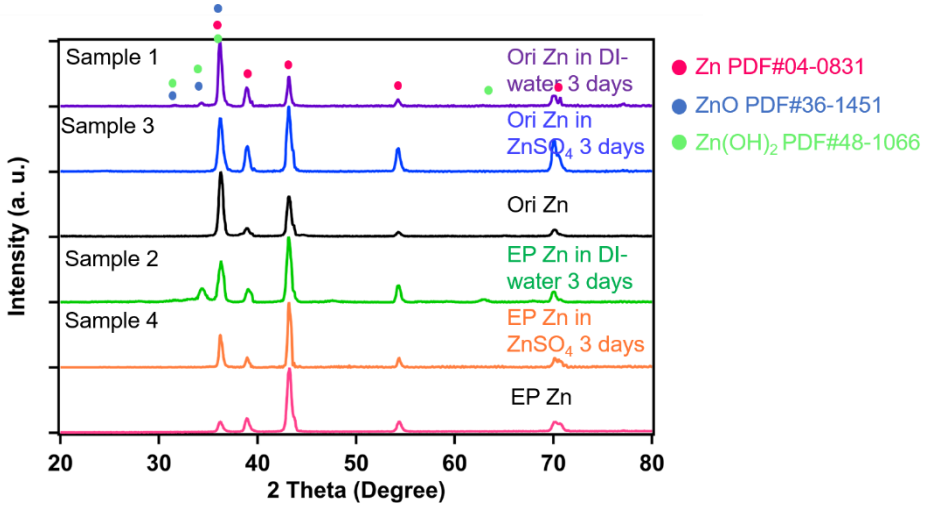

Figure 4.18 In-plane XRD patterns for different samples.

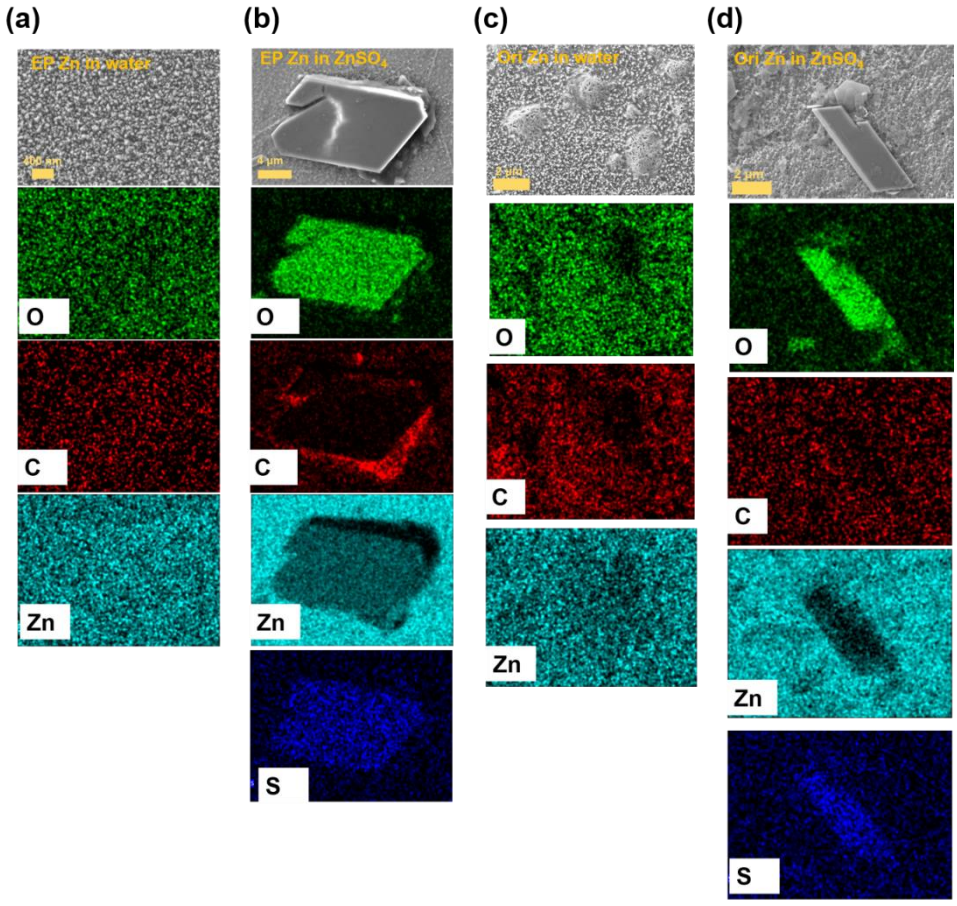

Figure 4.19 Elemental mapping of different samples. EP Zn foil that was soaked in (a) DI-water or (b) 2 mol L^{-1} $ZnSO_4$ for 3 days. Ori Zn foil that was soaked in (c) DI-water or (d) 2 mol L^{-1} $ZnSO_4$ for 3 days.

Here, two issues are needed to be clarified: (1) The difference between the samples that were immersed in DI-water and in the $ZnSO_4$ aqueous solution. (2) The difference between EP Zn and Ori Zn when they were immersed in the $ZnSO_4$ electrolyte. The difference between the passivation layers formed in DI-water and the one formed in $ZnSO_4$ aqueous solution were further characterized by glow discharge optical emission spectroscopy (GDOES), which was used to observe the depth elemental profiles. As shown in **Figure 4.20(a)**, the newly prepared EP Zn has a clean surface that contain only a small amount of C, O, S elements.

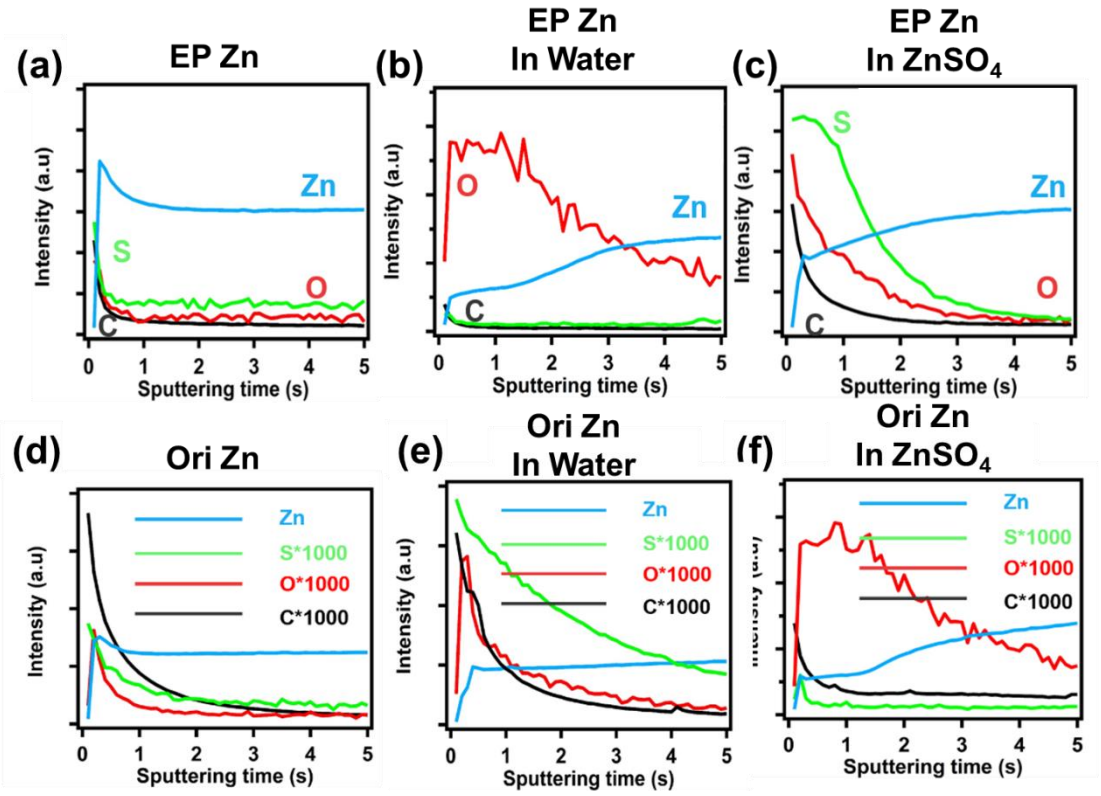

Figure 4.20 Qualitative depth profile analysis of (a) the as-prepared EP Zn foil, (b) the EP Zn foil after soaking in 2 M ZnSO4 for 3 days, (c) the EP Zn foil after soaking in DI-water for 3 days, (e) the Ori Zn and (f) the Ori Zn that was soaked in 2 M $ZnSO_4$ for 3 days and (g) the Ori Zn that was soaked in DI-water for 3 days, respectively.

After being soaked in DI-water, the peaks of Zn and O show similar intensities, which appear almost simultaneously, indicating that the surface of Sample 2 is covered by a thick and dense film mainly containing Zn and O (**Figure 4.20(b)**). In contrast, Sample 4 keeps a relatively clean surface, demonstrated by the rapidly disappearing C, O, and S peaks and the almost unchanged Zn peak (**Figure 4.20(c)**). The elemental depth profiles for the Ori Zn samples, as shown in **Figure 4.20(d-f)** are similar to that of the corresponding EP Zn samples; consequently, a dense and thick passivation layer is formed on Sample 1, while the corrosion product layer on Sample 3 is thinner. Comparing the elemental depth profiles for Sample 3 and Sample 4, it is concluded that the thickness of the surface layer on Sample 3 is much greater than Sample 4, indicating that the primitive surface layer on Ori Zn cannot be completely removed by immersing Zn foil into a weakly acidic electrolyte. The thickness and structure of the surface layer can significantly affect the electrochemical impedance of Zn electrodes, as presented in **Figure 4.21**; it can be seen that Sample 4 maintains its low impedance characteristics in the electrolyte, while all other zinc samples with heavily passivated surfaces exhibit higher impedance; thus the preference of Zn deposition will be different.

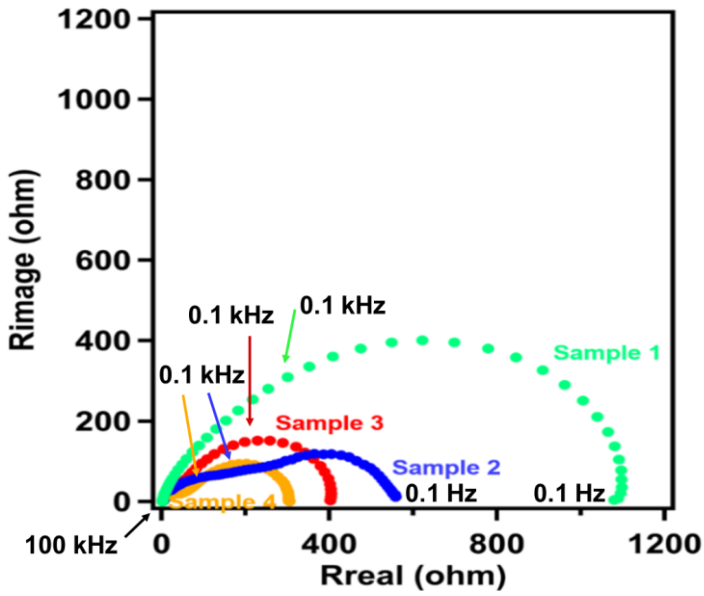

Figure 4.21 Nyquist plots of Sample 1 (green), Sample 2 (blue), Sample 3 (red) and Sample 4 (orange). The Nyquist plots were obtained in symmetric Zn||Zn cells.

To further reveal the difference between EP Zn and Ori Zn when they were immersed in the $ZnSO_4$ electrolyte, X-ray photoelectron spectroscopy (XPS) was also employed to detect the depth profiles of the corrosion product layers. As shown in **Figure 4.22(a),** the primitive surface layer on Ori Zn, which consists of zinc hydroxycarbonate, zinc hydroxide, and zinc oxide, is confirmed to be less than 60 nm. When Ori Zn was immersed into the electrolyte, the thickness of the surface layer increased unevenly, which is in conformity with the GDOES results. This is caused by the newly formed zinc hydroxy sulfate. As a comparison, both the as-prepared EP Zn and the one as-immersed in $ZnSO_4$ electrolyte have a very thin surface layer of less than 60 nm **(Figure 4.22(b, c)**. Meanwhile, the XPS depth profile analysis (**Figure 4.23(a))** of the samples soaked in DI water confirmed the above discussion. The surface of the samples immersed in DI-water showed an oxide layer with a thickness of > 180 nm. The main components were ZnO, $Zn(OH)_2$, and zinc hydroxycarbonate. The results of XPS and AFM (Figure 4.23(b)) indicate that EP Zn can maintain its uniform surface characteristics when soaked in a weakly acidic environment of $ZnSO_4$ electrolyte**,** by which the deposition of Zn will not be hindered on EP Zn. In contrast, the primitive surface film on Ori Zn cannot be effectively removed in the $ZnSO_4$ electrolyte; thereby, the uniform deposition of Zn is greatly obstructed. Based on these discussions, a possible mechanism can be proposed to explain the phenomenon of the preferential deposition of Zn on the electropolished surface, as shown in **Figure 4.24(a).** Although the surface layer, which contains zinc hydroxy sulfate and zinc hydroxycarbonate, will not be totally destroyed in the weak acidic environment during the plating process, the Zn-ion-concentration gradient as-generated on the surface of Zn electrode can force the surface layer to be dissolved into the electrolyte. As a result, Zn can be deposited uniformly on the surface of EP Zn without hindrance. At the same time, because the thicker and denser surface layer on Ori Zn cannot be completely dissolved by a slight Zn-ion-concentration gradient generated at low current densities, the uniform deposition of Zn is still blocked by the uneven surface layer on Ori Zn, resulting in the reported deposition selectivity on the “half-and-half” electrode.

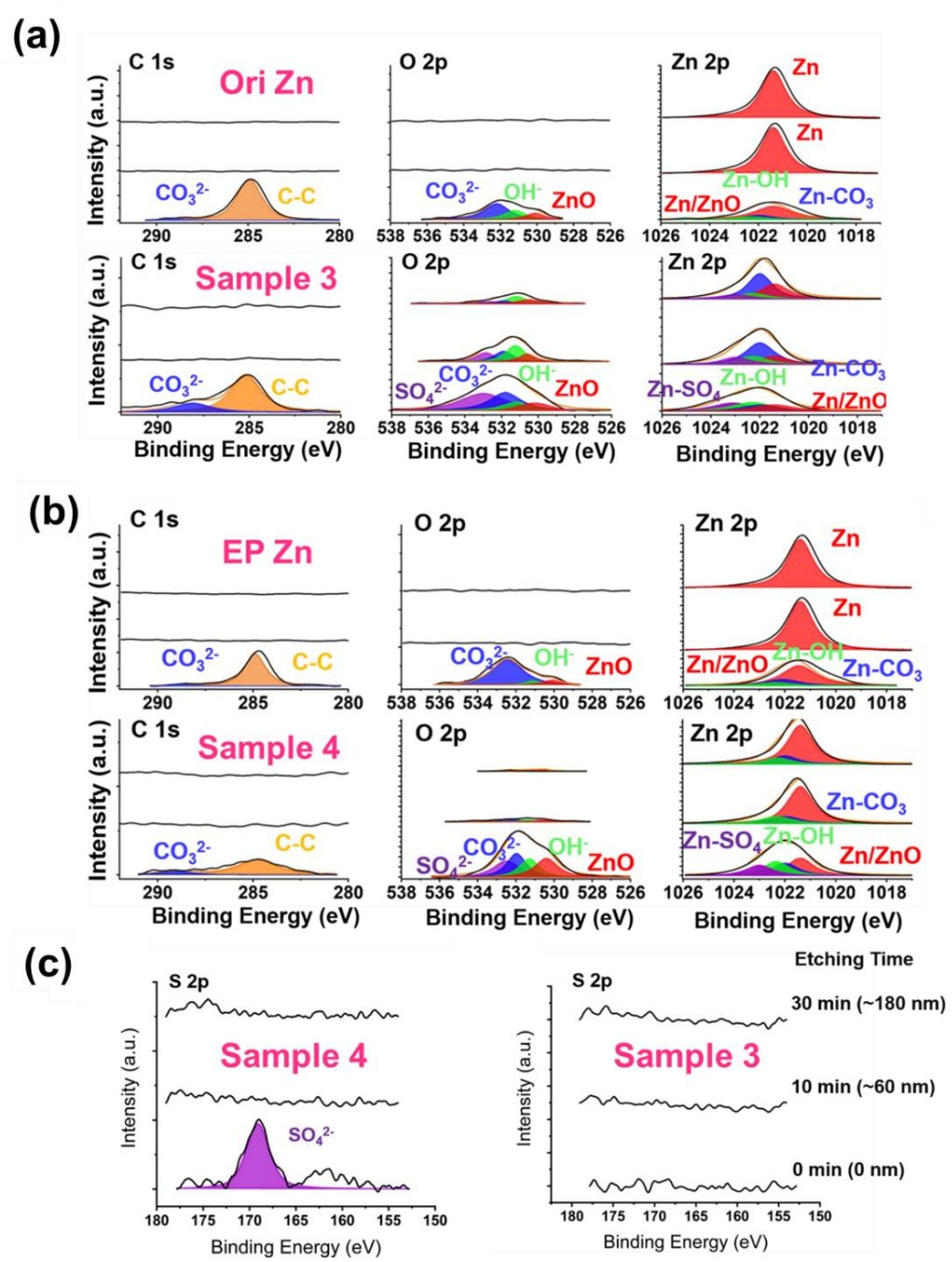

Figure 4.22 (a) XPS depth profile of (a) the Ori Zn foil (top) and the Ori Zn foil after soaking in 2 mol L^{-1} $ZnSO_4$ (bottom, Sample 3), (b) the EP Zn foil (top) and the EP Zn foil after soaking in 2 M $ZnSO_4$ (bottom, Sample 4), (c) XPS spectra of S 2p for the EP Zn after being soaked in 2 M $ZnSO_4$ and the Ori Zn after being soaked in 2 M $ZnSO_4$.

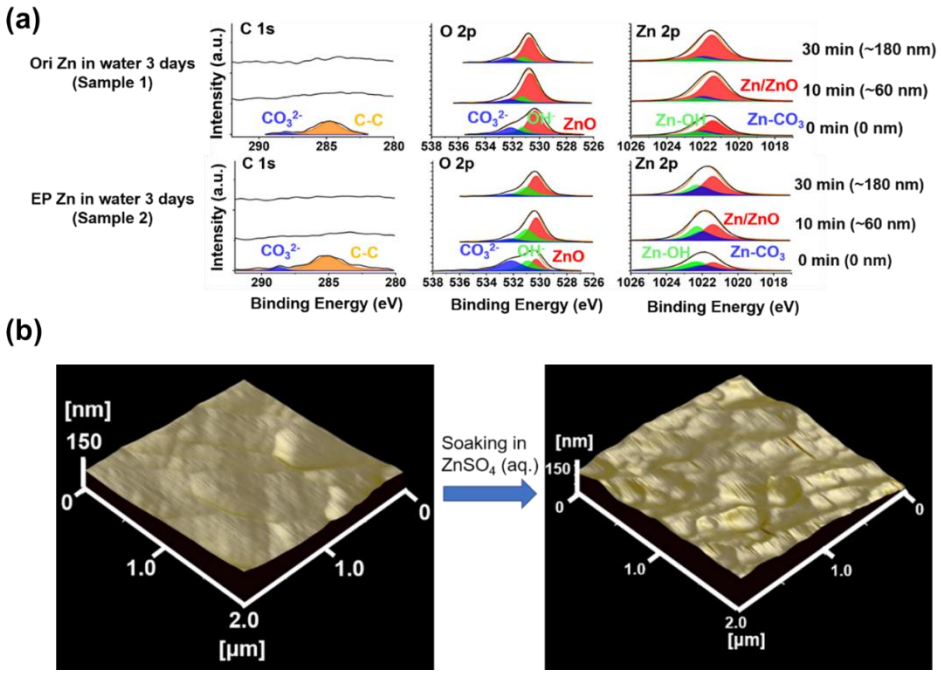

Figure 4.23 (a) XPS spectra of EP Zn and Ori Zn after being soaked in DI-water for 3 days (i.e. Sample 1 and Sample 2).

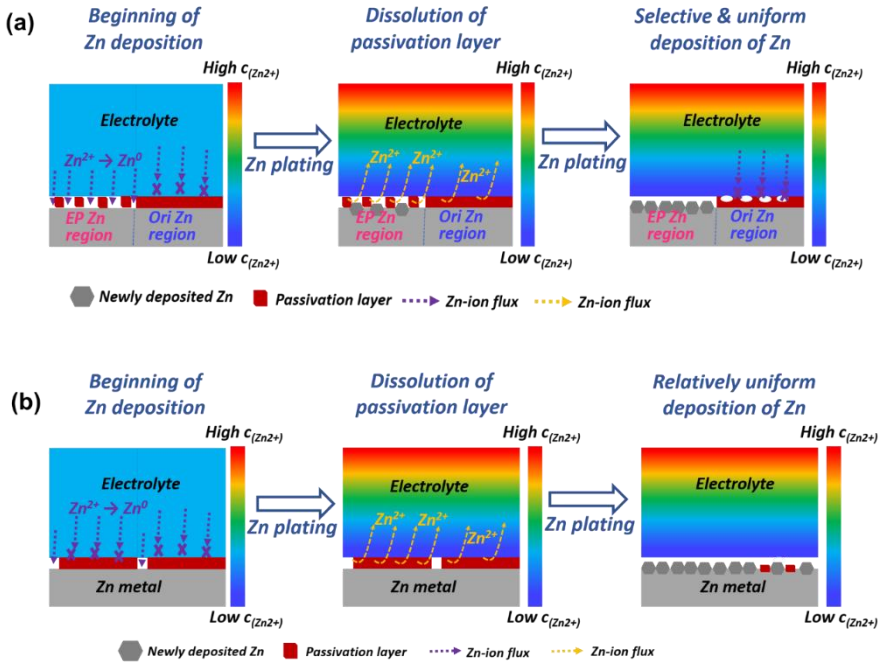

Figure 4.24 Schematic illustration for (a) the proposed mechanism for the selective deposition phenomenon and (b) the proposed mechanism of the uniformized Zn deposition under high galvanizing current density.

By employing this model, the reason why the deposition uniformity and cyclic performance of Ori Zn can also be improved during the high current density plating/stripping is also partially explained. In addition to the benefits of high current density described in Chapter 2, the thinner oxide passivation layer on the EP Zn surface and the more homogeneous surface properties also result in more uniform nucleation when electroplating Zn onto the EP Zn surface. This in turn leads to better cycling performance of EP Zn than Ori Zn even under high current densities. **(Figure 4.24(b))**. The change in the Zn-ion-concentration gradient at different conditions was visualized using a phase-field simulation model (**Figure 4.25**). It can be seen that the Zn-ion-concentration gradient as-generated on the surface of the Zn electrode is very small during the low potential (low current density) galvanizing, which cannot force the thick and dense oxide layer to be dissolved. However, when a high current density is applied, a significant Zn-ion-concentration gradient occurs and lasts for tens of seconds, which may help the dissolution of zinc compounds.

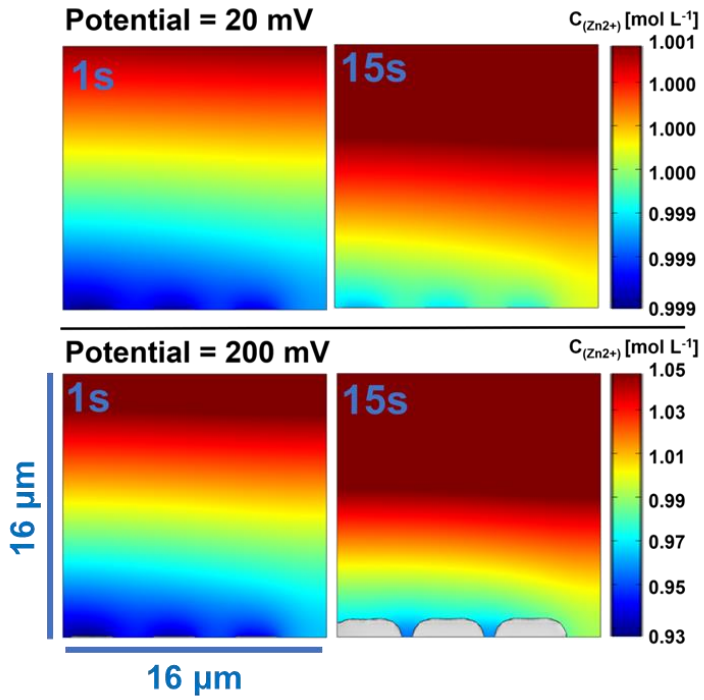

Figure 4.25 Simulation results of $c_{(Zn2+)}$ gradient during Zn plating under different conditions.

4.3.5 Cycling performance of full cells supported by electropolished Zn metal

In order to further demonstrate the importance of electropolishing the Zn anode in the development of practical Zn battery technologies, several kinds of full cells were assembled to compare the EP Zn and the Ori Zn in their practical performance. The Zn||MnO_2, Zn||VO_2, and Zn||AC full cells with different areal capacities were tested to show the performance differences. First, as shown in **Figure4.26(a)**, the low-capacity Zn||MnO_2 full cells tested under a high charge/discharge rate only shows a small difference in capacity retention. The slightly higher capacity retention of EP Zn||MnO_2 cell may benefit from the uniform anode surface during the cycling, which reduces the cell's internal resistance, as seen in **Figure 4.26(b, c).** For the Zn||VO_2 full cells, the use of EP Zn shows a more noticeable difference when compared with Ori Zn. As shown in **Figure 4.26(d)**, the Ori Zn||VO_2 full cells were trapped in a short circuit due to the growth of Zn dendrites after about 1000 cycles, while the EP Zn||VO_2 cell maintained its stable performance for at least 2000 cycles (the cell was stopped manually).

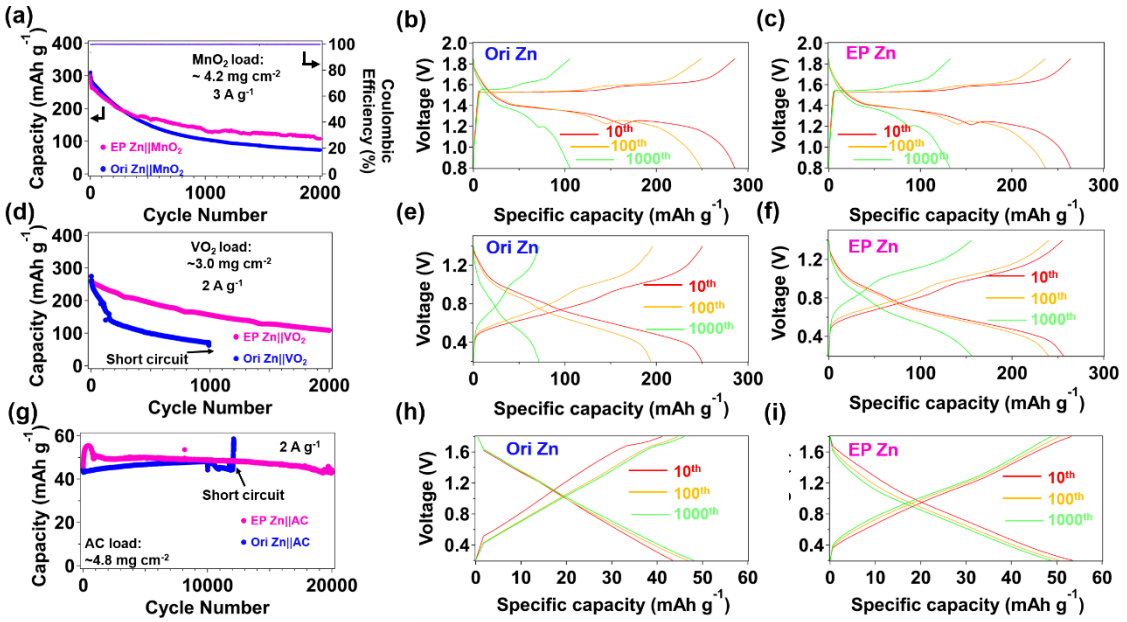

Figure 4.26 Full cells performance using different Zn anodes. (a) Cyclic performance of the Zn||MnO_2 cells. Voltage profiles of (b) the Ori Zn||MnO_2 cell and (c) the EP Zn||MnO_2 cell. (d) Cyclic performance of the Zn||VO_2 cells. Voltage profiles of (e) the Ori Zn||VO_2 cell and (f) the EP Zn||VO_2 cell. (g) Cyclic performance of the Zn||AC cells. Voltage profiles of (h) the Ori Zn||AC cell and (i) the EP Zn||AC cell.

Similar to the low capacity Zn||MnO_2 cells, EP Zn||VO_2 cell also exhibited better capacity retention, which also benefits from the maintained low internal resistance during cycling and can be demonstrated by the comparison of voltage profiles (**Figure 4.26(e)** and **Figure 4.26(f)**). The test of Zn||AC cells provided useful information when different Zn foils were used as anode for hybrid capacitors. Although the Zn||AC cells only had a low areal capacity (~ 0.24 mAh cm^{-2}) and were tested under high current (9.6 mA cm^{-2}), the Ori Zn||AC cell short-circuited after about 11000 cycles, while the EP Zn||AC cell can work stably for at least 20000 cycles (**Figure 4.26(g)**). Moreover, for the Ori Zn||AC cell, the voltage profiles of the several initial cycles show a fluctuation, indicating the Ori Zn may need to undergo a difficult activation process of dissolving the surface layer in the initial stage of charge/discharge. At the same time, the EP Zn maintained an almost coincident voltage profile during the whole test (**Figure 4.26(h, j)**). As depicted before, this process leads to uneven Zn deposition and becomes an opportunity for Zn dendrite growth.

Finally, to further investigate the performance of EP Zn anode in real-world applications, Zn||MnO_2 cells were assembled with ultra-high areal capacity (theoretical capacity: 24.6 mAh cm^{-2}), and a Zn||MnO_2 pouch cell with a large-size (about 45 cm^2). As shown in **Figure 4.27(a)** and **Figure 4.27(b)**, unsurprisingly, when the Ori Zn was used as the anode, the high-capacity Zn||MnO_2 cell became short-circuited in only 10 cycles while a low initial capacity was observed, which can be ascribed to the bad surface condition of the Ori Zn anode. The EP Zn anode helped the cell work stably for 32 cycles; afterward, the charge and discharge of the cell became no longer stable due to the dropping of the cathode materials (the electrode is too thick). However, the EP Zn||MnO_2 cell remained short-circuit-free for 50 cycles until the damaged cathode could no longer support the battery. Although this is still far from the requirement of real-world batteries, the finding has strongly demonstrated the importance of polishing the Zn anode before tests. As for the one-stack EP Zn||MnO_2 pouch cell with an area capacity of about 2 ~ 3 mAh cm^{-2} (during the whole charge/discharge test), which could work stably for 200 cycles (**Figure 4.27(c)**) and only show a slight deformation and bulge after cycling, indicating the electropolishing technology is also very convenient to be put into the development of practical RAZIBs. In addition, to realize the practical Zn metal anode, combining this electropolishing strategy with the optimization of

electrolytes, separator, and cathode will also be a highly potential solution.

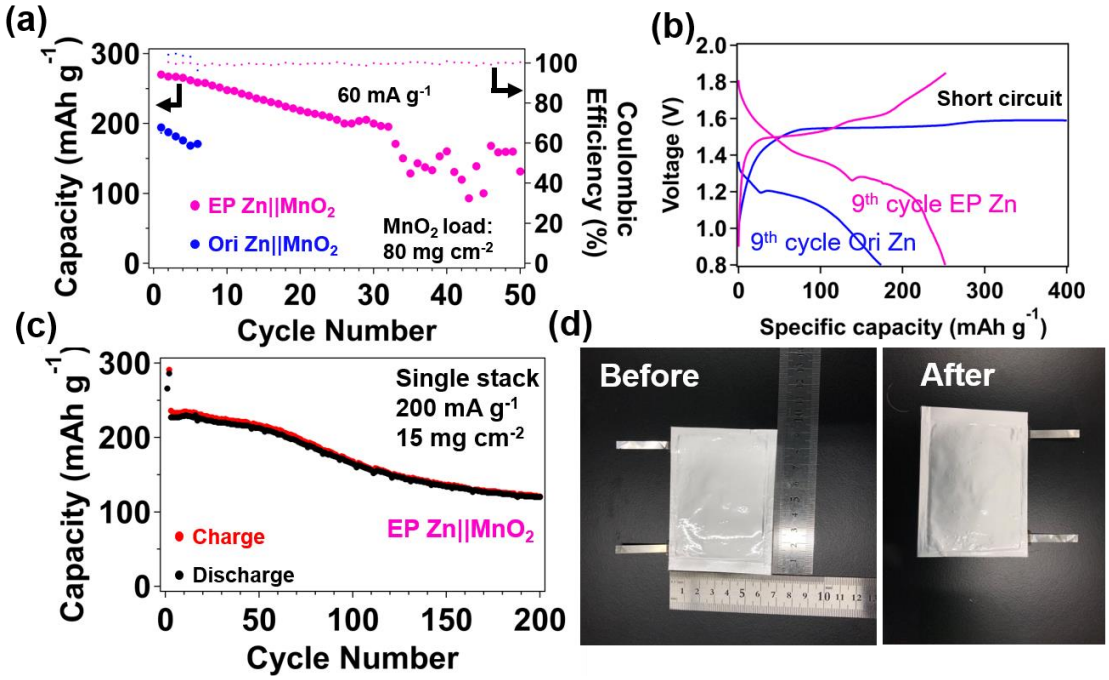

Figure 4.27 Cyclic performance of ultra-high-capacity Zn||MnO_2 cells and one-stack Zn||MnO_2 pouch cell. (a) Cyclic performance of the ultra-high-capacity Zn||MnO_2 cells and (b) the corresponding voltage profiles. (c) Cyclic performance of the EP Zn||MnO_2 pouch cell. (d) Optical photos of the pouch cell before and after cycle.

4.4 Conclusions

In summary, a low-cost, non-corrosive, non-toxic, and recyclable electropolishing strategy based on the NaCl/DEG electrolyte was employed for the first time, which is far more scalable and efficient than conventional polishing methods. The newly electropolished Zn metal with a very clean and smooth surface was demonstrated to be suitable as the anode of rechargeable aqueous Zn ion batteries in a neutral electrolyte, representing dendrite-free and long-life cyclic durability. The relationship between the surface oxide layer of Zn foil and the uniformity of Zn electrodeposition was revealed. For Zn foils without electropolishing, the oxide layer on the surface could not be completely dissolved in the weak acidic $ZnSO_4$ electrolyte, thus the uniform nucleation of Zn would be greatly affected, resulting in the following formation of Zn dendrites. Significantly, the newly electropolished Zn metal could maintain superior surface cleanliness in the weak acidic environment, thus seeding the uniform deposition of Zn and avoiding the formation of Zn dendrites. The cyclic stability of the electropolished Zn metal electrode could be improved to a considerable extent, which has exceeded most of the reported Zn metal anodes. The results not only demonstrate that the polishing pretreatment of Zn metal anode plays an important role in the research of RAZIBs, but also call for re-examining some current experimental results.

Chapter 5 High-strength double-network hydrogel electrolyte enables dendrite-free Zn metal anodes and high-capacity Zn-MnO_2 batteries.

5.1 Objective of this Chapter

The largest problem that limits the lifespan of RAZIBs and prevents their usage is that dendritic growth of Zn during electrodeposition will occur in aqueous solutions.[87, 187] Different from alkali metals (i.e., lithium, sodium, potassium), where dendritic growth is mainly attributed to the uneven distribution of the ion-flux, the growth of Zn dendrites generally starts from the deposition of Zn with preferred crystal orientation. The subsequent deposition of Zn crystals occurs along the identical crystal lattice as the pre-deposited Zn nucleus, magnifying the uneven distribution of the ion flux and forming large dendrites. Even worse, the dendritic growth during Zn plating can be highly aggressive when the electrode works at a high current density with a high areal capacity. Because of these problems, achieving rechargeable Zn metal batteries that are safe and reliable energy storage devices with high energy density is challenging. [149, 188-189] Therefore, current RAZIB technologies are still immature and require significant advances to enable their use in fields where they could excel, such as in flexible electronics. [190-194]

Current efforts that have been attempted to limit the growth of Zn dendrites have mainly focused on two aspects: 1) considering that the dendritic growth of metals in an electrodeposition process can be depicted by the Sand's time model, [195-196] some researchers believed that by regulating the Zn-ion flux and reducing the local current density, the growth of Zn dendrites could be delayed, resulting in a relatively uniform distribution of Zn deposition; [51, 119-121, 197-198] 2) others have pointed out that by optimizing the orientation of Zn metal during electrodeposition, the shape of the deposited Zn crystals can be nonaggressive, because a substrate with specific crystal symmetry and lattice parameters would facilitate heterogeneous nucleation.[35, 98, 104, 199] The heterogeneous nucleation of Zn may lead to "homoepitaxial deposition" in the subsequent electrodeposition process, and thus a uniform metal plating layer could be achieved.

Solid-state electrolytes (SSEs) with high modulus show excellent dendrite suppression capability in alkali metal batteries.[200-202] Recently, Hong et. al. pointed out that mechanically strong gel

polymer electrolytes (GPEs) can potentially to limit the growth of Zn dendrites.[203] In Hong's model, the volume change induced by the electrodeposited Zn atoms causes the Zn to interact with the GPE at the interface. The combination of the volume strain of the GPE and their bulk modulus is considered additional stress to inhibit Zn crystal growth. Additional stress on the Zn crystals causes a reduction in the exchange current density, and thereby forced uniform Zn metal deposition could be achieved.[204] It is commonly accepted that dendritic growth can be suppressed when a separator has a shear modulus 1.8 times higher than the anode metal. [205] The shear modulus of Li is 4.9 GPa, while Zn has a higher value of 38.8 GPa. Different from alkali metals, the modulus of Zn metal is very high, and conventional soft materials are not expected to possess Zn dendrite growth-restricting properties. Therefore, investigating whether novel, stiff GPEs can limit Zn dendrite growth is necessary. Furthermore, understanding why these materials can overcome previous theoretical limitations is required in order to enable next-generation RAZIBs.

In this chapter, the high-strength hydrogels as GPEs were utilized for efficiently suppressing Zn dendrite growth, with the ultimate-goal of achieving high-efficiency energy storage based on RAZIBs. By a two-step polymerization method, a double network (DN) hydrogel consisting of poly(2-acrylamido-2-methylpropanesulfonicacid)/polyacrylamide (PAMPS/PAM), which was embedded with a glass fiber (GF) skeleton, was prepared. The glass fiber-supported double network hydrogel (DNGF) shows a high Young's modulus in both compression and tension, which is several times higher than the best previously reported GPEs. The DNGF was used as a GPE for suppressing Zn dendrite formation. The superior mechanical strength of DNGF can eliminate the growth of Zn dendrites, forcing Zn to grow along the electrode surface and resulting in a flat Zn plating layer. At the same time, the high ionic conductivity of the DNGF-based GPE can also reduce the concentration polarization on the electrode surface, enabling the Zn anode to achieve cycle stability over thousands of hours with a low overpotential. Based on these results, a high-capacity Zn || MnO_2 battery that can effectively avoid short circuits has been developed. The successful use of the high-strength GPE provides a new route to design a separator that can prevent dendrite growth and shows excellent potential for achieving high-energy density RAZIBs.

5.2 Experimental Section

5.2.1 Preparation of the hydrogel polymer framework.

To prepare the PAMPS-GF hydrogel, 2-acrylamido-2-methylpropanesulfonic acid (AMPS, Toagosei Co. Ltd.) was dissolved in DI water to obtain 1 mol L^{-1} solution. Then, 2.5 % (mole ratio) N,N'-methylenebisacrylamide (MBAA, FUJIFILM Wako Pure Chemical Corporation) and 1 % (mole ratio) α-keto (FUJIFILM Wako Pure Chemical Corporation) were added to the solution. The AMPS solution was then transferred to an argon (Ar) filled glovebox. A glass fiber filter (Advantec. GA-100) was cut to 10 cm x 10 cm and soaked in the as-prepared AMPS solution for 30 minutes. Afterward, the glass fiber sheet was sandwiched between two glass plates and was exposed to UV light for 12 h.

The obtained PAMPS-GF composite was soaked in a 3 mol L^{-1} acrylamide (AM, Junsei Chemical) solution for 1 day to swell the PAMPS-GF skeleton with AM solution thoroughly. 0.01 % MBAA and 0.01 % α-keto were also added to the AM solution. The AM-swollen PAMPS-GF was transferred to a glovebox and was polymerized by a 12 h UV irradiation.

To prepare the PAM-GF and PAM, the aforementioned AM solution was used to infiltrate a glass fiber sheet. PAM-GF can be obtained by polymerizing the AM-filled glass fiber, while PAM was prepared by polymerizing the AM solution in a glass mold. All the obtained hydrogel samples were kept in DI water until use.

All the obtained hydrogel samples were kept in DI water until use.

5.2.2 Mechanical properties measurements.

Uniaxial tensile tests were performed on all the prepared hydrogels at the maximum water content. A tensile-compressive tester (INSTRON 5965, Instron Co.) was used to conduct the tensile tests. All the dumbbell-shaped samples (length of 12 mm, width of 2 mm, the thickness range is 2-3 mm depending on the sample) were stretched along the length direction at an extension rate of 100 mm min^{-1}.

Uniaxial compress tests were performed by using a compressive tester (Tensilon RTC-1310A, Orientec Co). Samples were firstly cut to a disk shape with a diameter of 10 mm before the test. The compression rate was set to 0.1 x min^{-1}, where the x is the thickness of the sample.

5.2.3 Electrochemical measurements

All the DNGF samples used in the Zn plating tests were dried in a vacuum box at room temperature for 48 h and then soaked in a 2 mol L^{-1} $ZnSO_4$ aqueous solution (as electrolyte) for 24 h. The electrolyte dosage for every GF-separated cell was 200 μL.

Swagelok Zn || Zn cells that DNGF or GF separated were assembled and connected to a battery tester for the galvanostatic galvanizing tests. Zn metal was electroplated to a piece of Zn disk electrode at a constant current density of 1 mA cm^{-2} for 16 h.

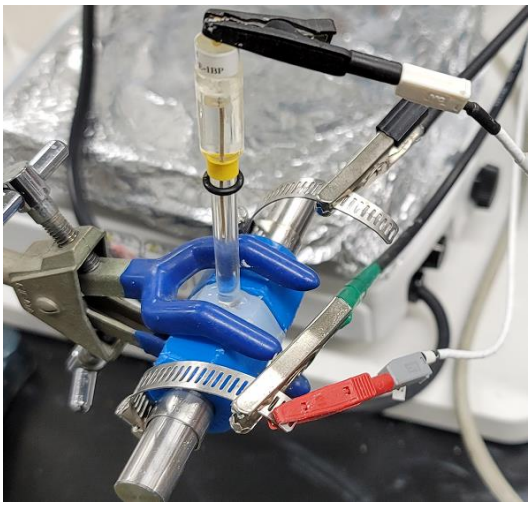

Figure 5.1 Optical photo of the three-electrode quasi-solid-state cell. An Ag/AgCl reference electrode was set in a drilled hole and contacted with the added liquid electrolyte.

Homemade three-electrode cells were assembled for the potentiostatic Zn plating tests, as shown in **Figure 5.1.** Two Zn disk electrodes were used as working and counter electrodes, respectively. An Ag/AgCl reference electrode was inserted into the window that was opened on the body of the Swagelok cell. An additional 200 μL electrolyte (2 mol L^{-1} $ZnSO_4$) was added to the cell to achieve contact between the reference electrode and electrolyte. As demonstrated in the context, Zn metal was electroplated at a constant potential. The experiments were stopped manually once the areal capacity of Zn plating met the specific value.

For the Zn || Zn symmetric cell tests, two-electrode Swagelok cells with two Zn disk electrodes were prepared. DNGF, PAM-GF, PAMPS-GF, and GF were used to separate the cells. All the GPE

samples used in the symmetric cell tests were dried in a vacuum box at room temperature for 48 h and then soaked in a 2 mol L^{-1} $ZnSO_4$ aqueous solution for 24 h. The electrolyte dosage for every GF-separated cell was 200 μL. Zn || Zn symmetric cells were tested on the SD8 battery tester. During the test, Zn metal plating/stripping between two Zn electrodes at a constant current density was repeated.

For the Zn || MnO_2 cells, the used electrolytic manganese dioxide (EMD, TOSOH, HH-TF 40 μm) was obtained from the TOSOH company. MnO_2 cathodes were prepared by mixing 65 wt% MnO_2 powder, 25 wt% carbon black (ketjen black, KB), and 10 wt% poly(tetrafluoroethylene) (PTFE, suspension, 10 wt%) in ethanol aqueous solution. The amount of active material was controlled by adjusting the thickness of the cathode. The freestanding electrode was prepared by pressing the carbon-MnO_2 mixture onto a Ti mesh (Nilaco, 100 mesh). The low-capacity MnO_2 cathode was prepared by mixing 65 wt% MnO_2 powder, 25 wt% KB, and 10 wt% poly(vinylidene fluoride) (PVDF, powder) in N, N-dimethylformamide (DMF). The mixture was then coated onto a Ti mesh and dried in a vacuum oven at room temperature overnight.

Zn || MnO_2 cells were assembled using Zn metal anodes and different MnO_2 cathodes. Swagelok cells were used as the cell casing, and DNGF or GF was used as the separator. All the DNGF samples used in the Zn || MnO_2 cell tests were dried in a vacuum box at room temperature for 48 h and then soaked in an aqueous solution containing 2 mol L^{-1} $ZnSO_4$ and 0.2 mol L^{-1} $MnSO_4$ for 24 h. The electrolyte dosage for every GF-separated cell was 200 μL. The Zn || MnO_2 cells were charged/discharged between 0.8 V and 1.8 V at the specific current densities.

For the GITT tests for the DNGF-separated Zn || MnO_2 cell, the GITT test for high-capacity Zn || MnO_2 cell was conducted by intermittently charging (or discharging) the cell until the cell voltage reached the cut-off voltage. Here, the Zn || MnO_2 cell was first discharged at a current density of 308 mA g^{-1} for 60 s, defined as one section. Then the cell would rest for 120 min for the completion of ion-diffusion. Once the cell voltage achieved the cut-off voltage of 0.8 V, the GITT test would be stopped. The capacity of GITT discharge was the sum of the capacities of all discharge sections.

Cyclic voltammetry (CV) and Electrochemical impedance spectra (EIS) were measured on an electrochemistry workstation (Princeton, VersaSTAT3). For Zn || MnO_2 cells, potentiostatic EIS measurements were conducted at a controlled voltage of 1.35 V (vs. Zn/Zn^{2+}), and the frequency range was 100 kHz to 0.1 Hz. Ionic conductivities of GPEs were calculated through EIS measurements. For GPEs, the hydrogel ionic conductor was sandwiched between two stainless steel disks with the same dimension. An O-ring was sandwiched between two stainless steel disks for the pure electrolyte. The ionic conductivity of different samples was calculated by ohmic resistance. The ionic conductivity σ was obtained by:

$$\sigma = l/RA \qquad \textbf{(Eq 5.1)}$$

where l is the thickness of the sample, R is the ohmic resistance, and A is the geometric surface area of the sample, respectively.

Before the ex-situ SEM observation of GPEs framework and as-tested Zn electrodes, all samples were soaked in sufficient DI water for 1 day after they were removed from the cells to remove the residue of electrolytes. Afterward, all the samples were freeze-dried and kept in a vacuum box before observation.

5.2.4 Simulation of the capacitive current

The total stored charge during a CV test was separated into these components: i) Faradaic contribution from the ion-insertion process; ii) Faradaic contribution from the charge-transfer process with surface atoms, namely the pseudocapacitance; iii) Nonfaradaic contribution from the electrical double-layer capacitance.[206] Here, the current that was contributed by pseudocapacitance and the double-layer capacitance was evaluated by:

$$I = av^b \qquad \textbf{(Eq 5.2)}$$

Where I is the current and v is the sweep rate, a is an adjustable parameter, b is the slope of the plot of log i vs log v. Eq. 5.2 can be modified to the following form in a separated CV cycle:

$$I(V)/v^{0.5} = k_1 v^{0.5} + k_2 \qquad \textbf{(Eq 5.3)}$$

where $I(V)$ is the measured current at a specific potential during a single CV cycle, k_1 and k_2 are two parameters obtained by linear fitting every $I(V)/v^{0.5}$ and $v^{0.5}$. The product of k_1 and v (the result

is current) is regarded as the contribution from pseudo-capacity. The capacitive current can be obtained by drawing a plot of $k_1 v$ and V.

5.2.5 Simulation of the Zn plating process

A three-dimensional (3D) model was employed to simulate the process of Zn deposition during a galvanizing test in a Swagelok cell. As depicted in **Figure 5.2**, electrochemical models were built using COMSOL Multiphysics with the "2D-Tertiary Current Distribution" interface. The geometric model included 3 parts: a cell chamber (the largest cuboid shown in **Figure 5.2**), a cathode zone (the red cuboid), and a certain number of ellipsoids. The height of the cathode zone is high enough to avoid the coating height break through the cathode zone during galvanizing. The surface of the ellipsoids above the anode surface was all used as active sites for galvanizing, and the electrolyte was filled with the entire battery chamber by default.

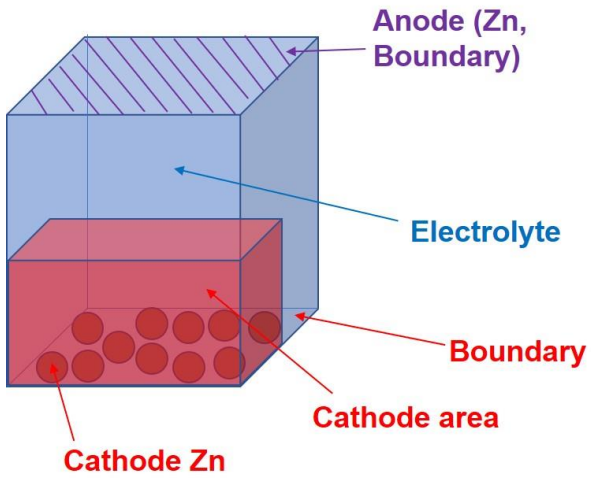

Figure 5.2. Geometric model for the simulation of Zn plating.

The entire battery is electrically neutral in the 1D direction through the Nernst-Planck-Poisson equation. The relationship between electrode reaction and overpotential is described by the Butler-Volmer equation. The simulation of galvanizing under different conditions was realized by adjusting the parameters. The relationship between electrode reaction and

overpotential is described by the Butler-Volmer equation. The simulation of galvanizing under different conditions was realized by adjusting the parameters. The potential of the electrolyte was obtained by combining the following relationship:

$$i_l = -\sigma_l \nabla E_l \quad \textbf{(Eq 5.4)}$$

$$\nabla \cdot i_l = 0 \quad \textbf{(Eq 5.5)}$$

where i_l is the current density of the electrolyte (vector), σ_l is the ionic conductivity of the electrolyte, and E_l is the potential of the electrolyte.

The Butler-Volmer equation was used to express the electrode reaction under dynamic conditions:

$$j_{loc} = j_0\left(\exp\left(\frac{\alpha_a F \eta}{RT}\right) - \exp\left(\frac{-\alpha_c F \eta}{RT}\right)\right) \quad \textbf{(Eq 5.6)}$$

where j_{loc} is the local current density, j_0 is the exchange current density, η is the overpotential, α_a is the anodic transfer coefficient, and α_c is the cathodic transfer coefficient.

The thickness of the Zn coating was calculated using Faraday's laws of electrolysis:

$$V = \frac{i_{loc} t M_{Zn}}{2F\rho_{Zn}} \quad \textbf{(Eq 5.7)}$$

where t is the deposition time, M_{Zn} is the molar mass of Zn, ρ_{Zn} is the mass density of Zn, and V is the volume of deposited Zn for a small area. The parameters are summarized in **Table 5.1**.

5.2.6 Characterization

X-ray diffraction (XRD) patterns were obtained using an X-ray diffractometer (Rigaku MiniFlex600) using Cu Ka radiation. Scanning electron microscope (SEM) observations and energy dispersive spectroscopy (EDS) measurements were conducted on an SEM (ZEISS Sigma 500). Atomic force microscopy (AFM) tests were conducted on an AFM (Hitachi, NanonaviSII) by using the dynamic force mode (DFM). In-situ Raman spectra were recorded by a Raman microscope (RENISHAW Raman spectrometer) using an excitation wavelength of 532 nm. Before the ex-situ SEM observation of GPEs framework and as-tested Zn electrodes, all

samples were soaked in sufficient DI water for 1 day after they were taken out from the cells to remove the residue of electrolytes. Afterward, all the samples were freeze-dried and kept in a vacuum box before observation.

Table 5.1 Parameters that were used in multi-physics simulation.

Parameter	Value	Ref.
$E^{\varphi}_{Zn/Zn2+}$	-0.76 V	-
$j_{0\ (no\ separator)}$	24.41 A m^{-2}	Experimental
$j_{0\ (DNGF)}$	5.42 A m^{-2}	Experimental
j	1 mA cm^{-2}	Experimental
M_{Zn}	65 g mol^{-1}	-
ρ_{Zn}	7140 kg m^{-3}	-
$\sigma_{(DNGF)}$	26.8 mS cm^{-1}	Experimental
$\sigma_{(no\ separator)}$	63 mS cm^{-1}	Experimental

5.3 Results and Discussion

5.3.1 Preparation of the high-strength hydrogel polymer electrolyte.

Figure 5.3 shows the schematic diagram of the DNGF preparation. AMPS and the cross-linker MBAA were firstly dissolved in water, and a piece of glass fiber separator was immersed in this solution. Then, the glass fiber with AMPS was placed under ultraviolet (UV) light to achieve the gelation of AMPS. Here, the glass fiber sheet was used as a skeleton to support the fragile PAMPS, which plays an important role in subsequent experiments. The obtained composite that consists of PAMPS and glass fiber was coded as PAMPS-GF. After that, a polyacrylamide (PAM) solution swelled the structure of PAMPS-GF, and a second UV polymerization resulted in a PAMPS-PAM double network hydrogel containing glass fiber, which was coded as DNGF. During the deformation of the DNGF, sacrificial rupture of the first network (PAMPS-GF) dissipates energy prior to global gel fracture.[207-208]

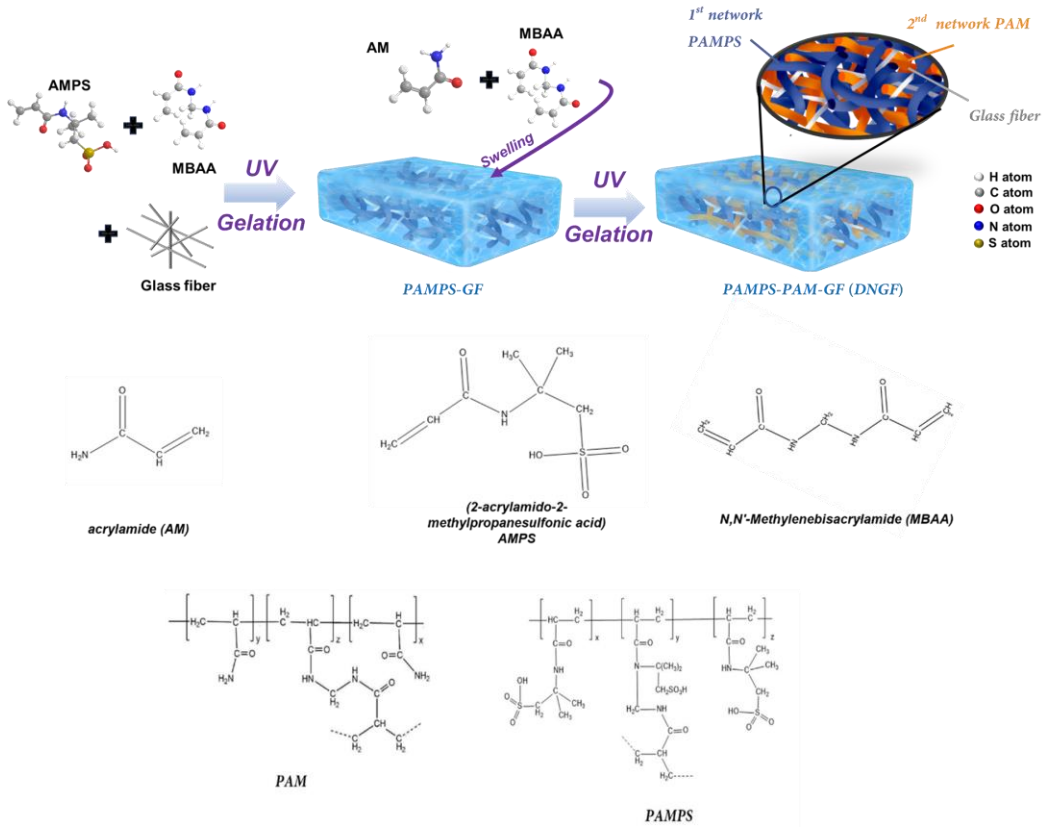

Figure 5.3 Schematic illustration for the fabrication of the DNGF gel matrix.

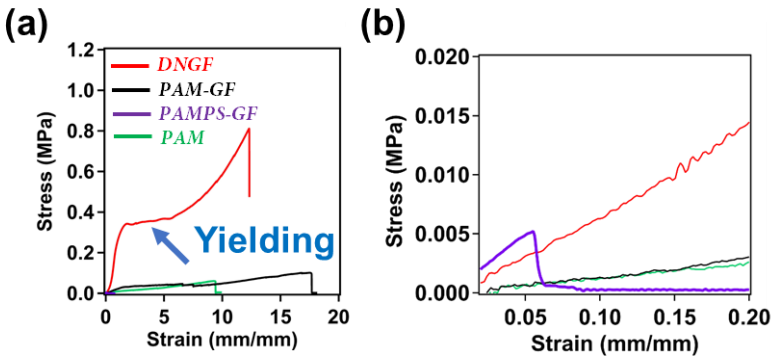

Figure 5.4 (a) Loading curves of different gels under uniaxial elongation. (b) The magnification of **Figure 5.4(a).**

The occurrence of sacrificial fracture can be observed during tensile testing by the presence of yield stress, denoted by the blue arrow in **Figure 5.4**. The entanglement between polymer strands from the first and second networks provides stress transfer between the two networks, enabling high strength of the DNGF. Thus, the DNGF could be stretched to a length 10 times longer than its original size while high stress was maintained. As a comparison, the single network (SN) PAM hydrogel and the PAM-GF composite hydrogel (see preparation details in the supporting information) can achieve high strain but only show very low stress during tensile testing. PAMPS, as a polyelectrolyte, swells to many times its initial volume in water and is extremely brittle. Similarly, the PAMPS-GF can only sustain up to 5.5% strain prior to failure. [209] The stress-strain curves of the gels under compression are compared in **Figure 5.5**. The DNGF can sustain a stress of 6.9 MPa at a strain of 80%, which is 10 times higher than the PAM SN gels.

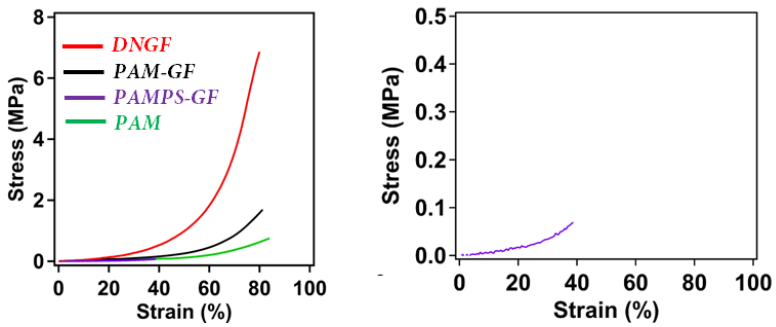

Figure 5.5 (a) Loading curves of different gels under uniaxial compression. (b) The magnification of **Figure 5.5(a).**

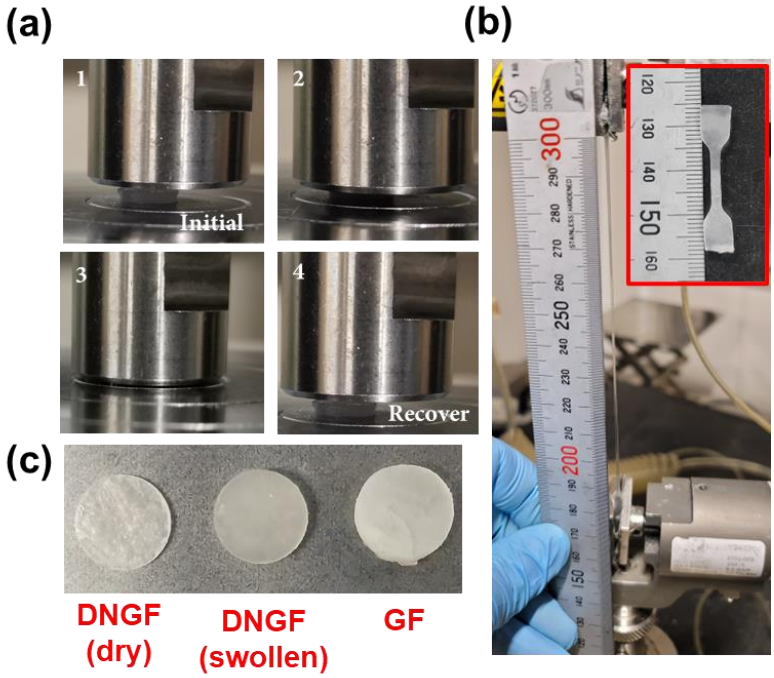

Figure 5.6 Photographs for demonstrating (a) the DNGF sustaining high compression, (b) the stretchability of the DNGF. The inset photo is the dumbbell-shaped DNGF sample before the test. (f) Photographs of DNGF and GF.

Figure 5.6(a, b) illustrates the straightforward tests of how the DNGF sustains a high compression or a high stretch, while **Figure 5.6(c)** shows the optical morphology of the translucent DNGF sample. In order to further understand the superiority in mechanical properties of DNGF, the shear modulus of the GPEs is summarized in **Table 5.2**. The DNGF has a shear modulus significantly higher than most conventional hydrogels and is more than an order of magnitude stiffer than either of its neat components (**Table 5.3**). These results indicate that the mechanical properties of the newly developed DNGF are sufficient to be termed as high-strength GPE for ZIBs.

Table 5.2 Physical parameters of the GPEs used in this work.

Sample	Weight before swelling (mg)	Weight after swelling (mg)	Swelling ratio (mL g^{-1}) [a]	Shear modulus (kPa) [b]
DNGF	29.8	240.9	7.1	94.2
PAM-GF	24.5	253.2	9.3	8.6
PAMPS-GF	13.6	172.3	11.7	-
PAM	11.6	146.8	11.6	3.2

a) The swelling ratio is calculated through the equation: $q=V_a/W_0$.

where V_a is the volume of the absorbed water at equilibrium, W_0 is the weight of the dried hydrogel.

b) The shear modulus is estimated by an empirical method, assuming a Poisson's ratio of 0.5: G=E/3, where G is the shear modulus, and E is Young's modulus (calculated by tensile testing).

Table 5.3 Comparing Young's modulus of different GPEs used in RAZIBs.

GPEs	Young's Modulus (kPa)	Ref.
EG-waPUA PAM GPE	8.06	192
Zwitterionic ZSC GPE	15.31	210
PAM	14.29	210
PVAA-GO	12.90	211
PVA	8.69	211
PAMPS-K30-MC2.0	32.22	194
DNGF	282.6	This work

5.3.2 Verification of the modified mechanical suppression effect of DNGF on Zn dendrite growth.

In order to verify the effect of high-strength GPE on the electrodeposition of Zn metal, the dried DNGF was firstly swollen by a $ZnSO_4$ aqueous solution (2 mol L^{-1}) to prepare the semi-solid hydrogel electrolyte.[212-213] The obtained GPE showed a high ionic conductivity of 26.8 mS cm^{-1} (**Figure 5.7**). The DNGF GPE was then placed in a two-electrode Zn || Zn cell with the configuration shown in **Figure 5.8**. The author first examined the deposition behavior of Zn metal at a constant current density. As shown in **Figure 5.9(a)**, when Zn metal was galvanostatically deposited on a planar Zn foil without a separator, Zn dendrites would grow at the very initial plating stage and rapidly expanded without any limitation. This observation shows that even in an aqueous electrolyte with extremely high Zn^{2+} diffusion coefficient, $D_{(Zn^{2+})}$, and excellent ionic conductivity, the growth of zinc dendrites can still be very aggressive, being very different from the cases observed in Li metal anodes. [174, 214-219]

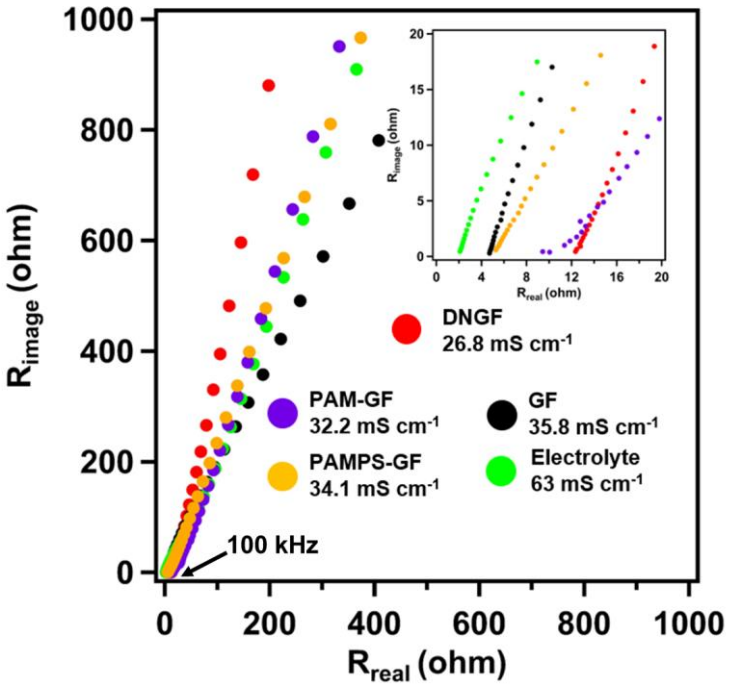

Figure 5.7 Nyquist plots of different separators (hydrogel electrolytes).

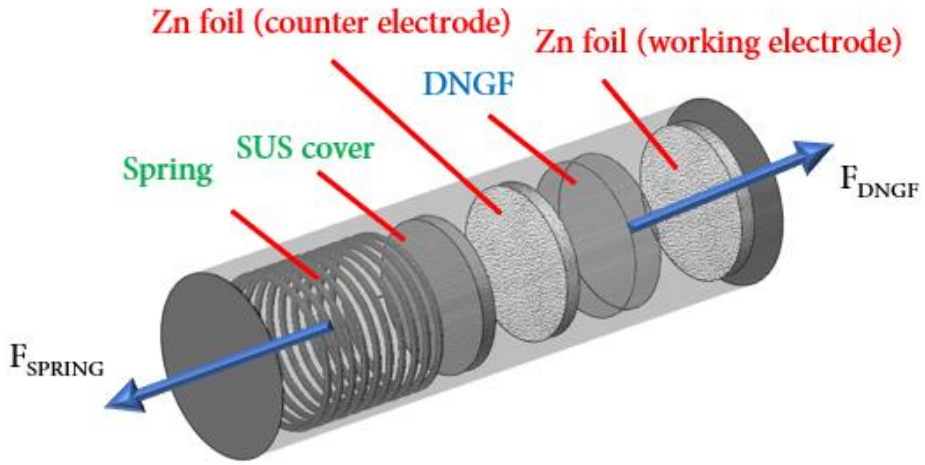

Figure 5.8 Configuration of the cell.

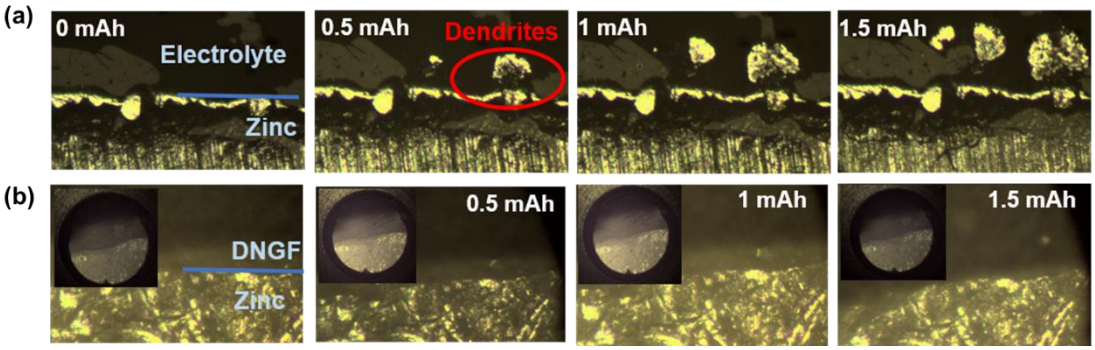

Figure 5.9 Configuration of the measurement cell. In-situ optical observations for the deposition of Zn (a) without the use of a separator and (b) using DNGF as the separator. The scale bar is 100 μm, while the insets are the panorama of the observation window under the optical microscope, the circular window comes from a 1 mm diameter observation window.

The dendrite growth of Li could be efficiently alleviated by optimizing the mobility of Li^+. When DNGF was used as the GPE, as shown in **Figure 5.9(b)**, no formation of Zn dendrites could be observed. In this case, the pictures from the small optical observation window indicate that the Zn coating layer gradually thickens. The electroplated Zn electrode was then taken out after the test, and it was found that the plating-layer was very uniform, as shown in **Figure 5.10**. High-

capacity galvanostatic plating tests were also conducted. Zn || Zn symmetric cells were assembled with a GF separator or DNGF, respectively. Zn was plated at a current density of 1 mA cm^{-2} for 16 h. For the Zn || Zn cell that used a GF separator, a short-circuit was observed after Zn deposition to a capacity of ~10.5 mA h cm^{-2} (**Figure 5.10(a)**). A large Zn dendrite with a length of about ~0.29 mm was observed by scanning electron microscopy (**Figure 5.10(b)**). It is conceived that the large Zn dendrite caused the internal short-circuit of the cell. The root reason of this dendrite formation can be traced back to the extremely uneven deposition of Zn. As shown in **Figure 5.10(c)**, the top view of the Zn plated electrode exhibits a disorganized morphology that consists of bare Zn plates and spherical Zn crystals. The top of the spherical Zn crystals was extensively covered with large and sharp Zn flakes (**Figure 5.10(d)**), which may be representative of Zn metal that is preferentially deposited along the [100], and [101] crystal planes in the aqueous electrolyte. [83, 220] When the Zn || Zn cell was separated by the DNGF GPE, a stable plating process was achieved during Zn deposition (**Figure 5.11(e)**). The recorded overpotential of the cell was from ~160 mV at the initial stage and gradually reduced to a stable value of ~ 65 mV. Because of the sluggish transfer of Zn^{2+} in the hydrogel electrolyte, both the initial overpotential and the overpotential platform in the DNGF separated cell were slightly higher than the values of the GF separated Zn || Zn cell. The top view of the Zn plated electrode, which is shown in **Figure 5.11(f)**, shows that the surface was covered by even and dense spherical Zn crystals. Through a closer observation of a spherical crystal in the red frame, the author found something curious. On the one hand, the left side of the selected spherical Zn crystal showed a morphology typical of Zn flakes (**Figure 5.11(g)**). These Zn flakes are almost the same size as those that were shown in **Figure 5.11(d)**. On the other hand, the top morphology of the selected spherical Zn crystal was flat and dense (**Figure 5.11(h)**). It seems that the upward growth of the Zn crystals was prevented by some external stress. The optical photograph embedded in **Figure 5.11(e)** shows the surface characteristics of the electrode after galvanizing.

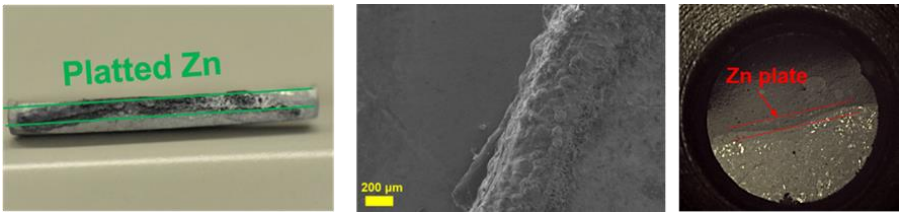

Figure 5.10 Optical photo (left) and SEM image (mid) and a zoom in view (right) of the Zn electrode corresponding to in-situ optical observation.

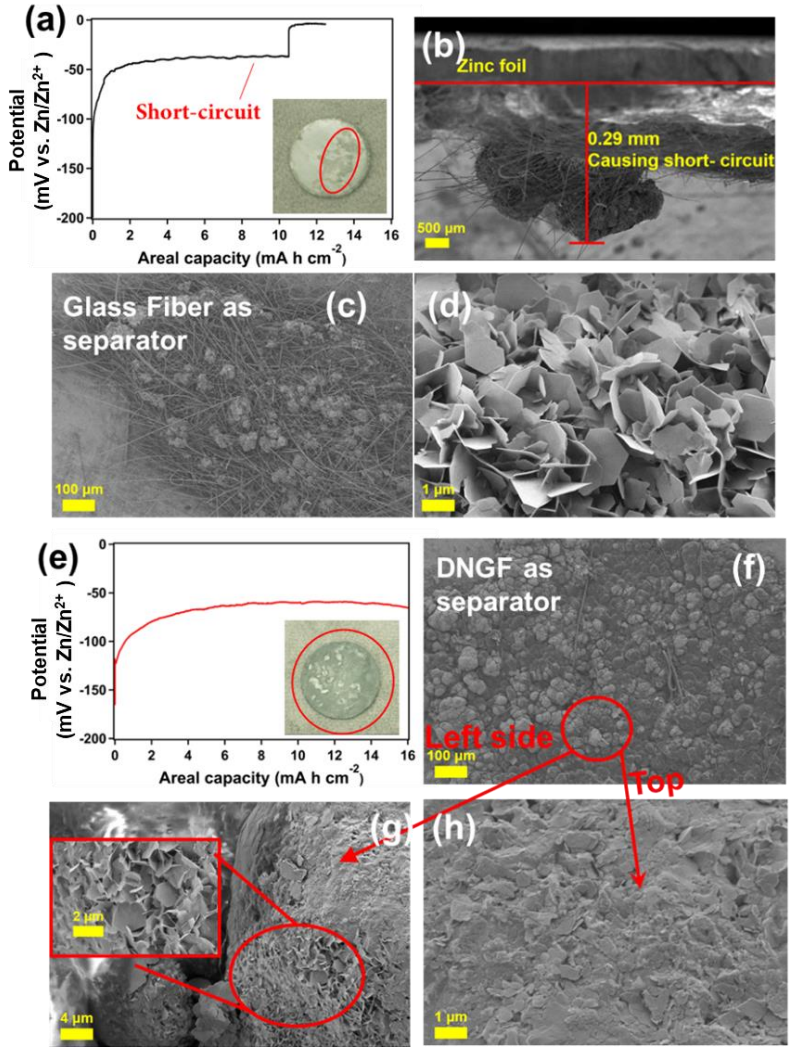

Figure 5.11 (a) Voltage profile during galvanization with the use of a glass fiber separator, and the inset optical photo is the corresponding Zn electrode. (b,c,d) SEM images of glass fiber separated Zn electrode after electroplating. (e) Voltage profile during galvanizing with the use of a DNGF GPE, and the inset optical photo is the corresponding Zn electrode. (f,g,h) SEM images of DNGF separated Zn electrode after electroplating.

In summary, two key points can be extracted from the galvanizing tests. First, the deposited Zn crystals in the 2 mol L^{-1} $ZnSO_4$-based aqueous electrolyte are generally micrometer-sized spheres. This phenomenon is attributed to the high ionic conductivity and high $D_{(Zn^{2+})}$ of the aqueous $ZnSO_4$ electrolyte. The high ionic conductivity of the electrolyte could eliminate the $c_{(Zn^{2+})}$ gradient at the electrode surface, generating spherical crystals.[221-222] Second, the sluggish transport of Zn^{2+} in DNGF does not influence the spherical morphology of the electrodeposited Zn, but an external restriction could terminate their upward growth.

Based on the understanding that the surface tension is the mechanical force that contributes to the chemical potential change across the interface between the GPE and Zn crystals, the mechanical interaction can result in the change of exchange current density during the reaction of Zn plating/stripping because of the decrease in chemical potential difference (for the Zn deposition reaction): [203, 223-224]

$Zn^{2+} + 2e^- \rightarrow Zn^0$ (Plating) (Eq. 5.8)

$Zn^0 - 2e^- \rightarrow Zn^{2+}$ (Stripping) (Eq. 5.9)

The modified Butler-Volmer equation that describes the current-overpotential relationship can be written as:

$$j = j_0\left[\frac{c_{Zn^{2+}(t\ surf)}}{c_{Zn^{2+}(bulk)}}\exp\left(-\frac{\beta F}{RT}\eta\right) - \frac{c_{Zn^{0}\ surf)}}{c_{Zn^{0}(bulk)}}\exp\left(\frac{(1-\beta)F}{RT}\eta\right)\right] \quad (\text{Plating}) \qquad \text{(Eq. 5.10)}$$

where j is the local current density during Zn plating and j_0 is the exchange current density of Zn plating. β is the symmetry factor, and η is the overpotential of the electrode. It can be found from this equation that when j_0 decreases, the current density of galvanizing will also decrease.

In order to further verify the mechanical suppression effect of the DNGF on the formation of Zn dendrites, a potentiostatic Zn plating test was conducted. As shown in **Figure 5.12(a)**, when the plating potential was set as -1.05 V vs. Ag/AgCl, the corresponding current profile showed two stages during the plating process. In the first stage, the current density of Zn plating gradually increased to ~ 3 mA cm^{-2}. Then, at about 890 min, the current density of Zn plating began to decrease. This plating time was considered sufficient for the $c_{(Zn^{2+})}$ in the cell to achieve equilibrium. Therefore, the decrease in current density is attributed to the decrease in j_0. The

decrease in j_0 should come from the chemical potential reduction of the Zn plating reaction because the expanded Zn crystals would induce better contact with the GPE framework during Zn deposition. As a comparison, the Zn || Zn cell without separator (**Figure 5.12(a)**, red line) showed a continuous increase in plating current density. After 490 min, the no-separator cell finally encountered a short circuit due to the unstoppable dendrite growth. Experiments under different plating potentials were employed to confirm the hypothesis. In the DNGF GPE-separated cells, when the capacity of Zn plating exceeded 30 mAh cm^{-2}, the current density decreased, indicating that the mechanical suppression effect existed during Zn plating. Since the plating/stripping capacity was very high, the Zn foil on the stripping side inevitably underwent a huge morphological change (**Figure 5.12(b)**). When the Zn electrode was stripped to such a condition, the open circuit voltage (OCV) of the cell in a two-electrode cell is generally several hundred milli-volts. Obviously, it is impossible to realize a potentiostatic Zn plating test in a two-electrode cell. Utilizing the three-electrode semi-solid-state cell ensured voltage stability during the tests (**Figure 5.12(c)**). The observation of the topography of the electrodes further confirmed the hypothesis. As shown in **Figure 5.13(a)**, the Zn electrode, after the potentiostatic plating at -1.13 V vs. Ag/AgCl, exhibited a flat Zn coating with a thickness of about 200 μm. The Zn coating consisted of spherical crystals instead of dendritic crystals (**Figure 5.13(b)**). The thickness of the Zn coating in the cases lasting at -1.05 V and -1.21 V was 110 μm and 240 μm, respectively (**Figure 5.13(e-h)**). The loose and thick Zn coating indicates that the deposition voltage of -1.21 V was too high, resulting in Zn crystals that could break the gel framework. The top-view of the Zn electrode indicated that most of the spherical crystals would merge to form a larger crystal aggregate structure with a flat surface (**Figure 5.13(c, d)**). Optical photos of the as-tested samples provided intuitive information on the Zn plating.

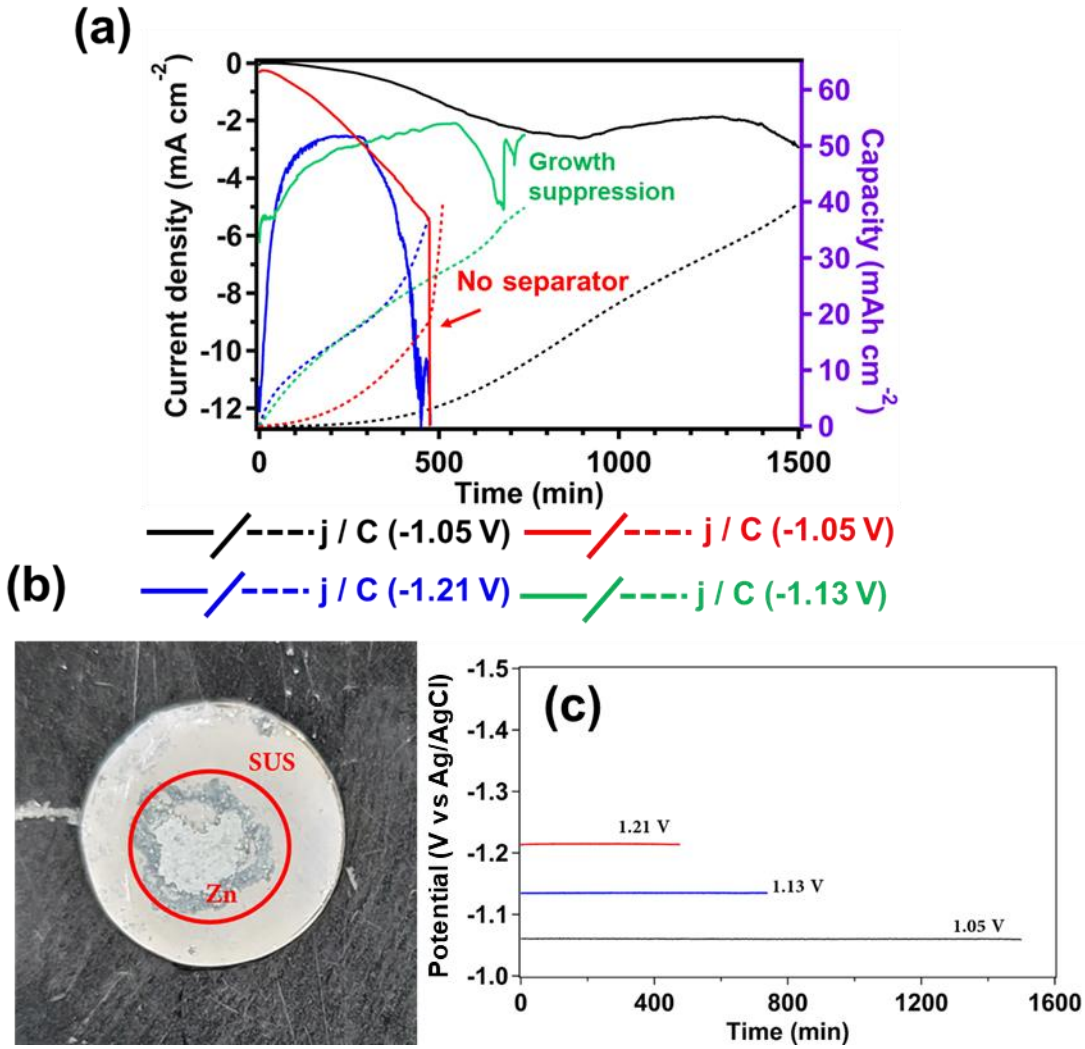

Figure 5.12 (a) Potentiostatic electrodeposition behavior of Zn under different conditions, the current profiles of Zn deposition using DNGF at a constant voltage of -1.05 V (solid black line), -1.13 V (solid green line), and -1.21 V (solid blue line) vs. Ag/AgCl. The solid red line refers to the no-separator cell, and the dotted lines are the corresponding capacity profiles. (b) Optical photo of the Zn electrode on the stripping side in the potentiostatic Zn deposition test. The substrate is a stainless-steel case (SUS316). (c) Voltage profiles corresponding to the potentiostatic Zn deposition tests.

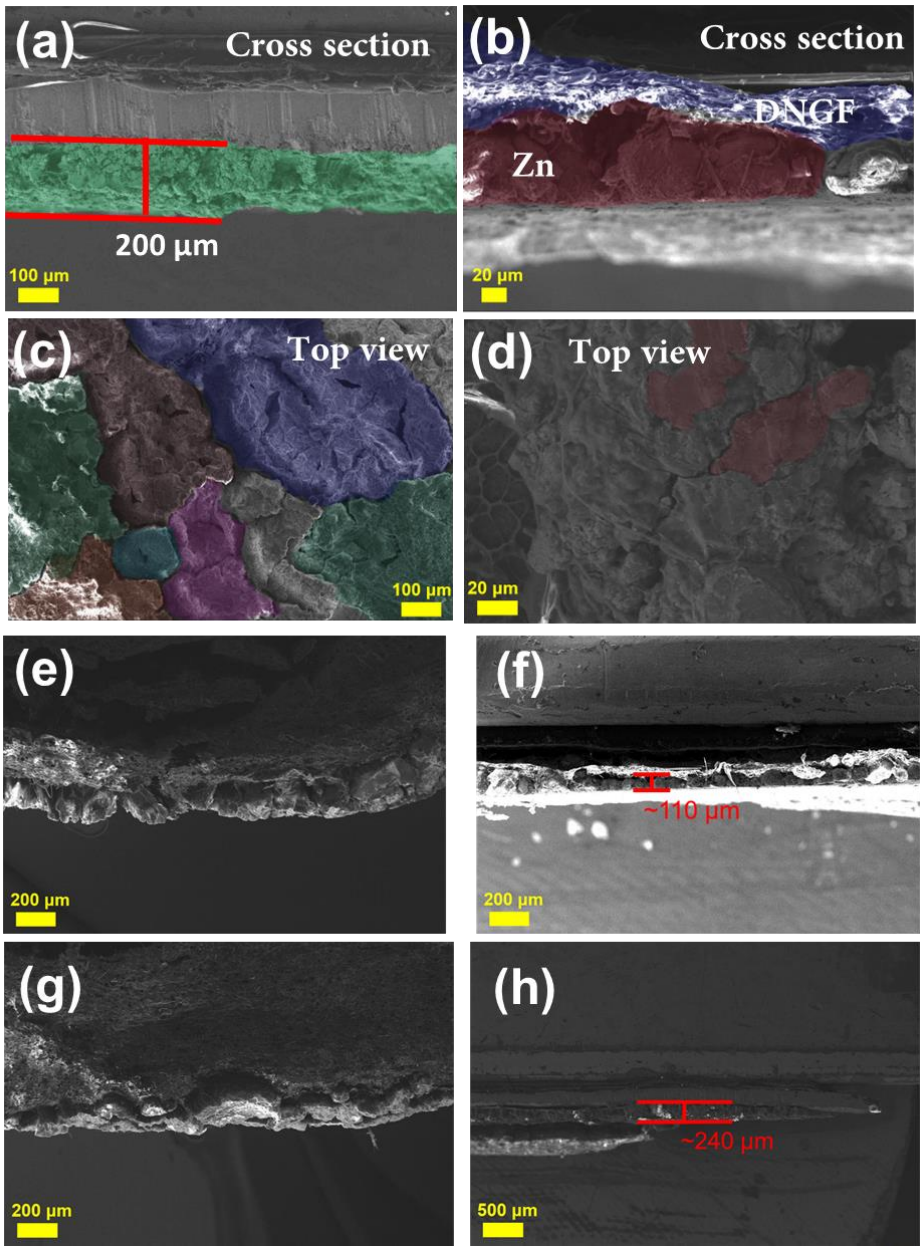

Figure 5.13 (a,b) Cross-sectional and (c,d) top-view SEM images of the Zn electrodes after Zn deposition at a constant voltage of -1.13 V vs. Ag/AgCl. (e,f) Cross-sectional SEM images of the Zn electrodes after Zn deposition at a constant voltage of -1.05 V vs. Ag/AgCl. (g,h) Cross-sectional SEM images of the Zn electrodes after Zn deposition at a constant voltage of -1.21 V vs. Ag/AgCl.

As shown in **Figure 5.14(a)**, the Zn disk electrode that used DNGF as a separator had a uniform Zn coating on its surface, while the one without a separator had several large Zn dendrites on its surface. Some Zn crystals grew into the gel matrix and were retained on the surface of the DNGF, which further confirmed the statement that the electrodeposited Zn crystals were in good contact with the GPE. Atomic force microscopy (AFM) was further used to detect the morphology of the newly deposited Zn crystals on the two electrodes shown in **Figure 5.14(b)**. Dynamic force mode (DFM) was employed to measure the topography. As shown in **Figure 5.14(c)**, in the case of the DNGF-separated cell, the newly deposited Zn crystal had a flat top surface with a global height difference of less than 40 nm. As a comparison, in the case of the no separator cell, the top surface is rough, and Zn flakes with a side length of around 0.5 μm were observed. At this point, sufficient evidence is available to support the hypothesis that the growth of Zn dendrites can be inhibited by the mechanical suppression effect by utilizing GPEs.

The mechanical suppression mechanism is discussed in **Figure 5.15**. As depicted in the left part of **Figure 5.15**, once the newly formed Zn nuclei appear on the substrate, Zn will grow along the preferential crystal orientation. Caused by the uneven distribution of the Zn^{2+} flux, the Zn crystals will grow in increasingly sharp peaks, which further induces dendritic growth. Unlike the free-growth mode, when a GPE framework is pressed onto the Zn plate, the Zn nuclei first deposit into the pores of the GPE framework and gradually ripen until achieving a size that can contact the polymer framework. Afterward, the further growth of Zn crystals applies strain to the GPE framework so that the further growth of Zn crystals will experience higher stress from the GPE. Once the height of the Zn crystals reaches a level where the external stress is high enough to stop the Zn plating reaction, the upward growth tendency of the Zn crystals becomes suppressed. Subsequently, the as-formed Zn crystals will grow parallel to the surface, causing the individual spherical crystals to gather together to form a flat Zn coating layer. The mechanical suppression shown here is slightly different from the well-known mechanical suppression effect from solid-state electrolytes; the latter uses hard-enough materials (e.g., ceramics) to completely prevent the upward growth of metals. Thus, a controllable metal deposition can be achieved. Since the mechanical suppression reported by the uniformizes Zn deposition by reducing the upward

growth tendency, it can be called the mechanical suppression observed in the experiments "the modified mechanical suppression effect". The effective suppression of Zn dendrites growth can be achieved through the modified mechanical suppression effect.

To theoretically illustrate the modified mechanical suppression effect, we can gain insight from the modified Butler-Volmer equation:

$$j=j_0 \exp[\frac{(\beta_m - \beta)\Omega\sigma_{h,surf}}{RT}][\exp(\frac{(1-\beta)F\eta}{RT}) - \exp(\frac{(-\beta)F\eta}{RT})] \quad \text{(Eq. 5.11)}$$

where β_m is the mechanical cathodic symmetry factor, $\sigma_{h,surf}$ is the hydrostatic pressure on the interface and Ω is the partial molar volume[225-226]. Including mechanical stress in the Butler-Volmer equation brings two effects: rescaling the exchange current density and the shift of the equilibrium potential. Increasing external stress results in the suppression of irregular Zn plating reactions. Moreover, the external stress helps to stop the unstable Zn ion transportation.[227-228] Hence, stable deposition can be achieved with the presence of mechanical restriction, which has also been confirmed by the direct observation of the Zn electrodes. It is worth mentioning that the intensity in the [002] direction did not increase after Zn plating in the in-plane XRD pattern of the Zn electrodes after the potentiostatic plating test (**Figure 5.16**). The electroplated Zn was still polycrystalline.

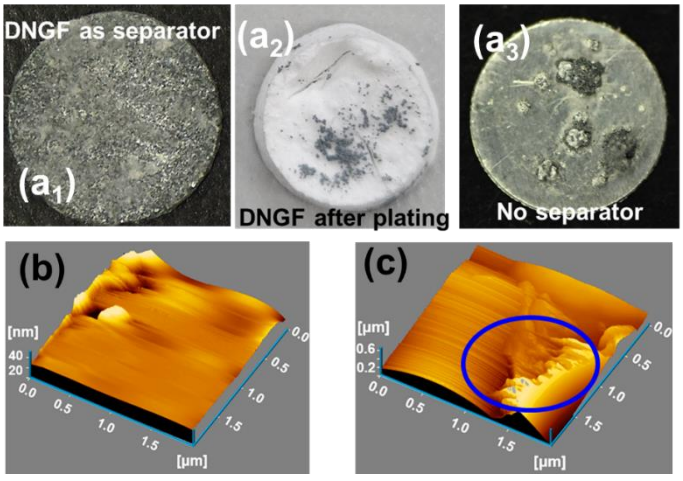

Figure 5.14 Optical photos of the (a_1) Zn electrode (left) and (a_2) DNGF (mid) after Zn deposition at a constant voltage of -1.13 V vs. Ag/AgCl, and (a_3) is the Zn electrode in the cell without a separator. AFM detection of (b) the Zn electrode after Zn deposition at a constant voltage of -1.13 V vs. Ag/AgCl and (c) the Zn electrode in the no-separator cell.

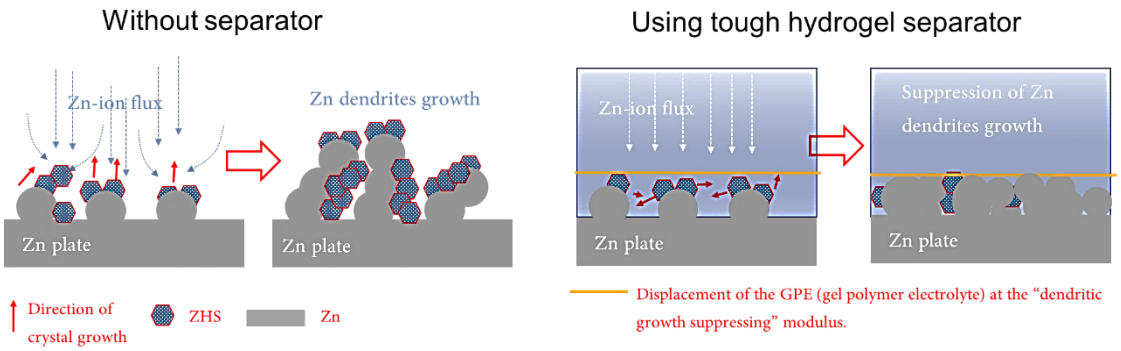

Figure 5.15 Schematic illustration for explaining the modified mechanical suppression behavior.

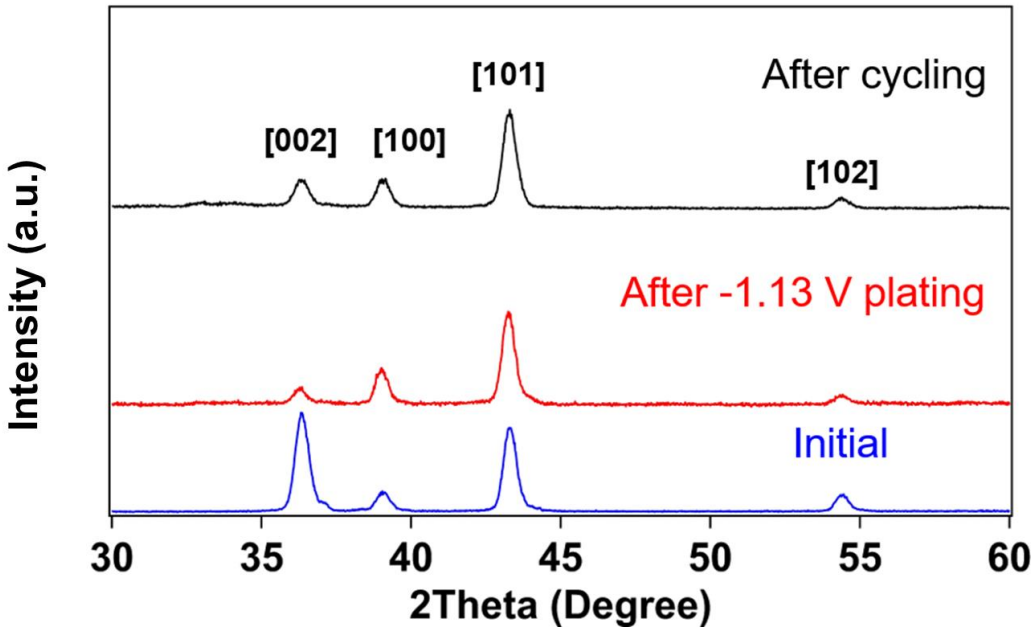

Figure 5.16 In-plane XRD pattern of Zn electrodes before treatment (blue), after potentiostatic (red) and after 1000 cycle (5 mA cm^{-2}, 2.5 mA h cm^{-2}).

An attempt was made to visualize the stress-affected Zn plating procedure using a Zn plating multi-field simulation based on the Butler-Volmer equation. **Figure 5.17(a)** shows the case when the initial nuclei distribution is uneven, in which Zn deposition is not subject to external mechanical stress, namely, the free deposition mode. In this case, based on the mechanism of Zn dendritic growth and the observed Zn electrode as mentioned above (**Figure 5.14(a)**), it can be assumed that the deposition of Zn only occurs on the as-deposited spherical Zn nuclei. Here, the final height of the Zn coating is around 40 μm, and the observed overpotential during Zn plating is -30 mV (at a current density of 1 mA cm^{-2}). Slightly different from **Figure 5.17(a)**, in **Figure 5.17(b)**, the initial distribution of Zn nuclei is more uniform, while the spherical Zn crystals are smaller than those in **Figure 5.17(a)**. The uniform initial distribution of Zn nuclei leads to a relatively low Zn coating thickness, around 34 μm. When the exchange current density is decreased to 5.72 A m^{-2} as obtained by linear sweep voltammetry (LSV) tests (**Figure 5.18(a, b)**), uniform deposition of Zn could be achieved (**Figure 5.17(c)**). The intense change of current at high voltage is ascribed to the fact that the concentration field inside the cell is difficult to achieve equilibrium (**Figure 5.18(c)**). The recorded plating overpotential calculated by the Butler-Volmer equation is 80 mV, consistent with the data obtained in **Figure 5.11(e)**. More specifically, the $c_{(Zn2+)}$ gradients near the electrode surface and across the whole cell are almost imperceivable (**Figure 5.17(a-c)**, right side) because of the ultra-high ionic conductivity of the 2 mol L^{-1} $ZnSO_4$ aqueous electrolyte. The rapid transportation of Zn^{2+} can eliminate the concentration gradient, facilitate the uniform deposition of Zn, and help the formation of spherical Zn crystals. This phenomenon is consistent with the previous observations. Geometric modeling of the Zn plating simulation can be found in **Figure 5.2**.

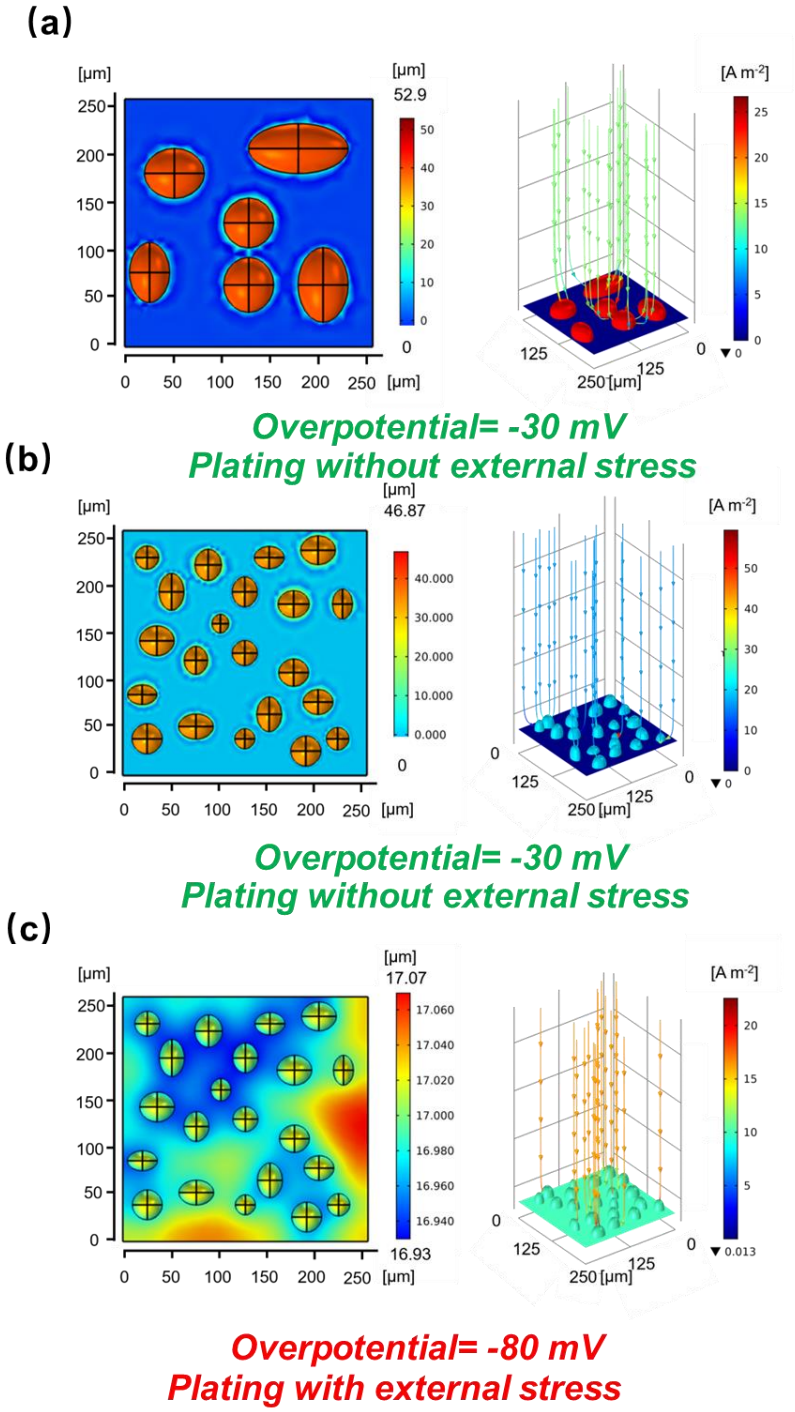

Figure 5.17 Simulated results of the thickness change during Zn plating under different conditions. (a,b) Growth of Zn during galvanostatic plating in a no-separator cell (left), and the corresponding current field is shown on the right side. (c) Growth of Zn during galvanostatic plating in a cell with DNGF separator (left), and the corresponding current field is shown on the right side.

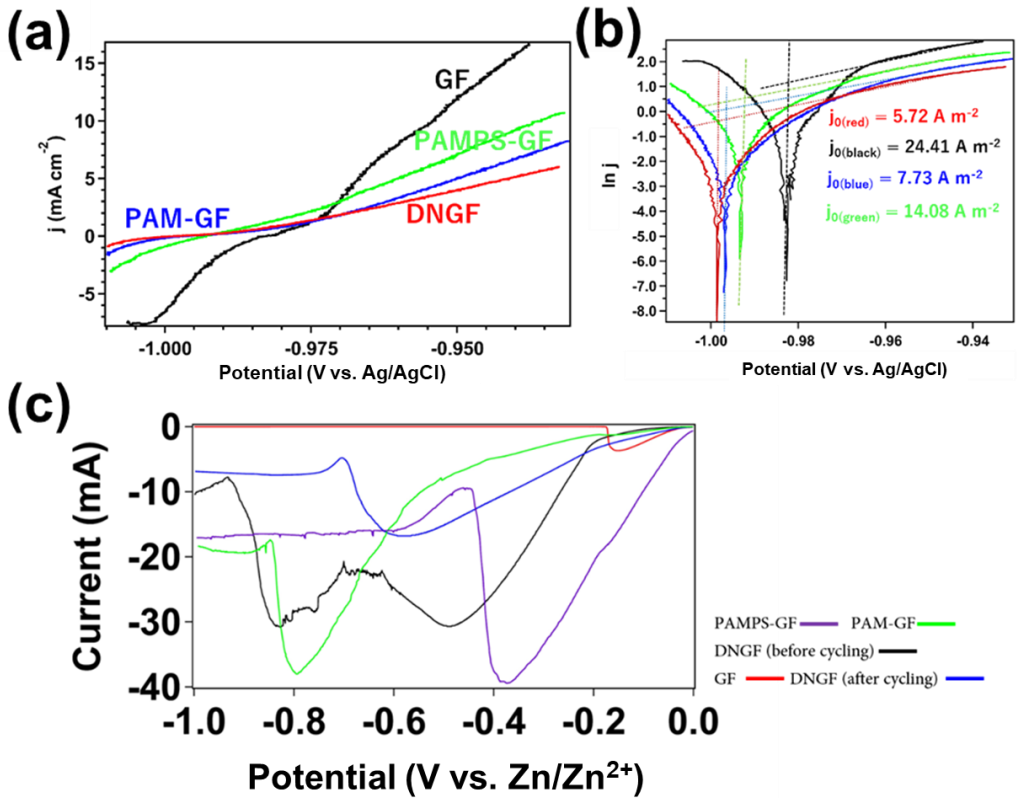

Figure 5.18 (a) Linear sweep voltammetry (LSV) of Zn || Zn symmetric cells with different separators (tested in the three-electrode Swagelok cell). The voltage range is -1.01 V to -0.93 V (vs Ag/AgCl) and the scan rate is 1 mV s^{-1}. (b) The Tafel plots that correspond to the LSV tests. The exchange current density is obtained by assuming the anodic transfer coefficient α_a (in the Butler-Volmer equation) is equal to the cathodic transfer coefficient α_c. (c) Linear sweep voltammetry (LSV) of Zn || Zn symmetric cells with different separators. The voltage range is -1V to 0 V (vs Zn/Zn^{2+}), the scan rate is 1 mV s^{-1}.

The Zn plating behavior under the GPE is illustrated in **Figure 5.19**. In agreement with the previous description, the upward growth tendency is suppressed by physical contact, and the deposition of Zn will finally evolve into a flat coating with a mechanically strong GPE. At this point, it is possible to alleviate Zn dendrite growth through the modified mechanical suppression effect with a separator that possesses a shear modulus less than 1.8 times that of the corresponding metal. Considering the thickness of the separator, the actual required modulus of the separator

may be much smaller than this value. It is possible to limit the growth of Zn dendrites by designing a polymer separator/electrolyte with proper mechanical strength.

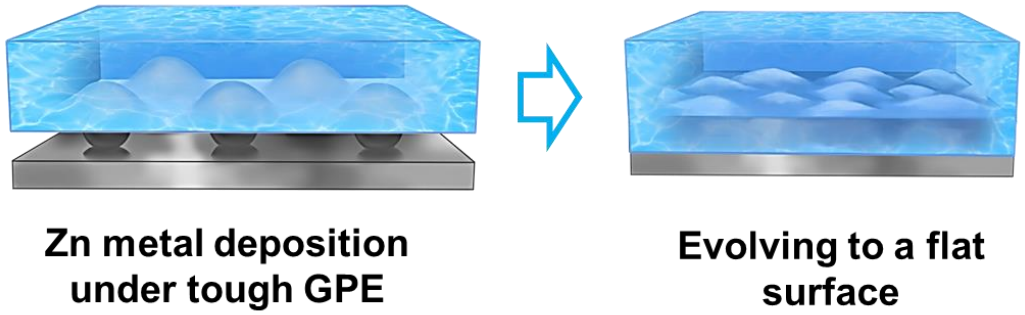

Figure 5.19 Schematic illustration of Zn growth behavior under the high-strength hydrogel electrolyte.

5.3.3 Cyclic Zn plating/stripping performance of Zn || Zn symmetric cells.

Based on the understanding that DNGF can suppress the growth of Zn dendrites, and to detect the cyclic stability of the DNGF GPE and confirm the unique superiority of DNGF among various GPEs, Zn || Zn symmetric cells separated by different GPEs were assembled. As shown in **Figure 5.20(a)**, Zn || Zn symmetric cells were tested at a constant current density of 1 mA cm^{-2} and a restricted areal capacity of 1 mAh cm^{-2}. PAM-GF, PAMPS-GF, and glass fiber were used as control groups. First, the glass fiber separated Zn || Zn symmetric cell short-circuited after 48 cycles. As a reference, the PAM-GF-separated cell could survive for nearly 100 cycles, while the PAMPS-GF-separated cell worked for over 200 cycles. These control groups all short-circuited due to uncontrollable dendrite growth. The DNGF-separated Zn || Zn symmetric cell could easily protect the cell from short-circuit for over 2500 h. The details of the voltage profiles for these Zn || Zn cells are shown in **Figure 5.20 (b)**. During the initial 10-15 cycles, the DNGF-separated cell showed a voltage hysteresis of around 180 mV, while the values for PAM-GF, PAMPS-GF, or GF separated cell were 200 mV, 120 mV, and 165 mV, respectively. The slightly higher overpotential for the DNGF-separated cell indicates a slightly sluggish Zn^{2+} transportation in the DNGF framework. During the following 100-105 cycles, voltage hysteresis for the DNGF-separated cell

increased to about 210 mV and was stable for a long time. This could be attributed to the surface and volume change of the Zn electrodes, namely, the thickening of the Zn electrode. The change in electrode morphology led to contact between Zn and the GPE framework, indicated by the increase in the overpotential. During the 1000-1005 cycles, voltage hysteresis recovered to ~ 170 mV, due to the aggregation of deposited Zn crystals, as the author has already emphasized in the above galvanizing experiments. The SEM observation helps confirm the conclusion, and a flat but polycrystalline surface of the as-cycled Zn electrode is shown in **Figure 5.21(a-f)**. The thickness of the Zn electrode is about 210 μm, and no dendritic crystals were observed. As a comparison, using PAM-GF and PAMPS-GF separators, Zn crystals damaged the GPE framework and produced large dendrites piercing the GPE (**Figure 5.21(h-m)**). Considering that the measuring condition of 1mA cm^{-2} 1mAh cm^{-2} is far from practical application values, the Zn || Zn symmetric cells were also tested under harsher conditions. Even when the current density was increased to 5 mA cm^{-2}, the DNGF-separated Zn || Zn could maintain stable cyclic performance for over 1000 h, while the GF-separated cell only worked for less than 100 h (**Figure 5.22**). In addition to the superior dendrite-suppressing capability of DNGF, the internal energy dissipation mechanism may prevent the gel framework from being destroyed by Zn crystals during repeated Zn electroplating/stripping. This also helps to guarantee the long life-span of the DNGF-separated cells.

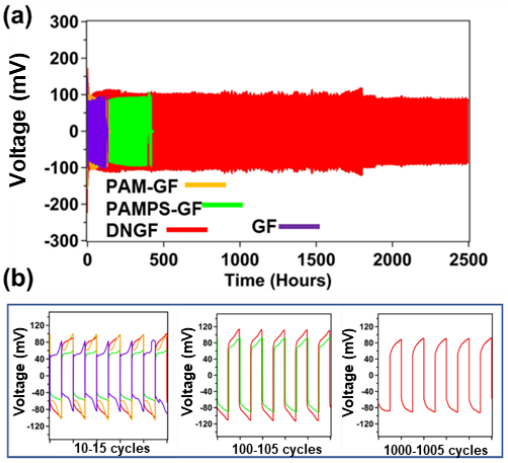

Figure 5.20 (a) Cyclic stability of symmetric cells with different separators. (b) Details of voltage profiles corresponding to symmetric cell tests.

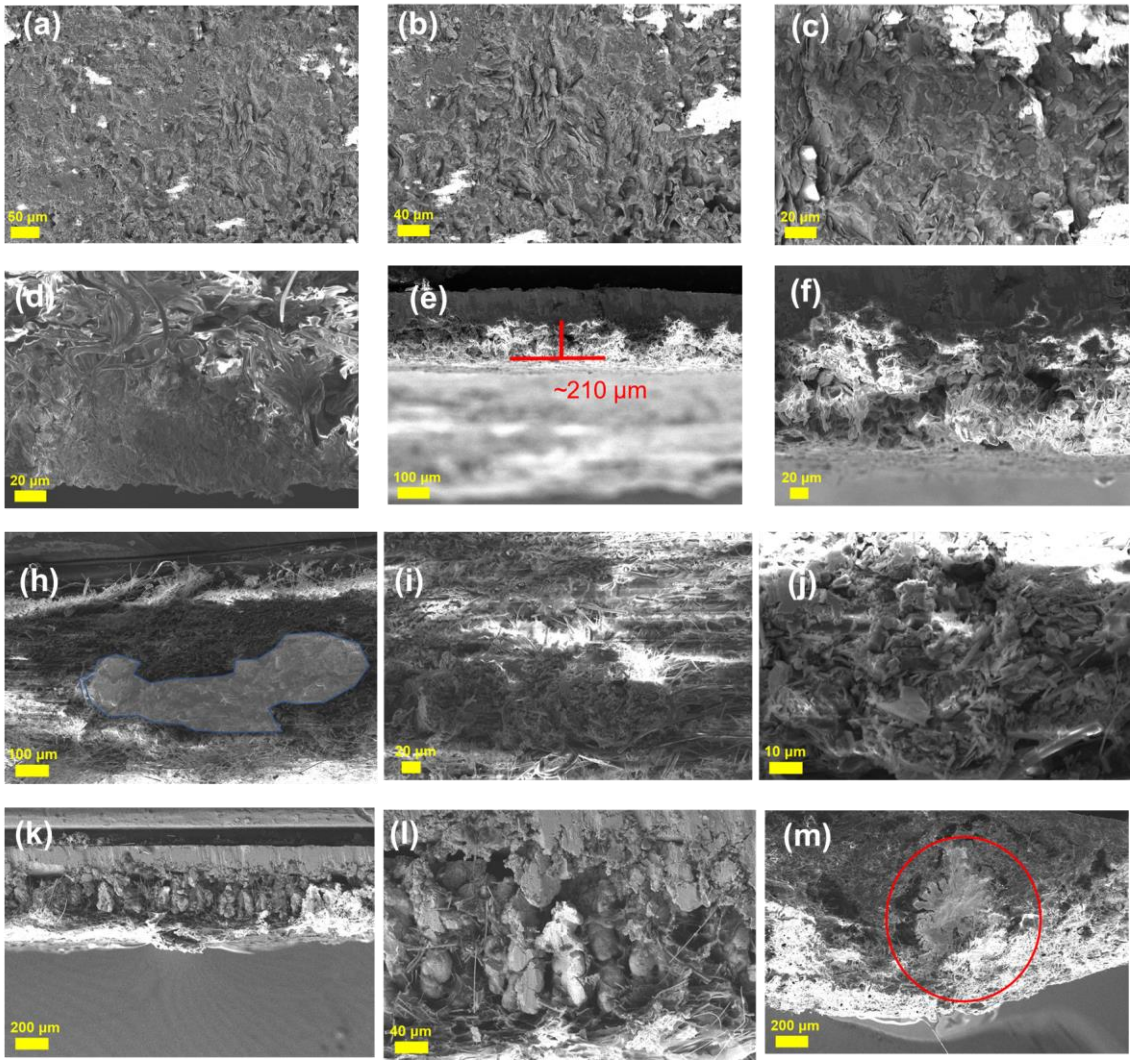

Figure 5.21 (a, b, c) Top view SEM images and (d, e, f) cross-sectional images of the DNGF protected electrodes after cycling. (h, i, j) SEM images of PAMPS-GF after cycling in the symmetric cell (1 mA cm^{-2}, 1 mA h cm^{-2}). The Zn crystal grew inside the PAMPS-GF (marked area), leading to the short-circuit. Cross-sectional observation of (k, l) the Zn electrode, (m) the PAM-GF separator. The Zn crystal grew vertically inside the PAM-GF, finally causing the short-circuit.

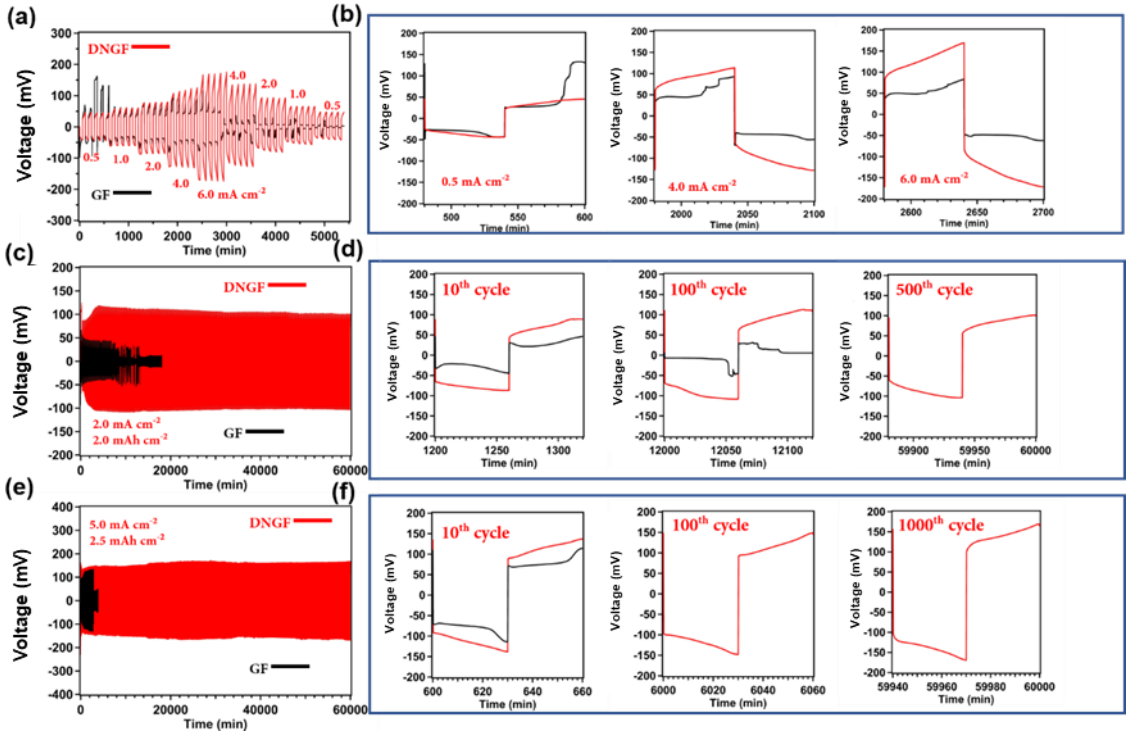

Figure 5.22 Performance of symmetric cells tested at a, b) 0.5 mA cm^{-2} to 6.0 mA cm^{-2}, c, d) 2.0 mA cm^{-2} with a capacity of 2 mA h cm^{-2} and e,f) 5 mA cm^{-2} with a capacity of 2.5 mA h cm^{-2}. Red lines refer to cells that used DNGF as a separator and electrolyte, and black lines refer to cells that used a glass fiber separator. Cells that were separated by DNGF were finally stopped manually in order to make way for other tests.

5.3.4 Full cell test in Zn || MnO_2 battery under low capacity.

Encouraged by the superior Zn plating/stripping stability, full cell tests were conducted using a MnO_2 cathode, which could help us to evaluate further the potential of the DNGF-protected Zn metal anode for RAZIB applications. MnO_2 cathodes are considered excellent candidates for developing high energy density RAZIBs, due to their high theoretical capacity (308 mAh g^{-1} considering the 1 e^- transfers from Mn (IV) to Mn (III)) and high reduction potential.[189, 229-231] In most reports, to avoid the cathode architecture's influence, Zn || MnO_2 cells have generally been tested by using MnO_2 cathodes with an areal mass loading of less than 2 mg cm^{-2}.[192, 232] Hence, the Zn || MnO_2 cells were tested first in such a condition. As shown in **Figure 5.23(a)**, the DNGF-separated Zn || MnO_2 cell achieved an initial capacity of 161 mAh g^{-1} at a charge/discharge rate

of 10 C (1C = 308 mA g^{-1}) and a capacity retention of 50% after 9500 cycles. At the same time, the GF-separated cell unsurprisingly short-circuited in the end. **Figure 5.23(b)** highlights the changes in voltage profiles during cycling. It is clear that the discharging voltage plateau at around 1.35 V (vs. Zn/Zn^{2+}) gradually disappeared with increasing cycling. This phenomenon is a signal of decreasing particle-size, namely, the dissolution of MnO_2. [233] The dissolution and deposition of MnO_2 make the energy storage mechanism of the Zn || MnO_2 cell gradually change from a "battery" to a "pseudo-capacitor". [233-236] By employing the model developed by Dunn and co-workers, the author distinguished the quantitative capacitive contribution to the current response by CV tests. [206] As shown in **Figure 5.23(c)**, the capacitive contribution of the DNGF-separated Zn || MnO_2 cell before cycling was 64.1% at a scan rate of 2 mV s^{-1}, and this value was increased to 91.0% after 9500 cycles. When the scan rate was increased to 5 mV s^{-1}, the capacitive contribution became more significant, which agreed with the conclusion. CV tests for the DNGF-separated Zn || MnO_2 cell before cycling are shown in **Figure 5.24(a)**. The oxidation peaks shifted from 1.6 V to 1.75 V, indicating that the oxidation of Mn species during charging could be processed normally when the cut-off voltage is set as 1.8 V. Moreover, the simulated capacitive current shows two oxidation peaks in **Figure 5.24(b)**, indicating that the oxidation peaks that observed in the CV tests might come from two different reactions. This phenomenon was also observed for the GF-separated Zn || MnO_2 cell (**Figure 5.24(c, d)**). Benefiting from the decreasing particle size, the oxidation peaks shifted to the left after cycling (**Figure 5.24(e)**), proving that the capacity decay for the DNGF-separated Zn || MnO_2 cell is not caused by the increase in cell resistance. When comparing **Figure 5.24(b)** and **Figure 5.24(f)**, the current of the first oxidation peak decreased while the second oxidation increased after cycling, demonstrating the existence of changes to MnO_2 during cycling. All of this evidence points to a conclusion: some amount of MnO_2 undergoes a dissolution-deposition mechanism during charging/discharging, and as cycling progresses, the cathode becomes more and more like a pseudo-capacitor rather than a battery under high current density.[235, 237-239]

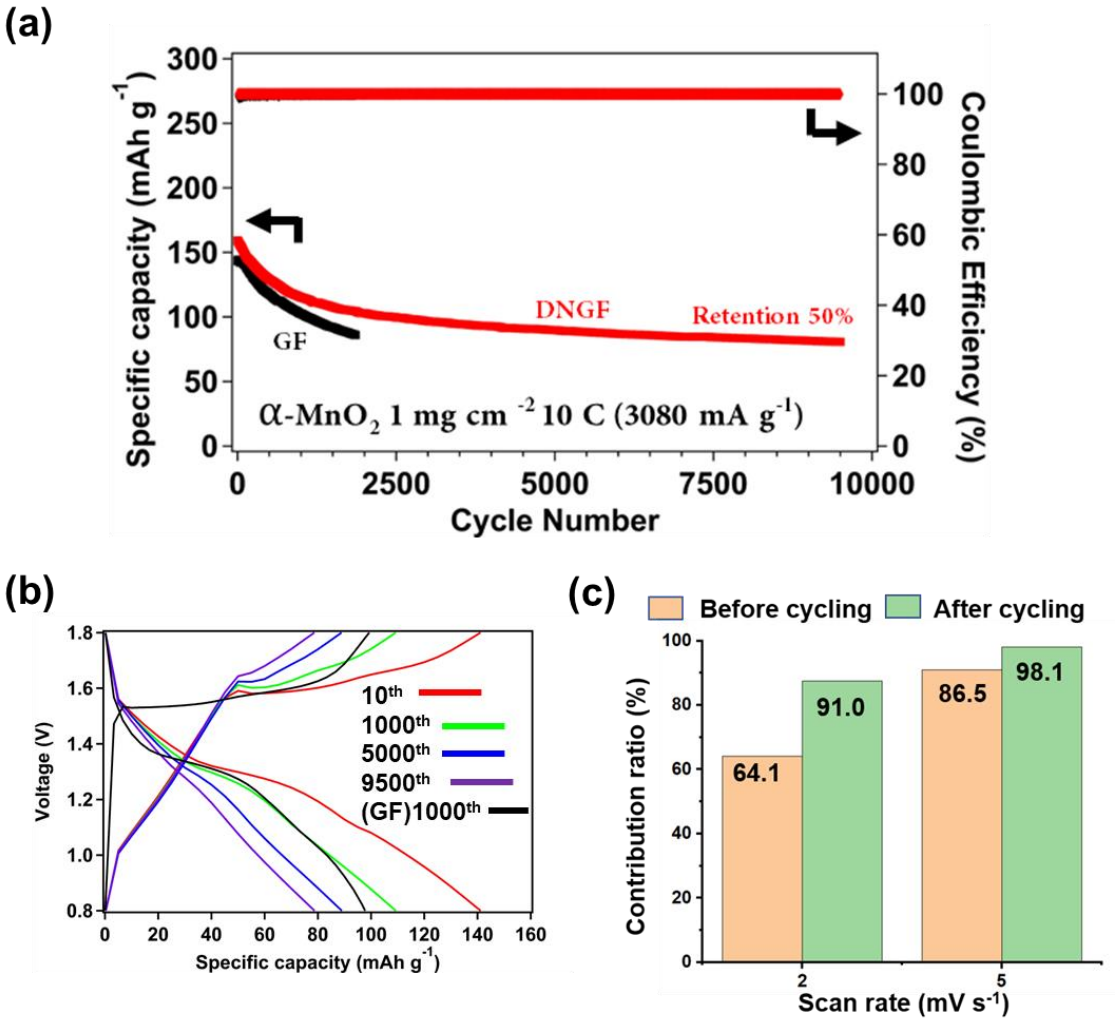

Figure 5.23 (a) Zn || MnO_2 battery performance under low areal capacity. (b) Zn || MnO_2 battery voltage profiles at the 10^{th} (red), 1000^{th} (green), 5000^{th} (blue), and 9500^{th} (purple) cycle using DNGF as a separator. The black line is the voltage profile of the Zn-MnO_2 battery at the 1000^{th} cycle in a Zn || MnO_2 battery using glass fiber as the separator. (c) Normalized capacitive contribution ratio of the DNGF separated Zn || MnO_2 battery at different scan rates.

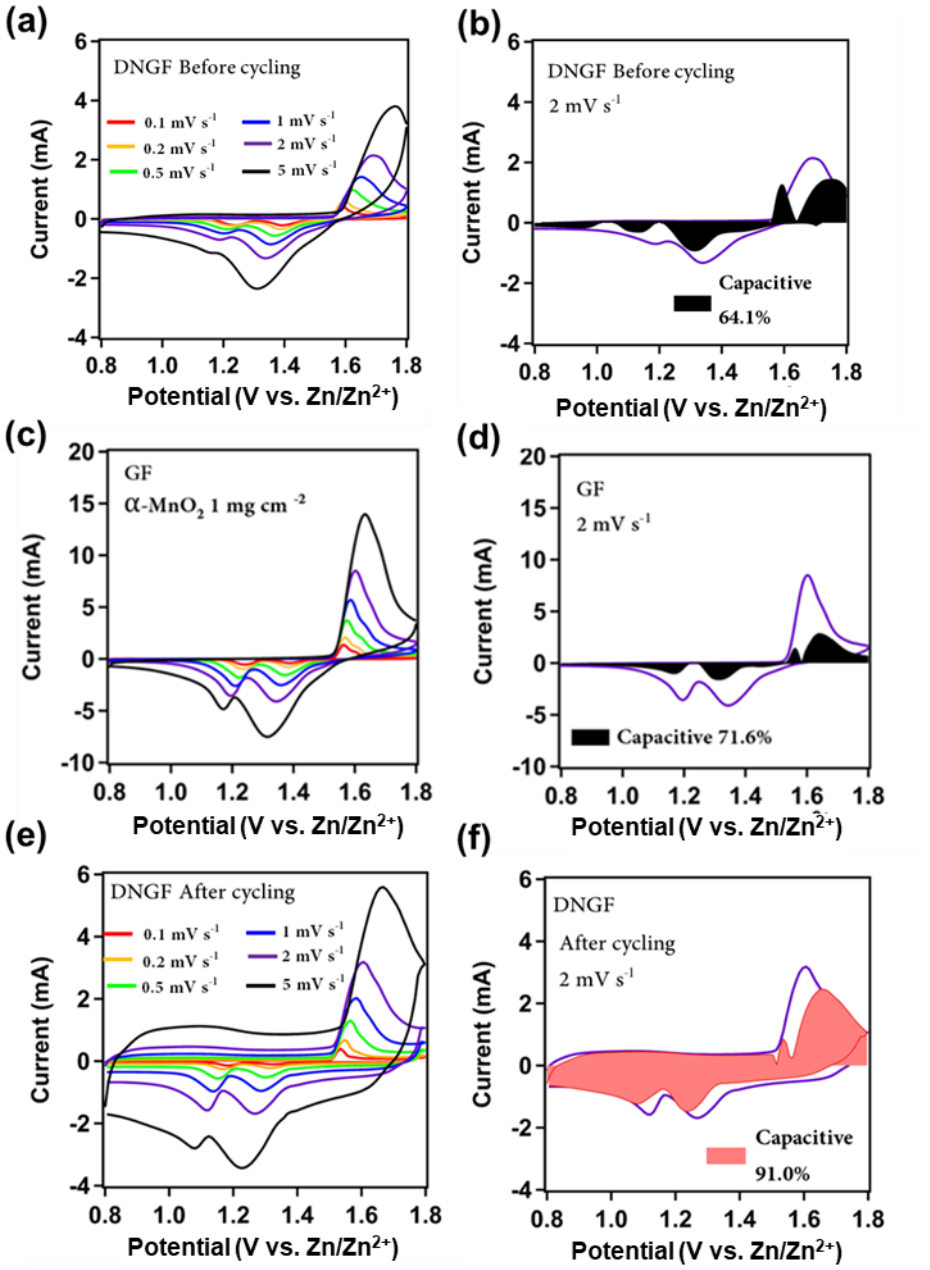

Figure 5.24 (a) CV curves of the DNGF separated Zn || MnO_2 battery before cycling. (b) Capacitive contribution of the DNGF separated Zn || MnO_2 battery to the total charge storage at 2 mV s^{-1} before cycling. (c) Cyclic voltammetry of the low-capacity Zn || MnO_2 battery using glass fiber as a separator. b) Capacitive contribution of glass fiber separated Zn || MnO_2 battery to the total charge storage at 2 mV s^{-1}. (h) CV curves of the DNGF separated Zn || MnO_2 battery after cycling. (i) Capacitive contribution of the DNGF separated Zn || MnO_2 battery to the total charge storage at 2 mV s^{-1} after cycling.

Consequently, the Zn || MnO_2 cell can readily achieve excellent cyclic performance at high charge/discharge rates, as demonstrated before. Obviously, it should be noted carefully that the cyclic performance of the Zn || MnO_2 batteries in this case cannot represent the practical performance of the studied Zn || MnO_2 batteries. Moreover, the author also assembled Zn || MnO_2 cells with different kinds of MnO_2 and various MnO_2 loadings. The observed capacity of the DNGF- separated Zn || MnO_2 cell is generally lower than the GF-separated Zn || MnO_2 cell due to the sluggish ion transport (**Figure 5.25**), but considering that all of the GF-separated Zn || MnO_2 cells ultimately short-circuited, GF is not a suitable material for separating RAZIBs.

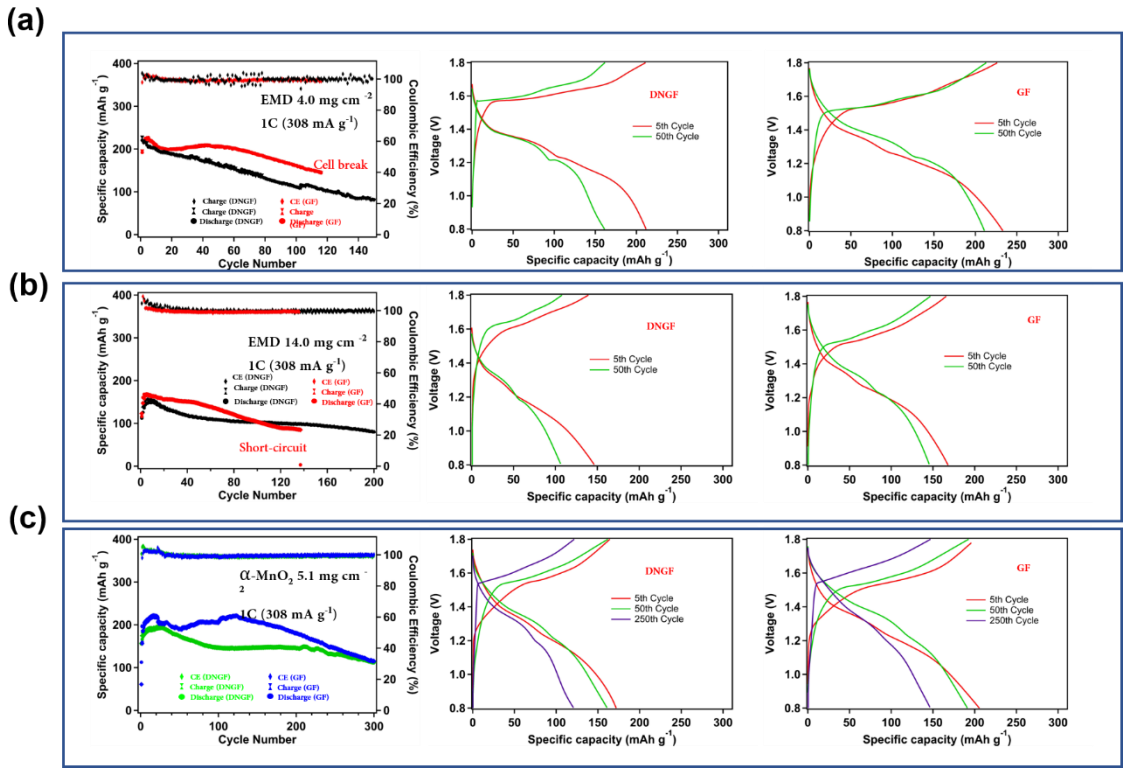

Figure 5.25 Charge/discharge performance of Zn || MnO_2 batteries using (a, b) commercial electrolytic manganese dioxide (EMD) and (c) α-MnO_2 cathode. Here, the left figure is cyclic performance of the batteries, where red points stand for batteries that used glass fiber as separator and black points stand for batteries that used DNGF.

5.3.5 Full cell test of Zn || MnO_2 batteries under high-capacity.

In order to provide valid information for developing RAZIBs with high energy density, high-capacity Zn || MnO_2 cells were assembled by using MnO_2 cathodes with ultra-high areal capacity. This is required because the cathode capacity, equivalent to the anode value, is necessary for the battery to achieve a high energy density. As shown in **Figure 5.26**, the MnO_2 cathode with an MnO_2 mass loading of 30 mg cm^{-2} (theoretical areal capacity: 9.2 mAh cm^{-2}) was prepared and referred to as the high-capacity MnO_2 cathode (HCM cathode). The HCM cathodes were used in Zn || MnO_2 cells that were separated by DNGF or GF. As shown in **Figure 5.27**, the specific capacity of the DNGF-separated high-capacity Zn || MnO_2 cell decreased rapidly with increasing charge/discharge rate. The discharge capacities at 0.1 C and 0.3 C were 290 mAh g^{-1} and 180 mAh g^{-1}. When the discharge rate was increased to 1 C, the Zn || MnO_2 cell with DNGF showed an initial capacity of 160 mAh g^{-1}. Then the capacity gradually decreased to 60 mAh g^{-1} with cycling (**Figure 5.28(a)**). No short-circuit was observed for the DNGF-separated Zn || MnO_2 cell, while the GF-separated cell was short-circuited after just 29 cycles. This implies that the most significant issue in RAZIBs, dendrite growth, can be solved by using a DNGF GPE. Voltage profiles at the 5th cycle, 50th cycle, 250th cycle, and 500th cycle maintained clear discharge plateaus at around 1.2 V, indicating that the Zn || MnO_2 cell was still a “battery” during cycling (**Figure 5.28(b)**). This phenomenon implies that the reason for capacity decay of the high-capacity cell may be different from the low-capacity one. A galvanostatic intermittent titration technique (GITT) was conducted to detect the reason for the capacity decay. By adding rest intervals to separate the discharge processes, ions have enough diffusion time to alleviate mass transfer resistance during the GITT test.[240] **Figure 5.29** shows the discharge behavior of the Zn || MnO_2 cell after 500 cycles. It can be clearly seen that the capacity of the cell had returned to 160 mAh g^{-1} during the GITT test, so the capacity difference between the GITT cycle and the normal cycle of the as-cycled HCM electrode is about 100 mAh g^{-1}.

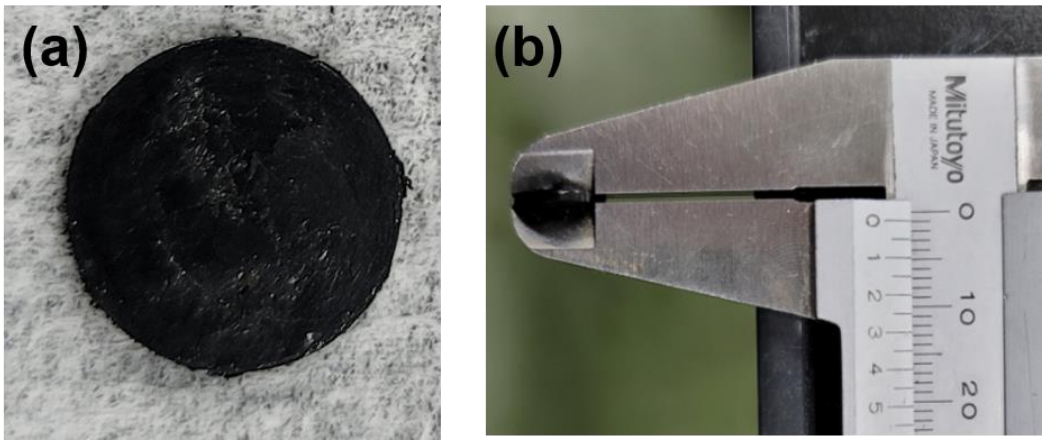

Figure 5.26 (a, b) Optical photos of the high-capacity MnO_2 cathode. Thickness of the cathode is around 1 mm.

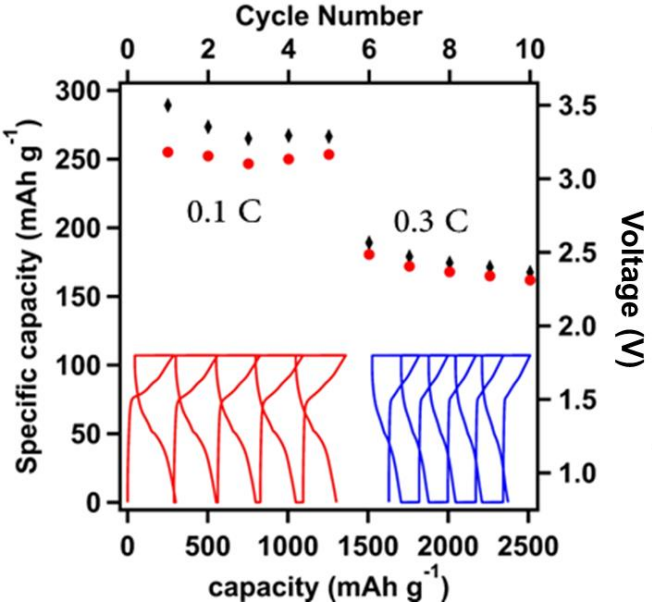

Figure 5.27 Low-rate performance of DNGF separated Zn || MnO_2 batteries, and the voltage profiles are inset within the figure.

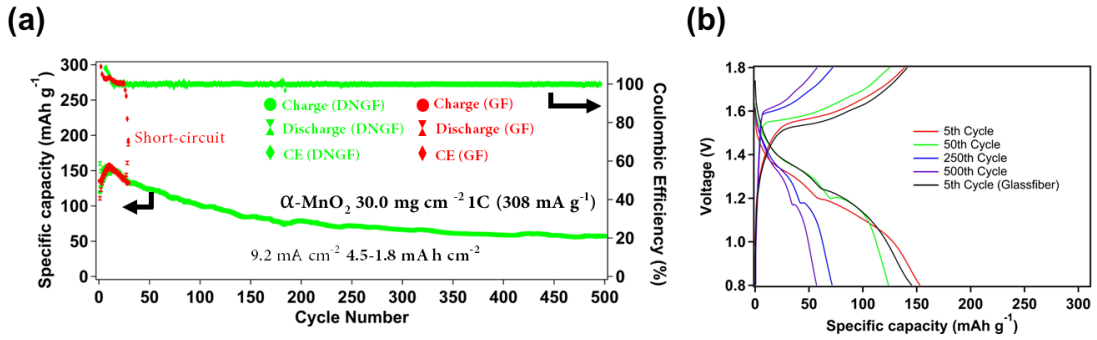

Figure 5.28 (a) Cyclic stability of high-mass loaded Zn || MnO_2 batteries at charge/discharge rate of 1 C. (b) Voltage profiles of the Zn || MnO_2 battery at the 5th (red), 50th (green), 250th (blue), and 500th (purple) cycle using DNGF as a separator. The black line is the voltage profile of the Zn || MnO_2 battery at the 5th cycle in a cell using glass fiber as a separator.

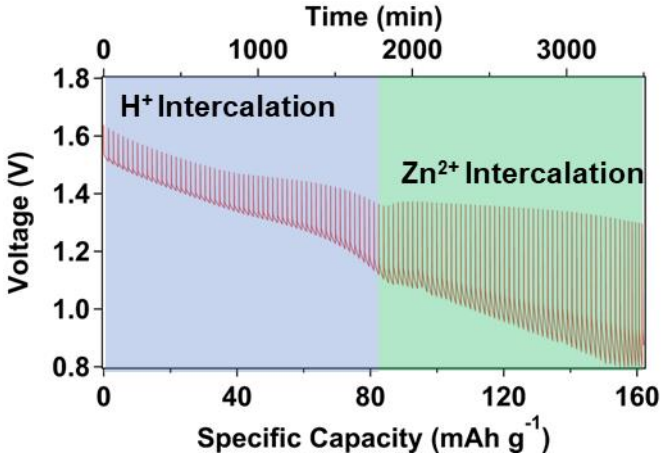

Figure 5.29 GITT measurement of the DNGF separated Zn || MnO_2 battery.

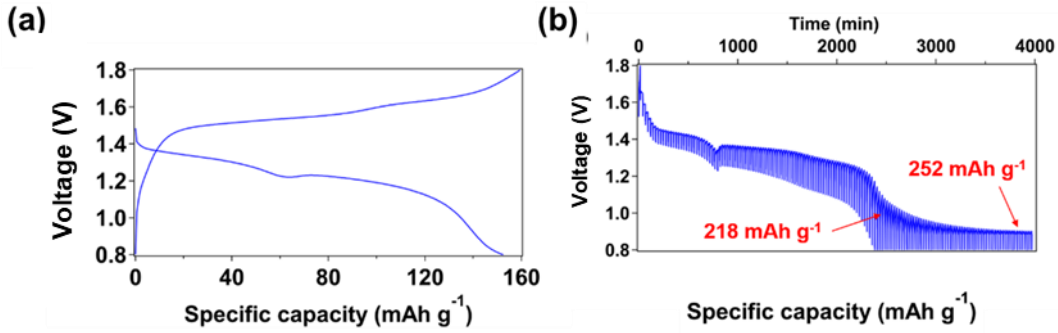

Figure 5.30 (a) Voltage profile of an additionally prepared Zn||MnO_2 cell with HCM cathode at 4th cycle. (b) GITT result of the Zn||MnO_2 cell after 4 cycles.

As a comparison, the newly prepared HCM electrode, which showed a discharge capacity of around 252 mAh g^{-1} during the GITT cycle, also exhibited the difference in capacity between the direct galvanostatic charge/discharge mode and the GITT mode is about 100 mAh g^{-1}. **(Figure 5.30(a, b))** These two close values indicate that the HCM electrode has undergone an irreversible loss of capacity during the cycle. Therefore, the author believes that the fading in the capacity of the HCM cathode can be attributed to two aspects: 1) α-MnO_2 gradually loses its activity during charging and discharging, which is the main reason for the irreversible capacity; 2) the poor electrode architecture causes the electrolyte inside the electrode to be quickly depleted and cannot be replenished, which in turn causes the electrode reactions can only occur on the surface. This part of the capacity loss can be recovered after the electrolyte is replenished to the inside of the HCM electrode, but when the gel electrolyte is used, or the charge/discharge rate is fast, the discharge capacity will quickly decay due to the high mass transfer resistance caused by poor ion diffusion. Based on the conclusions from Sun et al., we can define two regions in the GITT test related to Zn^{2+} intercalation and H^+ intercalation.[67]

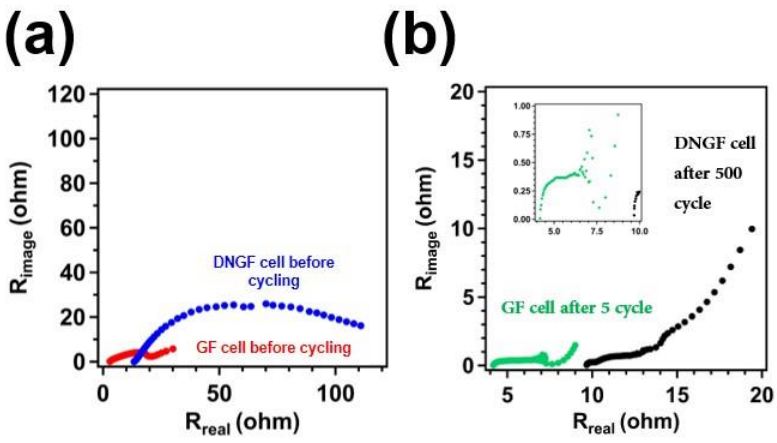

Figure 5.31 Nyquist plot of high-capacity Zn || MnO_2 batteries a) before and b) after cycling.

This is consistent with the results obtained from low-capacity Zn || MnO_2 cells. In GITT, the voltage jump immediately after applying current could be attributed to the ohmic impedance and charge transfer resistance. Therefore, the slow ion diffusion can explain the large overvoltage for the Zn^{2+} intercalation reaction. By comparing the electrochemical impedance spectra (EIS) before and after cycling, it can be found that the charge transfer resistance decreased after cycling while ohmic resistance increased slightly (**Figure 5.31(a, b)**). CV tests confirmed the author's idea from the electrochemical aspect. The oxidation peak at around 1.6 V in **Figure 5.32(a)** gradually disappeared with increasing scan rate. This shows that the huge overvoltage prevented the electrode reactions from proceeding. This phenomenon would become more serious with electrolyte depletion inside the cathode framework as the electrochemical cycling progresses (**Figure 5.32(b)**). The geometrically normalized capacitive contribution ratio of the as-cycled Zn || MnO_2 cell is shown in **Figure 5.32(c)**. The capacitive current ratio of the cell before cycling was only about 27% at low scanning speed, and this value barely changed during cycling, indicating that the high-capacity Zn-MnO_2 cell maintained the same discharge characteristics during low-rate charging/discharging. However, the ratio of the capacitive current increased rapidly as the scanning speed increased. One possible reason for this phenomenon might be the electrode reaction could only proceed on the surface of the cathode when the charge/discharge rate was very high. The electrolyte inside the cathode becomes depleted quickly at a high charge/discharge rate, and thus the further continuation of electrode reactions inside the cathode would be more difficult. However, the electrochemical process of the high-capacity Zn || MnO_2 cell during high-rate charge/discharge is very complicated and nonuniform, which makes it impossible to accurately predict the capacitor/battery characteristics of the material by using Dunn's model. For example, as shown in **Figure 5.32(d, e)** the simulated contribution is unreliable because the simulated capacitive current is higher than the real total current. This phenomenon is likely attributed to the electrode reactions being non-uniform in the high-capacity cathode. In the depths of the cathode, the reaction exhibited a serious hysteresis due to the concentration polarization. This is also the reason why the percentage of the capacitive current observed at a high scan rate exceeded 100%, which is obviously unrealistic.

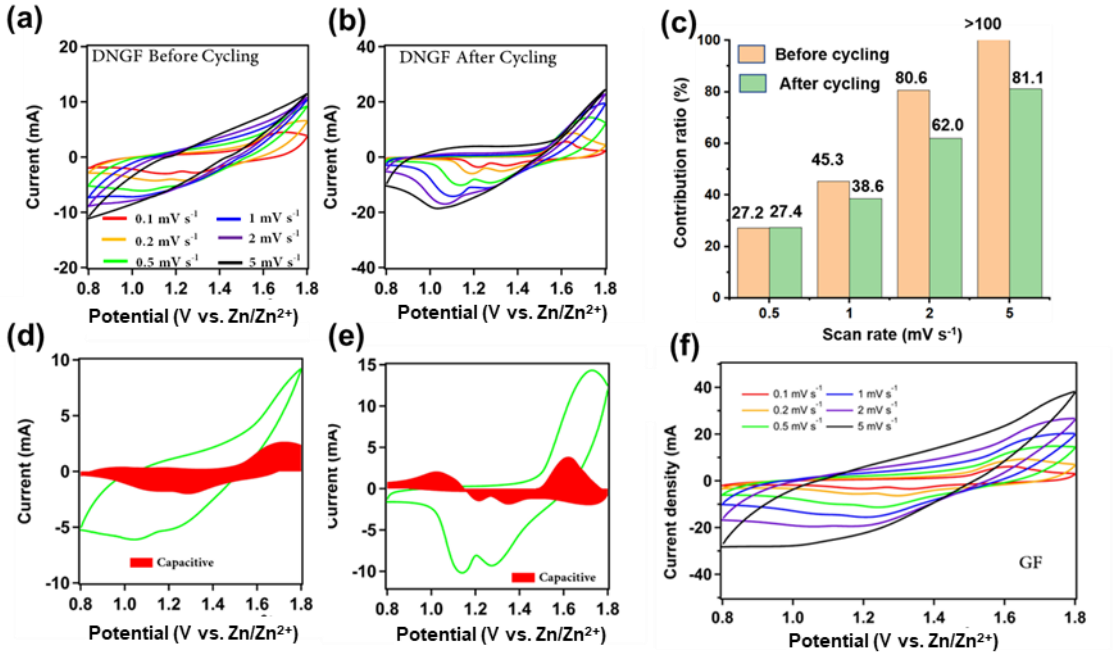

Figure 5.32 CV curves of the DNGF separated Zn || MnO_2 battery (a) before and (b) after cycling. (c) Normalized capacitive contribution ratio of the DNGF separated Zn || MnO_2 batteries at different scan rates. Capacitive contribution of DNGF separated Zn || MnO_2 battery to the total charge storage at 1 mV s^{-1} (d) before and (e) after cycling. (f) Cyclic voltammetry curve of the glass fiber separated high-capacity Zn || MnO_2 battery.

It is worth mentioning that the problem of cathode architecture was also observed in the GF-separated high-capacity Zn || MnO_2 cell, indicating that the hindrance of the electrode reactions did not come from the relatively low ion conductivity of DNGF (**Figure 5.32(f)**). Characterization of the HCM cathode before and after cycling is shown in **Figure 5.33(a)**. The HCM cathode was removed from the DNGF-separated Zn || MnO_2 cell undergoing 500 cycles (corresponding to **Figure 5.28**). **Figure 5.33(a)** shows that the HCM cathode before cycling shows a modified XRD pattern of α-MnO_2. During the first 500 cycles, the following reactions were processed:[241]

$$MnO_2 + H_2O + e^- \rightarrow MnOOH + OH^- \quad \text{(Eq. 5.11)}$$

$$yZn^{2+} + MnO_2 \cdot xH_2O + 2ye^- \rightarrow Zn_yMnO_2 \cdot xH_2O \quad \text{(Eq. 5.12)}$$

$$Zn^{2+} + 6OH^- + SO_4^{2-} + 5H_2O \rightarrow Zn_4(OH)_6SO_4 \cdot 5H_2O \quad \text{(Eq. 5.13)}$$

Therefore, peaks indicating $ZnMn_2O_4$, $Zn_4(OH)_6SO_4$, and MnOOH were observed after cycling. An additional galvanostatic discharge measurement was conducted after reassembling the DNGF-separated high-capacity Zn || MnO_2 cell. The HCM cathode was soaked in the electrolyte (2 mol L^{-1} $ZnSO_4$ + 0.2 mol L^{-1} $MnSO_4$) for 12 h before the test. The reassembled high-capacity Zn || MnO_2 cell surprisingly provided a capacity of 140 mAh g^{-1} (calculated by the HCM cathode), indicating that the electrochemical capacity, which was not utilized due to the poor architecture of the HCM cathode, could be reactivated after the infiltration of the electrolyte (**Figure 5.33(b)**.). In-situ Raman spectroscopy during the additional discharge test (corresponding to **Figure 5.33(b)**.) was also conducted. As shown in **Figure 5.33(c)**, in the discharge region of point 8 - point 23, the intensity of $ZnMn_2O_4$ and MnOOH increased slightly as the discharge proceeded. EDS was employed to compare the compositional differences of the HCM cathode before and after cycling. As shown in **Figure 5.34(a)**, the HCM cathode showed a carbon substrate covered by MnO_2 nanowires before cycling. While in **Figure 5.34(b)**, the as-cycled HCM cathode exhibited a surface covered by shapeless nanoparticles consisting of Zn, Mn, and O atoms. The change in morphology of the MnO_2 nanowires should be the result of the phase transition caused by the intercalation reaction, which possibly caused the irreversible capacity decay. Based on the analysis above, the main problem of utilizing the HCM cathode appears to come from the poor electrode architecture that inhibits the effective utilization of MnO_2, and the change in active materials that causes irreversible damage.

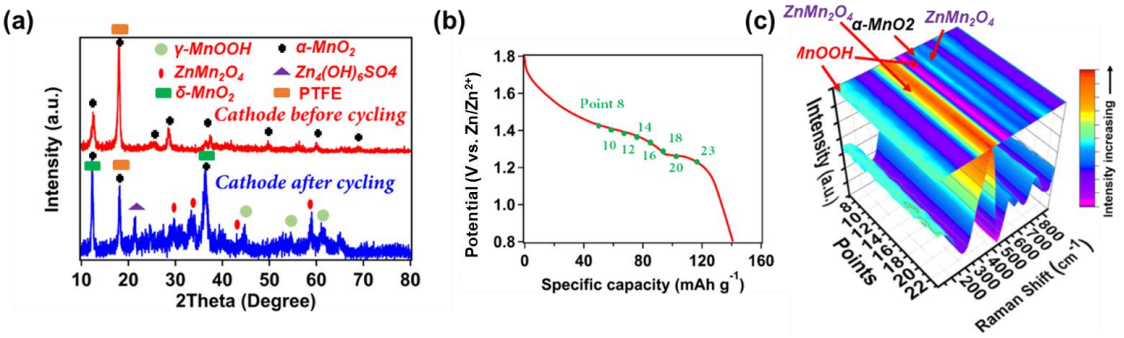

Figure 5.33 (a) Characterization of the MnO_2 cathode. (a) XRD patterns of the HCM cathode before and after cycling, corresponding to Figure 5.28 (b) Voltage profile of an independent galvanostatic discharge test for the HCM cathode after cycling. The inset points correspond to (c) in-situ Raman spectroscopy measurement during the discharge test.

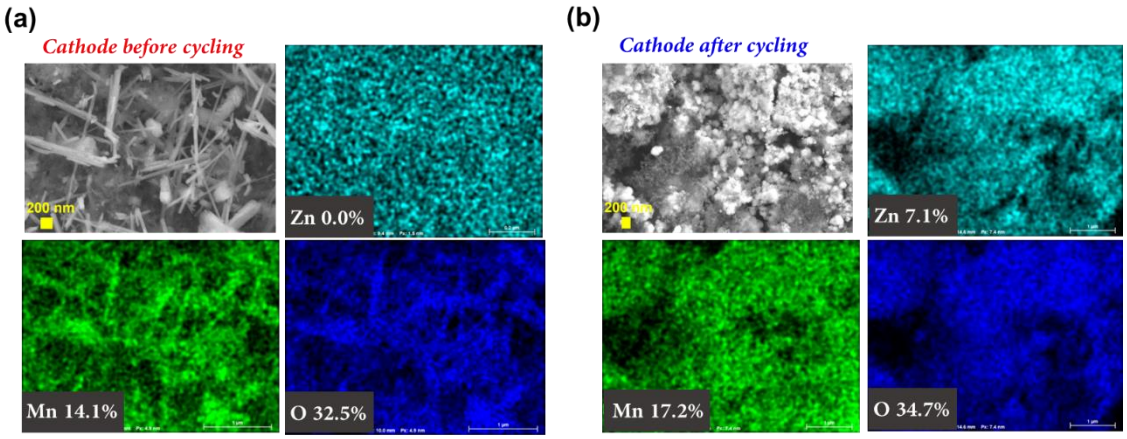

Figure 5.34 SEM and EDS images of HCM cathode (a) before and (b) after cycling.

5.4 Conclusions

In summary, the author achieved a dendrite-free Zn metal anode by using a novel high-strength DNGF gel polymer electrolyte. Thanks to the modified mechanical suppression effect, the dendrite-free Zn || Zn symmetric cell could survive for over 1000 h, even at a high current density of 5 mA cm^{-2}. Some interesting phenomena related to the deposition of Zn with GPEs were observed, and the modified mechanical suppression effect for preventing Zn dendrite growth was discussed. Firstly, when Zn was deposited under a GPE framework (e.g., DNGF), the deposition initially occurred in the pores of the porous GPE due to the lack of external stress inside the pores. The uniform pore distribution on the GPE surface ensured a uniform initial deposition of Zn. Secondly, the upward growth of Zn crystals could be restricted when contacting the GPE framework. Once the upward growth of Zn crystals was stopped, Zn crystals would grow parallel to form a flat surface. Hence, the pore size and mechanical strength of the GPE determine the maximum height of the Zn crystal. Thirdly, the mechanical suppression of dendrite growth occurred at the expense of increasing the deposition overpotential. A reasonable design of the GPE pore-size distribution would make it possible to reduce the thickness of the GPE and the overpotential of Zn deposition simultaneously. Similar ideas can be employed for designing porous separators to suppress dendrite growth with different metal anodes.

Finally, a high-capacity and long-life Zn || MnO_2 rechargeable battery was achieved by using the DNGF GPE. The Zn || MnO_2 battery was stable for over 500 cycles and showed capacity retention of 40%. This indicates that short-circuiting, the weakness most often shown in RAZIBs, can be solved by using the high-strength DNGF GPE. Moreover, the author further studied the capacity decay mechanism of the high-capacity Zn || MnO_2 battery, and two crucial conclusions were discovered: firstly, it is irrational to use the performance of low-capacity MnO_2 cathodes during high-rate charge/discharge as a real performance evaluation, because low-capacity MnO_2 cathodes exhibit obvious capacitor-characteristics during high-rate charge/discharge. This might be an important reason why previously reported Zn || MnO_2 batteries tested with low-capacity cathodes and high charge/discharge rates showed superior cyclic performance. Secondly, the author think that poor cathode architecture (thick, high tortuosity) is the main contributing factor

to capacity decay in high-capacity Zn || MnO_2 batteries. The changes to the cathode materials over 500 cycles do not lead to a significant capacity degradation of the battery. This could be seen by the fact that even after the cathode material has undergone significant changes in morphology and composition, the capacity of the cathode can still be maintained. This indicates that to develop high energy density Zn || MnO_2 batteries, the structural design of a high-capacity cathode will be an important subject in the future.

This chapter outlines the important criteria for developing GPEs that can suppress Zn dendrite growth and demonstrate their necessity for achieving high-energy-density RAZIBs. Furthermore, the author believes this work could pave the way for developing flexible and wearable electronics based on RAZIBs.

Chapter 6 General conclusions

6.1 General Summary and Conclusions

In this thesis, the deposition behavior of Zn in weakly acidic aqueous electrolytes is elucidated. The relationship between the deposition morphology of Zn and the current, the deposition substrate, and the genesis of Zn dendrites are analyzed in detail. The parasitic reaction brought about by HER to generate ZHS was found to be the main cause inducing Zn dendrite generation, and how to improve the affinity between Zn and deposited substrate while reducing the occurrence of HER is one of the key points to enhance the performance of Zn cycling. Furthermore, based on these results, three different schemes for optimizing the electrochemical performance of Zn metal anode and reducing dendrite growth are presented for three different interfaces: electrolyte/current collector, Zn anode/electrolyte, and newly deposited Zn/electrolyte interfaces. By introducing a coating with suitable PZC to the current collector, the production of ZHS can be reduced, and thus the performance of Zn deposition can be optimized. By polishing the Zn metal, the initial nucleation of Zn can be homogenized, and the resistance to Zn deposition can be reduced, thus safeguarding the electrochemical performance of the Zn anode. The use of a semi-solid electrolyte with high mechanical strength can suppress the growth of Zn dendrites mechanically, and the subsequent deposition of Zn can be forced to uniform. The summary of each chapter is depicted below.

After briefly introducing the significance of developing reliable RAZIBs energy-storage systems, Chapter 1 outlines the current studies on the growth mechanism of Zn dendrites in neutral/mildly acidic electrolytes and points out the controversies and contradictions in these studies. The search for a more reasonable growth mechanism of Zn dendrites is one of the immediate needs in the study of RAZIBs.

In Chapter 2, by investigating the deposition morphology of Zn under different conditions, a strong relation between Zn dendrites and ZHS is found, motivating the proposal of a Zn dendrite growth mechanism based on the ZHS-Zn metal co-growth model. In the mildly acidic electrolyte, the HER reaction elevates the OH^- concentration at the interface, resulting in the deposition of Zn

along with the ZHS, which grows along the concentration gradient of OH^-, causing the newly deposited solid to become dendritic. Hence, decreasing the HER activity at the deposition interface, increasing the affinity of the deposition interface for Zn, or increasing the deposition current can improve the reversibility of Zn deposition.

Guided by the findings in Chapter 2, a magnetron sputtered Nb coating on Al current collectors is designed in Chapter 3. Thanks to the low HER activity, excellent corrosion resistance, good electronic conductivity, and Zn affinity of the several nanometer-thick Nb_2O_5 passive films on Nb, the Zn deposition on the Nb coating is uniform and excellent reversible. A high Zn plating/stripping Coulombic efficiency of > 99% for 350 cycles can be maintained at a high deposition capacity of 6.25 mAh cm^{-2} (current density of 25 mA cm^{-2}). Using Al foil with Nb coating as cathode and anode current collectors for a Zn-MnO_2 cell, the cell can guarantee > 95% capacity retention within 120 cycles at a 3:1 NP ratio and a capacity of about 2.5 mAh cm^{-2}.

Considering that the optimized substrate is mainly for regulating the deposition behavior of Zn during nucleation, Chapter 5 confirms that the presence of a native oxide layer on the surface of Zn metal affects the electrochemical performance of the Zn metal anode in mildly acidic electrolytes. By electropolishing Zn metal, the surface properties of Zn can become homogeneous, making the plating/stripping of Zn more uniform. Moreover, Zn is found to be more inclined to deposit in electropolished areas. At the same time, the electrode surface of the polished Zn anode is almost completely utilized during cycling because the mildly acidic environment slows down the growth of the corrosion product layer on the Zn surface, allowing the Zn surface to remain clean for a long time. This also enables the assembled Zn||Zn symmetric cell to have a cycle life of more than 6000 cycles at 40 mA cm^{-2}/2 mAh cm^{-2}, and the Zn-MnO_2 pouch cell with a manganese dioxide loading of 15 mg cm^{-2} can also work for more than 200 cycles without short circuit.

However, after the capacity of the deposited Zn reaches a certain level, optimization for either the substrate or the Zn metal surface will lose effectiveness due to the huge morphological changes on the electrode surface. In order to ensure that the Zn anode does not generate dendrites during long-term cycling, a high-strength hydrogel electrolyte based on PAMPS-PAM was used

as a separator, i.e., a semi-solid electrolyte, the DNGF. Since Zn dendrite growth is not a strictly electrochemical process, despite the high modulus of the Zn metal, it is possible to limit dendrite growth through polymeric materials. As a result, the Zn deposition beneath the hydrogel electrolyte is forced to uniform due to the external stress from the polymer skeleton. The Zn||Zn cell, under DNGF protection, can easily cycle for more than 2500 hours at a surface capacity of 1 mA cm^{-2}. Meanwhile, Zn-MnO_2 cells with high manganese dioxide loading (30 mg cm^{-2}) can be cycled at a rate of 1 C for 500 cycles without any sign of a short circuit. This indicates that the choice of a diaphragm with high mechanical strength can indeed improve the cycling stability of the Zn negative electrode in the weak acid electrolyte to a great extent.

6.2 Future Prospects

This dissertation reveals a strong relation between Zn dendrites growth and ZHS formation in mildly acidic electrolytes. The three conditions of HER ratio, current densities, and Zn deposition substrates are shown to greatly affect Zn deposition morphology and deposition reversibility. Also, optimization at the anode-electrolyte interface has been shown to be effective in improving the electrochemical performance of Zn anode. Among them, the use of polymer separators (or semi-solid electrolytes) with high mechanical-strength can limit the generation of Zn dendrites during long-term plating/stripping cycles; reducing the current proportion of HER in the total current, i.e., increasing the Faraday efficiency of Zn plating, will effectively limit the generation of ZHS and improve the Coulombic efficiency of the Zn plating/stripping. Considering that charging/ discharging batteries at very high current densities is not achievable in practice, most batteries will be used in the rate range of 0.3 C-2 C (corresponding to charging current-densities of about 1-8 mA cm^{-2} for 4 mAh cm^{-2} capacity), it is also important to ensure the cycling performance of the Zn anode when charging and discharging at low current densities. Therefore, the development of polymeric separators/electrolytes that can simultaneously inhibit HER and have high mechanical- strength would be a highly likely way to help achieve a high-performance Zn anode.

In the subsequent studies, hydrogel electrolytes that can simultaneously reduce the activity of water molecules at the electrode-electrolyte interface without affecting zinc-ion transfer will be prepared by compounding hydrophilic hydrogel networks and hydrogel networks with hydrophobic properties. The hydrogel with double networks can be mechanically strong, while the hydrophobic network will reduce the proportion of water molecules at the interface. Furthermore, nanoparticles that can be used as anti-corrosion coatings (e.g. zeolite imidazolate framework, ZIF) will be added to the hydrogels to enhance the mechanical strength of the hydrogel while further reducing the possibility of HER occurrence at the interface. The development of the functionalized hydrogel electrolytes will provide a more comprehensive understanding of the study of Zn metal anodes and RAZIBs.

Reference

1. Galloway, W. E.; Hobday, D. K., Terrigenous clastic depositional systems applications to fossil fuel and groundwater resources.
2. Martins, F.; Felgueiras, C.; Smitkova, M.; Caetano, N., Analysis of Fossil Fuel Energy Consumption and Environmental Impacts in European Countries. *Energies* **2019,** *12* (6), 964.
3. York, R., Do alternative energy sources displace fossil fuels? *Nature Climate Change* **2012,** *2* (6), 441-443.
4. Hondo, H., Life cycle GHG emission analysis of power generation systems: Japanese case. *Energy* **2005,** *30* (11-12), 2042-2056.
5. Agency for Natural Resources and Energy from Ministry of Energy, Trade and Industry (経済産業省資源エネルギー庁), Japan's Renewable Energy Policy (今後の再生可能エネルギー政策について), **2021**.
6. Beaudin, M.; Zareipour, H.; Schellenberglabe, A.; Rosehart, W., Energy storage for mitigating the variability of renewable electricity sources: An updated review. *Energy for Sustainable Development* **2010,** *14* (4), 302-314.
7. Díaz-González, F.; Sumper, A.; Gomis-Bellmunt, O.; Villafáfila-Robles, R., A review of energy storage technologies for wind power applications. *Renewable and Sustainable Energy Reviews* **2012,** *16* (4), 2154-2171.
8. Zhao, H.; Wu, Q.; Hu, S.; Xu, H.; Rasmussen, C. N., Review of energy storage system for wind power integration support. *Applied Energy* **2015,** *137*, 545-553.
9. Hill, C. A.; Such, M. C.; Chen, D.; Gonzalez, J.; Grady, W. M., Battery Energy Storage for Enabling Integration of Distributed Solar Power Generation. *IEEE Transactions on Smart Grid* **2012,** *3* (2), 850-857.
10. Divya, K. C.; Østergaard, J., Battery energy storage technology for power systems—An overview. *Electric Power Systems Research* **2009,** *79* (4), 511-520.
11. Yang, Y.; Bremner, S.; Menictas, C.; Kay, M., Battery energy storage system size determination in renewable energy systems: A review. *Renewable and Sustainable Energy Reviews* **2018,** *91*, 109-125.
12. Bhatia, S. R.; Jain, S. P.; ain, D. K.; Singh, B., Battery Energy Storage System for Power Conditioning of Renewable Energy Sources. *2005 International Conference on Power Electronics and Drives Systems* **2005,** 501-506.
13. Ould Amrouche, S.; Rekioua, D.; Rekioua, T.; Bacha, S., Overview of energy storage in renewable energy systems. *International Journal of Hydrogen Energy* **2016,** *41* (45), 20914-20927.

14. Kim, T.; Song, W.; Son, D.-Y.; Ono, L. K.; Qi, Y., Lithium-ion batteries: outlook on present, future, and hybridized technologies. *Journal of Materials Chemistry A* **2019,** *7*, 2942.
15. Li, M.; Lu, J.; Chen, Z.; Amine, K., 30 Years of Lithium-Ion Batteries. *Advanced Materials* **2018**, e1800561.
16. Etacheri, V.; Marom, R.; Ran Elazari; Salitra, G.; Aurbach, D., Challenges in the development of advanced Li-ion batteries: a review. *Energy & Environmental Science* **2011,** *4*, 3243.
17. Bandhauer, T. M.; Garimella, S.; Fuller, T. F., A Critical Review of Thermal Issues in Lithium-Ion Batteries. *Journal of The Electrochemical Society* **2011,** *158*, R1-R25.
18. Hannan, M. A.; Hoque, M. M.; Hussain, A.; Yusof, Y.; Ker, P. J., State-of-the-Art and Energy Management System of Lithium-Ion Batteries in Electric Vehicle Applications: Issues and Recommendations. *IEEE Access* **2018,** *6*, 19362-19378.
19. Harper, G.; Sommerville, R.; Kendrick, E.; Driscoll, L.; Slater, P.; Stolkin, R.; Walton, A.; Christensen, P.; Heidrich, O.; Lambert, S.; Abbott, A.; Ryder, K.; Gaines, L.; Anderson, P., Recycling lithium-ion batteries from electric vehicles. *Nature* **2019,** *575* (7781), 75-86.
20. Kennedy, B.; Patterson, D.; Camilleri, S., Use of lithium-ion batteries in electric vehicles. *Journal of Power Sources* **2000,** *90*, 156-162.
21. Yabuuchi, N.; Kubota, K.; Dahbi, M.; Komaba, S., Research development on sodium-ion batteries. *Chemical Reviews* **2014,** *114* (23), 11636-11682.
22. Vaalma, C.; Buchholz, D.; Weil, M.; Passerini, S., A cost and resource analysis of sodium-ion batteries. *Nature Reviews Materials* **2018,** *3*, 1-11.
23. Hwang, J. Y.; Myung, S. T.; Sun, Y. K., Sodium-ion batteries: present and future. *Chemical Society Review* **2017,** *46* (12), 3529-3614.
24. Delmas, C., Sodium and Sodium-Ion Batteries: 50 Years of Research. *Advanced Energy Materials* **2018,** *8* (17), 1703137.
25. Chayambuka, K.; Mulder, G.; Danilov, D. L.; Notten, P. H. L., Sodium-Ion Battery Materials and Electrochemical Properties Reviewed. *Advanced Energy Materials* **2018,** *8* (16), 1800079.
26. Young, K.-h.; Yasuoka, S., Capacity Degradation Mechanisms in Nickel/Metal Hydride Batteries. *Batteries* **2016,** *2* (1), 3.
27. Putois, F., Market for nickel-cadmium batteries. *Journal of Power Sources* **1995,** *57*, 67-70.
28. Sakai, T.; Uehara, I.; Ishikawa, H., R&D on metal hydride materials and Ni–MH batteries in Japan. *Journal of Alloys and Compounds* **1999,** *293-295*, 762-769.

29. Taniguchi, A.; Fujioka, N.; Ikoma, M.; Ohta, A., Development of nickel/metal-hydride batteries for EVs and HEVs. *Journal of Power Sources* **2001,** *100*, 117-124.
30. Ruetschi, P.; Meli, F.; Desilvestro, J., Nickel-metal hydride batteries. The preferred batteries of the future? *Journal of Power Sources* **1995,** *57*, 85-91.
31. Weber, A. Z.; Mench, M. M.; Meyers, J. P.; Ross, P. N.; Gostick, J. T.; Liu, Q., Redox flow batteries: a review. *Journal of Applied Electrochemistry* **2011,** *41* (10), 1137-1164.
32. Noack, J.; Roznyatovskaya, N.; Herr, T.; Fischer, P., The Chemistry of Redox-Flow Batteries. *Angewandte Chemie International Edition* **2015,** *54* (34), 9776-9809.
33. Xie, C.; Duan, Y.; Xu, W.; Zhang, H.; Li, X., A Low-Cost Neutral Zinc-Iron Flow Battery with High Energy Density for Stationary Energy Storage. *Angewandte Chemie International Edition* **2017,** *56* (47), 14953-14957.
34. Wan, F.; Zhang, Y.; Zhang, L.; Liu, D.; Wang, C.; Song, L.; Niu, Z.; Chen, J., Reversible Oxygen Redox Chemistry in Aqueous Zinc-Ion Batteries. *Angewandte Chemie International Edition* **2019,** *58* (21), 7062-7067.
35. Yin, Y.; Wang, S.; Zhang, Q.; Song, Y.; Chang, N.; Pan, Y.; Zhang, H.; Li, X., Dendrite-Free Zinc Deposition Induced by Tin-Modified Multifunctional 3D Host for Stable Zinc-Based Flow Battery. *Advanced Materials* **2019**, 1906803.
36. Wang, W.; Luo, Q.; Li, B.; Wei, X.; Li, L.; Yang, Z., Recent Progress in Redox Flow Battery Research and Development. *Advanced Functional Materials* **2013,** *23* (8), 970-986.
37. Goodenough, J. B.; Park, K. S., The Li-ion rechargeable battery: a perspective. *Journal of the American Chemical Society* **2013,** *135* (4), 1167-1176.
38. Fan, X.; Liu, B.; Liu, J.; Ding, J.; Han, X.; Deng, Y.; Lv, X.; Xie, Y.; Chen, B.; Hu, W.; Zhong, C., Battery Technologies for Grid-Level Large-Scale Electrical Energy Storage. *Transactions of Tianjin University* **2020,** *26* (2), 92-103.
39. Chen, D.; Lu, M.; Cai, D.; Yang, H.; Han, W., Recent advances in energy storage mechanism of aqueous zinc-ion batteries. *Journal of Energy Chemistry* **2021,** *54*, 712-726.
40. Rogulski, Z.; Czerwiński, A., Cathode modification in the Leclanché cell. *Journal of Solid State Electrochemistry* **2003,** *7* (2), 118-121.
41. Parker, J. F.; Chervin, C. N.; Nelson, E. S.; Rolison, D. R.; Long, J. W., Wiring zinc in three dimensions re-writes battery performance—dendrite-free cycling. *Energy & Environmental Science.* **2014,** *7* (3), 1117-1124.
42. Cheng, J.; Zhang, L.; Yang, Y.-S.; Wen, Y.-H.; Cao, G.-P.; Wang, X.-D., Preliminary study of single flow zinc–nickel battery. *Electrochemistry Communications* **2007,** *9* (11), 2639-2642.

43. Goodkin, J., Long Life Stable Zinc Electrodes for Alkaline Secondary Batterie. *Quarterly report No. 4,* **1967**. [Teflonated anodes]. United States: N. p., 1968.
44. Guo, J.; Ming, J.; Lei, Y. J.; Zhang, W. L.; Xia, C.; Cui, Y.; Alshareef, H. N., Artificial Solid Electrolyte Interphase for Suppressing Surface Reactions and Cathode Dissolution in Aqueous Zinc Ion Batteries. *ACS Energy Letters* **2019,** *4* (12), 2776-2781.
45. Deng, Y. P.; Liang, R. L.; Jiang, G. P.; Jiang, Y.; Yu, A. P.; Chen, Z. W., The Current State of Aqueous Zn-Based Rechargeable Batteries. *ACS Energy Letters* **2020,** *5* (5), 1665-1675.
46. Demir-Cakan, R.; Palacin, M. R.; Croguennec, L., Rechargeable aqueous electrolyte batteries: from univalent to multivalent cation chemistry. *Journal of Materials Chemistry A* **2019,** *7* (36), 20519-20539.
47. Selvakumaran, D.; Pan, A.; Liang, S.; Cao, G., A review on recent developments and challenges of cathode materials for rechargeable aqueous Zn-ion batteries. *Journal of Materials Chemistry A* **2019,** *7* (31), 18209-18236.
48. Liu, H.; Wang, J.-G.; You, Z.; Wei, C.; Kang, F.; Wei, B., Rechargeable aqueous zinc-ion batteries: Mechanism, design strategies and future perspectives. *Materials Today* **2021,** *42*, 73-98.
49. Li, C.; Xie, X.; Liang, S.; Zhou, J., Issues and Future Perspective on Zinc Metal Anode for Rechargeable Aqueous Zinc-ion Batteries. *Energy & Environmental Materials* **2020,** *3* (2), 146-159.
50. Yang, H.; Zhu, R.; Yang, Y.; Lu, Z.; Chang, Z.; He, P.; Zhu, C.; Kitano, S.; Aoki, Y.; Habazaki, H.; Zhou, H., Sustainable high-energy aqueous zinc–manganese dioxide batteries enabled by stress-governed metal electrodeposition and fast zinc diffusivity. *Energy & Environmental Science* **2023**.
51. Zeng, Y.; Zhang, X.; Qin, R.; Liu, X.; Fang, P.; Zheng, D.; Tong, Y.; Lu, X., Dendrite-Free Zinc Deposition Induced by Multifunctional CNT Frameworks for Stable Flexible Zn-Ion Batteries. *Advanced Materials* **2019,** *31* (36), e1903675.
52. Cao, Z.; Zhuang, P.; Zhang, X.; Ye, M.; Shen, J.; Ajayan, P. M., Strategies for Dendrite-Free Anode in Aqueous Rechargeable Zinc Ion Batteries. *Advanced Energy Materials* **2020,** *10* (30), 2001599.
53. Yuksel, R.; Buyukcakir, O.; Seong, W. K.; Ruoff, R. S., Metal-Organic Framework Integrated Anodes for Aqueous Zinc-Ion Batteries. *Advanced Energy Materials* **2020,** *10* (16), 1904215.
54. Zhao, R.; Yang, Y.; Liu, G.; Zhu, R.; Huang, J.; Chen, Z.; Gao, Z.; Chen, X.; Qie, L., Redirected Zn Electrodeposition by an Anti-Corrosion Elastic Constraint for Highly Reversible Zn Anodes. *Advanced Functional Materials* **2020**, 2001867.

55. Naveed, A.; Yang, H.; Shao, Y.; Yang, J.; Yanna, N.; Liu, J.; Shi, S.; Zhang, L.; Ye, A.; He, B., A Highly Reversible Zn Anode with Intrinsically Safe Organic Electrolyte for Long-Cycle-Life Batteries. *Advanced Materials* **2019,** *31* (36), 1900668.
56. Pan, H.; Ellis, J. F.; Li, X.; Nie, Z.; Chang, H. J.; Reed, D., Electrolyte Effect on the Electrochemical Performance of Mild Aqueous Zinc-Electrolytic Manganese Dioxide Batteries. *ACS Appllied Materials Interfaces* **2019,** *11* (41), 37524-37530.
57. Jin, Y.; Zou, L.; Liu, L.; Engelhard, M. H.; Patel, R. L.; Nie, Z.; Han, K. S.; Shao, Y.; Wang, C.; Zhu, J.; Pan, H.; Liu, J., Joint Charge Storage for High-Rate Aqueous Zinc-Manganese Dioxide Batteries. *Advanced Materials* **2019,** *31* (29), e1900567.
58. Fan, W.; Liu, F.; Liu, Y.; Wu, Z.; Wang, L.; Zhang, Y.; Huang, Q.; Fu, L.; Wu, Y., A high voltage aqueous zinc-manganese battery using a hybrid alkaline-mild electrolyte. *Chemical Communications* **2020,** *56* (13), 2039-2042.
59. Ghosh, M.; Dilwale, S.; Vijayakumar, V.; Kurungot, S., Scalable Synthesis of Manganese-Doped Hydrated Vanadium Oxide as a Cathode Material for Aqueous Zinc-Metal Battery. *ACS Appllied Materials Interfaces* **2020,** *12* (43), 48542-48552.
60. Hu, P.; Zhu, T.; Ma, J.; Cai, C.; Hu, G.; Wang, X.; Liu, Z.; Zhou, L.; Mai, L., Porous V2O5 microspheres: a high-capacity cathode material for aqueous zinc-ion batteries. *Chemical Communications* **2019,** *55* (58), 8486-8489.
61. Zhou, W.; Chen, J.; He, C.; Chen, M.; Xu, X.; Tian, Q.; Xu, J.; Wong, C.-P., Hybridizing δ-type $NaxV_2O_5 \cdot nH_2O$ with graphene towards high-performance aqueous zinc-ion batteries. *Electrochimica Acta* **2019,** *321*, 134689.
62. Chen, D.; Rui, X. H.; Zhang, Q.; Geng, H. B.; Gan, L. Y.; Zhang, W.; Li, C. C.; Huang, S. M.; Yu, Y., Persistent zinc-ion storage in mass-produced V2O5 architecture. *Nano Energy* **2019,** *60*, 171-178.
63. Yang, Y. Q.; Tang, Y.; Liang, S. Q.; Wu, Z. X.; Fang, G. Z.; Cao, X. X.; Wang, C.; Lin, T. Q.; Pan, A. Q.; Zhou, J., Transition metal ion-preintercalated V_2O_5 as high-performance aqueous zinc-ion battery cathode with broad temperature adaptability. *Nano Energy* **2019,** *61*, 617-625.
64. Gao, X.; Wu, H.; Li, W.; Tian, Y.; Zhang, Y.; Wu, H.; Yang, L.; Zou, G.; Hou, H.; Ji, X., H(+) -Insertion Boosted alpha-MnO_2 for an Aqueous Zn-Ion Battery. *Small* **2020,** *16* (5), e1905842.
65. Zhao, Q.; Chen, X.; Wang, Z.; Yang, L.; Qin, R.; Yang, J.; Song, Y.; Ding, S.; Weng, M.; Huang, W.; Liu, J.; Zhao, W.; Qian, G.; Yang, K.; Cui, Y.; Chen, H.; Pan, F., Unravelling H(+) /Zn(2+) Synergistic Intercalation in a Novel Phase of Manganese Oxide for High-Performance Aqueous Rechargeable Battery. *Small* **2019,** *15* (47), e1904545.
66. Wang, C.; Wei, S.; Chen, S.; Cao, D.; Song, L., Delaminating Vanadium Carbides for

Zinc-Ion Storage: Hydrate Precipitation and H^+/Zn^{2+} Co-Action Mechanism. *Small Methods* **2019,** *3* (12), 1900495.
67. Sun, W.; Wang, F.; Hou, S.; Yang, C.; Fan, X.; Ma, Z.; Gao, T.; Han, F.; Hu, R.; Zhu, M.; Wang, C., Zn/MnO2 Battery Chemistry With H(+) and Zn(2+) Coinsertion. *Journal of the American Chemical Society* **2017,** *139* (29), 9775-9778.
68. Wu, W.; Shi, H.-Y.; Lin, Z.; Yang, X.; Li, C.; Lin, L.; Song, Y.; Guo, D.; Liu, X.-X.; Sun, X., The controlled quinone introduction and conformation modification of polyaniline cathode materials for rechargeable aqueous zinc-polymer batteries. *Chemical Engineering Journal* **2021,** *419*.
69. Gong, J.; Li, H.; Zhang, K.; Zhang, Z.; Cao, J.; Shao, Z.; Tang, C.; Fu, S.; Wang, Q.; Wu, X., Zinc-Ion Storage Mechanism of Polyaniline for Rechargeable Aqueous Zinc-Ion Batteries. *Nanomaterials* **2022,** *12* (9).
70. Zampardi, G.; La Mantia, F., Prussian blue analogues as aqueous Zn-ion batteries electrodes: Current challenges and future perspectives. *Current Opinion in Electrochemistry* **2020,** *21*, 84-92.
71. Li, Y.; Zhao, J.; Hu, Q.; Hao, T.; Cao, H.; Huang, X.; Liu, Y.; Zhang, Y.; Lin, D.; Tang, Y.; Cai, Y., Prussian blue analogs cathodes for aqueous zinc ion batteries. *Materials Today Energy* **2022,** *29*.
72. Zeng, Y.; Lu, X. F.; Zhang, S. L.; Luan, D.; Li, S.; Lou, X. W. D., Construction of Co-Mn Prussian Blue Analog Hollow Spheres for Efficient Aqueous Zn-ion Batteries. *Angewandte Chemie International Edition* **2021,** *60* (41), 22189-22194.
73. Cao, T.; Zhang, F.; Chen, M.; Shao, T.; Li, Z.; Xu, Q.; Cheng, D.; Liu, H.; Xia, Y., Cubic Manganese Potassium Hexacyanoferrate Regulated by Controlling of the Water and Defects as a High-Capacity and Stable Cathode Material for Rechargeable Aqueous Zinc-Ion Batteries. *ACS Appllied Materials Interfaces* **2021,** *13* (23), 26924-26935.
74. Yadav, G. G.; Wei, X.; Huang, J.; Gallaway, J. W.; Turney, D. E.; Nyce, M.; Secor, J.; Banerjee, S., A conversion-based highly energy dense Cu^{2+} intercalated Bi-birnessite/Zn alkaline battery. *Journal of Materials Chemistry A* **2017,** *5* (30), 15845-15854.
75. Yadav, G. G.; Wei, X.; Huang, J.; Turney, D.; Nyce, M.; Banerjee, S., Accessing the second electron capacity of MnO2 by exploring complexation and intercalation reactions in energy dense alkaline batteries. *International Journal of Hydrogen Energy* **2018,** *43* (17), 8480-8487.
76. Guo, N.; Huo, W.; Dong, X.; Sun, Z.; Lu, Y.; Wu, X.; Dai, L.; Wang, L.; Lin, H.; Liu, H.; Liang, H.; He, Z.; Zhang, Q., A Review on 3D Zinc Anodes for Zinc Ion Batteries. *Small Methods* **2022,** *6* (9), e2200597.
77. Mansfeld, F.; Gilman, S., The Effect of Several Electrode and Electrolyte Additives

on the Corrosion and Polarization Behavior of the Alkaline Zinc Electrode. *Journal of The Electrochemical Society* **1970,** *117*, 1328-1333.
78. Kaveevivitchai, W.; Manthiram, A., High-capacity zinc-ion storage in an open-tunnel oxide for aqueous and nonaqueous Zn-ion batteries. *Journal of Materials Chemistry A* **2016,** *4* (48), 18737-18741.
79. He, P.; Chen, Q.; Yan, M.; Xu, X.; Zhou, L.; Mai, L.; Nan, C.-W., Building better zinc-ion batteries: A materials perspective. *EnergyChem* **2019,** *1* (3), 100022.
80. Zhang, L.; Rodríguez-Pérez, I. A.; Jiang, H.; Zhang, C.; Leonard, D. P.; Guo, Q.; Wang, W.; Han, S.; Wang, L.; Ji, X., $ZnCl_2$ "Water-in-Salt" Electrolyte Transforms the Performance of Vanadium Oxide as a Zn Battery Cathode. *Advanced Functional Materials* **2019,** *29* (30), 1902653.
81. Zhang, C.; Holoubek, J.; Wu, X.; Daniyar, A.; Zhu, L.; Chen, C.; Leonard, D. P.; Rodriguez-Perez, I. A.; Jiang, J. X.; Fang, C.; Ji, X., A $ZnCl_2$ water-in-salt electrolyte for a reversible Zn metal anode. *Chemical Communications* **2018,** *54* (100), 14097-14099.
82. Zhang, N.; Cheng, F.; Liu, Y.; Zhao, Q.; Lei, K.; Chen, C.; Liu, X.; Chen, J., Cation-Deficient Spinel ZnMn2O4 Cathode in Zn(CF3SO3)2 Electrolyte for Rechargeable Aqueous Zn-Ion Battery. *Journal of the American Chemical Society* **2016,** *138* (39), 12894-12901.
83. Shin, J.; Lee, J.; Park, Y.; Choi, J. W., Aqueous zinc ion batteries: focus on zinc metal anodes. *Chemical Science* **2020,** *11* (8), 2028-2044.
84. Islam, S.; Alfaruqi, M. H.; Sambandam, B.; Putro, D. Y.; Kim, S.; Jo, J.; Kim, S.; Mathew, V.; Kim, J., A new rechargeable battery based on a zinc anode and a NaV 6 O 15 nanorod cathode. *Chemical Communications* **2019,** *55* (26), 3793-3796.
85. Xia, C.; Guo, J.; Li, P.; Zhang, X.; Alshareef, H. N., Highly Stable Aqueous Zinc-Ion Storage Using a Layered Calcium Vanadium Oxide Bronze Cathode. *Angewandte Chemie International Edition* **2018,** *57* (15), 3943-3948.
86. Wang, L. P.; Li, N. W.; Wang, T. S.; Yin, Y. X.; Guo, Y. G.; Wang, C. R., Conductive graphite fiber as a stable host for zinc metal anodes. *Electrochimica Acta* **2017,** *244*, 172-177.
87. Yang, Q.; Liang, G.; Guo, Y.; Liu, Z.; Yan, B.; Wang, D.; Huang, Z.; Li, X.; Fan, J.; Zhi, C., Do Zinc Dendrites Exist in Neutral Zinc Batteries: A Developed Electrohealing Strategy to In Situ Rescue In-Service Batteries. *Adv Mater* **2019,** *31* (43), e1903778.
88. Ma, L.; Schroeder, M. A.; Pollard, T. P.; Borodin, O.; Ding, M. S.; Sun, R.; Cao, L.; Ho, J.; Baker, D. R.; Wang, C.; Xu, K., Critical Factors Dictating Reversibility of the Zinc Metal Anode. *Energy & Environmental Materials* **2020**, 0, 1-6.
89. Wang, N.; Wan, H.; Duan, J.; Wang, X.; Tao, L.; Zhang, J.; Wang, H., A review of

zinc-based battery from alkaline to acid. *Materials Today Advances* **2021,** *11*, 100149.
90. R. Mainar, A.; Leonet, O.; Bengoechea, M.; Boyano, I.; de Meatza, I.; Kvasha, A.; Guerfi, A.; Alberto Blázquez, J., Alkaline aqueous electrolytes for secondary zinc-air batteries: an overview. *International Journal of Energy Research* **2016,** *40* (8), 1032-1049.
91. Kim, H. J.; Kim, S.; Heo, K.; Lim, J. H.; Yashiro, H.; Myung, S. T., Nature of Zinc-Derived Dendrite and Its Suppression in Mildly Acidic Aqueous Zinc-Ion Battery. *Advanced Energy Materials* **2022,** *13* (2), 2203189.
92. Li, Q.; Zhao, Y.; Mo, F.; Wang, D.; Yang, Q.; Huang, Z.; Liang, G.; Chen, A.; Zhi, C., Dendrites issues and advances in Zn anode for aqueous rechargeable Zn-based batteries. *EcoMat* **2020**, 1-14.
93. Zhang, Q.; Luan, J.; Fu, L.; Wu, S.; Tang, Y.; Ji, X.; Wang, H., The Three-Dimensional Dendrite-Free Zinc Anode on a Copper Mesh with a Zinc-Oriented Polyacrylamide Electrolyte Additive. *Angewandte Chemie International Edition* **2019,** *58* (44), 15841-15847.
94. Kim, J. Y.; Liu, G.; Shim, G. Y.; Kim, H.; Lee, J. K., Functionalized Zn@ZnO Hexagonal Pyramid Array for Dendrite-Free and Ultrastable Zinc Metal Anodes. *Advanced Functional Materials* **2020,** *30* (36).
95. Sun, P. X.; Cao, Z.; Zeng, Y. X.; Xie, W. W.; Li, N. W.; Luan, D.; Yang, S.; Yu, L.; Lou, X. W. D., Formation of Super-Assembled TiO(x) /Zn/N-Doped Carbon Inverse Opal Towards Dendrite-Free Zn Anodes. *Angewandte Chemie International Edition* **2022,** *61* (7), e202115649.
96. Lu, W.; Xie, C.; Zhang, H.; Li, X., Inhibition of Zinc Dendrite Growth in Zinc-Based Batteries. *ChemSusChem* **2018,** *11* (23), 3996-4006.
97. Zuo, Y.; Wang, K.; Pei, P.; Wei, M.; Liu, X.; Xiao, Y.; Zhang, P., Zinc dendrite growth and inhibition strategies. *Materials Today Energy* **2021,** *20*, 100692.
98. Foroozan, T.; Yurkiv, V.; Sharifi-Asl, S.; Rojaee, R.; Mashayek, F.; Shahbazian-Yassar, R., Non-Dendritic Zn Electrodeposition Enabled by Zincophilic Graphene Substrates. *ACS Appllied Materials Interfaces* **2019,** *11* (47), 44077-44089.
99. Yang, Z.; Lv, C.; Li, W.; Wu, T.; Zhang, Q.; Tang, Y.; Shao, M.; Wang, H., Revealing the Two-Dimensional Surface Diffusion Mechanism for Zinc Dendrite Formation on Zinc Anode. *Small* **2022,** *18* (43), e2104148.
100. He, P.; Huang, J., Detrimental Effects of Surface Imperfections and Unpolished Edges on the Cycling Stability of a Zinc Foil Anode. *ACS Energy Letters* **2021,** *6* (5), 1990-1995.
101. Zhu, R.; Xiong, Z.; Yang, H.; Huang, T.; Jeong, S.; Kowalski, D.; Kitano, S.; Aoki, Y.; Habazaki, H.; Zhu, C., A low-cost and non-corrosive electropolishing strategy for

long-life zinc metal anode in rechargeable aqueous battery. *Energy Storage Materials* **2022,** *46*, 223-232.
102. Zhang, R.; Chen, X. R.; Chen, X.; Cheng, X. B.; Zhang, X. Q.; Yan, C.; Zhang, Q., Lithiophilic Sites in Doped Graphene Guide Uniform Lithium Nucleation for Dendrite-Free Lithium Metal Anodes. *Angewandte Chemie International Edition* **2017,** *56* (27), 7764-7768.
103. Yang, C. P.; Yin, Y. X.; Zhang, S. F.; Li, N. W.; Guo, Y. G., Accommodating lithium into 3D current collectors with a submicron skeleton towards long-life lithium metal anodes. *Nature Communications* **2015,** *6*, 8058.
104. Zheng, J.; Zhao, Q.; Tang, T.; Yin, J.; Quilty, C. D.; Renderos, G. D.; Liu, X.; Deng, Y.; Wang, L.; Bock, D. C.; Jaye, C.; Zhang, D.; Takeuchi, E. S.; Takeuchi, K. J.; Marschilok, A. C.; Archer, L. A., Reversible epitaxial electrodeposition of metals in battery anodes. *Science* **2019,** *366* (6465), 645-648.
105. Yang, Q.; Li, L.; Hussain, T.; Wang, D.; Hui, L.; Guo, Y.; Liang, G.; Li, X.; Chen, Z.; Huang, Z.; Li, Y.; Xue, Y.; Zuo, Z.; Qiu, J.; Li, Y.; Zhi, C., Stabilizing Interface pH by N-Modified Graphdiyne for Dendrite-Free and High-Rate Aqueous Zn-Ion Batteries. *Angewandte Chemie International Edition* **2022,** *61* (6), e202112304.
106. Lee, Y.-H.; Jeoun, Y.; Lee, S.-H.; Kim, J. H.; Kim, S.-Y.; Yu, S.-H.; Ahn, K.-S.; Sung, Y.-E., Byproduct reverse engineering to construct unusually enhanced protection layers for dendrite-free Zn anode. *Chemical Engineering Journal* **2023,** *464*.
107. Han, D.; Wu, S.; Zhang, S.; Deng, Y.; Cui, C.; Zhang, L.; Long, Y.; Li, H.; Tao, Y.; Weng, Z.; Yang, Q. H.; Kang, F., A Corrosion-Resistant and Dendrite-Free Zinc Metal Anode in Aqueous Systems. *Small* **2020,** *16* (29), e2001736.
108. Chao, D.; Qiao, S.-Z., Toward High-Voltage Aqueous Batteries: Super- or Low-Concentrated Electrolyte? *Joule* **2020,** *4* (9), 1846-1851.
109. Guo, S.; Qin, L.; Zhang, T.; Zhou, M.; Zhou, J.; Fang, G.; Liang, S., Fundamentals and perspectives of electrolyte additives for aqueous zinc-ion batteries. *Energy Storage Materials* **2021,** *34*, 545-562.
110. González, M. A.; Trócoli, R.; Pavlovic, I.; Barriga, C.; La Mantia, F., Layered double hydroxides as a suitable substrate to improve the efficiency of Zn anode in neutral pH Zn-ion batteries. *Electrochemistry Communications* **2016,** *68*, 1-4.
111. Liu, C.; Xie, X.; Lu, B.; Zhou, J.; Liang, S., Electrolyte Strategies toward Better Zinc-Ion Batteries. *ACS Energy Letters* **2021,** *6* (3), 1015-1033.
112. Zhu, Y.; Yin, J.; Zheng, X.; Emwas, A.-H.; Lei, Y.; Mohammed, O. F.; Cui, Y.; Alshareef, H. N., Concentrated dual-cation electrolyte strategy for aqueous zinc-ion batteries. *Energy & Environmental Science* **2021,** *14* (8), 4463-4473.

113. Sun, K. E.; Hoang, T. K.; Doan, T. N.; Yu, Y.; Zhu, X.; Tian, Y.; Chen, P., Suppression of Dendrite Formation and Corrosion on Zinc Anode of Secondary Aqueous Batteries. *ACS Applied Materials Interfaces* **2017,** *9* (11), 9681-9687.
114. Bayaguud, A.; Luo, X.; Fu, Y.; Zhu, C., Cationic Surfactant-Type Electrolyte Additive Enables Three-Dimensional Dendrite-Free Zinc Anode for Stable Zinc-Ion Batteries. *ACS Energy Letters* **2020,** *5* (9), 3012-3020.
115. Xiao, P.; Li, H.; Fu, J.; Zeng, C.; Zhao, Y.; Zhai, T.; Li, H., An anticorrosive zinc metal anode with ultra-long cycle life over one year. *Energy & Environmental Science* **2022,** *15* (4), 1638-1646.
116. Xie, C.; Li, Y.; Wang, Q.; Sun, D.; Tang, Y.; Wang, H., Issues and solutions toward zinc anode in aqueous zinc-ion batteries: A mini review. *Carbon Energy* **2020,** *2* (4), 540-560.
117. Lu, Q.; Liu, C.; Du, Y.; Wang, X.; Ding, L.; Omar, A.; Mikhailova, D., Uniform Zn Deposition Achieved by Ag Coating for Improved Aqueous Zinc-Ion Batteries. *ACS Appllied Materials Interfaces* **2021,** *13* (14), 16869-16875.
118. Yang, H.; Qiao, Y.; Chang, Z.; Deng, H.; Zhu, X.; Zhu, R.; Xiong, Z.; He, P.; Zhou, H., Reducing Water Activity by Zeolite Molecular Sieve Membrane for Long-Life Rechargeable Zinc Battery. *Advanced Materials* **2021**, e2102415.
119. Kang, L.; Cui, M.; Jiang, F.; Gao, Y.; Luo, H.; Liu, J.; Liang, W.; Zhi, C., Nanoporous $CaCO_3$ Coatings Enabled Uniform Zn Stripping/Plating for Long-Life Zinc Rechargeable Aqueous Batteries. *Advanced Energy Materials* **2018,** *8* (25), 1801090.
120. Ko, J. S.; Geltmacher, A. B.; Hopkins, B. J.; Rolison, D. R.; Long, J. W.; Parker, J. F., Robust 3D Zn Sponges Enable High-Power, Energy-Dense Alkaline Batteries. *ACS Applied Energy Materials* **2018,** *2* (1), 212-216.
121. Kang, Z.; Wu, C. L.; Dong, L. B.; Liu, W. B.; Mou, J.; Zhang, J. W.; Chang, Z. W.; Jiang, B. Z.; Wang, G. X.; Kang, F. Y.; Xu, C. J., 3D Porous Copper Skeleton Supported Zinc Anode toward High Capacity and Long Cycle Life Zinc Ion Batteries. *Acs Sustainable Chemistry & Engineering* **2019,** *7* (3), 3364.
122. Liu, B.; Wang, S.; Wang, Z.; Lei, H.; Chen, Z.; Mai, W., Novel 3D Nanoporous Zn-Cu Alloy as Long-Life Anode toward High-Voltage Double Electrolyte Aqueous Zinc-Ion Batteries. *Small* **2020,** *16* (22), e2001323.
123. Garcia, G.; Ventosa, E.; Schuhmann, W., Complete Prevention of Dendrite Formation in Zn Metal Anodes by Means of Pulsed Charging Protocols. *ACS Appllied Materials Interfaces* **2017,** *9* (22), 18691-18698.
124. Yufit, V.; Tariq, F.; Eastwood, D. S.; Biton, M.; Wu, B.; Lee, P. D.; Brandon, N. P., Operando Visualization and Multi-scale Tomography Studies of Dendrite Formation and

Dissolution in Zinc Batteries. *Joule* **2019,** *3* (2), 485-502.
125. Grier, D.; Ben-Jacob, E.; Clarke, R.; Sander, L. M., Morphology and microstructure in electrochemical deposition of zinc. *Physical Review Letters* **1986,** *56* (12), 1264-1267.
126. Chu, M. G.; McBreen, J.; Adzic, G., Substrate Effects on Zinc Deposition from Zincate Solutions: I . Deposition on Cu, Au, Cd and Zn. *Journal of The Electrochemical Society 128*, 2281-2286.
127. Wei, X.; Desai, D.; Yadav, G. G.; Turney, D. E.; Couzis, A.; Banerjee, S., Impact of anode substrates on electrodeposited zinc over cycling in zinc-anode rechargeable alkaline batteries. *Electrochimica Acta* **2016,** *212*, 603-613.
128. Zheng, J.; Deng, Y.; Li, W.; Yin, J.; West, P. J.; Tang, T.; Tong, X.; Bock, D. C.; Jin, S.; Zhao, Q.; Garcia-Mendez, R.; Takeuchi, K. J.; Takeuchi, E. S.; Marschilok, A. C.; Archer, L. A., Design principles for heterointerfacial alloying kinetics at metallic anodes in rechargeable batteries. *Science Advances* **2022,** *8*, eabq6321.
129. Hendrikx, J.; Visscher, W.; Barendrecht, E., Interaction of Zinc Deposited from an Alkaline-Solution with a Polycrystalline Silver Substrate. *Electrochimica Acta* **1983,** *28* (5), 743-749.
130. Gabe, D. R., The role of hydrogen in metal electrodeposition processes. *Journal of Applied Electrochemistry* **1997,** *27*, 908-915.
131. Zhang, Y.; Zhang, Y.; Mathur, A.; Ben-Yoseph, S.; Xia, S.; Wu, Y.; Liu, N., An effective and accessible cell configuration for testing rechargeable zinc-based alkaline batteries. *Journal of Power Sources* **2021,** *491*.
132. Goyal, A.; Koper, M. T. M., The Interrelated Effect of Cations and Electrolyte pH on the Hydrogen Evolution Reaction on Gold Electrodes in Alkaline Media. *Angewandte Chemie International Edition l* **2021,** *60* (24), 13452-13462.
133. Trudgeon, D. P.; Loh, A.; Ullah, H.; Li, X.; Yufit, V.; Brandon, N.; Liu, M.; Kong, L., The influence of zinc electrode substrate, electrolyte flow rate and current density on zinc-nickel flow cell performance. *Electrochimica Acta* **2021,** *373*.
134. Lee, B.; Seo, H. R.; Lee, H. R.; Yoon, C. S.; Kim, J. H.; Chung, K. Y.; Cho, B. W.; Oh, S. H., Critical Role of pH Evolution of Electrolyte in the Reaction Mechanism for Rechargeable Zinc Batteries. *ChemSusChem* **2016,** *9* (20), 2948-2956.
135. Moezzi, A.; Cortie, M. B.; McDonagh, A. M., Zinc hydroxide sulphate and its transformation to crystalline zinc oxide. *Dalton Trans* **2013,** *42* (40), 14432-14437.
136. Godeffroy, L.; Aguilar, I.; Médard, J.; Larcher, D.; Tarascon, J. M.; Kanoufi, F., Decoupling the Dynamics of Zinc Hydroxide Sulfate Precipitation/Dissolution in Aqueous Zn–MnO_2 Batteries by Operando Optical Microscopy: A Missing Piece of the Mechanistic Puzzle. *Advanced Energy Materials* **2022**.

137. Chen, H.; Dai, C.; Xiao, F.; Yang, Q.; Cai, S.; Xu, M.; Fan, H. J.; Bao, S. J., Reunderstanding the Reaction Mechanism of Aqueous Zn-Mn Batteries with Sulfate Electrolytes: Role of the Zinc Sulfate Hydroxide. *Advanced Materials* **2022,** *34* (15), e2109092.
138. Despić, A. R.; Pavlović, M. G., Deposition of zinc of foreign substrates. *Electrochimica Acta* **1982,** *27*, 1539-1549.
139. Popov, K. I.; Pavlović, M. G.; Spasojević, M. D.; Nakić, V. M., The critical overpotential for zinc dendrite formation. *Journal of Applied Electrochemistry* **1979,** *9*, 533-536.
140. Cao, L.; Li, D.; Pollard, T.; Deng, T.; Zhang, B.; Yang, C.; Chen, L.; Vatamanu, J.; Hu, E.; Hourwitz, M. J.; Ma, L.; Ding, M.; Li, Q.; Hou, S.; Gaskell, K.; Fourkas, J. T.; Yang, X. Q.; Xu, K.; Borodin, O.; Wang, C., Fluorinated interphase enables reversible aqueous zinc battery chemistries. *Nature Nanotechnology* **2021,** *16* (8), 902-910.
141. Degen, A.; Kosec, M., Effect of pH and impurities on the surface charge of zinc oxide in aqueous solution. *Journal of the European Ceramic Society* **2000,** *20*, 667-673.
142. Li, Q.; Chen, A.; Wang, D.; Zhao, Y.; Wang, X.; Jin, X.; Xiong, B.; Zhi, C., Tailoring the metal electrode morphology via electrochemical protocol optimization for long-lasting aqueous zinc batteries. *Nature Communications* **2022,** *13* (1), 3699.
143. Liu, H.; Zhang, Y.; Wang, C.; Glazer, J. N.; Shan, Z.; Liu, N., Understanding and Controlling the Nucleation and Growth of Zn Electrodeposits for Aqueous Zinc-Ion Batteries. *ACS Appllied Materials Interfaces* **2021,** *13* (28), 32930-32936.
144. Conway, B. E.; Jerkiewicz, G., Relation of energies and coverages of underpotential and overpotential deposited H at Pt and other metals to the 'volcano curve' for cathodic H_2 evolution kinetics. *Electrochimica Acta* **2000,** *45*, 4075-4083.
145. Venkatraman, K.; Gusley, R.; Yu, L.; Dordi, Y.; Akolkar, R., Electrochemical Atomic Layer Deposition of Copper: A Lead-Free Process Mediated by Surface-Limited Redox Replacement of Underpotentially Deposited Zinc. *Journal of The Electrochemical Society* **2016,** *163* (12), D3008-D3013.
146. Yan, Y.; Shu, C.; Zeng, T.; Wen, X.; Liu, S.; Deng, D.; Zeng, Y., Surface-Preferred Crystal Plane Growth Enabled by Underpotential Deposited Monolayer toward Dendrite-Free Zinc Anode. *ACS Nano* **2022,** *16* (6), 9150-9162.
147. Zhao, J.; Ren, H.; Liang, Q.; Yuan, D.; Xi, S.; Wu, C.; Manalastas, W.; Ma, J.; Fang, W.; Zheng, Y.; Du, C.-F.; Srinivasan, M.; Yan, Q., High-performance flexible quasi-solid-state zinc-ion batteries with layer-expanded vanadium oxide cathode and zinc/stainless steel mesh composite anode. *Nano Energy* **2019,** *62*, 94-102.
148. Yu, J.; Chen, F.; Tang, Q.; Gebremariam, T. T.; Wang, J.; Gong, X.; Wang, X., Ag-

Modified Cu Foams as Three-Dimensional Anodes for Rechargeable Zinc–Air Batteries. *ACS Applied Nano Materials* **2019,** *2* (5), 2679-2688.
149. Wang, X.; Wang, F.; Wang, L.; Li, M.; Wang, Y.; Chen, B.; Zhu, Y.; Fu, L.; Zha, L.; Zhang, L.; Wu, Y.; Huang, W., An Aqueous Rechargeable Zn//Co3 O4 Battery with High Energy Density and Good Cycling Behavior. *Advanced Materials* **2016,** *28* (24), 4904-11.
150. Ni, Q.; Kim, B.; Wu, C.; Kang, K., Non-Electrode Components for Rechargeable Aqueous Zinc Batteries: Electrolytes, Solid-Electrolyte-Interphase, Current Collectors, Binders, and Separators. *Advanced Materials* **2022,** *34* (20), e2108206.
151. Banczek, E. P.; Rodrigues, P. R. P.; Costa, I., The effects of niobium and nickel on the corrosion resistance of the zinc phosphate layers. *Surface and Coatings Technology* **2008,** *202* (10), 2008-2014.
152. Li, Y.; Xu, J., Is niobium more corrosion-resistant than commercially pure titanium in fluoride-containing artificial saliva? *Electrochimica Acta* **2017,** *233*, 151-166.
153. So, S.; Ahn, Y. N.; Ko, J.; Kim, I. T.; Hur, J., Uniform and oriented zinc deposition induced by artificial Nb2O5 Layer for highly reversible Zn anode in aqueous zinc ion batteries. *Energy Storage Materials* **2022,** *52*, 40-51.
154. Mozalev, A.; Vázquez, R. M.; Bittencourt, C.; Cossement, D.; Gispert-Guirado, F.; Llobet, E.; Habazaki, H., Formation–structure–properties of niobium-oxide nanocolumn arrays via self-organized anodization of sputter-deposited aluminum-on-niobium layers. *Journal of Materials Chemistry C* **2014,** *2* (24).
155. Luo, H.; Wang, B.; Wang, C.; Wu, F.; Jin, F.; Cong, B.; Ning, Y.; Zhou, Y.; Wang, D.; Liu, H.; Dou, S., Synergistic deficiency and heterojunction engineering boosted VO2 redox kinetics for aqueous zinc-ion batteries with superior comprehensive performance. *Energy Storage Materials* **2020,** *33*, 390-398.
156. Kresse, G.; Furthmuller, J., Efficiency of ab-initio total energy calculations for metals and semiconductors using a plane-wave basis set. *Computational Materials Science* **1996,** *6*, 15-50.
157. Kresse, G.; Furthmuller, J., Efficient iterative schemes for ab initio total-energy calculations using a plane-wave basis set. *Physical Review B* **1996,** *54*, 11169-11186.
158. Perdew, J. P.; Burke, K.; Ernzerhof, M., Generalized Gradient Approximation Made Simple. *Physical Review Letters* **1996,** *77*, 3865-3868.
159. Kresse, G.; Joubert, D., From ultrasoft pseudopotentials to the projector augmented-wave method. *Physical Review B* **1999,** *59*, 1758-1775.
160. Blochl, P. E., Projector augmented-wave method. *Physical Review B* **1994,** *50* (24), 17953-17979.

161. Zähr, J.; Ullrich, H.-J.; Oswald, S.; Türpe, M.; Füssel, U., Analyses about the influence of the natural oxide layer of aluminium on the brazeability in a shielding gas furnace. *Welding in the World* **2013,** *57* (4), 449-455.
162. Sato, N., An overview on the passivity of metals. *Corrosion Science* **1990,** *31*, 1-19.
163. Bach, D.; Stormer, H.; Schneider, R.; Gerthsen, D.; Verbeeck, J., EELS investigations of different niobium oxide phases. *Microsc Microanal* **2006,** *12* (5), 416-23.
164. Cui, Y.; Zhao, Q.; Wu, X.; Chen, X.; Yang, J.; Wang, Y.; Qin, R.; Ding, S.; Song, Y.; Wu, J.; Yang, K.; Wang, Z.; Mei, Z.; Song, Z.; Wu, H.; Jiang, Z.; Qian, G.; Yang, L.; Pan, F., An Interface-Bridged Organic-Inorganic Layer that Suppresses Dendrite Formation and Side Reactions for Ultra-Long-Life Aqueous Zinc Metal Anodes. *Angewandte Chemie International Edition* **2020,** *59* (38), 16594-16601.
165. Zheng, J.; Cao, Z.; Ming, F.; Liang, H.; Qi, Z.; Liu, W.; Xia, C.; Chen, C.; Cavallo, L.; Wang, Z.; Alshareef, H. N., Preferred Orientation of TiN Coatings Enables Stable Zinc Anodes. *ACS Energy Letters* **2021,** *7* (1), 197-203.
166. Yoon, R. H.; Salmon, T.; G.Donnay, Predicting points of zero charge of oxides and hydroxides. *Journal of Colloid Interface Science* **1979,** *70*, 483.
167. D. A. Sverjensky, Zero-point-of-charge prediction from crystal chemistry and solvation theory. *Geochim. Cosmochim. Acta* **1994,** *58*, 3123.
168. Kosmulski, M., Attempt To Determine Pristine Points of Zero Charge of Nb_2O_5, Ta_2O_5, and HfO_2. *Langmuir* **1997,** *13*, 6315-6320.
169. Gheytani, S.; Liang, Y.; Jing, Y.; Xu, J. Q.; Yao, Y., Chromate conversion coated aluminium as a light-weight and corrosion-resistant current collector for aqueous lithium-ion batteries. *Journal of Materials Chemistry A* **2016,** *4* (2), 395-399.
170. Zhu, R.; Yang, H.; Cui, W.; Fadillah, L.; Huang, T.; Xiong, Z.; Tang, C.; Kowalski, D.; Kitano, S.; Zhu, C.; King, D. R.; Kurokawa, T.; Aoki, Y.; Habazaki, H., High strength hydrogels enable dendrite-free Zn metal anodes and high-capacity Zn–MnO_2 batteries via a modified mechanical suppression effect. *Journal of Materials Chemistry A* **2022,** *10* (6), 3122-3133.
171.Muster, T. H.; Cole, I. S., The protective nature of passivation films on zinc: surface charge. *Corrosion Science* **2004,** *46* (9), 2319-2335.
172. Chen, L.; Zhang, H. W.; Liang, L. Y.; Liu, Z.; Qi, Y.; Lu, P.; Chen, J.; Chen, L.-Q., Modulation of dendritic patterns during electrodeposition: A nonlinear phase-field model. *Journal of Power Sources* **2015,** *300*, 376-385.
173. Jacquet, P. A., Electrolytic and Chemical Polishing. *Metallurgical Reviews* **2013,** *1* (1), 157-238.

174. Cogswell, D. A., Quantitative phase-field modeling of dendritic electrodeposition. *Physical Review E* **2015,** *92* (1), 011301.
175. Kovacheva, R.; Gidikova, N.; Lilova, A., A New Electropolishing Technique for Metallographic Specimen Preparation of Zinc and Zinc Alloys. *Materials Characterization* **1992,** *28*, 205-211.
176. Wan, T. H.; Saccoccio, M.; Chen, C.; Ciucci, F., Influence of the Discretization Methods on the Distribution of Relaxation Times Deconvolution: Implementing Radial Basis Functions with DRTtools. *Electrochimica Acta* **2015,** *184*, 483-499.
177. Ciucci, F.; Chen, C., Analysis of Electrochemical Impedance Spectroscopy Data Using the Distribution of Relaxation Times: A Bayesian and Hierarchical Bayesian Approach. *Electrochimica Acta* **2015,** *167*, 439-454.
178. Effat, M. B.; Ciucci, F., Bayesian and Hierarchical Bayesian Based Regularization for Deconvolving the Distribution of Relaxation Times from Electrochemical Impedance Spectroscopy Data. *Electrochimica Acta* **2017,** *247*, 1117-1129.
179. Chen, K.-H.; Wood, K. N.; Kazyak, E.; LePage, W. S.; Davis, A. L.; Sanchez, A. J.; Dasgupta, N. P., Dead lithium: mass transport effects on voltage, capacity, and failure of lithium metal anodes. *Journal of Materials Chemistry A* **2017,** *5* (23), 11671-11681.
180. Wang, L.; Huang, K. W.; Chen, J.; Zheng, J., Ultralong cycle stability of aqueous zinc-ion batteries with zinc vanadium oxide cathodes. *Science Advances* **2019,** *5* (10), eaax4279.
181. Pan, H. L.; Shao, Y. Y.; Yan, P. F.; Cheng, Y. W.; Han, K. S.; Nie, Z. M.; Wang, C. M.; Yang, J. H.; Li, X. L.; Bhattacharya, P.; Mueller, K. T.; Liu, J., Reversible aqueous zinc/manganese oxide energy storage from conversion reactions. *Nature Energy* **2016,** *1* (5).
182. Aleshin, A.; Bravo, S.; Redquest, K.; Wood, K. N., Rapid Oxidation and Reduction of Lithium for Improved Cycling Performance and Increased Homogeneity. *ACS Applied Materials Interfaces* **2021,** *13* (2), 2654-2661.
183. Chamoun, M.; Brant, W. R.; Tai, C. W.; Karlsson, G.; Noreus, D., Rechargeability of aqueous sulfate Zn/MnO_2 batteries enhanced by accessible Mn^{2+} ions. *Energy Storage Materials* **2018,** *15*, 351-360.
184. Kundu, D.; Vajargah, S. H.; Wan, L. W.; Adams, B.; Prendergast, D.; Nazar, L. F., Aqueous vs. nonaqueous Zn-ion batteries: consequences of the desolvation penalty at the interface. *Energy & Environmental Science* **2018,** *11* (4), 881-892.
185. T. Falk; Svensson, J. E.; Johansson, L. G., The Role of Carbon Dioxide in the Atmospheric Corrosion of Zinc: A Laboratory Study. *Journal of The Electrochemical Society 145*, 39-44.

186. Zhou, J.; Xie, M.; Wu, F.; Mei, Y.; Hao, Y.; Huang, R.; Wei, G.; Liu, A.; Li, L.; Chen, R., Ultrathin Surface Coating of Nitrogen-Doped Graphene Enables Stable Zinc Anodes for Aqueous Zinc-Ion Batteries. *Advanced Materials* **2021**, e2101649.
187. Fu, J.; Liang, R.; Liu, G.; Yu, A.; Bai, Z.; Yang, L.; Chen, Z., Recent Progress in Electrically Rechargeable Zinc-Air Batteries. *Advanced Materials* **2019,** *31*(31), e1805230.
188. Wang, D. H.; Han, C. P.; Mo, F. N.; Yang, Q.; Zhao, Y. W.; Li, Q.; Liang, G. J.; Dong, B. B.; Zhi, C. Y., Energy density issues of flexible energy storage devices. *Energy Storage Materials* **2020,** *28*, 264-292.
189. Chao, D.; Zhou, W.; Ye, C.; Zhang, Q.; Chen, Y.; Gu, L.; Davey, K.; Qiao, S. Z., An Electrolytic Zn-MnO_2 Battery for High-Voltage and Scalable Energy Storage. *Angewandte Chemie International Edition* **2019,** *58* (23), 7823-7828.
190. Guo, Z.; Ma, Y.; Dong, X.; Huang, J.; Wang, Y.; Xia, Y., An Environmentally Friendly and Flexible Aqueous Zinc Battery Using an Organic Cathode. *Angewandte Chemie International Edition* **2018,** *57* (36), 11737-11741.
191. Zhao, J.; Sonigara, K. K.; Li, J.; Zhang, J.; Chen, B.; Zhang, J.; Soni, S. S.; Zhou, X.; Cui, G.; Chen, L., A Smart Flexible Zinc Battery with Cooling Recovery Ability. *Angewandte Chemie International Edition* **2017,** *56* (27), 7871-7875.
192. Mo, F.; Liang, G.; Meng, Q.; Liu, Z.; Li, H.; Fan, J.; Zhi, C., A flexible rechargeable aqueous zinc manganese-dioxide battery working at −20 °C. *Energy & Environmental Science* **2019,** *12* (2), 706-715.
193. Huang, Y.; Zhang, J. Y.; Liu, J. W.; Li, Z. X.; Jin, S. Y.; Li, Z. G.; Zhang, S. D.; Zhou, H., Flexible and stable quasi-solid-state zinc ion battery with conductive guar gum electrolyte. *Materials Today Energy* **2019,** *14*, 100349.
194. Sun, N.; Lu, F.; Yu, Y.; Su, L.; Gao, X.; Zheng, L., Alkaline Double-Network Hydrogels with High Conductivities, Superior Mechanical Performances, and Antifreezing Properties for Solid-State Zinc-Air Batteries. *ACS Appllied Materials Interfaces* **2020,** *12* (10), 11778-11788.
195. Cheng, X.-B.; Zhang, Q., Dendrite-free lithium metal anodes: stable solid electrolyte interphases for high-efficiency batteries. *Journal of Materials Chemistry A* **2015,** *3* (14), 7207-7209.
196. Sand, H. J. S., III. On the concentration at the electrodes in a solution, with special reference to the liberation of hydrogen by electrolysis of a mixture of copper sulphate and sulphuric acid. *The London, Edinburgh, and Dublin Philosophical Magazine and Journal of Science* **2010,** *1* (1), 45-79.
197. Li, C.; Sun, Z.; Yang, T.; Yu, L.; Wei, N.; Tian, Z.; Cai, J.; Lv, J.; Shao, Y.; Rummeli,

M. H.; Sun, J.; Liu, Z., Directly Grown Vertical Graphene Carpets as Janus Separators toward Stabilized Zn Metal Anodes. *Advanced Materials* **2020,** *32* (33), e2003425.
198. Parker, J. F.; Nelson, E. S.; Wattendorf, M. D.; Chervin, C. N.; Long, J. W.; Rolison, D. R., Retaining the 3D framework of zinc sponge anodes upon deep discharge in Zn–air cells. *ACS Appllied Materials Interfaces* **2014,** *6* (22), 19471-19476.
199. Yan, K.; Lu, Z.; Lee, H.-W.; Xiong, F.; Hsu, P.-C.; Li, Y.; Zhao, J.; Chu, S.; Cui, Y., Selective deposition and stable encapsulation of lithium through heterogeneous seeded growth. *Nature Energy* **2016,** *1* (3).
200. Krauskopf, T.; Richter, F. H.; Zeier, W. G.; Janek, J., Physicochemical Concepts of the Lithium Metal Anode in Solid-State Batteries. *Chem Rev* **2020,** *120* (15), 7745-7794.
201. Takeda, Y.; Yamamoto, O.; Imanishi, N., Lithium Dendrite Formation on a Lithium Metal Anode from Liquid, Polymer and Solid Electrolytes. *Electrochemistry* **2016,** *84* (4), 210-218.
202. Yang, C.; Fu, K.; Zhang, Y.; Hitz, E.; Hu, L., Protected Lithium-Metal Anodes in Batteries: From Liquid to Solid. *Advanced Materials* **2017,** *29* (36).
203. Hong, Z.; Ahmad, Z.; Viswanathan, V., Design Principles for Dendrite Suppression with Porous Polymer/Aqueous Solution Hybrid Electrolyte for Zn Metal Anodes. *ACS Energy Letters* **2020,** *5* (8), 2466-2474.
204. Monroe, C.; Newman, J., The Effect of Interfacial Deformation on Electrodeposition Kinetics. *Journal of The Electrochemical Society* **2004,** *151*, 880-886.
205. Zhang, X.; Wang, A.; Liu, X.; Luo, J., Dendrites in Lithium Metal Anodes: Suppression, Regulation, and Elimination. *Accounts of Chemical Ressearch* **2019,** *52* (11), 3223-3232.
206. Wang, J.; Polleux, J.; Lim, J.; Dunn, B., Pseudocapacitive Contributions to Electrochemical Energy Storage in TiO_2 (Anatase) Nanoparticles. *The Journal of Physical Chemistry C* **2007,** *111*, 14925-14931.
207. Gong, J. P., Why are double network hydrogels so tough? *Soft Matter* **2010,** *6* (12), 2583.
208. Nakajima, T.; Furukawa, H.; Tanaka, Y.; Kurokawa, T.; Osada, Y.; Gong, J. P.; True Chemical Structure of Double Network Hydrogels. *Macromolecules* **2009,** *42*, 2184-2189.
209. Gong, J. P.; Katsuyama, Y.; Kurokawa, T.; Osada, Y., Double-Network Hydrogels with Extremely High Mechanical Strength. *Advanced Materials* **2003,** *15* (14), 1155-1158.
210. Mo, F.; Chen, Z.; Liang, G.; Wang, D.; Zhao, Y.; Li, H.; Dong, B.; Zhi, C., Zwitterionic Sulfobetaine Hydrogel Electrolyte Building Separated Positive/Negative Ion Migration Channels for Aqueous Zn-MnO_2 Batteries with Superior Rate Capabilities. *Advanced Energy Materials* **2020,** *10* (16), 2000035.

211. Song, Z.; Ding, J.; Liu, B.; Liu, X.; Han, X.; Deng, Y.; Hu, W.; Zhong, C., A Rechargeable Zn-Air Battery with High Energy Efficiency and Long Life Enabled by a Highly Water-Retentive Gel Electrolyte with Reaction Modifier. *Advanced Materials* **2020,** *32* (22), e1908127.
212. Lu, Y.; Zhu, T.; Xu, N.; Huang, K., A Semisolid Electrolyte for Flexible Zn-Ion Batteries. *ACS Applied Energy Materials* **2019,** *2* (9), 6904-6910.
213. Chao, D.; Zhu, C. R.; Song, M.; Liang, P.; Zhang, X.; Tiep, N. H.; Zhao, H.; Wang, J.; Wang, R.; Zhang, H.; Fan, H. J., A High-Rate and Stable Quasi-Solid-State Zinc-Ion Battery with Novel 2D Layered Zinc Orthovanadate Array. *Advanced Materials* **2018,** *30* (32), e1803181.
214. Zhang, Y.; Zhong, Y.; Shi, Q.; Liang, S.; Wang, H., Cycling and Failing of Lithium Metal Anodes in Carbonate Electrolyte. *The Journal of Physical Chemistry C* **2018,** *122* (37), 21462-21467.
215. Ely, D. R.; Jana, A.; García, R. E., Phase field kinetics of lithium electrodeposits. *Journal of Power Sources* **2014,** *272*, 581-594.
216. Jana, A.; García, R. E., Lithium dendrite growth mechanisms in liquid electrolytes. *Nano Energy* **2017,** *41*, 552-565.
217. Ren, X.; Chen, S.; Lee, H.; Mei, D.; Engelhard, M. H.; Burton, S. D.; Zhao, W.; Zheng, J.; Li, Q.; Ding, M. S.; Schroeder, M.; Alvarado, J.; Xu, K.; Meng, Y. S.; Liu, J.; Zhang, J.-G.; Xu, W., Localized High-Concentration Sulfone Electrolytes for High-Efficiency Lithium-Metal Batteries. *Chem* **2018,** *4* (8), 1877-1892.
218. Zhang, H.; Eshetu, G. G.; Judez, X.; Li, C.; Rodriguez-Martinez, L. M.; Armand, M., Electrolyte Additives for Lithium Metal Anodes and Rechargeable Lithium Metal Batteries: Progress and Perspectives. *Angewandte Chemie International Edition* **2018,** *57* (46), 15002-15027.
219. Xu, K., Nonaqueous Liquid Electrolytes for Lithium-Based Rechargeable Batteries. *Chemical Reviews* **2004,** *104*, 4303-4417.
220. Cao, J.; Zhang, D.; Zhang, X.; Sawangphruk, M.; Qin, J.; Liu, R., A universal and facile approach to suppress dendrite formation for a Zn and Li metal anode. *Journal of Materials Chemistry A* **2020,** *8* (18), 9331-9344.
221. Yang, F., Modeling analysis for the growth of a Li sphere and Li whisker in a solid-state lithium metal battery. *Phys Chem Chem Phys* **2020,** *22* (24), 13737-13745.
222. Wang, Y.; Wang, Z.; Lei, D.; Lv, W.; Zhao, Q.; Ni, B.; Liu, Y.; Li, B.; Kang, F.; He, Y. B., Spherical Li Deposited inside 3D Cu Skeleton as Anode with Ultrastable Performance. *ACS Appl Mater Interfaces* **2018,** *10* (24), 20244-20249.
223. Monroe, C.; Newman, J., The Impact of Elastic Deformation on Deposition Kinetics

at Lithium/Polymer Interfaces. *Journal of The Electrochemical Society* **2005,** *152*, A396-404.
224. Nørskov, J. K.; Bligaard, T.; Logadottir, A.; Kitchin, J. R.; Chen, J. G.; Pandelov, S.; Stimming, U., Trends in the Exchange Current for Hydrogen Evolution. *Journal of The Electrochemical Society* **2005,** *152*, J23-26.
225. Yurkiv, V.; Foroozan, T.; Ramasubramanian, A.; Ragone, M.; Shahbazian-Yassar, R.; Mashayek, F., Understanding Zn Electrodeposits Morphology in Secondary Batteries Using Phase-Field Model. *Journal of The Electrochemical Society* **2020,** *167* (6).
226. Wu, B.; Lu, W., A consistently coupled multiscale mechanical–electrochemical battery model with particle interaction and its validation. *Journal of the Mechanics and Physics of Solids* **2019,** *125*, 89-111.
227. Ahmad, Z.; Viswanathan, V., Stability of Electrodeposition at Solid-Solid Interfaces and Implications for Metal Anodes. *Physical Review Letters* **2017,** *119* (5), 056003.
228. Ahmad, Z.; Viswanathan, V., Role of anisotropy in determining stability of electrodeposition at solid-solid interfaces. *Physical Review Materials* **2017,** *1* (5).
229. Jiang, Y.; Ba, D.; Li, Y.; Liu, J., Noninterference Revealing of "Layered to Layered" Zinc Storage Mechanism of delta-MnO_2 toward Neutral Zn-Mn Batteries with Superior Performance. *Advanced Science* **2020,** *7* (6), 1902795.
230. Mateos, M.; Makivic, N.; Kim, Y. S.; Limoges, B.; Balland, V., Accessing the Two-Electron Charge Storage Capacity of MnO_2 in Mild Aqueous Electrolytes. *Advanced Energy Materials* **2020,** *10* (23), 2000332.
231. Jiang, Y.; Ba, D.; Li, Y.; Liu, J., Noninterference Revealing of “Layered to Layered” Zinc Storage Mechanism of δ-MnO_2 toward Neutral Zn–Mn Batteries with Superior Performance. *Advanced Science* **2020**, 1902795.
232. Wang, D.; Wang, L.; Liang, G.; Li, H.; Liu, Z.; Tang, Z.; Liang, J.; Zhi, C., A Superior delta-MnO_2 Cathode and a Self-Healing Zn-delta-MnO_2 Battery. *ACS Nano* **2019,** *13* (9), 10643-10652.
233. Augustyn, V.; Simon, P.; Dunn, B., Pseudocapacitive oxide materials for high-rate electrochemical energy storage. *Energy & Environmental Science* **2014,** *7* (5).
234. Wang, L.; Wang, X. T.; Zhong, J. H.; Xiao, K.; Ouyang, T.; Liu, Z. Q., Filling the Charge-Discharge Voltage Gap in Flexible Hybrid Zinc-Based Batteries by Utilizing a Pseudocapacitive Material. *Chemistry* **2021**.
235. Liang, G.; Mo, F.; Li, H.; Tang, Z.; Liu, Z.; Wang, D.; Yang, Q.; Ma, L.; Zhi, C., A Universal Principle to Design Reversible Aqueous Batteries Based on Deposition–Dissolution Mechanism. *Advanced Energy Materials* **2019,** *9* (32), 1901838.
236. Seo, J. K.; Shin, J.; Chung, H.; Meng, P. Y.; Wang, X.; Meng, Y. S., Intercalation and

Conversion Reactions of Nanosized β-MnO_2 Cathode in the Secondary Zn/MnO2 Alkaline Battery. *The Journal of Physical Chemistry C* **2018,** *122* (21), 11177-11185.
237. Simon, P.; Gogotsi, Y.; Dunn, B., Where Do Batteries End and Supercapacitors Begin? *Science* **2014,** *343*, 1210-1211.
238. Augustyn, V.; Come, J.; Lowe, M. A.; Kim, J. W.; Taberna, P. L.; Tolbert, S. H.; Abruna, H. D.; Simon, P.; Dunn, B., High-rate electrochemical energy storage through Li^+ intercalation pseudocapacitance. *Nature Materials* **2013,** *12* (6), 518-22.
239. Chen, H.; Cai, S.; Wu, Y.; Wang, W.; Xu, M.; Bao, S. J., Successive electrochemical conversion reaction to understand the performance of aqueous Zn/MnO_2 batteries with Mn^{2+} additive. *Materials Today Energy* **2021,** *20*.
240. Zhu, Y.; Wang, C., Galvanostatic Intermittent Titration Technique for Phase Transformation Electrodes. *Journal of Physical chemistry C* **2010,** *6*, 2830-2841.
241. Jia, X.; Liu, C.; Neale, Z. G.; Yang, J.; Cao, G., Active Materials for Aqueous Zinc Ion Batteries: Synthesis, Crystal Structure, Morphology, and Electrochemistry. *Chemical Reviews* **2020,** *120* (15), 7795-7866.

List of Publication

1. **Ruijie Zhu**, Nan Sheng, Zhonghao Rao, Chunyu Zhu, Yoshitaka Aoki, Hiroki Habazaki, "Employing a T-shirt template and variant of Schweizer's reagent for constructing a low-weight flexible, hierarchically porous and textile structured copper current collector for dendrite suppressed Li metal", *Journal of Materials Chemistry A*, **2019**, 7, 27066-27073.

2. **Ruijie Zhu**, Chunyu Zhu, Nan Sheng, Zhonghao Rao, Yoshitaka Aoki, Hiroki Habazaki, "A widely applicable strategy to convert fabrics into lithiophilic textile current collector for dendrite-free and high-rate capable lithium metal anode", *Chemical Engineering Journal*, **2020**, 385 124256.

3. **Ruijie Zhu**, Huijun Yang, Laras Fadillah, Zetao Xiong, Damian Kowalski, Chunyu Zhu, Sho Kitano, Yoshitaka Aoki, Hiroki Habazaki, "A lithiophilic carbon scroll as a Li metal host with low tortuosity design and "Dead Li" self-cleaning capability", *Journal of Materials Chemistry A*, **2021**, 9, 13332-13343.

4. **Ruijie Zhu**, Huijun Yang, Wei Cui, Laras Fadillah, Tianhong Huang, Zetao Xiong, Chunmei Tang, Damian Kowalski, Sho Kitano, Chunyu Zhu, Daniel R. King, Takayuki Kurokawa, Yoshitaka Aoki, Hiroki Habazaki, "High strength hydrogels enable dendrite-free Zn metal anodes and high-capacity Zn–MnO_2 batteries via a modified mechanical suppression effect", *Journal of Materials Chemistry A*, **2022**, 10, 3122-3133.

5. **Ruijie Zhu**, Zetao Xiong, Huijun Yang, Tianhong Huang, Seongwoo Jeong, Damian Kowalski, Sho Kitano, Yoshitaka Aoki, Hiroki Habazaki, Chunyu Zhu, "A low-cost and non-corrosive electropolishing strategy for long-life zinc metal anode in rechargeable aqueous battery", *Energy Storage Materials*, **2022**, 46, 223-232.

6. **Ruijie Zhu**†, Zetao Xiong†, Huijun Yang, Ning Wang, Sho Kitano, Yoshitaka Aoki, Hiroki Habazaki, Chunyu Zhu, "Anode/cathode Dual-purpose Aluminum Current Collectors for Aqueous Zinc-ion Batteries", *Advanced Functional Materials*, **2022**, 2211274.

7. Huijun Yang†, **Ruijie Zhu†**, Zhi Chang, Ping He, Chunyu Zhu, Sho Kitano, Yoshitaka Aoki, Hiroki Habazaki, Haoshen Zhou, "High-energy aqueous batteries enabled by stress-governed zinc electrodeposition", *Energy &Environmental Science*

(DOI https://doi.org/10.1039/D2EE03777G).

8. Pan Guo, Nan Sheng, **Ruijie Zhu,*** Chunyu Zhu,* and Zhonghao Rao, "Improved Anisotropic Thermal Transfer Property of Form-Stable Phase Change Material Supported by 3D Bionic Porous Copper",*ACS Sustainable Chemistry & Engineering.* **2023**, 11, 3324-3333.

The 4, 5, 6 three papers are included in this dissertation.

(†: These authors contributed equally)

Acknowledgement

It is with immense gratitude and warmth that I begin the acknowledgements for those people who help me a lot during my doctor course. As I reflect upon the invaluable journey of the past five years spent in Japan, I cannot help but be deeply appreciative of the incredible experiences, opportunities, and relations I have been fortunate enough to encounter. Although there was an outbreak of COVID-19 in the middle of my study- abroad-life, this also caused some trouble in my life and study, the kindness and generosity of the people I encountered have left an indelible mark on my heart, and it is to them that I owe a debt of gratitude that goes beyond words.

I would firstly like to express my gratitude to my two main supervisors: **Professor Hiroki Habazaki** and **Professor Chunyu Zhu**. I would like to extend my heartfelt gratitude to Prof. Habazaki, a remarkable mentor, and an inspiring figure. Prof. Habazaki's vast knowledge, kindness, and unwavering dedication to research have been a constant source of motivation and guidance throughout my academic journey. I am incredibly fortunate to have had the opportunity to learn from and work under his tutelage. Prof. Habazaki's enthusiasm for exploring new ideas and his open-mindedness towards novel topics have provided me with a nurturing research environment where my imagination could flourish. This atmosphere has played a pivotal role in enabling me to persevere through the challenging path of academic research. I am eternally grateful for Prof. Habazaki's support and for the invaluable lessons he has imparted upon me, both in research and life.

And I would like to express my profound appreciation to Prof. Zhu, who has generously provided me with unwavering support and assistance throughout my academic journey. Prof. Zhu has devoted a significant amount of time to meticulously reviewing and correcting my thesis, offering invaluable guidance at every step of the process. In addition to being a remarkable mentor, Prof. Zhu has been a true friend, and it is difficult to imagine the successful completion of my studies without his help. I am extremely grateful for the constant encouragement, insights, and expertise that Prof. Zhu has offered me during this journey.

To my two main supervisors, Prof. Habazaki and Prof. Zhu, I extend my deepest respect and

gratitude. Your dedication and commitment to my academic and personal growth have been nothing short of extraordinary.

Before showing my appreciation to the other teachers who helped me a lot, I would like to express my gratitude to **Dr. Daniel R. King** alone, although Dr. Daniel sadly passed away in 2022. Since I came to Hokkaido University and joined the ALP program, and met Dr. Dan, Dan took on the task of helping me revise various English proposals and papers for a long time. He was also my guide in polymer physics and chemistry, and we designed many interesting materials and experiments together, Dan was always supportive of my strange imaginations and designs. Dan is also a great friend to me during my studies at Hokkaido University, he is an enthusiastic but relaxed person, and his tea-time was once a port of call for many Chinese students. Although Daniel probably will not be able to read this, I would like to express my most sincere gratitude to him: Thank you, and R.I.P.

Furthermore, I would like to extend my sincere gratitude to two other esteemed professors in our research group, **Prof. Yoshitaka Aoki** and **Dr. Sho Kitano**. I am deeply appreciative of the numerous ways they have supported and guided me throughout the years, both in the laboratory and in my daily life. Their help in various aspects of my academic and personal growth has been invaluable, and I am truly grateful for their unwavering commitment to my success.

Then I wish to express my gratitude to all the professors who have provided me with selfless assistance during my doctoral studies, including: **Professor Kiyoharu Tadanaga**, **Professor Kei Murakoshi**, **Professor Jianping Gong**, **Professor Kazuhisa Azumi**, **Professor Koji Fushimi**, **Professor Nan Sheng**, and **Professor Damian Kowalski**, I would like to express my most sincere thanks to you.

Also, I would like to express my appreciation to people in all the research groups that I have studied in. To everyone in the Laboratory of Interfacial Electrochemistry, thank you for your help and support during my study abroad. Special thanks to **Dr. Ning Wang**, **Dr. Yuki Sato**, **Dr. Seongwoo Jeong**, **Dr. Laras Fadillah**, **Dr. Chunmei Tang**, **Dr. Hajime Toriumi**, **Mr. Zetao Xiong, Ms. Yoko Iwata, and Ms. Miki Oda**. Thank you all for your selfless help and I hope to

stay in touch with you all in the future as well. I would also like to thank **Dr. Kim Cheong**, **Mr. Naohito Yamada** and other graduates for their help when I first came to Japan. To everyone in the Laboratory of Soft & Wet Matter, thank you also for your long-term understanding and support. Special thanks to **Dr. Wei Cui**, **Dr. Qifeng Mu**, **Dr. Yong Zheng**, **Dr. Xueyu Li**, and **Dr. Yanan Ye**. Thank you all for helping me with my life and experiments. It was a very happy time for me to chat with everyone at LSW. Special thanks to Junjun, **Dr. Huijun Yang**, my closest friend and partner since I came to Japan, for his help during these years. In the most difficult period we complemented each other's strengths and weaknesses to support each other to today, and I wish us all the best for the future.

I am truly honored and humbled to have had the opportunity to learn from and work with such these outstanding individuals.

In addition, I would like to thank the ALP program of Hokkaido University for their support and assistance in my career development and research. And I would like to express my gratitude to all the teachers and staffs of the Ambitious Leader's Program (ALP) at Hokkaido University. In particular, I would like to express my gratitude to **Prof. Atsushi Nanasawa**, **Prof. Akiko Nakatomi**, **Prof. Schuko Ohtsu** and **Ms. Kumi Fukuda**. Also, I would like to thank Hokkaido University and Japan Society for the Promotion of Science (JSPS) for their support in economics and research during my study.

Moreover, I would like to thank my friends, **Dr. Tianhong Huang**, **Mr. Jingzhong Zhang**, **Mr. Jingmao Wu**, **Mr. Shuolin Zhu**, **Mr. Yufang Zheng**, **Mr. Ruochen Pan**, **Mr. Liwei Wang** and some others for their continuous support and help with my studies. I would like to thank you all for your contribution to my studies and your willingness to help me relieve my stress.

Many thanks to **Ms. Lili Tang** for helping me with the beautiful schematic diagram of my papers. Thank you for your constant silent support, and for the soft and gentle shell you gave me during my saddest period. I must apologize for that the squirrel couldn't be the hero for the bear, but I hope the bear will be happy and smooth sailing in the future life.

At the end of the acknowledgement section, I would be remiss if I did not express my heartfelt gratitude to the constant source of strength and encouragement in my life – my family. Foremost, I would like to extend my sincerest thanks to my father, Mr. Jun Zhu, and my mother, Mrs. Aize Luo. Their unwavering dedication, selflessness, and support in every decision I have made have been instrumental in shaping the person I am today. Their love and guidance have provided me with a strong foundation, and for that, I am eternally grateful. Well, it may be sad and inappropriate to say this finally, but my life so far has been full of all kinds of absurd drama, thus I was once very afraid that these ridiculous scenes would stay with me for my whole life. But even so, I still hope and believe that someday in the future I will be able to smile and proudly say thank you, my dearest student, also, my wife.